WALL BUILD-UP IN SPRAY DRYERS

by

Guy James Hassall

A thesis submitted to

The University of Birmingham

for the degree of

Engineering Doctorate (EngD)

School of Chemical Engineering

University of Birmingham

July 2011

Abstract

Most granular laundry detergents are manufactured through spray drying. One drawback of this process is wall build-up, which negatively effects process operation, safety and product quality.

Macro and micro-scale observations showed the amount and micro-structure of deposits changed significantly across the dryer. These changes were linked to changes in particle properties during drying. Measurements of deposition ranged from 1 - 10 kgm^{-2}, or 2 - 10% of the total slurry sprayed, depending on location, operating conditions and slurry/powder properties. Wall deposition appeared to be time dependent.

Wall deposition was broken down into two critical steps; collision frequency, describing how many and how often particles hit the wall and, collision success rate which describes particle's behaviour upon contact with the wall. Collision frequency was investigated using Particle Imagine Velocimetry (PIV) to measure both fluid and particle dynamics. Finding both to be time dependent, and to vary with position and operating conditions.

To investigate collision success rate, particle physical and mechanical properties were studied, revealing mutual dependence of all properties on both formulation and particle size. Impacting these particles at a range of velocities and angles found that the fraction of particles that broke ranged from 0 - 100% and restitution coefficients from 0.1 - 0.8.

This thesis is dedicated to my parents

“All’s well that ends well”

- William Shakespeare (1605)

Acknowledgements

First of all I would like to thank my supervisors, each of whom, in their own way have helped, encouraged and enabled me to produce this thesis. Mark Simmons who has supervised me academically, ensuring that my collection of work and ideas finally became a submittable thesis. Carlos Amador who challenged me to think and sometimes even act like an engineer. I would like to thank Andrew Bayly for setting up the project and inputting his expertise.

I also want to acknowledge people beyond my supervisors who helped. Richard Greenwood deserves great credit for dealing with both me and the administrative side of the EngD. At P&G Zayeed Alam who managed my work within the company. I also have to give special mention to HongSing Tan for the advice, wisdom and sometimes therapy he gave me. I'd like to thank Nicola Tilt for her help with statistics. It is only right that I take this opportunity to thank the students who I had the fortune of working with in some capacity and whose work contributed towards this thesis, my thanks go out to Lena, Wan and Andrew. I also acknowledge the support of P&G and EPSRC. I would like to thank Martin Hyde of TSI for his technical input and support on the PIV work.

I'd like to thank family and friends, especially my parents for their support during my many years of education. All of the people in Newcastle who I have had the pleasure of calling friends over the last 5 years, you are too numerous to name, but thanks to all of you, the Iranians, French, Scots, Malaysians, Irish and Spaniards, not to forget the Geordies. You all made my time in Newcastle something I will struggle to either forget or get over easily. Special thanks to Becks for her help and support, especially at the beginning and end of this EngD.

Table of Contents

List of Figures

List of Tables

Nomenclature

Symbols

A_w	water activity
C	particle number concentration
d	diameter
e	restitution coefficient
I	turbulence intensity – dimensionless
L_{IA}	interrogation area length - m
n	number of velocity values
m	mass
k	turbulence kinetic energy - $kJ.kg^{-1}$
r	radial position
R	Reynolds stresses
R	spatial cross-correlation function of the transmitted light intensity
S	swirl number
ū	mean velocity - ms^{-1}
u’	fluctuating components of velocity - ms^{-1}
ũ	root mean square of fluctuating components of velocity - ms^{-1}
U	instantaneous velocity - ms^{-1}
v	volume
x	x position in Cartesian coordinates
y	y position in Cartesian coordinates
θ	the angle between the x dimension and tangent to curvature of wall - radians
μ	viscosity

ρ	density
τ	relaxation time
σ	stress

Subscripts

h	horizontal plane
i	impact
n	normalised
p	particle
r	radial in cylindrical coordinates
r	rebound
x	tangential Cartesian coordinates
y	radial in Cartesian coordinates
z	axial in both Cartesian and cylindrical coordinates
Θ	tangential in cylindrical coordinates

Chapter 1 – Introduction

1.1 Introduction

The focus of this thesis is wall deposition in spray dryers formed during the manufacture of granular laundry detergents. This project was undertaken as an Engineering Doctorate (EngD) in Formulation Engineering at the School of Chemical Engineering at the University of Birmingham, with Procter and Gamble (P&G) as the industrial partner.

Laundry detergents are used all over the globe to aid the cleaning of garments during washing. Detergent products are supplied in a variety of physical forms (Bajpai and Tyagi (2007)) such as powders, liquids and bar soaps. Additionally unit dose forms such as solid tablets (compressed powder of a different formulation to loose powder) and liquitabs (liquid detergent encased in a membrane that dissolves upon water contact) have been introduced in recent years. The type of detergent and how the consumer uses the product depends mainly on their geographical location (de Groot *et al.* (1995)). In industrialised geographies the majority of consumers use automatic washing machines (where the main cleaning action is carried out mechanically), however the type of machine and detergent compatibility varies between country and region. In developing nations the majority of consumers still wash their laundry by hand.

Consumers have different requirements from laundry detergents, depending on their location and wash method. In general, consumers want a product to perform well and deliver good cleaning whilst protecting their garments. Consumers also expect the product to look and smell appealing. The challenge of detergent manufacturers is to delight the

consumer by meeting, and where possible, exceeding, these expectations so that the consumers become regular users of their products. In the 21st century society is demanding increased levels of environmental consideration from products and from the companies that make them, adding further pressure on manufacturers to consistently improve their environmental impact and sustainability credentials of their products (Huntington (2004)).

This research is concerned with granular laundry detergents. There are two main process routes for manufacturing granular detergents, agglomeration and spray drying. Agglomeration involves mixing small particles together with a liquid binder to form bigger granules with more desirable properties such as flowability. Spray drying is the process of atomising a feed slurry into small droplets which are then contacted with hot air to dry them and form a powder product. This project is focussed solely on detergents produced through spray drying.

Spray drying is defined by Masters (1991) as "the transformation of feed from a fluid state into a dried particulate form by spraying the feed into a hot drying medium". The process of using spray drying to manufacture detergents was developed in the 1930s and 1940s (Dyer *et al.* (2004)). Masters (1991) describes 4 main stages in the generic spray drying process:

1. Atomisation – the break-up of the feed slurry to form small droplets.

2. Spray air contact – the movement of the atomised droplets through the drying air, resulting in heat transfer from the air to the droplet.

3. Drying of droplets/sprays – the process of mass transfer of drying as the water migrates from the droplets.

4. Separation and recovery of dried product – capture and handling of the powder product after drying.

In addition to these four generic stages, detergent manufacture includes two other major steps, slurry preparation and pumping before atomisation and powder mixing, handling and packing after the powder is dried. Figure 1.1 shows a simplified layout of the detergent spray drying process taken from Bayly (2004).

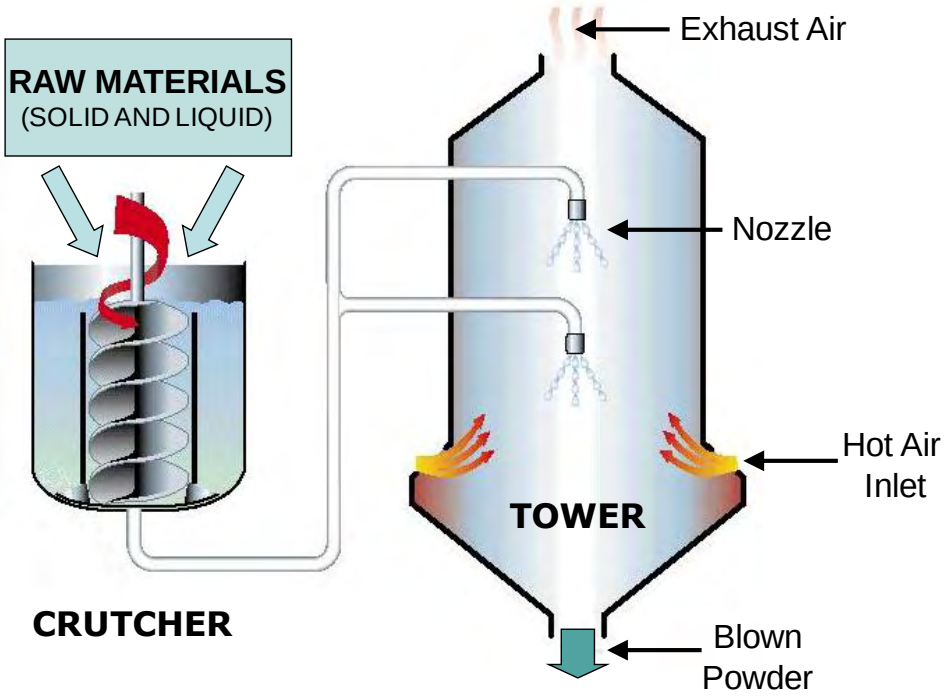

Figure 1.1: Simplified Detergent Spray Drying Process taken from Bayly (2004)

Spray drying has several advantages for manufacturing detergents over its rival processes such as agglomeration, these can be summarised as:

1. Ability to form a free flowing powder directly from a liquid (slurry) feedstock (Oakley (2004)).

2. High throughput and continuous operation of the process (Masters (1991)).

3. Control of particle/powder properties such as size distribution, porosity and bulk density. All of which are desired by the consumer (de Groot *et al.* (1995)).

4. Proven technology widely used with large amounts of operational experience (Chaloud *et al.* (1957)).

Spray drying also has several drawbacks, including wall deposition which has a negative effect on both product quality and process operation. This phenomenon is the focus of this research and the reasons behind this choice are discussed in detail in the next section.

1.2 Business Case and Benefits

Wall deposition, or wall build-up is the collection of layers of material onto the walls of process equipment in powder handling operations. It is formed when product particles adhere to the surface (Cleaver (2008)). The amount of wall build-up observed varies depending on location, process operating conditions, material formulation and duration of operation. As mentioned before, this is one of the major drawbacks in spray drying as a manufacturing route for products such as detergents.

Wall build-up is observed in virtually all spray drying processes according to Bayly (2005) and Masters (1991). Detergent spray drying is no different, with build-up observed at all stages of the process where powder is present. Build-up is observed within the drying chamber, exhaust system and post-dryer handling systems where powder is mixed, stored and packed. The focus of this research is on build-up in the drying chamber which has the most significant effect on process operation and product quality as described by Bayly (2005).

Wall build-up in the drying chamber can have a significant effect on process operating conditions, operational safety, process reliability and maintenance/cleaning requirements. Perhaps more importantly it also has an effect on product quality. Product colour, particle size distribution, particle morphology and chemical activity can all be affected. Each of these is interlinked and is described in more detail in Chapter Two as the background to this work is laid out.

The work presented in this thesis is part of a larger program of work within Procter and Gamble to develop better understanding and therefore modelling capability of spray drying processes for detergent manufacture. Understanding and modelling of spray drying enables the process to be operated more efficiently in terms of materials and energy usage, production capacity to be optimised, product quality improved and delivered more consistently and quicker scale-up and process development which requires less experimental work and fewer pilot plant trials. All of these factors improve the economics of granular detergent manufacture and process development.

1.3 Project Objectives

The overall aim of this project is to develop an understanding of wall build-up in spray dryers. In order to focus the research, this goal can be broken down into a logical sequence of steps, the first being to understand the nature of wall deposition and then breaking the mechanism that leads to wall deposition into two steps, particles coming into contact with the walls (collision frequency) and then what happens when particles hit the wall (impact behaviour). These steps are broken down into the following questions:

1. Where in the spray drying process does wall deposition occur? Thus, which areas of the spray drying process experience the highest levels of deposition?
2. How does product formulation and plant operating conditions affect wall deposition?
3. What airflow patterns are formed within the dryer? How do these influence the movement of particles through the dryer?
4. How do particles move through the spray dryer? How do particles impact on the dryer walls? What are the properties of particles striking the dryer walls?
5. Can the impacts of particles on the dryer walls be reproduced in the laboratory and how do particle characteristics affect these impacts?

1.4 Outline of Thesis

Chapter Two – Literature Review

This chapter introduces granular detergent products, their formulation and manufacture through spray drying. Published research of relevance in the area of spray drying and detergents is examined and critically reviewed such that the context of this work is laid out. Details of theories and principles used and applied during this work are also given.

Chapter Three – Materials and Methods

The experimental methods, equipment and materials used in this work are described in chapter three. The justification for each technique and the set-up used for each set of experiments is also provided.

Chapter Four – Wall Deposition in Detergent Spray Dryers

The spray drying process is examined to identify areas where deposition occurs and methods developed to measure this deposition during plant operation with different formulations

and conditions. Chapter four tackles the first two questions posed earlier in this chapter "Where in the spray drying process does wall deposition occur? Which areas experience the highest levels of deposition?" and "How does formulation and plant operating conditions affect wall deposition?"

Chapter Five – Fluid Dynamics inside a Detergent Spray Dryer

The air flow patterns inside spray dryers are widely acknowledged to heavily influence particle movement through the dryer, and therefore both product quality and process operation. Chapter five covers experiments to study air flow patterns inside a counter current detergent spray dryer to answer the questions "What airflow patterns are formed within the dryer? How do these patterns influence the movement of particles through the dryer?"

Chapter Six – Particle Dynamics inside a Detergent Spray Dryer

Experiments to visualise particles drying inside of the spray dryer are reported here. The size distribution, concentration, volume fraction and velocities of particles are presented as a function of both location within the dryer and dryer operating conditions. This enabled the following questions to be answered "How particles move through the spray dryer? How do particles impact on the dryer walls? What are the properties of particles striking the dryer walls?"

Chapter Seven – The Properties and Impact Behaviour of Spray Dried Detergent Granules

The physical and mechanical properties of detergent particles are known to significantly affect the impact behaviour and therefore deposition of detergent particles. The first part of this chapter covers experiments and measurements to characterise these properties for various detergent formulations. The impact behaviour of detergent granules determines if

particles will stick to process equipment walls to form wall build-up. The second part of this chapter covers experiments to investigate the particle impact behaviour to tackle the questions, “Can these impacts be reproduced in the laboratory? How do particle characteristics affect these impacts?”

Chapter Eight – Conclusions

The final chapter of the thesis brings together the previous chapters to draw overall conclusions on the research. These are collated into a detailed summary of wall deposition and the variables which affect it. Recommendations for further work and future projects are discussed along with their relevance to the current detergent industry.

1.5 Publications Arising from this Work

Hassall, G.J., Amador, C., Bayly, A.E. and Simmons, M.J.H, *The Impact Behaviour of Spray Dried Detergent Granules*, 16th International Drying Symposium (IDS 2008), November 2008, Hyderabad (India). Oral presentation and conference paper.

Hassall, G.J., Amador, C., Bayly, A.E. and Simmons, M.J.H, *The Impact Behaviour of Spray Dried Detergent Granules*, (In preparation)

Hassall, G.J., Amador, C., Bayly, A.E. and Simmons, M.J.H, *Particle and Fluid Dynamics inside a Counter-current Detergent Spray Dryer* , (In preparation)

Chapter 2 – Literature Review

2.1 Introduction

This Chapter introduces granular laundry detergents, their formulation and manufacture through spray drying, together with details of theories and experimental methods used and applied during this work; these include areas of particle technology, particle characterisation and fluid dynamics. Published research of relevance in the area of spray drying and detergents is examined and critically reviewed such that the context of this work is laid out. The literature reviewed here comes from both external sources, such as open published scientific literature from journals and conferences and from internal sources at P&G.

2.2 Granular Laundry Detergents

Soaps have been used to clean both people and objects since ancient times. Traditional soaps were manufactured by boiling fats and oils with an alkali. Soaps manufactured this way were used well into the 20th century. Synthetic detergents were first developed in Germany as a response to the lack of fats and oils available during the First World War (Bajpai and Tyagi (2007)). However, these initial synthetic detergents did not deliver the cleaning power of natural soaps. It took until the 1930s and 1940s for the technology of synthetic detergents to develop sufficiently to match and surpass the cleaning performance of natural soaps. This development allowed Procter and Gamble to launch the first modern "built" synthetic detergent powder "Tide" in the USA during 1946, (Dyer *et al.* (2004)). This launch represented a major development not only in cleaning performance, but also in the manufacturing process as new spray drying towers were built to manufacture the synthetic formulation, which differed greatly from early soap based formulas. The launch of "Tide"

was a huge success as it became the market leader soon after launch (Dyer *et al.* (2004)), consuming the market share of soap based products, leading to the eventual replacement of soaps with synthetic detergents.

Detergent powders are used to wash clothes and therefore their purpose is to remove soils from clothing during the wash cycle. After washing the garments should be left soil and stain free with a pleasant fragrance. Consumers expect detergents to consistently deliver and improve on these criteria. Detergent manufacturers strive to impress consumers, retaining their custom whilst winning over new consumers to their brand. This means constantly improving their products in terms of powder appearance and fragrance, cleaning performance and soil removal as well as the fragrance and appearance of laundry after washing. These requirements are tensioned against needs to reduce costs to maintain profit margins, especially during times of increasing raw materials costs. A summary of the requirements for detergent powders from both consumer and manufacturing viewpoints are given in Table 2.1.

Table 2.1: A summary of detergent powder requirements adapted from de Groot *et al.* (1995).

Detergent Powder User Requirements	**Detergent Powder Product (Manufacturers') Requirements**
Good overall performance	Correct balance of components
High solubility	Components of good quality
Appealing shape, colour and perfume	Free flowing and homogenous powders
No side effects on skin or fabrics	Correct perfuming

In order to perform and deliver the required cleaning, detergent powders contain many components, all of which have different roles during the wash cycle. The main component groups of a typical detergent powder, according to de Groot *et al.* (1995), are summarised in Table 2.2 below, where the italics denote ingredients included in the slurry for spray drying (§2.3).

Yangxin *et al.* (2008) list six groups of components which laundry detergents generally comprise of, surfactants, builders, enzymes, bleaching agents, fillers and minor additives (such as dispersing agents, fabric softening clay, dye transfer inhibitors and brighteners). They highlight surfactants and builders as the two most important of these component groups, as they play a key role in cleaning. Current and future developments in detergents will be focused on these component groups to both improve performance and reduce environmental impact of laundry detergent products.

Fifteen different groups of components are listed and described by Bajpai and Tyagi (2007) as they break the groups listed by de Groot *et al.* (1995) and Yangxin *et al.* (2008) into more specific divisions.

The chemical ingredients of detergent powders vary significantly between brands, geographies and manufacturers. These changes are driven by consumers' expectations and trends in how they use the product, availability and cost of raw materials in that specific geography and both local and international environmental legislation. There are many different chemical compounds and materials used in each group of detergent components. Examples of commonly used chemical ingredients for each active group of components are given in Table 2.2.

Table 2.2:Detergent powder component groups, functions and examples of chemical compounds adapted from de Groot *et al.* (1995).

Active Group	Function	Chemical Compounds	
Surfactants	Surface active agents to remove fatty/oily soils and wet surfaces	Anionic	Linear-Alkylbenezene-Sulphonate (LAS)
		Non-ionic	Alcohol-ethoxylate (AE) Alkylphenol ethoxylate (APE)
Builders	Enhance the action of surfactants	Zeolite Sodium Tripolyphosphate (STPP) Sodium Carbonate Sodium Silicate	
Bleaches (and Activators)	Remove Stains	Sodium Perborate Sodium Percarbonate	
Fillers (and Processing Aids)	Aid processing and physical structure	Sodium Sulphate Water	
Enzymes	Remove blood and protein stains	Alcalase Protease	
Specific Additives (and Minors)	Improve performance aside from cleaning	Polymers (polycarboxylate) Brighteners (fluorescers)	
Perfumes	Fragrance		

2.3 Detergent Manufacture: Spray Drying

Spray drying is the main process route for manufacturing granular laundry detergents, in terms of both volume and sales, with volumes still growing annually, making research into this process hugely important in the detergent industry (Huntington (2004) and Bayly *et al.* (2008)). This section covers both generic spray drying and the spray drying process specific to detergent powder manufacture and an overview of both is given.

2.3.1 Spray Drying

Spray drying is the transformation of a feed from a fluid state into a dried particulate form by spraying the feed into a hot drying medium. It is a unique drying process, since it involves both particle formation and drying (Masters (1991)). This process is an attractive choice of unit operation for drying processes because of its ability of spray dryers to transform a liquid feed into dry spherical particles at high throughputs (Oakley (2004)).

Spray drying has a wide range of applications and many different process layouts and techniques are used to achieve the desired product properties for each specific application. The main way of classifying dryers is through their layout which can be co-current or counter-current, as shown in Figure 1.1, taken from Masters (1991). In a co-current dryer both the spray and air move in the same direction, with both usually entering at the top of the drying chamber and leaving through the bottom. Counter-current systems operate with the air and spray moving in opposite directions where the feed is sprayed downwards through a current of rising air. This is the system that is used for manufacturing detergent powders so this review will focus on counter-current systems. However, several phenomena

of spray drying have been investigated much more deeply in co-current rather than counter-current units and hence work in co-current dryers is reported for these phenomena.

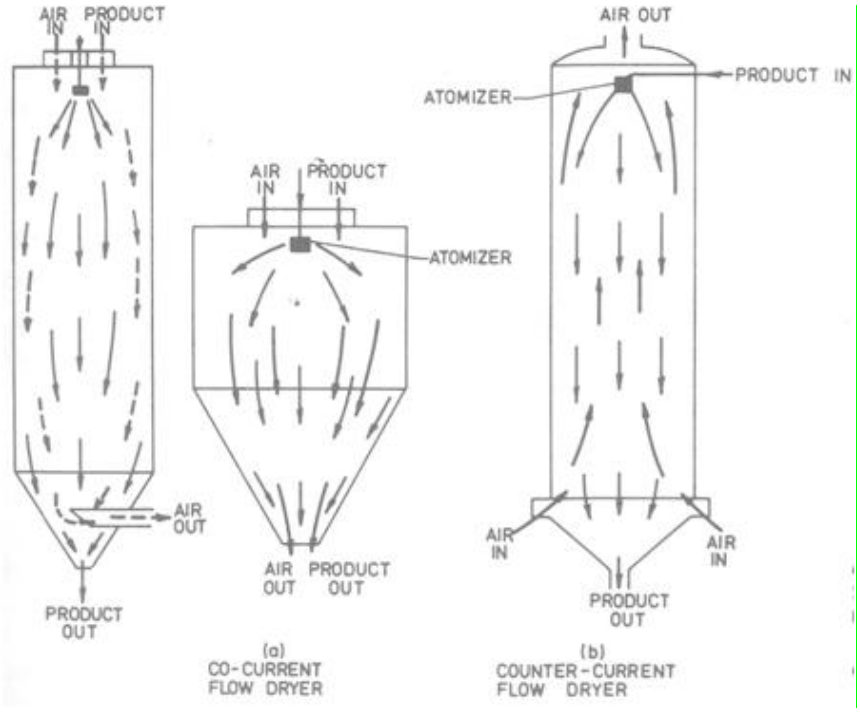

Figure 2.1: Spray Dryer Configurations taken from Masters (1991)

Masters (1991) lists four main stages of the generic spray drying process:

1. Atomisation
2. Spray air contact
3. Drying of droplets/sprays
4. Separation and recovery of dried product

These four process stages only cover the actually spray drying step. To cover the entire detergent manufacturing process, slurry preparation and pumping, post-drying component addition and packing can be added to form a list of seven process stages.

2.3.2 Detergent Spray Drying and Processing

Detergent powders are manufactured using counter-current spray-drying systems. A simplified cross-section of a typical detergent spray dryer is shown in Figure 2.2.

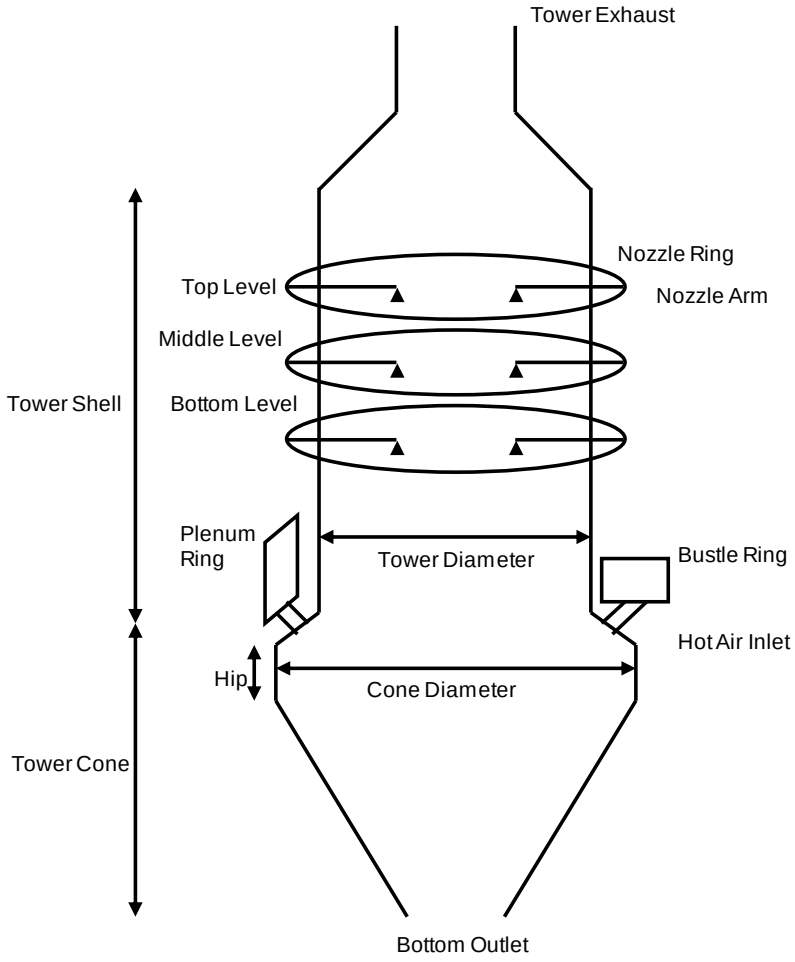

Figure 2.2: Detergent spray dryer geometry

The two main parts of the tower are the shell (cylindrical section) and the cone. The cone is the lower part of the tower which slopes inwards to form the base outlet, the shell is the tubular section above the cone. The detergent slurry enters the tower through the nozzles that are located in the shell, often spread across three levels. The hot air inlets are located at

the top of the tower cone just above the hip. The diagram below shows both bustle and plenum rings on the hot air inlet system.

The slurry is prepared by mixing all of the required ingredients in a constantly agitated heated vessel, referred to as the crutcher. Once mixed the slurry is moved onto another heated and agitated vessel, known as the drop tank, which acts a buffer between the batch process of crutching and continuous process of spraying. The slurry is then pumped and atomised through nozzles in the spray tower.

The atomised droplets are dried by evaporating their water content off by exposing them to the hot air flow inside the tower. The droplets enter the tower through nozzles located towards the top of the dryer shell and travel downwards through the rising hot air flow until they reach the bottom of the tower. They are collected on a moving belt, cooled and then mixed with any additional components that are heat sensitive and therefore cannot be added into the crutcher mix. The powder mixture is then packed into either boxes or bags before being stored and distributed.

An overview of the detergent manufacturing process is shown in figure 2.2. The stages of the process are covered in turn in the following sections.

Process Stages	
1	Slurry Preparation and Pumping
2	Atomisation
3	Spray Air Contact
4	Drying
5	Separation and Recovery of Dried Product
6	Post Drying Component Addition
7	Packing

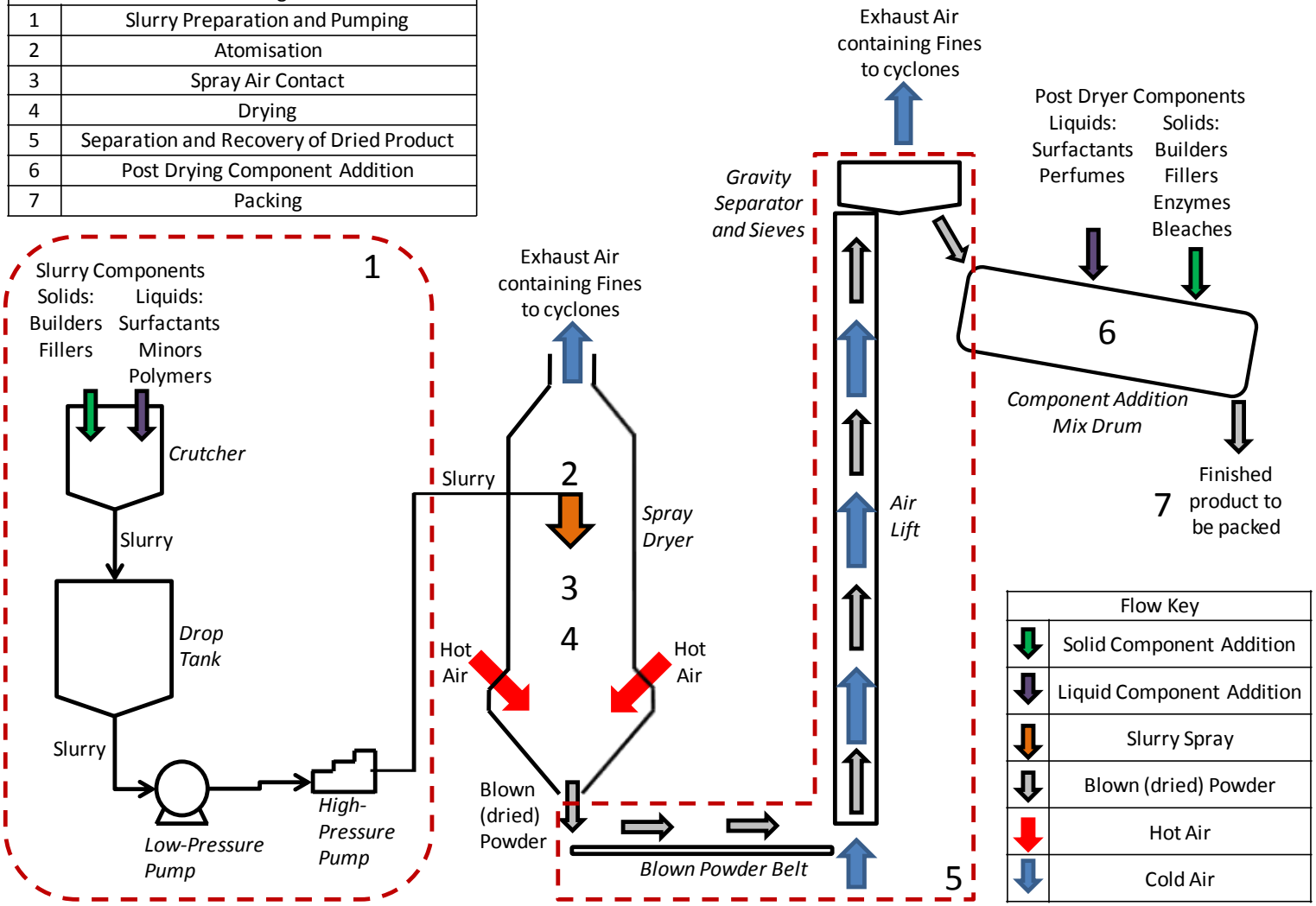

Figure 2.3: Detergent Manufacturing Process Overview

2.3.3 Slurry Preparation and Pumping

The preparation of the detergent slurry occurs in the crutcher - a heated, continuously stirred vessel. Both liquid and solid components of the spray-drying slurry are mixed together into an aqueous solution. It is important that the crutcher mix is developed into a consistent, homogenous, stable mixture with appropriate rheological properties, to allow it to be pumped continuously and for suitable atomisation to be achieved. Additional water can be added, if required in order to achieve the correct rheological properties, although process economics mean that it is desirable to keep the water content within the crutcher mix to a minimum in order to reduce the amount of water that has to be evaporated in the drying process. Crutching is a batch process and another stirred vessel, referred to as the drop tank is used to form a buffer between the crutcher and the continuous spraying process. The slurry is then pumped up to a pressure for atomisation (50-100 bar), via a two stage pumping system.

2.3.4 Atomisation

The purpose of atomisation is to physically break the feed/slurry into a large number of droplets, generating the distinct elements that become the powder product. This also generates a high surface to mass ratio, improving heat and mass transfer and therefore drying.

Breaking the feed/slurry into small droplets requires energy input to overcome the viscosity and surface tension of the feed material. There are several different mechanisms of

atomisation available for spray drying, each of these utilises a different mechanism to provide energy and break the feed into droplets, three main types are listed below:

- Pressure energy utilised through pressure nozzles
- Kinetic energy generated through two-fluid nozzles
- Centrifugal energy utilised through rotating disks (wheel atomisers)

Atomisation of detergent slurry is achieved using pressure nozzles (50-100 bar). By passing the slurry through the nozzle, pressure energy is converted to kinetic energy resulting in a high speed film that readily disintegrates as the film is unstable. The feed is made to rotate within the nozzle, which means that a cone shaped spray is developed.

Pressure nozzles expose detergent slurry to extreme shear rates and therefore rheological behaviour the slurry is critical in detergent atomisation, as it controls how viscosity changes with shear rate and therefore governs the breakup of the slurry into droplets. The challenges of understanding atomisation of complex fluids such as detergent slurries was discussed by Hecht (2005) and Hecht and Bayly (2009), who linked controlling droplet (and therefore particle) size to nozzle type, the pressure used and slurry properties.

2.3.5 Spray-Air Contact

Contact between the atomised droplets (spray) and the heated air is responsible for drying of the droplets and their transformation into particles. This contact is determined by the flow patterns of the air. In virtually all spray dryers, the drying air is given a swirling motion which increases the residence time of the drying droplets/particles and increases the relative

velocities between particles and air (Muller *et al.* (2001)). This increases the heat transfer coefficient and thus ensures better heat exchange and drying (Hecht and King (2000)), resulting in more energy efficient dryers. The swirl also aids flow stability. Tall form counter current detergent dryers offer significantly longer residence times than their co-current counterparts (Masters (1991)).

Air flow patterns in spray dryers and their effect on product quality and dryer operation have been given particular attention by researchers and this work as well as the fundamental fluid dynamics that affect these is covered later in the literature review (§2.5). Air flow patterns dictate the movement of particles through the dryer, controlling collisions between particles and particles, leading to agglomeration, and collision between particles and wall leading to wall deposition, the dynamics of particles inside spray dryers is also covered later in this literature review (§2.6).

During drying large amounts of heat energy are required to transfer from the air to droplets/particles in order to remove moisture. This energy is provided by heating the inlet air: temperatures of between 200°C and 400°C are typical for detergents depending on product formulation, dryer design and throughput. There are several different methods of heating employed in spray drying, but heating air through combustion of oil or gas is the preferred method for detergents as it is capable of generating large amounts of heat and contact between flue gases and the product is not an issue.

2.3.6 Drying

Drying of droplets is the key stage of spray drying as droplets are transformed into particles and consequently the powder product is created. Understanding this process is critical to successful operation of spray drying and production of a suitable product (Hecht (2004)). Of particular relevance to this project are understanding the changes that goes on during the drying process as droplets turn into particles as they travel though the spray dryer and come into contact with the walls at various stages of the drying process.

Many papers have been published on the subject of droplet drying. This literature can generally be split into two groups: modelling and understanding of the phases of droplet drying and the production and modelling of drying curves. The relevance of work to detergents varies greatly due to the nature of the drying material studied, whether they contain dissolved or undissolved solids etc. This section of the literature review will cover the publications and literature most relevant to detergent spray drying.

The evaporation of water from the atomised droplets involves simultaneous heat and mass transfer. When the droplets are dispersed in the drying air, heat is transferred from the air to the droplets. This heat energy is then converted to latent heat when the water evaporates. The drying of droplets is almost always broken down into stages in literature. These stages are based on two related items, the rate of drying and moisture content of the droplet/particle and its physical state at that specific point in the drying process.

One of the earliest studies into drying of droplets containing solids was carried out by Charlesworth and Marshall (1960). They investigated the drying rates of drops containing

dissolved solids, dividing the drying process into three stages and developing a detailed understanding of the particle morphologies created through different drying mechanisms. Nesic and Vodnik (1991) developed this work further, describing five stages of drying and using differential equations to describe the rate of droplet drying.

Figure 2.4 below gives a simplified summary of the mechanisms of droplet drying and the particle morphologies formed. The most relevant of these mechanisms to detergents is the formation of a hollow sphere. This was considered by Sano and Keey (1982) who studied the drying of a droplet containing colloidal material into a hollow sphere.

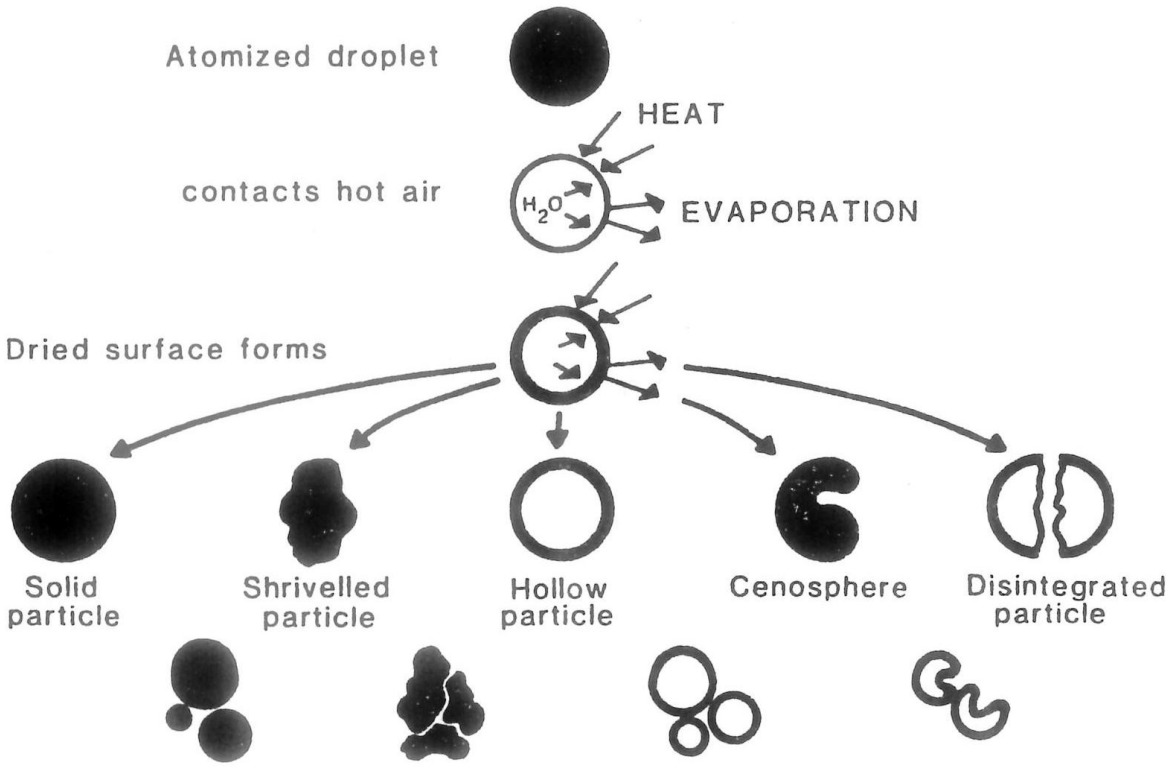

Figure 2.4: Mechanisms of droplet drying (simplified). Adapted from Masters (1991).

In terms of the rate during the various stages of drying, Masters (1991) states that the rate at which moisture is removed from a droplet peaks during the initial period drying and then

slows down as drying progresses. This can be explained through consideration of the physical state of droplet as it becomes a particle and mass and heat transfer become increasing limited by the internal resistance of the drying particle as the internal solid structure is formed. The influence of these characteristics on drying rates was investigated both experimentally and through modelling by Hecht and King (2000) and Hecht and King (2000).

The general understanding of the three stages of the drying process for detergent slurries is summarised by Hecht (2004):

1. *Surface Drying:* Any moisture on or close to the surface of the droplet is evaporated first. This results in the outer part of the particle drying whilst the centre still contains moisture.

2. *Diffusion Drying:* Water diffuses from the internal part of the particle and evaporates. Initially this process is fast enough that the particle maintains a constant temperature. However as this process slows down the particle temperature starts to rise and that leads to the third stage of drying.

3. *Steam Puffing:* is the result of a situation where the outer part of a particle is dry and solid enclosing a core which has a large moisture content. The core of the particle heats up (as the rate of diffusion slows, see above) and this results in the entrapped water evaporating. This evaporation produces an expansion which rips the outer solid shell apart. This affect is known as puffing and results in a lower product density and also more porous particles.

2.3.7 Product Separation and Transportation

The dried product leaves the spray-drying chamber through the outlet in the bottom of the cone and is collected on the tower belt. The tower belt carries the base powder to the airlift, which carries the powder back up to the top of the process facility. The main purpose of the airlift is to cool the powder, thus reducing its stickiness and ensuring that it does not cake during later stages of the process (de Groot *et al.* (1995)). As a consequence of this stickiness, wall deposition of powder is often observed in the air lift. The air lift also provides an opportunity for any additional drying of the blown powder to occur.

2.3.8 Post-Drying Component Addition

Once the product has been carried up by the airlift it is processed through several stages where the additional components are added. These post-drying add components include solid components added here to increase capacity by reducing the fraction of the final product that is spray dried, thus improving process economics. Additionally components such as perfumes, bleaches and enzymes too sensitive to survive the excessive temperatures of the spray drying process are therefore added after drying (de Groot *et al.* (1995)).

2.3.9 Packing

Once all the components have been added the product is passed into large bins ready to be packaged and delivered to the consumer. The most common types of detergent packaging are cardboard cartons and plastic bags. Both types of packaging are designed to increase product shelf life through minimising moisture transfer with the surrounding environment as covered by Godridge (2009).

2.4 Modelling and Simulation of Spray Dryers

As with virtually all operations in the processing industries the design and operation of spray dryers can be improved through modelling and simulation. These improvements, often referred to as optimisation, can bring wide ranging benefits to e.g. product quality, dryer throughput, energy usage, maintenance requirements and operational safety.

One of the aims of this project is to contribute towards the development of a mathematical model of wall build within the spray drying tower, therefore it is essential to understand previous work that has been carried on the modelling of spray drying process.

Modelling of spray dryers is particularly important due to the difficulty in applying traditional chemical engineering scale-up techniques from pilot plant to full scale towers. This is covered by Oakley (1994) who states

"in the case of spray dryers simple scale-up rules are hard to find because of the complex interaction of the process variables: the complex gas flow patterns usually found, the atomisation process, and the mixing of spray and gas".

Oakley (1994) also explains how because of the lack of understanding of complex gas flows meant that spray dryers used to be designed using non-theoretical correlations based on experience with existing installations and pilot plants. Computational Fluid Dynamics (CFD) has increasingly allowed these complex gas flows to be modelled and therefore predicted, allowing spray dryers to be designed based on principle based models as opposed to experience.

Reviews of mathematical modelling techniques for spray drying before the widespread availability of CFD include Zbicinski *et al.* (1988) and Langrish (2009) who both split models into three categories depending on the complexity of the mathematics used. Currently there are varying levels of mathematical complexity used for modelling spray dryers, these were reviewed by Oakley (2004), who classified them as:

1. Heat and mass balances
2. Equilibrium based models
3. Rate based models
4. Computational fluid dynamics (CFD) models

Equilibrium based models are only applicable to co-current spray dryers and therefore will not be discussed further in this review. Each of the remaining levels is described in the following section, with the relevant literature on each type of model reviewed and compared. A summary is given in Table 2.3. More depth on modelling of specific aspects of spray dryers is given in the relevant sections following in this literature review.

2.4.1 Heat and Mass Balances

The simplest form of modelling involves heat and mass balances over the volume of the dryer. The inputs required by the model are specification of inlet streams, exit streams, moisture contents and simple thermal properties (enthalpy of components). These balances are used to predict items such as drying load, exhaust conditions and process capacity, depending on the model inputs specified.

These models are usually applied as a preliminary step in process or product design to check feasibility before resources are dedicated to detailed design and modelling. An example of this preliminary step is described by Velic *et al.* (2003), who used spreadsheet based heat and mass balances to study the potential for reuse of process heat to improve spray dryer efficiency.

2.4.2 Rate Based Models

If particles in a spray dryer are not close to equilibrium then a model which takes account of the drying rate of the particles and their residence time is required for realistic prediction of exit solids moisture content. Oakley (2004) describes how rate based models can be used to calculate the drying rate of a droplet and its final moisture content, but avoid the need to calculate detailed gas flow patterns and particle trajectories which would necessitate costly CFD simulations.

These methods encompass models of droplet-particle drying rates and estimates of droplet-particle residence times, both of which can be determined either through calculation or experimentation. An example of application of rate based model principles is given by Parti and Palancz (1974) who built a model for designing dryers and drying processes using drying rate equations. A dynamic model for controlling food spray dryer was developed by Perez-Correa and Farias (1995). More recently Montazer-Rahmati and Ghafele-Bashi (2007) constructed a rate based differential model of a counter-current spray dryer and validated it against industrial data.

2.4.3 Computational Fluid Dynamics (CFD) Models

The most complex technique for modelling spray drying processes is to use Computational Fluid Dynamics (CFD). CFD simulations are now frequently used to model spray dryers and vary in levels of complexity depending on the number of phenomena they include.

CFD is a technique which uses numerical methods to solve the equations which govern the flow of fluids: the Navier-Stokes equations, which define any single-phase fluid flow. CFD is described in detail by Chung (2002) and most packages use finite volume methods to solve the equations. The procedure for any CFD simulation is to firstly define the geometry of the problem and then the volume occupied by the fluid is divided into discrete cells, this is referred to as meshing. The boundary conditions of the problem are defined, specifying the fluid behaviour and properties at the boundary of the problem and the initial conditions on time-dependent simulations. The equations required for the modelling being conducted are then solved in each cell of the mesh and the results collated before being displayed.

The suitability of CFD to applications for spray drying are discussed by workers including, Oakley (1994). Recent reviews of the application of CFD simulations to modelling of spray dryers include Langrish and Fletcher (2003) and Fletcher *et al.* (2006).

Early work on applying CFD to spray dryers only captured the air flow patterns present as described by Langrish and Fletcher (2003) (§2.5.5). A major step forward in using CFD was to include discrete droplets and particles in the simulation, so that their movement through the dryer could be predicted. This coupling with inclusion of drying models allowed particle

properties to be predicted, early workers using this approach include, Oakley and Bahu (1992), Livesley *et al.* (1992), Oakley (1994) and Kieviet and Kerkhof (1996).

More advanced models that have included air flow patterns, droplets/particles, drying and/or particle-wall interaction include, Southwell *et al.* (1999), Straatsma *et al.* (1999), Harvie *et al.* (2001), Harvie *et al.* (2002), Huang *et al.* (2003), Huang *et al.* (2004) and Fletcher and Langrish (2009). CFD studies including particles from both external and internal sources are discussed in depth in the particle dynamics section of this literature review (§2.6). More detail on how submodels of particle-wall interaction are built into CFD are given later (§2.7.6).

Table 2.3: Spray Dryer Model Levels of Complexity

Level	Model Type	Normal Inputs	Normal Outputs	Software	Run Time	Application
1	Heat and Mass Balance	Inlet Streams Exit moisture content	Exhaust gas conditions Heat requirements	Spreadsheet (MS Excel)	Seconds	Scoping Preliminary design
2	Equilibrium-based	Inlet Streams Desorption Isotherm	As (1) plus: Exit moisture at equilibrium	Spreadsheet (MS Excel)	Seconds	Scoping Preliminary design Process simulation
3	Rate-based with Simplified particle Motion	As (2) plus: Chamber Volume Chamber coefficient Droplet-Particle sizes Drying kinetics	Exit moisture vs. time Variations in performance	Spreadsheet (MS Excel) Technical Programming Package (MatLab)	Seconds	Overall process simulation Process optimisation
4	Rate-based with full simulation of fluid and particle motion (CFD)	As (3) plus: Detailed chamber geometry Detailed gas inlet conditions Detailed spray inlet conditions	As (3) plus: Gas flow field Gas temperature field Particle trajectories Particle temperature - history	CFD Package (Fluent)	Hours Days weeks	Detailed designs Investigation of aerodynamics Investigation of product quality Capacity increase studies

2.5 Fluid Dynamics in Spray Dryers

Key to understanding any spray-drying process is to understand the air flow patterns within the dryer as it is widely established the movement, loading and residence times of particles in the drying chamber is dictated by the air flow patterns present (Fletcher *et al.* (2006)). This in turn controls the critical transformations occurring to particles, such as drying, agglomeration and wall-deposition (Bayly (2008)). These determine dryer operation and product quality.

This part of the literature review covers all aspects of fluid dynamics in spray dryers, starting with an introduction to the theoretical principles of fluid dynamics used in this work. A review of flow diagnostic techniques available is given to highlight the reasons behind the choice of Particle Image Velocimetry (PIV) in this work. Finally published literature on investigations, both experimentally and simulatory, into fluid dynamics in spray dryers is reviewed, such that it will provide an context for and allow comparison with results on fluid dynamics in spray dryers presented later in this thesis.

Previous experimental and simulation studies have been conducted into air flow patterns inside of spray dryers, however, the majority of this work has been conducted on co-current spray dryers and counter-current dryers have received little attention. Therefore opportunities exist to further develop knowledge and understanding of counter-current spray-drying. However, workers on counter-current systems must be aware of the limits in applying co-current research and findings to their own dryers

2.5.1 Flow Diagnostic Techniques

Many different techniques are available for measuring fluid velocities and studying flow patterns. The aim of this section is to give a brief overview of commonly available flow diagnostics techniques which are suitable for studying air flow patterns in spray dryers. Particle Image Velocimetry (PIV), the main flow diagnostic technique chosen and applied during this research, is described in detail. Reviews of flow diagnostic techniques include Durst (1990), who reviewed optical techniques employed in momentum and heat transfer studies, Bryanston-Cross *et al.* (2000) described the limitations and strengths of optical flow visualisation techniques and Mavros (2001) who reviewed flow visualisation methods for application in stirred vessels. Both Adrian (1991) and Kurada *et al.* (1993) reviewed particle-imaging techniques for quantitative fluid flow measurements and visualisation.

For the purpose of this review the techniques have been divided into two categories, single point measurements and ensemble measurements. A summary of the techniques covered here is given in Table 2.4, which includes the basis of the technique and comparison of their temporal and spatial resolution. Single point techniques include pitot tube and hot wire anemometry, which are both intrusive to the flow. Laser Doppler anemometry has the benefit of being able to be installed without intruding into the flow field. Ensemble techniques are generally based on optical or nucleonic techniques which again are non-intrusive.

Table 2.4: Summary of flow diagnostic techniques

	Technique	Basis of Measurement	Components of Set-up	Temporal Resolution	Spatial Resolution
Single Point Techniques	Pitot Tube	Measurement of the dynamic pressure of the flow to calculate fluid velocity	Two concentric tubes, measuring dynamic and static pressure	Continuous	Hole in end of tube
	Hot-wire Anemometry	Detection of the cooling effect of the fluid flow is related to fluid velocity	Single hot wire in flow and electronics	Up to 50 kHz	Length of wire
	Ultrasonic Anemometry	Time of flight measurements to detect effect of fluid movement on speed of sound	Transducers to send and receive ultrasound	Up to 100 Hz	Distance between transducers
	Laser Doppler Anemometry (LDA)	Detection of seeding particles through interference on laser light	Seeded flow, laser beams, optics and computer	Up to 100 Hz	1 or 2 mm^2
Ensemble Techniques	Simple imaging	Influence of flow on objects or seeding visualises flow and is capture in images or series of images	Objects or seeding in the flow and camera	Up to 10 kHz (depends on camera)	Large areas up to m^2
	Chemical Tracers	Chemical detection of tracers	Flow with tracer and chemical detector	Sampling rate of detector	Whole flow systems
	Particle Image Velocimetry (PIV)	Optical detection of seeding particles	Seeded flow, Lasersheet, camera and computer	Up to 2 kHz	Up to 200 mm^2

	Positron Emission Particle Tracking (PEPT)	A dynamically similar (to the particles or fluid medium) radioactive particle is tracked as its decay leads to two back-to-back photons so that its position can be inferred.	Radioactive tracer particle(s) and positron camera positioned to track decay within flow.	Up to 250 Hz	0.5mm inside an area of 60 x 60 x 60 cm^3
	Computer-automated radioactive particle tracking (CARPT)	A dynamically similar (to the particles or fluid medium) radioactive particle that emits constant energy gamma radiation. An array of strategically positioned detectors detect the gamma radiation and then software is used to calculate/infer the particles position.	Radioactive tracer particle(s), gamma ray detectors and computer running tracking software.	Up to 50 Hz	0.5mm inside an area of 60 x 60 x 60 cm^3

2.5.2 Particle Image Velocimetry

Particle Image Velocimetry has been employed during this work. The technique can be thought of as an advanced version of imaging of seeded flows, where digital images of seeded flow are used to produce a velocity flow field automatically through computer analysis.

2.5.2.1 Background

The term Particle Image Velocimetry was first used over twenty five years ago and its development over the last four decades is reviewed by Adrian (2005). Further reviews of this technique include, Adrian (1991), Grant (1997), Stanislas and Monnier (1997) and Saareninne *et al.* (2001).

A generic PIV set-up is shown in Figure 2.5 and consists of four main components:

Seeded fluid flow

Lasersheet

Camera

Synchroniser

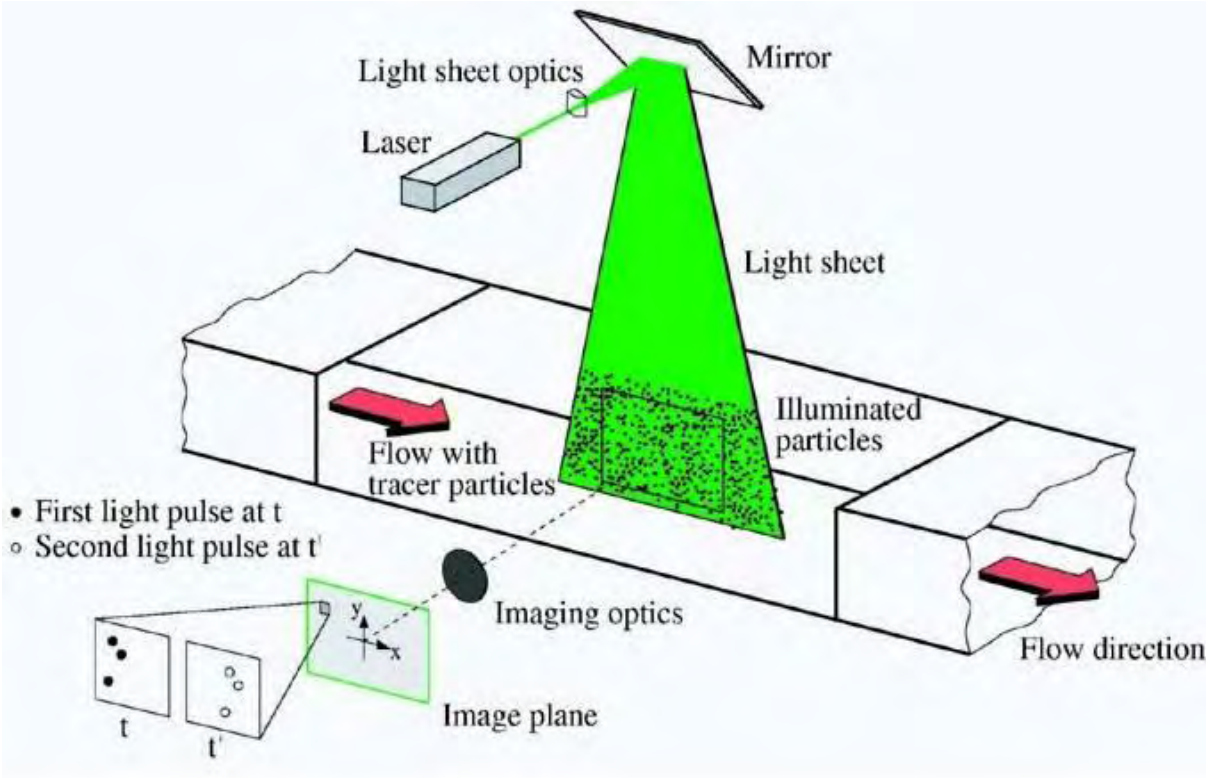

Figure 2.5: Typical PIV Experimental Set-up taken from Raffel *et al.* (2007)

The principle of operation of PIV is that two images of a seeded flow are taken in quick succession. Cross-correlation is then conducted by splitting the image up into interrogation windows where the greyscale of the two images is overlapped until the strongest match is found, the displacement required for this match is divided by the time between the two images to generate the velocity vector in that window.

2.5.2.2 Seeding of Flow

To enable the measurement of a fluid velocity the flow being studied with PIV must be seeded with particles which reflect light from the laser to the camera and thus enable fluid motion to be detected. Melling (1997) explored and reviewed seeding options for PIV summarising that the key principle of PIV is that this seeding faithfully follows the fluid

movement, thus allowing accurate measurements of its velocity. This is achieved by ensuring the particles are neutrally buoyant and sufficiently small. Seeding particles which effectively follow the flow will have a short relaxation time, given by:

$$\tau_s = d_p^2 \frac{\rho_p}{18\mu} \qquad (2.1)$$

Melling (1997) also emphasised the importance that seeding particles are evenly distributed within the flow and have a narrow size range, to avoid errors in image analysis (cross-correlation). Additionally seeding particles should be chemically-inert, non-volatile, non-abrasive and preferably non-toxic. Typical examples of seeding particles for liquid measurements include polypropylene, hollow glass spheres and alumina. For gaseous flows oil droplets and smoke are commonly used.

2.5.2.3 Laser

Lasers are the main form of light source used for PIV, because of their ability to emit monochromatic light with high energy density, which can be bundled into thin lightsheets, (Raffel *et al.* (2007)). Lasers are available in many forms, as either continuous or pulsed light sources. Lasers used for PIV are reviewed by, Raffel *et al.* (2007) and Stanislas and Monnier (1997). PIV requires a pulsed laser, capable of high repetition rates, with solid state Nd:YAG (Neodym, yttrium-aluminium-garnet) lasers being commonly used for PIV applications due their suitability and cost advantages over other suitable laser types. The wavelength of light produced by Nd:YAG lasers is typical either 1064 nm (infra-red) or 532 nm (green).

2.5.2.4 Camera

One of the main drivers of PIV development since the 1970s and 1980s has been the advancement in digital camera technology, allowing high resolution digital images to be used in PIV applications. This has enabled fast computer processing of images to determine flow field velocities (Raffel *et al.* (2007)).

Digital cameras rely on Charge-Coupled Devices (CCD) which are electrical sensors, which convert light (photons) into an electrical charge (electrons). This electrical charge is then passed on as a digital signal to either a frame grabber or memory within the camera. An individual CCD element is referred to as a pixel and CCD devices use arrays of these to build-up an image, Raffel *et al.* (2007). Typical resolutions of PIV cameras range between 512 x 512 pixels and 2048 x 2048 pixels, larger resolutions are appearing continuously, with the continuous development of digital camera technology.

Cross-correlation used in PIV relies on capturing sequential images with a very short time between them. In order to achieve this a “frame-straddling” technique is used, where two laser pulses are captured as either separate sequential frames (single-frame, single-exposure) or on one frame (single-frame, multiple-exposure) separated by a time period controlled by the synchroniser.

2.5.2.5 Synchroniser

To capture suitable images of the flow field studied, the laser pulse and camera must be triggered with both the correct sequence and timing for the flow field being studied. A computer-controlled synchroniser performs the task of triggering both the camera and laser,

such that they operate as an integrated automated system. During image acquisition the synchroniser locks into the frame of the camera and controls the laser pulses to match up with the frames as required. More details of synchroniser operation as part of PIV is given by Raffel *et al.* (2007).

2.5.2.6 Image Analysis – Cross Correlation

The principle of operation for PIV is to measure the movement of seeding particles, and thus the fluid velocity. In images containing large amounts of similar seeding particles, tracking of individual particles quickly becomes impossible and therefore statistical methods have been developed to predict the most probable displacement of a group of particles rather than tracking individual particles.

In order to calculate the most probable displacement of a group of particles, the image is divided in a number of squares, called interrogation areas (IA). Typical interrogation areas are 8x8 pixels, 16x16 pixels, 32x32 pixels or 64x64 pixels. The statistical method most commonly chosen for PIV is referred to as cross-correlation, which is conducted for each interrogation window between the first and second frames, the equation for this is shown below:

$$R(x,y) = \int\int I(x,y)I'(x+x_0, y+y_0)dxdy \qquad (2.2)$$

Where R is the spatial cross-correlation function of the transmitted light intensity, I and I' in the first and second frame respectively. To simplify and speed-up the cross-correlation, the Fast Fourier Transform (FFT) technique is used to solve the above equation. The cross-correlation function represents the probability distribution of all possible displacements of

the particles in the sample area. This process is illustrated in Figure 2.6 where the peak on the left hand plot represents the most probable displacement, which is then used to generate the velocity vector for that interrogation window.

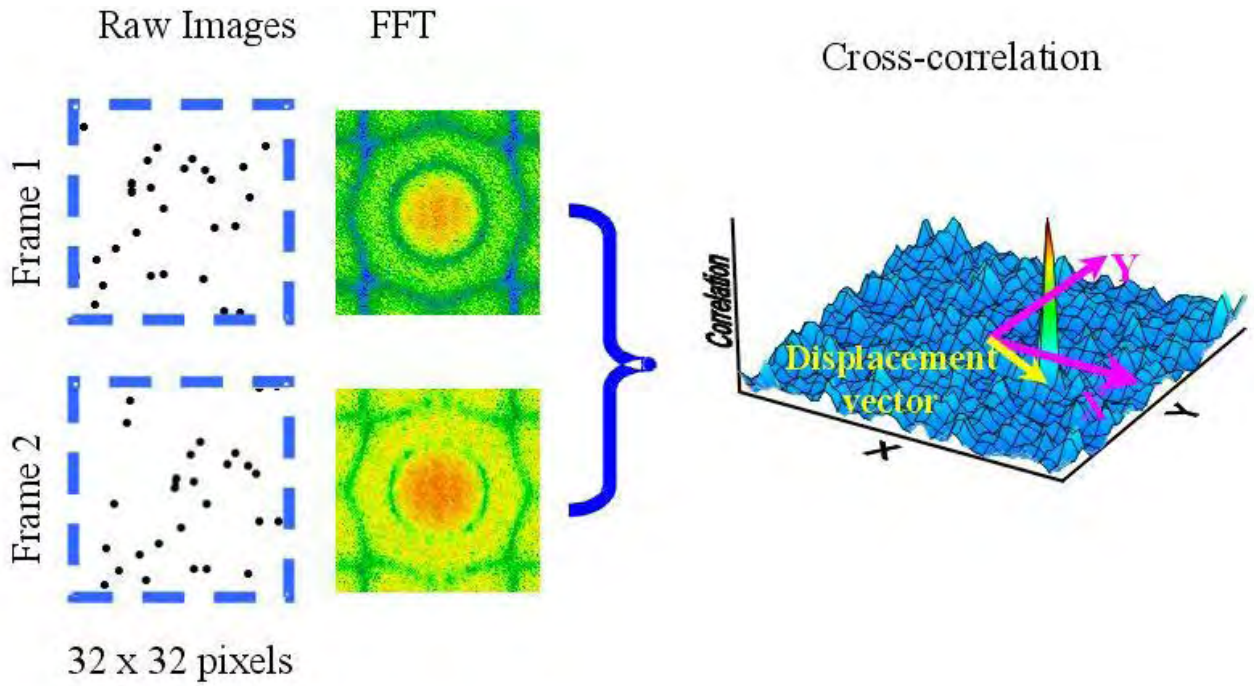

Figure 2.6: FFT Cross Correlation Analysis taken from Raffel *et al.* (2007)

To ensure the velocity vector produced is realistic and not a statistical inaccuracy, criteria such as peak to peak ratio and signal to noise ratios are used on cross-correlation and then criteria such as maximum velocity or comparison with neighbouring vectors, are usual set on whether a velocity vector is carried forward or not.

2.5.2.7 Limitations

PIV resolves velocity fields on a finite scale, determined by the interrogation area sizes (§2.5.2.6). This means that PIV may not have the resolution to pick up the smallest scales of turbulence in the flow and thus PIV effectively acts as a low pass filter, smoothing out the smallest eddies, as discussed by Sheng *et al.* (2000). This limitation is not exclusive to PIV as

even single point techniques such as LDA will operate over a finite area which may be bigger than the smallest scale eddies.

Temporal resolution issues were also considered a limitation during the early development of PIV, with techniques such as LDA offering much larger sampling frequencies. However, recent advances in PIV have largely eliminated issues with temporal resolution and high-speed PIV systems are now capable of sampling at rates above 2 kHz (Adrian (2005)).

2.5.3 Fluid Dynamic Parameters

In a three dimensional flow system, using Cartesian co-ordinates, the mean velocity magnitude, ū, at any point can be computed from the three mean velocity components in each dimension, u_x, u_y and u_z:

$$\bar{u} = \sqrt{\bar{u}_x^{\,2} + \bar{u}_y^{\,2} + \bar{u}_z^{\,2}} \qquad (2.3)$$

In a two dimensional system the mean velocity magnitude in the horizontal plane, $\bar{u}_h$, can be calculated from $\bar{u}_x$ and $\bar{u}_y$:

$$\bar{u}_h = \sqrt{\bar{u}_x^{\,2} + \bar{u}_y^{\,2}} \qquad (2.4)$$

In a cylindrical vessel such as a spray dryer it is more appropriate to describe the velocity components in cylindrical coordinates, i.e. in terms of tangential, radial and axial directions. The velocity magnitude and axial velocity remain the same, but the tangential velocity, u_Θ, and radial velocities, $\bar{u}_r$, can be calculated from $\bar{u}_x$ and $\bar{u}_y$, respectively.

$$\bar{u}_\theta = \bar{u}_x.\cos\theta - \bar{u}_y.\sin\theta \qquad (2.5)$$

$$\bar{u}_r = \bar{u}_y.\cos\theta + \bar{u}_x.\sin\theta \qquad (2.6)$$

θ is the angle between the x dimension and the tangent to the curvature of the dryer wall, at that position.

Flows inside spray dryers are considered to be turbulent. Turbulent flow can be described as subject to random fluctuations in all directions at any point in the system. For a flow which is steady on average, the instantaneous velocity, U, at any point can be decomposed into the time averaged velocity, ū, and the fluctuating component (deviation from the mean), u', (Reynolds decomposition):

$$U = u' + \bar{u} \qquad (2.7)$$

As the deviation from the mean velocity, u', has both positive and negative values it is usually characterised using the Root Mean Square (RMS) velocity, ũ:

$$\tilde{u} = \sqrt{u'^2} = \sqrt{(U - \bar{u})^2} \qquad (2.8)$$

The turbulence intensity (turbulence level) is the ratio of the RMS velocity to the mean velocity. This was calculated the following equations:

$$I_h = \frac{\tilde{u}_h}{|\bar{u}_h|} \qquad (2.9)$$

Turbulent Kinetic Energy (TKE) is the mean kinetic energy per unit mass of fluid associated with eddies in turbulent flow and for time-averaged flows. It can be expressed (per unit mass) as:

$$k = \frac{1}{2}\tilde{u}^2 \qquad (2.10)$$

Where ū is calculated using equ 8.

Using PIV only yields two velocities, but 3D kinetic energy can be estimated, as done by Sheng *et al* (2000), through assuming that the axial velocity is the mean of radial and tangential velocities (isotropic assumption). Applying this assumption to equ (2.8) and substituting this into equ (2.10) gives equ (2.11):

$$k = \frac{3}{4}\left(\tilde{u}_\theta^{\,2} + \tilde{u}_r^{\,2}\right) \qquad (2.11)$$

The Reynolds stress tensor is defined as

$$R_{ij} = \rho\overline{u_i' u_j'} \qquad (2.12)$$

They can be physically interpreted as the stress applied to the mean flow by the fluctuating velocity component. The turbulent kinetic energy is determined from the diagonal components of this tensor. Since 2D PIV measures both tangential and radial components it is also possible to calculate the non-diagonal component described as equ (2.13) below:

$$R_{\theta r} = \overline{(U_\theta - \bar{u}_\theta)(U_r - \bar{u}_r)} \qquad (2.13)$$

Thus 2-D PIV can resolve three out of the six terms in the tensor (assuming $R_{ij} = R_{ji}$). In this work the Reynolds stress components have been normalised against the tangential inlet velocity using:

$$R_{ijn} = \frac{R_{ij}}{U^2} \qquad (2.14)$$

2.5.4 Flow Patterns in Spray Dryers

So far this section has covered theoretical aspects of fluid dynamics and flow diagnostic techniques applied in this work. Here, the characteristics and the phenomena observed within air flows inside spray dryers are introduced. Work on all types of dryers is reported. However, this review is focused on building up a picture of the characteristics of air flows and the phenomena encountered inside tall-form counter-current detergent spray dryers. This will provide a context for and allow comparison with results on fluid dynamics in spray dryers presented later in this thesis. To aid this context and comparison, theoretical aspects of the characteristics of flows observed are also included.

Air flows in spray dryers are usually imparted with a swirling motion, forming a vortex within the drying chamber. This is usually achieved by angling the air inlets. The advantages of imparting swirl to air flows in spray dryers is discussed by Southwell and Langrish (2001) (co-current), and Muller *et al.* (2001) (counter-current). The key advantages of using a swirling flow are:

- Improvement in flow stability in terms of uniformity across the dryer
- Spray-air contact is improved through the spreading effect of swirl on the spray cone

- Relative velocities between particles and air are increased, increasing heat and mass transfer coefficients and therefore improving drying efficiency

2.5.4.1 Experimental Studies into Fluid Dynamics in Spray Dryers

Workers performing experimental measurements of air flow patterns have used a wide range of techniques. Stafford *et al.* (1997) used Particle Image Velocimetry (PIV) to investigate both air and spray flow patterns inside a co-current spray dryer. Bayly *et al.* (2004) measured air velocities in a counter-current spray dryer using LDV to build-up air-flow profiles showing how both axial and tangential velocities change with radial position across the dryer (§ 2.5.4.2).

Langrish *et al.* (1992) and Southwell and Langrish (2000) both used smoke to allow flow visualisation in co-current pilot plant spray dryers, observing turbulent flows. The residence time in detergent spray dryers has been investigated through use of chemical tracers by Taylor (1994), Place *et al.* (1959), Paris *et al.* (1971), Keey and Pham (1976) and AdeJohn and Jeffreys (1978) who used both a tracer to investigate air residence times and smoke for flow visualisation.

2.5.4.2 Rankine Vortex

The characteristics of the vortex formed within the flow, is dependent upon the dryer design. For tall form counter-current spray dryers Bayly *et al.* (2004) describe how a Rankine type vortex is formed in the drying chamber. The type of vortex formed changes with axial position, starting as a forced vortex close to the air inlets and changing towards a Rankine type vortex moving up the dryer away from the air inlets. This development in the vortex

structure formed leads to a change in the shape of the tangential velocity profile across the dryer, with the peak tangential velocity moving towards the centre of the tower with increasing axial position. This is also reported by Nijdam (2004) and Sharma (1990).

The Rankine vortex model consists of a free vortex containing a forced vortex core. Tangential velocities increase with distance inward from the dryer wall, until a point at which the velocity starts to decrease, reaching a minimum at the centre of the dryer. Mathematically this can be described as the tangential velocity at a radial point, r is given by:

$$U_\theta = \begin{cases} \frac{U_\theta r}{R} (r \le R) \\ \frac{U_\theta R}{r} (r \ge R) \end{cases} \qquad (2.\ 15\ )$$

Where R is the radius of the vortex core and U_θ is the maximum velocity at the peak.

2.5.4.3 Transient Flows

Several workers have examined the phenomena of time-dependency and instability of air flows in spray dryers. Oscillations and instabilities in the vortex within a spray dryer have specifically been linked to increased deposition of material on the dryer walls by LeBarbier *et al.* (2001) and Southwell and Langrish (2001), who give a detailed explanation of how the formation of precessing vortex cores leading to periodic oscillations in velocity profile across the drying chamber for co-current dryers.

Both experimental and simulatory investigations have been conducted into this phenomenon. Langrish *et al.* (1993) measured air velocities in a co-current dryer and conducted FFT analysis on the velocity signal to obtain a period of between 1 and 3 seconds,

comparing well with simulation predictions of 1 second. Muller *et al.* (2001) used ultrasonic anemometry to study time-dependent behaviour in a tall-form counter-current detergent spray-dryer, finding periods in oscillation of velocities between 1 and 5 seconds. Southwell and Langrish (2001) used LDV and flow visualisation to investigate the effect of increasing swirl angle (swirl number) on flow stability in a co-current dryer, they found that no amount of swirl would deliver steady flow and that 25° (swirl number 0.45) gave the most suitable flow stability combined with good air-spray mixing without increased wall deposition.

LeBarbier *et al.* (2001) conducted flow visualisation experiments and observed a time-dependent precession of the vortex which depended on the inlet angle. They ran transient simulations and found agreement between these and the experiment data for time-dependent behaviour. Guo *et al.* (2003) used transient CFD simulations of the sudden expansion followed by contraction as found on the inlet to a co-current spray dryer and found time-dependent behaviour in the flows simulated. Langrish *et al.* (2004) ran transient simulations of flow with varying swirl, highlighting the need to run transience simulation of spray dryers to capture the important time-dependent flow phenomena.

Most recently Fletcher and Langrish (2009) and Gabites *et al.* (2010) both used CFD simulations to study transience in flow inside spray dryers, highlighting the need for yet further development of CFD simulations to increase accuracy of predictions of time dependent flows.

2.5.5 Modelling and Simulations Studies into Fluid Dynamics in Spray Dryers

Investigations into air flow patterns using modelling and simulation techniques such as Computational Fluid Dynamics (CFD) have been widely conducted. Harvie *et al.* (2001) and Harvie *et al.* (2002) used CFD to investigate air-flow patterns in a tall-form co-current milk spray-dryer, linking air flow-patterns to wall deposition, they concluded that the relationship between initial particle momentum and gas flow field determines dryer performance. More recently Fletcher and Langrish (2009) considered the effect of two different turbulence models in time dependent simulations of spray dryers, concluding that although both methods gave similar time averaged results, only scale-adaptive simulations captured large scale eddies.

Several CFD simulations of air flow patterns in spray dryers have been compared and validated against experiments to measure air flow patterns, these include Kieviet *et al.* (1997) and Livesley *et al.* (1992) who found good agreement between CFD simulations and experimentally measured velocity values. Southwell *et al.* (1999) compared CFD simulations with previous work on using turbulence in spray dryers, finding reasonable agreement. More recently Gabites *et al.* (2010) used flow visualisation to observe movements in the vortex inside a milk powder dyrer and thus validate their time dependent simulations.

One important aspect of CFD simulations of spray dryers is experimental validation to ensure that air and particle dynamics are being correctly predicted by the model. With simpler models validation is easily conducted by comparing the results to the exit streams observed and product obtained, however for CFD validation is more complex. Oakley (2004) covers this when stating,

"experimental validation of the gas flow patterns and particle trajectories predicted by these models was an important aspect of getting their widespread acceptance."

He adds "non-invasive measurement of gas and particle motion within an enclosed spray chamber are by no means straightforward and have normally been achieved by either laser or hotwire anemometry. Most published data is on lab-scale spray dryers, data on industrial scale spray dryers are limited because of the practical difficulties and propriety nature of such measurements."

Workers who have sought to validate their CFD simulations of spray dryers include, Kieviet *et al.* (1997) and Livesley *et al.* (1992) who found good agreement between CFD simulations and experimentally measured velocity values. More recently validation of CFD was carried out by Southwell and Langrish (2001), Harvie *et al.* (2002) and Huang *et al.* (2004), who all again found agreement between measurements and CFD predictions. Bayly *et al.* (2004) found good agreement between CFD simulations and LDV measurements in tall-form counter-current spray dryers, making their work particularly relevant to this thesis. Most recently Gabites *et al.* (2010) used flow visualisation to validate the time dependent aspects of their simulations.

2.6 Particle Dynamics in Spray Dryers

The air flow patterns in a spray drier control movement, loading and residence times of particles in the drying chamber and therefore the critical transformations occurring to particles, such as drying, agglomeration and wall-deposition. These determine dryer operation and product quality. This section considers particle dynamics in spray dryers and reviews the techniques available to study particle trajectories and velocities, sizes and

concentrations., Previous studies into particle movement, loading, sizes and residence times are discussed and finally simulation of particle dynamics is discussed and reviewed.

Literature on studies of particles inside spray dryers is relatively sparse in comparison to that on air flow patterns within spray dryers, limitations of modelling techniques for particle dynamics have also restricted the number of simulation investigations published. Therefore a clear gap exists in understanding the size, concentration and movement of particles within spray dryers.

2.6.1 Techniques for Measuring Particle Size, Loading and Trajectories In-Situ

Techniques for measuring particle size are frequently split into three categories, physical, imaging and light scattering, as done by both Tayali and Bates (1990) and Black *et al.* (1996). Only imaging and light scattering techniques are applicable for in-situ measurement of particle sizes and several of these techniques allow particle loading and velocities to be measured along with particle size, these techniques are briefly reviewed here.

2.6.1.1 Imaging Techniques

Photography – capturing images of particles within the process will allow image analysis to calculate size and loading parameters. Particle tracking to obtain velocities and trajectories is also a possibility, depending on both spatial and temporal resolution of the images captured.

Particle Image Velocimetry – following on from photography, PIV can be used to obtain images and therefore the same parameters with the addition of using cross-correlation to obtain particle velocity flow fields. PIV has been explained previously (§2.5.2). Stafford *et al.*

(1997), used this technique to study the movement of both air and drying droplets in a co-current spray dryer.

2.6.1.2 Light-Scattering Techniques

Laser Doppler Anemometry/Phase Doppler Anemometry – can be applied to flows containing particles rather than seeding, where similarly the velocity and size of particles can be obtained via interference patterns.

2.6.2 Particle Residence Time Studies

Several experimental studies have been conducted into the residence time of particles inside spray dryers. Despite this being a critical parameter in controlling particle drying and therefore product quality Taylor (1994) described literature on this subject as “sparse”. Since then several studies have been conducted to understand and quantify particle Residence Time Distributions (RTD).

Powder RTDs in two different size counter-current spray dryers were measured using an inorganic salt tracer by Taylor (1994) who found that residence time in the larger tower was greater and that air flow patterns affected powder RTD in both sizes of dryers. This technique was employed again by Taylor (1998) to study the difference in particle residence times in co and counter current spray dryers, with the later found to have the largest mean residence time. The co-current dryer was found to have the greater variance in its RTD and this was linked to increased turbulence in the co-current dryer and resulting changes in drag forces on particles, as were differences in particle morphology observed. Both of these

studies were used to aid construction of mixing models to understand flow patterns and mixing in spray dryers.

The importance of understanding particle RTD in scaling up spray drying processes was emphasised by Zbicinski *et al.* (2002). Their studies in a counter-current spray dryer, found variation in RTD for particles of different sizes. They also concluded that particle RTD will always be less than for the drying medium (usually air) and that there is no simple link between the two. This was also concluded by Kieviet and Kerkhof (1995), who worked with a co-current dryer.

2.6.3 Particle Size Studies

Studies of particle sizes in-situ, during drying inside spray drying processes have been relatively scarce. One such study was conducted by Zbicinski *et al.* (2004) who investigated particle size as a function of location (radial and axial positions) inside a counter-current spray dryer using LDA. They concluded that agglomeration led to an increase in mean particle size with increasing distance from nozzle and that changes in inlet air temperature and flowrate also affected this agglomeration, with higher temperatures below the nozzle leading to increased agglomeration. Mean particle size was found to increase with radial distance from the centre of the dryer, meaning bigger particles tend to move towards the dryer walls.

2.6.4 Particle Velocity and Trajectory Studies

Again, literature on particle velocities and trajectories measured in-situ during spray drying is scarce. Publications on this area are an assortment of different types of experiments on different areas of spray drying.

Zbicinski *et al.* (2004) measured particle velocities at various axial positions in a counter-current spray dryer, observing particle movement in both directions and at velocities up to 2.5 ms^{-1}, with both air flowrate and temperature influencing particle velocities.

2.6.5 Simulation Studies of Particle Dynamics

As discussed previously (§2.4.3), more recent CFD simulation of spray dryers have included droplets/particles dispersed in the gas phase. However, the capability of these simulations, in terms of the number of particle simulated, is currently limited by computational power available. CFD simulations of spray dryers that include particles usually use the Euler-Lagrangian method to track discrete particles as they move through the fluid flow within the drying chamber.

More advanced models that have included air flow patterns, droplets/particles, drying and/or particle-wall interaction include, Southwell *et al.* (1999), Straatsma *et al.* (1999), Harvie *et al.* (2001), Harvie *et al.* (2002), Huang *et al.* (2003), Huang *et al.* (2004) and Fletcher and Langrish (2009).

Sub-models describing the collision of a particle with other particles and the dryer walls are used to allow particle deposition to be included in these simulations. The complexity of

these submodels has increased in recent years and are covered by Crowe *et al.* (1998) and Crowe (2006).

Studies of incorporating particles into CFD simulations within P&G include, modelling atomisation, Ng and Amador (2008), evaluating plant layout based on particle movement, Ng and Amador (2008) and modelling of particle-wall interaction, Ng (2009).

2.7 Wall Deposition in Spray Dryers

The main focus of this research is wall deposition in spray dryers and this section of the literature review examines published work on wall deposition, including studies into its effect on the process, theoretical descriptions of the phenomena and both experimental and modelling studies to understand the mechanisms behind its occurrence.

During virtually all spray-drying operations product is found to build-up on the drying chamber walls. This build up can have a significant effect on the process operation and product quality. Wall deposition is frequently cited as one of the main drawbacks of spray drying as a manufacturing process (Masters (1991), Fletcher *et al.* (2006) and Woo *et al.* (2010)).

Wall deposition/build-up has been an issue in spray drying detergents since the technology was first developed in the first half of the 20th century. In fact the first synthetic detergent, “Tide”, had to be reformulated to make it processable as its original formula was prone to build-up on the dryer walls (Dyer *et al.* (2004)).

2.7.1 Disadvantages of Wall Deposition

Masters (1991) explains that retention of product at the chamber wall over lengthy time intervals is undesirable, because of the increased cleaning requirement and the potential effect on product quality. This was expanded on by Bayly (2005), who describes the following negative aspects of wall deposition specific to manufacturing detergents.

- *Process Operating Conditions.* The presence of large amount of material on the dryer walls will negatively affect the operation of the spray drying process through changing air flow patterns, heat transfer and therefore temperature profiles and also affecting instrumentation used to monitor the process.

- *Operational Safety*. Wall deposits can be exposed to elevated temperatures if located close to the air inlets, this can result in over heating of this material and possible combustion causing fires and explosions in dryers. (Ozmen and Langrish (2003), Langrish et al. (2007) and Chen et al. (2005)).

- *Maintenance and Cleaning Requirements*. Material stuck to the wall needs to be removed periodically through cleaning of the drying chamber. From an economic point of view, this means lost production time through increased downtime for cleaning as well as increased costs through labour and equipment required for cleaning (Masters, (1991)).

- *Product Quality*. Wall deposition affects product quality mainly through contamination of product with material that has been deposited in the wall for a long period of time. This material will have been exposed to the high temperatures within the dryer for

longer periods of time than the bulk of the powder, possibly causing further chemical reactions and degradation. These can result in oxidation, de-colouring and possible combustion. Re-entrained wall deposits may have agglomerated and therefore particle size and morphology can be altered (Bayly (2005)).

- *Process Reliability*. All of the above factors will affect process reliability in terms of being able to operate the process safely and efficiently, whilst making product of the required standard. In addition wall deposition can have a significant effect on the yield of the process, therefore dictating how much useful powder product can be obtained. Maury *et al.* (2004) stu*died th*e effect of process variables on the yield of powder product and found that using higher air temperatures increased yield, by reducing wall deposition through increased drying of droplets before they contacted the dryer walls.

2.7.2 Methods Reducing Wall Deposition

Several methods have been examined for reducing the amount of deposition during dryer operation. Masters (1991) describes the use of air jets and air brooms close to the dryer walls to stop particle sticking and therefore reduce deposition. However, the effectiveness of these methods has been questioned by Woo *et al.* (2009) amongst others. Langrish and Zbicinski (1994) examined the effect of the varying swirl of the air flow patterns and the spray cone angle of wall deposition in a co-current dryer, finding that maximising both swirl and spray cone angle minimises deposition. Conversely Ozmen and Langrish (2003) found that increasing swirl increased wall deposition in a similar co-current dryer. Another avenue of investigation has been to manipulate dryer wall surface energies, Woo *et al.* (2009) found that reducing wall surface energy by replacing stainless steel with Teflon reduced wall

deposition. They also investigated the deposit strength by using an air spray tester to remove deposits, finding that wall surface energy only affects the tendency of deposits to remain attached in certain conditions.

2.7.3 Methods of Removing Wall Deposits

As stated previously, material deposited on the walls of any spray dryer will have to be removed through periodic cleaning. The frequency and type of cleaning used depends on the product being manufactured, dryer designed and throughput. For example bulk chemical items do not have the hygiene restrictions of food and pharmaceutical products that may require Cleaning in Place (CIP) systems to maintain a sterile and chemically uncontaminated system. A variety of different methods exist for removing wall deposits and cleaning spray dryers, the most common being either washing with water and mechanical removal of the deposits either manually or with automated systems.

2.7.4 Theoretical Explanations of Wall Deposition

Langrish and Fletcher (2003) describe the process of wall-build up in spray dryers:

“Particles build up on the walls of spray dryers due to adhesion of particles to initially clean walls. Subsequent layers of particles become attached to this initial layer (cohesion). On the other hand, particles maybe removed from the wall deposits by the shear stress created from the gas flowing past the wall. Eventually a dynamic equilibrium is established between newly attached particles and detaching layers.”

Masters (1991) synthesises the following generic list of causes of wall deposits in spray drying:

1. Semi-wet deposits caused by the coarse droplets of the spray travelling to the wall in a time sufficient for such droplets to acquire dry surfaces.

2. Sticky deposits caused by the nature of the product at the temperature of the dryer.

3. Surface dusting of wall by dry powder.

4. Deposits caused by product build-up at positions of any distortion on the inner drying chamber surface

5. Deposits caused by product build-up at positions of excessive heat loss from the inner drying chamber surface (i.e. cold bridges in connection with the design of the structure, or at doors, pressure relief vents etc.).

Descriptions of mechanisms behind formation of deposits in certain areas of dairy spray dryers are offered by Chen *et al.* (1993), Chen *et al.* (1994), Ozmen and Langrish (2003) and Kota and Langrish (2006).

Hanus and Langrish (2007) theoretically examine the phenomena of re-entrainment of wall deposits, based on published literature and theory, concluding that this process is strongly dependent upon particle size and gas velocity.

2.7.5 Experimental Investigations into Wall Deposition

A number of studies have been conducted to experimentally investigate wall deposition in spray dryers. These have focused on either dairy or food applications using co-current dryers and vary in complexity from simply measuring deposition rates to investigating the effect of

process variables and material properties on deposition. The following is a brief review of publications reporting experiment work into wall deposition.

Chen *et al.* (1993) measured the amount of deposition in a co-current dairy spray dryer by scraping samples of deposits from areas of the walls and ceiling, also measuring the particle size distribution in these samples. They found that particle size and amount of deposition was lower towards the top of the dryer, and that deposition was related to temperature distribution within the dryer. This work was followed up by Chen *et al.* (1994), who studied the deposition of milk powder using a laboratory rig that mimicked the ceiling of a co-current dairy spray dryer. They found that the effect of particle size and water activity on deposition rate was related to the cohesiveness of the powder. The rate of deposition was found to decrease at the later stages of the deposition and electrostatics appeared to have no effect of the deposition rate.

Langrish and Zbicinski (1994) measured the amount of material deposited over an entire four hour operation of a pilot plant by collecting the material deposited on the internal wall. These rates were used to study the effect of swirl and spray cone angle on deposition as well for validation of a CFD containing a wall deposition submodel.

Ozmen and Langrish (2003) used stainless steel plates installed on and designed to mimic the walls of pilot plant spray dryer to measure the rate of deposition. The airflow patterns (swirl of the inlet air) and particle stickiness were altered so that the effect of these on deposition could be studied. They found that decreasing the swirl of the air flow gave the least deposition and that increasing particle temperature relative to the sticky-point curve

increased deposition. A similar approach to measuring wall deposition rates was used by Kota and Langrish (2006) to study the effect of the flow rate and solid content of liquid feed, finding deposition to increase as a function of liquid feed solids content. They also studied the material deposited on the walls, concluding re-entrainment of these was unlikely as they were found to be fused together to form a solid material. This technique for measuring deposition rate was also applied by Langrish *et al.* (2007) to compare the rate of deposition of maltodextrin and skim milk, showing that skim milk suffers the larger deposition rates.

Woo *et al.* (2008) examined wall deposits formed during spray drying of a sucrose-maltodextrin solution, finding that the moisture content, particle size and morphology of deposits was a function of location within the dryer and also drying conditions.

2.7.6 Modelling and Simulation of Wall Deposition

Publication of work on modelling of wall deposition in spray dryers has been infrequent. Those references that do exist are mainly focused around developing algorithms (submodels) to describe particle-wall collisions, which can be built into CFD simulations of dairy and food spray dryers.

Initially these submodels used a stick on contact criteria, i.e. any particle that came into contact with the wall during the simulation would become stuck. This approach was used by Langrish and Zbicinski (1994) and Huang *et al.* (2004) amongst others. Although, this method was a pioneering step to model wall deposition, it suffered from inaccuracy as it does not

take particle properties into account, meaning there is no change in particle impact behaviour (likelihood of sticking) to account for the drying of particles.

Later workers have taken steps to include particle properties, such as deformability and stickiness, into particle-wall collision submodels to increase accuracy and account for changes in particles during drying (Woo *et al.* (2010)). The need to understand changes in particle properties during drying has created a need for experimental tests to understand these. Literature published on this subject is covered later (§2.9.3).

Harvie *et al.* (2002) used the concept of a sticky point curve to describe whether particles stuck to the wall or not, above this temperature sticking occurred and below particles remained in the air flow. The rheological viscoelastic characteristics of particles (which change as the particle dries) are employed to model the stick or not stick criteria in a model produced by Woo *et al.* (2010).

2.8 Particle Characterisation

This research is concerned with the process of spray drying detergent powders and therefore being able to understand and account for the characteristics of particulate materials is an essential element of this work. This section of the literature review introduces theoretical concepts on particle characterisation and work on measuring / characterisation these, with a focus on granular detergents and spray dried powders.

2.8.1 Particle Size

The characterisation of particle size is critical to any analysis involving particulate processing. Describing particle size is easily done for spherical particles using either their radii or

diameter. However, this is not so easily done for irregularly shaped particles and has been widely discussed in literature. Rhodes (1997) gives an indication of how difficult the problem of describing the physical characteristics of irregular-shaped particles by stating

“the description of the shapes of irregular-shaped particles is a branch of science itself”

and

“it will be clear to the reader that no single physical dimension can adequately describe the size of an irregularly shaped particle”.

Despite this there are a widely used range of diameters used to describe irregular particles, these are described by Rhodes (1997). The diameter used in this work, the equivalent diameter of a circle with same area as the projected area of the particle resting in a stable position, as shown in Figure 2.7.

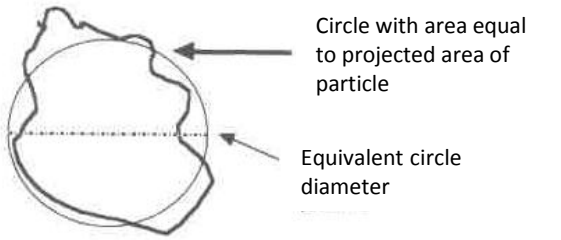

Figure 2.7: Particle Equivalent Circle Diameter

Most problems involving particles usually have a population of particles, the size for a population of particles can be described using a particle size distribution. For the purpose of this work, both size distributions and volume mean particle sizes were calculated in terms of mass distribution, thus:

$$D_{43} = \frac{\sum d^4}{\sum d^3} \tag{2.15}$$

2.8.2 Particle Morphology

Particle morphology describes the physical characteristics of particles, such as shape, texture, structure and porosity amongst others. These characteristics of particles will dictate the processability of a powder, in terms of the tendency of it suffer attrition, deposition and caking, and also the final product characteristics of the product such as flowability, appearance and density (Walton and Mumford (1999)).

Studies into generic spray dried particle morphology are discussed in Walton and Mumford (1999), Walton and Mumford (1999) and Walton (2000), where both spray drying and single droplet drying were applied to a range of materials to understand the influence of process and material parameters on the morphology of particles formed. The main features of particles observed in this work were hollowness, agglomeration and both spherical and irregular shapes. Particles were split into three classifications depending on their structure and morphology:

Agglomerate – A particle composed of individual grains of material bound together

Skin-Forming – A particle composed of a continuous non-liquid phase which is polymeric or sub-micron crystalline in nature.

Crystalline Structure – A particle composed of large individual crystal nuclei bound together by a continuous microcrystalline phase

These classifications are simplified cases involving basic materials, for complex detergent slurries all three can be considered to occur at once. The morphology and microstructure of detergent granules is a complex topic and depends on formulation, the drying process and also the microstructure of the slurry being dried (Stewart (2008) and Bayly (2006)). The relationship between these factors and granule morphology is not trivial (Stewart (2008)).

The microstructure of slurry depends heavily on its formulation, with slurries typically thought to contain three phases, inorganic (undissolved builders etc), organic (surfactants and polymers) and aqueous (water containing dissolved inorganics). Of particular importance is the phase chemistry of surfactant components (Stewart (2008)), this microstructure affects the rheology and therefore atomisation of the slurry, which in turn affects particle formation and drying (Bayly (2006)). In addition aspects of the slurry microstructure can be carried forward into the dried granules. Spray dried detergent granules tend to be porous, agglomerated, non-spherical particles with a wide range of sizes and shapes (Bayly (2006) and Stewart (2008)). These characteristics can also be linked with the various stages of drying (§ 2.3.6), particularly steam puffing which leads the formation of hollow and porous, non-spherical particles.

2.8.3 Particle Density

The density of a material is defined as its mass divided by its volume. For solid materials this is easily defined and quantified as both their mass and volume can be easily measured. But for porous materials, the volume becomes harder to define and therefore the density is not as easily quantified. Various different definitions of density for particulate and porous materials such as detergent powders exist and are shown in Figure 2.8.

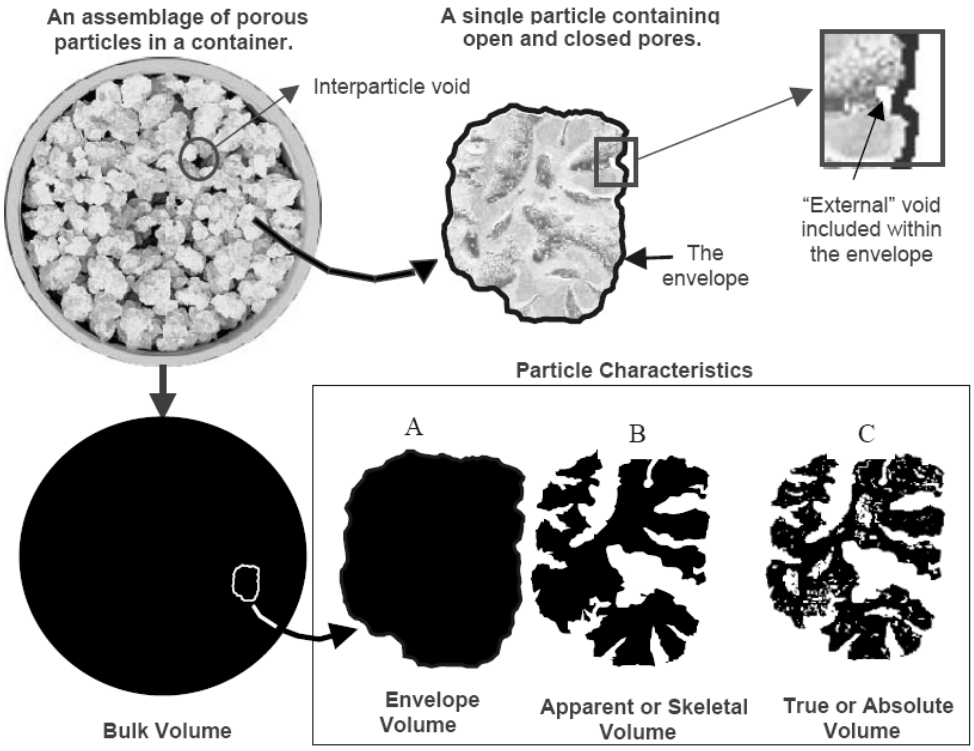

Figure 2.8: Illustrations of various types of particle volume taken from Webb (2001)

Three types of density are widely used to characterise detergent powder density, with the later two used in this work:

Bulk Density – is the density of an assembly of particles and includes interparticle voids as well as all internal and external pores.

$$\rho_{bulk} = \frac{m_{solid}}{V_{solid} + V_{closedpores} + V_{openpores} + V_{voids}} \qquad (2.16)$$

Envelope or Hydrodynamic Density – excludes the interparticle voids to draw an envelope density of the particle as illustrated in Figure 2.8.

.

$$\rho_{envelope} = \frac{m_{solid}}{V_{solid} + V_{closedpores} + V_{openpores}} \qquad (2.17)$$

Skeletal or Apparent Density – excludes open pores and interparticle voids to calculate the skeletal density of particles and is usually measured using helium pycnometry.

$$\rho_{apparent} = \frac{m_{solid}}{V_{solid} + V_{closedpores}} \qquad (2.18)$$

2.8.4 Hydroscopic Behaviour

Detergent powders are formed by drying an aqueous slurry to form a hydroscopic material. This means that their moisture content is constantly changing during the manufacturing process. It is widely accepted that the moisture content of detergent powder will have a significant effect on its physical and mechanical properties (Bayly (2006)). A detergent powder that contains the wrong amount of moisture may be difficult to produce and package, unstable whilst in storage and will ultimately reach the consumer in a poor condition. These factors mean that moisture content of detergent powders can greatly affect the economics of their production and sale (Bayly (2009)).

2.8.4.1 Bound and Free Moisture

The moisture contained within a detergent powder slurry can be split into two separate phases, free moisture and bound moisture (Bayly (2009)). These are defined as:

Free-moisture – any water that is not chemically bound is referred to as free moisture. This moisture comes from either raw materials or is added to aid processing. Within the granule this moisture will be contained within the organic phase of the granule and in open and close pores.

Bound Moisture – any water that is chemically bound is referred to as bound moisture. For example any hydrated water that is chemically contained in substances such as Sodium Carbonate hydrates.

2.8.4.2 Equilibrium Relative Humidity

Equilibrium Relative Humidity (eRH) is defined as the maximum value of relative humidity (expressed as a percentage between 0% and 100%) that a hygroscopic material can be placed in for there to be no resulting exchange of moisture between the sample and the environment. This is sometimes quoted as water activity (A_w), which is expressed as a number between 0 and 1, such that 100% eRH is equal to 1 A_w. The importance of Equilibrium Relative Humidity is that it used as an indicator of "free" moisture within a sample and thus this measurement is frequently used to characterise the moisture content of detergent powder samples.

2.8.5 Mechanical Properties

All materials will deform under the application of stresses, this deformation is governed by the nature and magnitude of the stresses applied and the properties of the material being deformed. The properties that govern deformation of materials under stress are frequently referred to as mechanical properties. In particle technology mechanical properties of both individual particles and bulk powders are of great importance as they will determine their behaviour as they are subject to stresses and strains during processing. Of particular relevance to this work is the role of mechanical properties in governing the deformation of particles upon impact with process equipment walls, a key parameter in caking and deposition (Cleaver (2008)).

Mechanical properties of materials can be described using a stress-strain curve which shows the extent of deformation (strain) under a range of stresses. An idealised stress-strain curve for a solid material is shown in Figure 2.9. Where stress is a measure (σ) of the average amount of force exerted per unit area and strain is a measure (ε), defined as the ratio of deformation with respect to the original length.

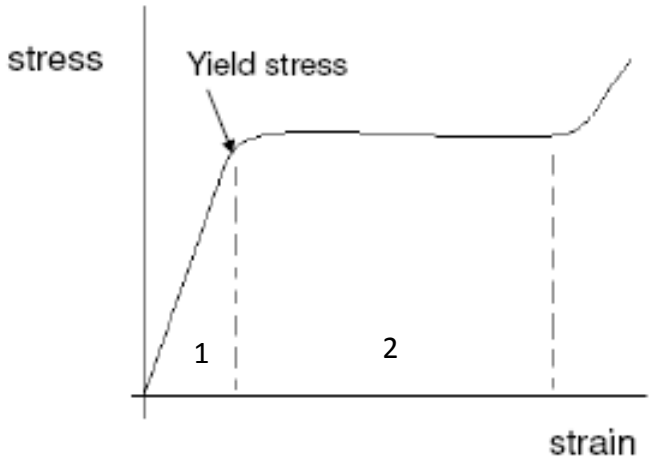

Figure 2.9: Typical strain-stress curve, where region 1) – elastic deformation, 2) – plastic deformation

Observation of these curves for solid materials usually identifies two types of deformation:

Elastic deformation – is temporary, as the material returns to its original shape when the stress is removed. Elastic deformations are caused by the deformations of chemical bonds thus such deformations are reversible i.e. the energy consumed to deform that material is returned when it reverts back it to its original shape. The elastic regime is characterized by a linear relationship between stress and strain, denoted linear elasticity and known as Hooke's law (region 1 on Figure 2.9). The gradient of this region is referred to as Young's (or the elastic) modulus, which is used to describe elastic deformation of a material.

Plastic deformation – causes non-reversible changes in a material such that it does not return to its original shape and retains its final shape when the stress is removed. These permanent deformations are a result of a breakdown in material structure as internal friction consumes the energy used to deform the material. Plastic deformation begins at a point referred to as the yield stress, below which only elastic deformation occurs and above which plastic deformation occurs. Plastic deformation of material is dependent on load rate but independent of time, i.e. under a constant load the material will not change shape.

Both Young's modulus and yield stress are of importance in powder technology and a variety of methods have been developed for obtaining stress-strain curves of particulate materials. The most common methods are centred around compression of material whilst recording both the stress and strain. Other methods include nano-indentation, which is described by Li and Bhushan (2002). Compression methods can be divided into confined and unconfined compression:

Confined compression – A bed of powder is compressed in a die and therefore has limited volume in which to deform. This measurement takes into account both particle structure and material properties (Figure 2.10 (a)). This method and the theory behind its application have been reviewed by Kawakita and Ludde (1970) and Nordstorm *et al.* (2008).

Unconfined compression – Either an individual particle (Figure 2.10 (c)) or a tablet (Figure 2.10 (b)) of the material is compressed between two plates and is free to deform horizontally as far as possible. The difficultly in handling and compressing single granules which are small and irregular in nature needs to be considered with the single particle

compression. Publications on these techniques include Pitchumani *et al.* (2004), Iveson and Page (2005) and Samimi *et al.* (2005).

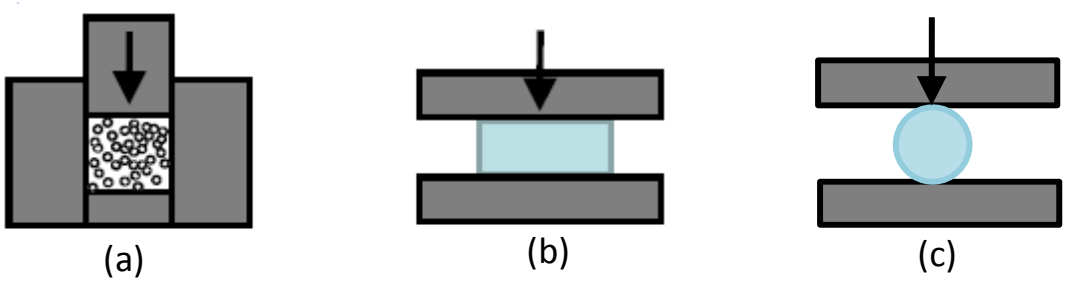

Figure 2.10: Methods of characterising powder mechanical properties (a) confined compression; (b) unconfined compression of several particles; (c) unconfined compression of one particle

Examples of studies in particle mechanical properties include, Adams *et al.* (1994) who used confined uniaxial compression to test the strength of agglomerates, Berggren *et al.* (2004) who again used confined compression to study spray dried particles, Samimi *et al.* (2005) who compared both single unconfined and confined bulk compression to DEM simulations, concluding that bulk compression should be used with caution to indicate the properties of single particles. Yap *et al.* (2007) used both single and bulk compression to evaluate the mechanical properties of pharmaceutical excipients.

2.9 Particle Impact Behaviour

Wall deposition during the spray drying process is caused by particles impacting and sticking to the process equipment walls, therefore understanding the impact behaviour of particles is critical to this work and is covered in this section of the literature review.

2.9.1 Restitution

When two bodies are brought into contact they may remain in contact, but if the bodies separate again after contact they are described as rebounding, or bouncing off of one and another. Restitution is the description of how the bodies rebound and move apart.

2.9.1.1 Restitution Coefficient

During inelastic collisions some of the kinetic energy is transformed into other forms of energy such as heat, sound and deformation of the material. The coefficient of restitution is a measure of the elasticity of a collision between two bodies, and is specifically defined as the ratio of the velocity of a body after impact to its velocity before impact.

Assuming that the body remains intact, then the coefficient of restitution, e, can be calculated as the ratio of velocities before and after impact thus:

$$e = \frac{v_r}{v_i} \qquad (2.19)$$

A perfectly elastic collision between two bodies will result in all velocities being unchanged and therefore the restitution coefficient has a value of exactly one. For a completely inelastic collision where the two bodies remain in contact the restitution coefficient will have a value of zero.

The coefficient of restitution is affected by both the conditions of the impact and the properties of the bodies coming into contact. For impacts of particular materials with surfaces and other granules the coefficient of restitution is frequently referred to as a “property” of the material.

2.9.1.2 Experimental Investigations into Restitution Coefficients

Many experimental studies have been conducted into the restitution of particulate materials. Experiments to study restitution usually employ high-speed photography to film the impact of particles on a surface and thus obtain the impact rebound velocities. These studies can be split into two groups, experiments to understand the fundamentals of impacts and restitution using idealised materials and experiments to study the effect of particle properties on impacts and restitution. This later group tend to be focused on agglomerates with the aim of better understanding and modelling granulation processes in industries such as pharmaceuticals and consumer goods.

Investigations into the fundamentals of restitution of idealised materials include, Gorham and Kharaz (2000) who measured the rebound characteristics (velocity, angle and rotation) of 5mm aluminium oxide spheres impacting on different surfaces (soda-lime glass and aluminium alloy) so that they achieved both fully elastic responses along with plastic deformation. One relevant result of this work was to show that impact angle affects both the normal and tangential restitution coefficients. Kharaz *et al.* (2001) conducted similar experiments to expand this work finding close agreement between their results and previous published numerical work. Dong and Moys (2006) study the effect of initial spin on oblique impacts of steel balls, finding that the value of the restitution coefficient increases with forward spin in the direct of impact and decreases with backward spin.

Studies of agglomerated granules include those of Iveson and Litster (1998) who made and impacted liquid-bound granules finding that these highly plastic particles had a restitution coefficient less than 1.0%. Fu *et al.* (2004) studied the impacts of wet granules measuring

their coefficient of restitution along with the maximum contact area. They found changing the parameters of the granulation process and materials used to manufacture their granules (liquid to solid ratio, primary particle size, binder viscosity and granulation time), changed the restitution coefficient, with a minimum of 97% of kinetic energy dissipated through viscous flow. Fu *et al.* (2004) also studied the impact behaviour of wet granules, examining the effect of variation in the manufacturing process on mechanical properties and therefore restitution coefficient, finding that more tightly controlled manufacture led to less variation in granule properties and therefore restitution coefficients. The restitution coefficient was found to be a function of granule structure by Mangwandi *et al.* (2007), who impacted three different types of granules described as binderless (autoadhesion), wet (liquid bridges) and melt (solid bridges). Clear differences between the values of restitution coefficient were observed for the different types of granules. This was explained by the presences of different bonding mechanisms, which dictate the energy dissipation mechanism upon impact.

An additional aspect of non-ideal particle restitution is the effect of shape. The impact of irregularly shaped particles has been studied by Li *et al.* (2004) using a two camera set-up to capture motion in all directions. The low value of restitution coefficients obtained for ore particles was attributed to small scale fragmentation of particles, owing to their irregular shape.

2.9.1.3 Theoretical Investigations into Restitution Coefficients

A theoretical analysis of the restitution coefficient of elastic-plastic spheres was conducted by Thornton and Ning (1998) to model the stick and bounce behaviour of these spheres with and without adhesion forces present. By considering the contact mechanics and adhesion

forces present the coefficient of restitution is expressed in terms of a critical sticking velocity, above which the particle deforms plastically and sticks and below which the impact is considered to be elastic. Weir and Tallon (2005) examined the theoretical regimes underlying the collision and recoil of elasto-plastic particles in low-velocity normal impacts. They found the coefficient of restitution to be a function of the ratio of the relative impact velocity to the system compression wave speed, and the ratio of the yield stress to Young's Modulus.

2.9.2 Breakage and Attrition

Particle breakage describes the size reduction of particulate solids. This is of importance during the manufacture and processing of spray dried detergent granules as reduction in particle size will affect powder processability (flowability and wall deposition) as well as product quality. This subject has been widely covered in literature. This review aims to cover the most relevant work and ensure that the theory and terms used in this work are well defined for the reader.

Attrition is defined as unintentional breakage of particles and conversely comminution is deliberate size reduction. Attrition was discussed by Bemrose and Bridgwater (1987) and comminution by Peukert and Vogel (2001).

2.9.2.1 Factors Affecting Breakage

Factors that breakage of particulate solids can by be grouped into material properties, environmental conditions and process conditions, as summarised in Table 2.5 (Bemrose and

Bridgwater (1987) (attrition), Peukert and Vogel (2001) (comminution) and Reynolds *et al.* (2005) (during granulation)).

Table 2.5: Summary of Factors Affecting Particle Breakage

Material Properties	**Contact Conditions**		**Environmental Conditions**
	Single	**Bulk**	
Density	Frequency		Temperature
Young's Modulus	Contact Area	Consolidation Stress	Humidity
Hardness	Contact Force	Shear Stress	Fluid Pressure
Fracture Toughness	Impact Angle (Oblique/Normal)	Shear Strain	Fluid Viscosity
Yield Stress	Time	Strain Rate	
Shape Size	Friction	Bed Height	
Surface Roughness	Velocity	Size Distribution	
Porosity			
Number and Size of Flaws			

2.9.2.2 Mechanisms of Breakage and Failure

Owing to the large amounts of literature published there are a wide range of terms used to describe the mechanisms of particle breakage. The following is a summary of definitions of these terms.

Wear – damage to the surface of the particle, which can be caused by abrasion (friction with a surface) or erosion (by impact on a surface). These mechanisms have been reviewed by Hutchinsons (1993) and Ennis and Sunshine (1993).

Chipping – sub-surface cracks form during the application of stress to the particle, resulting in removal of small pieces (significantly smaller than particle) from the particle surface (Ghadiri (1997)).

Fragmentation – larger cracks develop within the particle application of stress to the particle, meaning that the particle breaks into two or more fragments (Ghadiri (1997)).

Fatigue – repeated application of stresses, usually small stresses, which develop cracks leading to particle failure (Goder *et al.* (2002)).

2.9.2.3 Breakage Tests and Experimental Studies

Test methods into breakage are reviewed by Bemrose and Bridgwater (1987), Reynolds *et al.* (2005) and Ahmadian (2008). Test methods can be split into two categories, single particle tests that apply forces/stresses to particles through either compression (similar to mechanical properties measurement (§2.8.5)) or through impact onto a surface, and bulk tests that apply forces/stresses to a population of particles through either, compression, impact or shearing. Applications of the various test methods have been widely reported in literature and given here is a summary of relevant work to this thesis, namely single particle impacts.

Published work has reported experiments to study breakage behaviour in order to understand the effect of particle properties (material/chemical composition, morphology

and mechanical properties) and impact parameters (velocity and angle). The effect of particle impact velocity has been examined by most workers, including, Salman *et al.* (1995), Boerefijn *et al.* (1998), Boerefijn *et al.* (1998; Salman *et al.* (2002),Samimi *et al.* (2003), Samimi *et al.* (2004) and Reynolds *et al.* (2005). The unanimous conclusion of all workers is that increasing impact velocity increases the amount of particles broken, as there is more kinetic energy available to deform the particle to the point of failure. The mechanism of breakage also changes with increased impact velocity, with increased fragmentation instead of chipping, reported by several workers, including Salman *et al.* (2004), who specifically studied the failure modes of spheres at a range of velocities.

Workers examining the effect of impact angle on particle breakage include, Salman *et al.* (1995), Salman *et al.* (2002) and Samimi *et al.* (2003) who specifically targeted understanding the effect of angle on breakage of two types of synthetic detergent granules. In general, decreasing impact angle away from normal was found to decrease both the amount of particles broken and the extent of fragmentation. Samimi *et al.* (2003) elaborate on this, indentifying that at low velocities, where the chipping regime of breakage dominated, that the normal component of the impact velocity determined the extent of breakage, independent of impact angle. At higher impact velocities, the tangential component played a major role in the fragmentation of the granules, as the breakage increased significantly with decreasing impact angle under constant normal component of impact velocity. Samimi *et al.* (2004) studied the effect of angle on breakage mechanism finding that reducing angle from away from normal decreased failure of particles and led to asymmetrical breakage.

The majority of studies into breakage have featured some kind of examination of how breakage varies between different size particles, including, Salman *et al.* (2002), Samimi *et al.* (2003), Pitchumani *et al.* (2003), Salman *et al.* (2004), Samimi *et al.* (2004) and Reynolds *et al.* (2005). In general it is concluded that larger particles are more likely to suffer breakage and a greater extent of failure.

Studies into the effect of granule morphology of particular relevance to this work include, Samimi *et al.* (2003) and Samimi *et al.* (2004) who studied the breakage of two types of synthetic detergent granules with the same formulation, but produced by two different manufacturing processes (granulation and spray drying). Their main findings were that the different morphologies created by different manufacturing processes affect breakage, with the spray dried granule showing more breakage.

2.9.2.4 Theoretical Investigations and Models of Breakage

Theoretical investigations into particle breakage include, Ghadiri and Zhang (2002), Schonert (2004) and Herbst and Potapov (2004). Two main types of models of particle breakage have been published, empirical models constructed based on experimental data from studies similar to those described in the previous section (§2.9.1.3), or theoretical as described above. Empirical models include the work of Ghadiri and Zhang (2002) and more complex models include the DEM work of Herbst and Potapov (2004).

2.9.3 Deposition

Deposition describes the process of particles becoming attached to a surface. This is a result of attractive forces between particles and the surface, and for further layers of deposition on

top of the initial layer inter-particle attractive forces. This process is similar to caking, as described by Cleaver (2008) ”the undesired aggregation of particles resulting in the transformation of a free flowing powder into a coherent solid mass”.

2.9.3.1 Stickiness, Adhesion and Cohesion

Stickiness is an ambiguous term widely used to describe the state of materials that have a tendency to stick, or become adhered to other materials. Specific to particulate materials, Pasley and Haloulos (1995) state “Stickiness is used to define a state in which mass of powder resists movement and is no longer free flowing”. They go on to define the term as two properties, cohesion and adhesion:

Cohesion – is the measure of inter particle attractive forces

Adhesion – is a measure of particle-wall interaction.

2.9.3.2 Interparticle Forces

The attraction between particles and surfaces and between particles and other particles are caused by a range of forces acting between the bodies. These have been reviewed by Rumpf (1990), Seville *et al.* (1997) and Cleaver (2008) in terms of their influence on particulate materials. The following is a short summary of the main attractive forces that need to be considered when dealing with particulate materials.

van der Waals Forces – these forces occur between molecules in the two bodies and are electrostatic in nature. The electrostatic forces are caused by dipoles in the molecules present. The magnitude of van der Waals forces between two bodies can be predicted by

either the Hamaker theory or Lifshitz theory, which are described in detail by Seville *et al.* (1997).

Electrostatics – if particles become electrically charged in relation to each other and/or surfaces they will experience attractive forces. There are a variety of mechanisms by which particles can become charged in relation to their surroundings and these are again described by Seville *et al.* (1997).

Liquid Bridges – liquid present between particles and particles and surfaces will provide attractive forces through capillary actions, provided the liquid wets both surfaces. This phemonena is described by Cleaver (2008) and Seville *et al.* (1997).

Solid Bridges – contact of solid bridges between particles and particles and surfaces can be caused by solidifying of liquid bridges as they dry, or by processes such as sintering.

Mechanical Inter-Locking – with non-spherical particles and/or rough surfaces, outlying features can become physically inter locked and lead to particles becoming attached.

2.9.3.3 Measurement of Interparticle Forces and Surface Properties

Plentiful work has been published to describe the flowability and deposition of particulate materials as a result of interparticle forces. Methods to measure interparticle forces have been reviewed by Pasley and Haloulos (1995) and Boonyai *et al.* (2004), with the summary diagram below taken from the later.

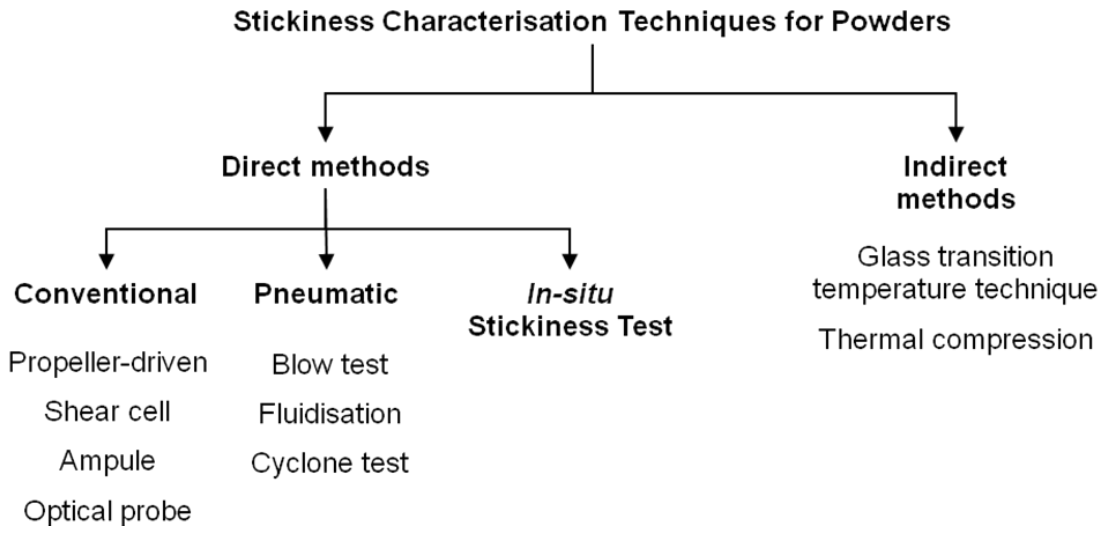

Figure 2.11: Stickiness Characterisation Techniques for Powders taken from Boonyai *et al.* (2004)

Research conducted with the aim of understanding powder stickiness during drying processes has been focused on construction of a stickiness curve and identification of a so called sticky-point or sticky region on this plot. A stickiness curve is usually a plot of temperature against moisture content for a particulate material, onto which areas of different flowability or stickiness properties are marked, an example is shown in Figure 2.12. The definition and identification of sticky regions was described by Kudra (2003).

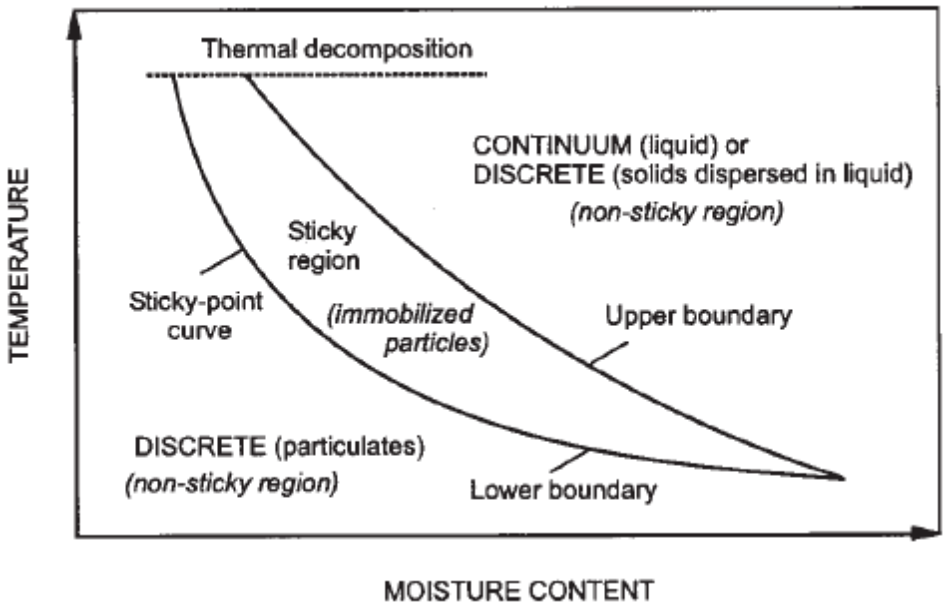

Figure 2.12: Sticky-point curve for an idealised material taken from Kudra (2003)

Workers developing stickiness curves for spray dried products include, Adhikari *et al.* (2003) and Adhikari *et al.* (2005) who worked with sugar rich food stuffs, developing both a physical stickiness tester and glass transisiton approach. The cohesion and stickiness of dairy powders for focus on wall deposition during spray drying of milk has been studied by Rennie *et al.* (1999), Kim *et al.* (2005) and Nijdam and Langrish (2006), with a particular focus on the effect of surface composition (fat migration).

2.10 Literature Review Summary

Granular laundry detergents are complex mixtures of chemicals that are predominantly manufactured through spray drying. The process of spray drying detergents is mature, yet there exists several opportunities to improve its operation in terms of efficiency, safety and product quality, one of these is wall deposition.

Understanding of this phenomenon in spray drying is limited, along with understanding of fluid and particle dynamics in spray dryers. Published work from both internal and external

sources varies greatly on all of these aspects of spray drying. Therefore an opportunity to expand understanding of all three these exists, and is covered in the first three results chapters of this thesis.

Wall deposition in spray dryers is known to be the result of particles striking the wall so process equipment, a wide range of literature is available on particle technology, including characterisation particle properties and relating these to particle impact behaviour. However, little work has been conducted on either using spray dried detergents and therefore the last two chapters of this thesis aim to apply particle technology to greater understand spray dried detergent particles and their impact behaviour, thus further exploring wall deposition in spray dryers.

Chapter 3 – Materials and Methods

3.1 Introduction

The aim of this chapter is to introduce the experimental methods, equipment and materials used in this research. The justification for the selection of each technique and the set-up used for each set of experiments is described in detail. Firstly, the pilot plant spray dryer used for all experimentation and manufacture of powders used in this work is covered. This is followed by detail on the formulations used during experiments, both used for experiments in the dryer and subsequent analysis. The techniques and experimental set-ups used for experimentation on the dryer are then described, starting with the observation and measurement of wall deposition, then moving on to the use of Particle Image Velocimetry (PIV) to study air and particle dynamics. Experiments on detergent powders are described in final parts of this Chapter, firstly the impact experiments, and secondly the characterisation of the physical and mechanical properties of the powders.

3.2 Pilot Plant Spray Dryer

The Integrated Pilot Plant (IPP) spray dryer is a pilot plant counter current detergent spray dryer (§2.3), designed to be “directly scalable” with full-scale manufacturing plants. The principles of this scalability are described later in this section. It is used within P&G to test the processability of new formulations and also to manufacture small amounts of formulations for consumer testing. Both of these tasks are undertaken before full-scale manufacture of formulations. This brings several benefits to the company, in particular it reduces the scale, and therefore cost of experimentation with new formulations, reduces downtime in production plants and allows small scale consumer trials to happen without

interruption of production plant schedules. This facility is thus the most important step in process and product development within Procter and Gamble's dry laundry business.

Figure 3.1: P&G Integrated Pilot Plant

The IPP, similar to all large-scale detergent spray dryers, operates in a counter-current manner. The drying air enters the drying chamber through angled inlets on the tower hip as shown in Figure 3.2. This results in the air travelling upwards through the tower in a swirling motion. The slurry is atomised using a pressure nozzle located approximately half way up the tower. The droplets of slurry are contacted with the hot air, resulting in drying. Owing to the

swirling motion of the air the droplets/particles move the drying in a circular motion (maximising residence and therefore drying time) until they reach the tower cone where they leave the dryer as powder product. The exhaust drying air is drawn out the top of the tower. This air stream contains fine particles and is cleaned by either cyclones or filters before being released to atmosphere.

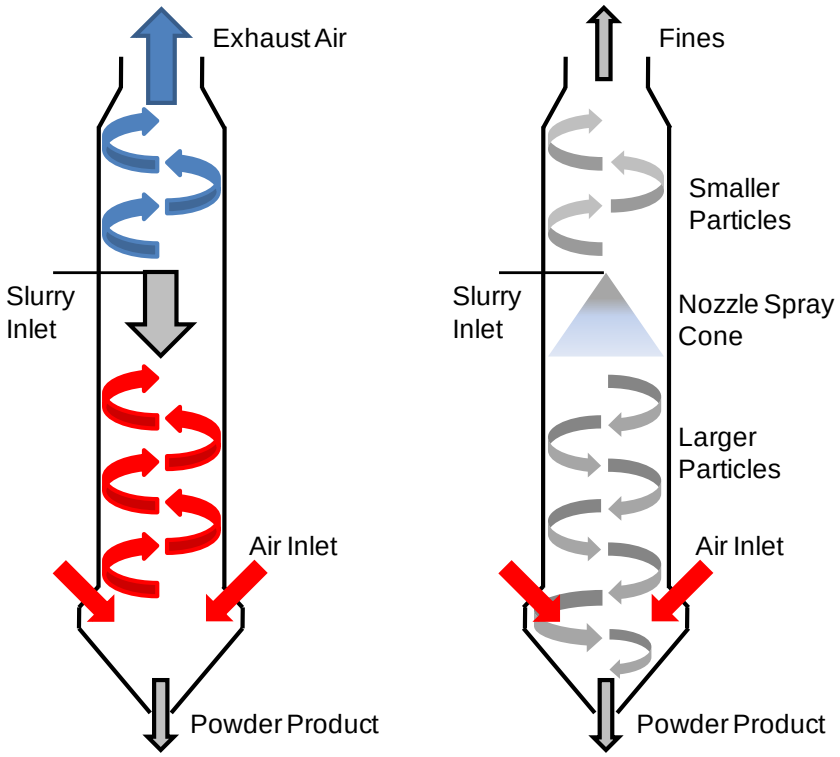

Figure 3.2: Counter-current Spray Dryer (air movement left and particle movement right)

As mentioned above, the IPP is designed to be "directly scalable" with full-scale manufacturing plants and therefore as many design features as possible have been kept identical to the full-scale plants. Spray dryers are known to suffer from poor scalability: Oakley (1994), Langrish and Fletcher (2003) and Huntington (2004), amongst others describe this (§2.4). The design of the IPP was a radical change from previous pilot plants, (Niederkorn (2000)), in that its layout is based on a horizontal section of a full-scale plant (tall and thin), rather than being a scaled down version in all dimensions (short and relatively

wide). The critical parameter for ensuring “scalability” of spray drying is the residence time of droplets/particles within the drying chamber (Oakley (1994)), as this dictates the drying of the droplet and therefore the properties of the particles produced (Huntington (2004)). The IPP layout (tall and thin) was designed to ensure that this key parameter was constant between full-scale and pilot-scale dryers. However, despite the constant residence time, the scalability of the IPP is not exact, because of the variation in mechanisms, such as drying and agglomeration which affect product properties, between it and full-scale plants. Therefore the scalability relies on previous experience and modelling tools to translate results obtained from the IPP to full-scale plants. The IPP is therefore termed “directly-scalable” rather than “absolutely scalable”.

A scale diagram of the IPP spray dryer is shown in Figure 3.3. This diagram includes the positions of experimental equipment used in experiments during this work, which are referred to later in this thesis, each position is labelled with a letter.

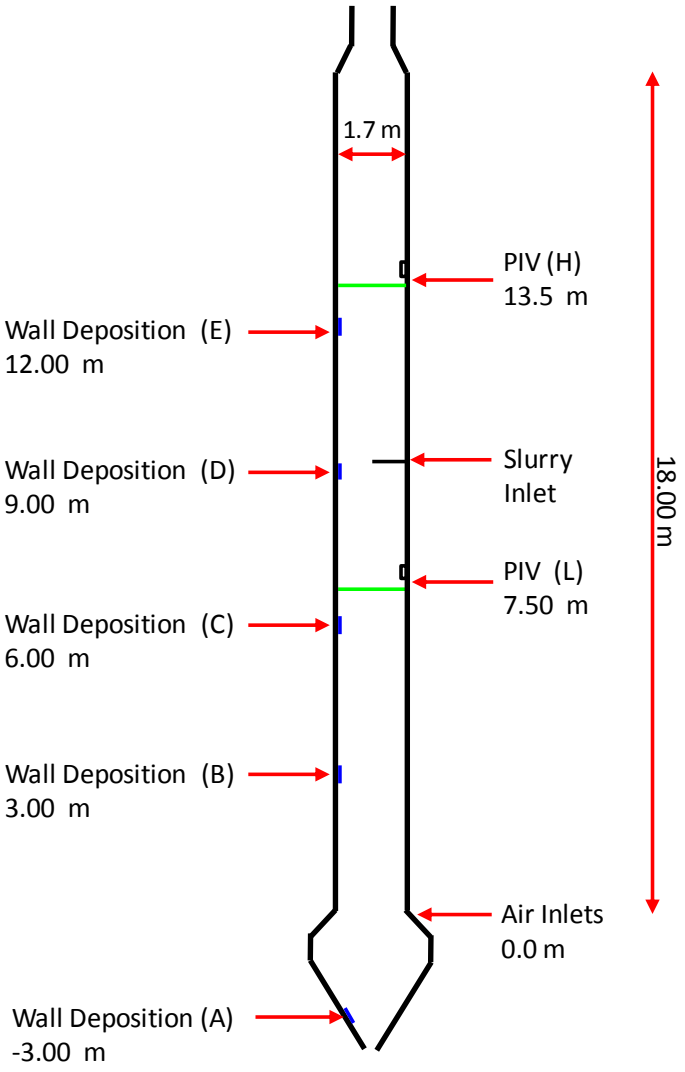

Figure 3.3: P&G Integrated Pilot Plant Experimental Layout (to scale) showing vertical measurement positions for wall deposition (left) and PIV (right)

3.3 Detergent Formulations

Several different detergent formulations were used in this research. This section explains the methods of manufacture and preparation of powders used along with details of the components and their levels in each formulation.

3.3.1 Detergent Formulas Manufacture and Preparation

All powders used during this work were manufactured using the IPP. Once manufactured the powders were stored before preparation and use.

To allow the effect of particle size to be studied in experimentation, samples of powder were separated into five different particle size ranges, namely, 150-250, 250-425, 425-710, 710-1180 and 1180-1800 micrometres. This was achieved using a series of wire sieve trays of mesh sizes 1800 µm, 1180 µm, 710 µm, 425 µm, 250 µm and 150 µm. The sieve trays used were 8 inches (200 mm) in diameter. Approximately 100 g of powder was placed on the top sieve and the stack was mechanically shaken for 5 minutes on the Ro-Tap supplied by Gilson Co. The powder was then collected from each sieve tray and the process repeated until enough of each size cut had been obtained.

3.3.2 Detergent Formulation Used for PIV Experiments

A single formulation was manufactured throughout all plant trials on which PIV experiments were conducted, as shown in Table 3.1.

Table 3.1: Detergent Formulation for PIV Experiments

Component Function	Component	Fraction by mass (wt)
Surfactant	LAS (linear Alkylbenzene-Sulphonate)	11.0%
Polymer	Polycarboxylate	2.0%
Builders	Phosphate	10.0%
	Sodium Silicate	5.0%
	Sodium Sulphate	65.0%
Others (minor components and processing aids)		7.0%

Using one formulation allowed the elimination of any changes in plant operation and product properties owing to changes in formulation. This was a simplified formulation that had been used before in previous studies of tower operation. Its processability and the operating conditions required for successful drying were known, reducing the time taken to achieve steady state operation whilst producing powder with the desired properties, thus maximising useful experimental time.

3.3.3 Detergent Formulations used for Particle Characterisation and Impacts Experiments

Four different formulations were used for the particle impacts experiments and subsequent characterisation work discussed in Chapter 7. These formulations were chosen to allow the effect of chemical composition on both the physical and mechanical properties and the impact behaviour of spray dried detergent particles to be studied. These formulations are summarised in Table 3.2.

Table 3.2: Detergent Formulations for Impact Experiments

Component Function	Component	Fraction by mass (wt)			
		High SiO_2 High LAS	**High SiO_2 Low LAS**	**Low SiO_2 High LAS**	**Low SiO_2 Low LAS**
Surfactant	LAS (linear Alkylbenzene-Sulphonate)	23.0%	5.0%	30.0%	5.0%
Polymer	Polycarboxylate	2.0%	2.0%	2.0%	2.0%
Builders	Phosphate	20.0%	20.0%	20.0%	20.0%
	Sodium Silicate	14.4%	20.0%	0.0%	0.0%
	Sodium Sulphate	30.4%	42.8%	37.8%	62.8%
Others (minor components including processing aids)		10.2%	10.2%	10.2%	10.2%

The amount of a surfactant, LAS (linear Alkylbenzene-Sulphonate) was altered along with the amount of a builder, Sodium Silicate (SiO_2) and Sodium Sulphate was used to balance the formulation to 100% of the required mass. These two materials were chosen as they are key to the development of future detergent formulations (Yangxin *et al.* (2008)), and are believed to have a significant effect on the mechanical properties of spray dried detergent particles. A particle with a high level of LAS will be paste-like, sticky, soft and therefore easily deformable. Sodium silicate increases the strength of particles, such that particles high in silicate will be strong yet brittle (Bayly (2006)).

3.4 Wall Deposition

An important part of this research was to develop methods for quantifying the amount of material deposited on the spray dryer walls during operation. During this work two main

methods were used, firstly deposition was measured at the end of an entire period of dryer operation, secondly deposition was measured for increments of time during dryer operation (time dependent measurement). Both rely on collecting and weighing the material deposited on a known area, giving a mass of material deposited per unit area, similar to experiments described by Langrish and Zbicinski (1994) and Woo *et al.* (2008). Measurements were made at several different axial positions (heights, in relation to air inlets) on the spray dryer at -3 m (A), 3 m (B), 6 m (C), 9 m (D) and 12 m (E) as shown on Figure 3.3, so that the amount of deposition could be studied as a function of position within the dryer (it has to be noted that position B was not available for all of the work conducted and is therefore absent from some data sets). Various formulations and operating conditions were used to allow the effect of formulation and drying operating conditions on wall deposition to be examined.

3.4.1 Whole Operation Deposition Measurement

A simple but effective method to measure the amount of wall deposition over a whole period of operation of the pilot plant spray dryer was to collect the material deposited on the inside of the numerous inspection hatches. This allowed calculation of the deposition per unit area for an entire period of operation.

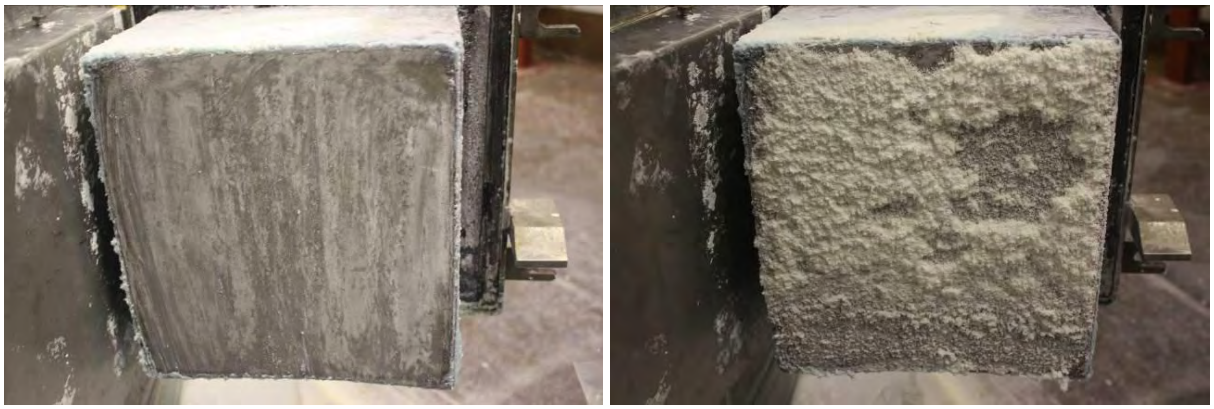

Figure 3.4: Spray Dryer Inspection Hatch Deposition Measurement (before and after operation)

An example of the material deposited on an inspection hatch during operation is shown in Figure 3.4. Each hatch was 260 mm by 240 mm, giving an internal surface area for deposition of 0.0624 m^2. This method was open to potential error through loss of deposits from around the edge of the hatch, when opening and also from any powder which was not collected for weighing. Efforts were made to minimise these potential errors by ensuring all deposited material was collected.

The deposit per unit area measured for hatches in various positions on the dryer was extrapolated over the entire internal wall of the dryer (by splitting it into sections where the value of the hatch in that area was applied, see appendix B for an example of this calculation) to allow the total amount of material deposited on the walls to be estimated. In turn this figure was used to calculate an estimate of the fraction of slurry sprayed that became deposited on the dryer walls, a yield calculation for product lost through wall deposition. Specific details of the experiments utilising this technique and the calculations on the data obtained are given in Chapter 4 (§ 4.4).

3.4.2 Time Dependent Deposition Measurement

To enable measurement of the amount of material deposited for increments of time during operation of the spray dryer, a removable plate was installed on the inside of the inspection hatch at 6 metres above the air inlets (position C) (Figure 3.5). The plates was held in place by guides which over lapped the edge of the plate, leaving an surface area of 260 mm by 200 mm (0.052 m^2) exposed for deposition.

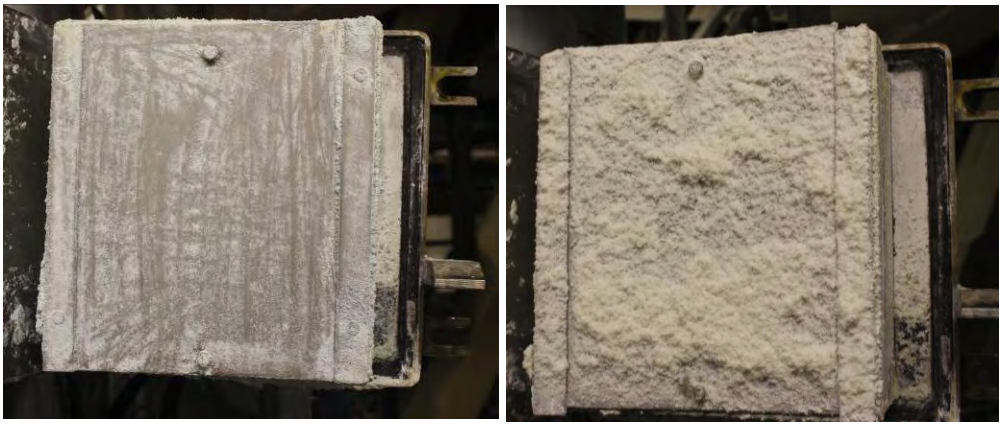

Figure 3.5: Spray Dryer Inspection Hatch Deposition Plates (before and after operation)

This allowed the amount of material deposited over a certain time period to be measured by removing and weighing the plates, then positioning back inside the tower for the next time increment, before repeating the process to build-up data on the amount of material deposited as a function of time, i.e. a deposition rate for time increments during operation. The use of plates made sure that material was being deposited on a layer of already deposited material, rather than on a clear steel surface as would be the case if the inspection hatch scraping method (§3.4.1) had been employed for these measurements. Specific details of the experiments utilising this technique and the calculations on the data obtained are given in Chapter 4 (§ 4.5).

3.5 Particle Image Velocimetry

In this section the experimental set-up and procedure for all the PIV work conducted in the IPP spray dryer is described. The PIV equipment used, how this equipment was installed and operated on the pilot plant is presented. Finally a description of how the data obtained was analysed to produce the results presented in Chapters 5 and 6 is given.

3.5.1 Particle Image Velocimetry Installation on Spray Dryer

The key challenge with using PIV in a large scale piece of equipment, such as the IPP spray dryer, is to achieve the correct arrangement between the camera and laser sheet so that movement of particles in the horizontal plane can be imaged. In this section, how the PIV equipment was installed on the spray dryer is explained. Experiments were conducted in two locations, position L which is below the spray nozzle (7.5 m above the air inlets) and in position H, which is above the spray nozzle (13.5 m above the air inlets), as is shown on Figure 3.3. These two locations were chosen so that air and particle motion could be observed in the two different flow regimes within the dryer, namely, low particle concentration above the nozzle and high particle concentration below the nozzle, (Bayly (2008)).

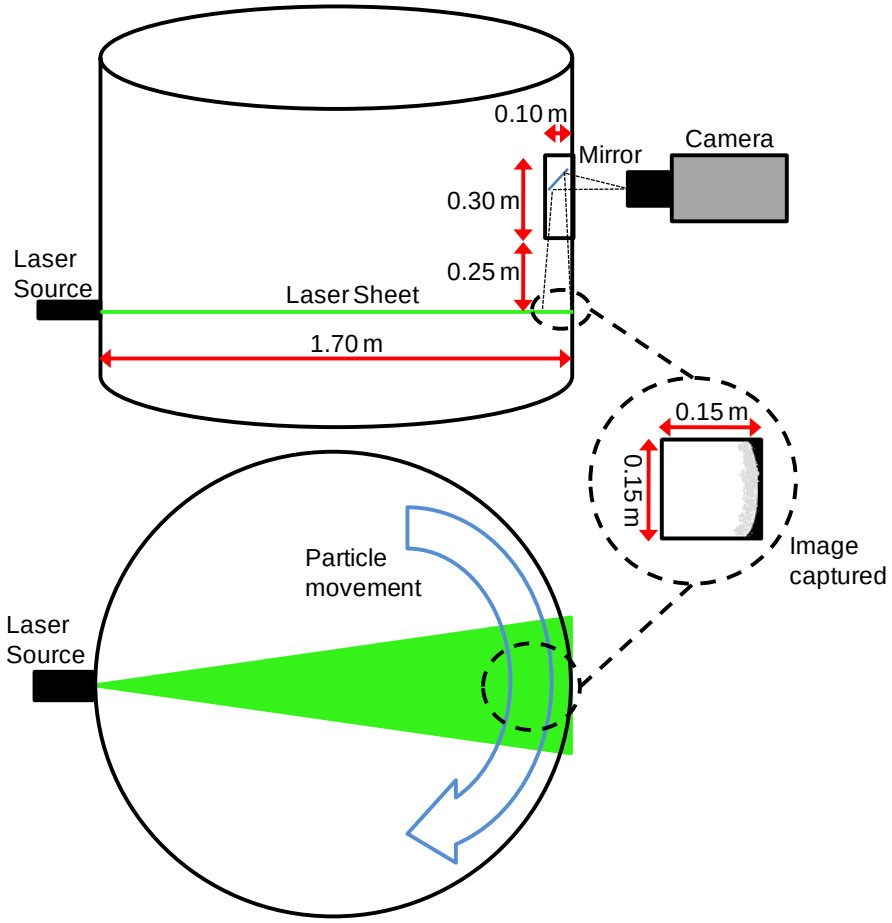

Figure 3.6: PIV experimental set-up installed on spray dryer

An overview of the experimental set-up installed each location is given in Figure 3.6. The lasersheet was projected horizontally across the drying chamber and the camera was focussed on this through a mirror arrangement as shown at the top of Figure 3.6. The bottom of Figure 3.6 shows a top-down view of the lasersheet and the motion of air/particles it captures in the horizontal plane. The area of this plane captured within the image captured by the camera is highlighted by the square illustrated on the right hand side of Figure 3.6.

3.5.2 PIV Equipment and Settings

Two different PIV systems were used in this work. Both were supplied from the EPSRC Instrument pool by TSI Inc. A low speed system was used for air flow experiments, and a high speed system was used for the experiments with particles present. The system used for each dataset is indicated later.

The low speed system consisted of a dual head Nd:YAG Solo laser (New Wave Research, Fremont, California) and a 4 mega pixel CCD camera (TSI PowerView Plus 4MP PIV Camera, TSI Inc.) with a resolution of 2048 x 2048 pixels^2, where each pixel represented approximately 4.9 x 10^{-9} m^2 (length of 7.0 x 10^{-5} m). The camera and the laser were both controlled by a TSI LaserPulse 610035 Synchroniser (TSI Incorporated, Shoreview, New Mexico) and a Dell Precision workstation running TSI Insight 3G software.

The high-speed PIV system consisted of a dual head Nd:YAG Pegasus laser (New Wave Research, Fremont, California) and a 1 mega pixel CCD camera (TSI PowerView HS-3000 Camera Model 630064, TSI Inc.) with a resolution of 1024 x 1024 pixels^2, where each pixel represented approximately 2.0 x 10^{-8} m^2 (length of 1.4 x 10^{-4} m). The camera and the laser were both controlled by a TSI LaserPulse 610035 Synchroniser (TSI Incorporated, Shoreview, New Mexico) and a Dell Precision workstation running TSI Insight 3G software.

3.5.3 Spray Dryer Operation

Two types of plant operation were undertaken during this work:

- Cold air was passed through the dryer with no detergent present, for observation of air flow patterns.

- Operation of the dryer, where detergent is sprayed into a hot air stream to allow the movement of particles within the air to be observed.

For the cold air only trials three different airflow rates were used, these are shown below in Table 3.3. The air flow rate was controlled by adjusting the air inlet and outlet fan speeds until the required flow rate was reached. The air used was at ambient temperature (10-20 °C). The other process variable that was controlled during these trials was the pressure within the drying chamber. Like many spray dryers, detergent dryers are operated under vacuum (a pressure below atmospheric), this prevents unwanted escape of product through any holes/gaps in the dryer. For the purpose of this work the tower underpressure was kept constant at 124.5 Pa (0.5 inches of water).

Table 3.3: Air flowrates used for PIV trials

Flow Condition	**Air flowrate ($kghr^{-1}$)**	**Inlet Tangential Velocity (ms^{-1})**
Low	6500	3.3
Medium	8000	4.1
High	10000	5.1

In the trials where detergent was sprayed three operational parameters of the dryer were adjusted, namely the air inlet and slurry flow rates and the air inlet temperature. This allowed the effect of different combinations of air and slurry flow rates to be studied, whilst ensuring that the moisture content (drying) of the powder remained unchanged. The conditions used for these PIV experiments are shown in Table 3.4 and Table 3.5. A simple mass balance model (§2.4.1) was used to calculate these operating conditions, although they

were changed occasionally by the plant operators to ensure the correct product moisture content was achieved.

Table 3.4: Operating parameters used for measurements above nozzle

Relative Slurry Flowrate	Air Flowrate ($kghr^{-1}$)	Air Inlet Temperature (°C)
1.0	6000	240
1.2	6000	260
1.2	8000	220

Table 3.5: Operating parameters used for measurements below nozzle

Relative Slurry Flowrate	Air Flowrate ($kghr^{-1}$)	Air Inlet Temperature (°C)
1.0	6000	240
1.2	6000	260
1.2	8000	220

3.5.4 Airflow Experiments and Analysis

To allow the measurement of air velocities and the observation of air flow patterns the ambient airflow was seeded with olive oil droplets. Droplets in the order of 1 µm were used and have a sufficiently small relaxation time (3×10^{-6} seconds, calculated as the Stokes drag relaxation time as described by Raffel *et al.* (2007) that they can be considered to faithfully follow the air flow. An aerosol of oil droplets was provided by a TSI 9307-6 seeding device. This device uses pressurised air to atomise oil into fine droplets, forming an aerosol, an impactor plate is situated inside the vessel to collect larger droplets and ensure a narrow size range of oil droplets is supplied. The stream of air and oil droplets entered the drying

chamber through a specially constructed flange and lance fitting. The location of this lance in the drying chamber was optimised through trial and error to find the position that gave the most consistent seeding of the air flow in the area being studied.

Fast Fourier Transform (FFT) cross correlation was used with a Gaussian peak engine, to interrogate the images, which were divided into Interrogation Areas (IA) of length L_{IA}. 1000 image pairs were captured for each experiment. The images were processed using a recursive Nyquist grid. For the first pass the interrogation areas were 64 x 64 pixels^2 with 32 x 32 pixels^2 being used for the second pass. The vectors generated were then filtered using a local vector validation, which rejected any vector with velocity value greater than 5 times the local mean (3 x 3 grid). After this filtering, the vector field condition was used to recursively fill any holes in the vector field with a local mean (3 x 3 grid). The resulting vector files were loading into and processed using MATLAB 7.1 software (Mathworks Inc.), with fluid dynamic parameters (described in §2.5.3) calculated by subroutines (examples of which are displayed in appendix A) before being displayed.

3.5.5 Spraying Experiments and Analysis

Particle velocities and trajectories were calculated using the high-resolution particle image velocimetry analysis algorithm of the TSI Insight PIV 3G software. This application is designed to allow the particles that are used for cross-correlation to be specified based on size and greyscale. To ensure only particles that were contained in the lasersheet were used in this analysis, images were thresholded using the MATLAB 7.1 software (Mathworks Inc.). The threshold limit used was selected through observation of the greyscale values of in and out of focus particles within each set of images, details of this process are given in Appendix D.

The thresholded data were saved as TIFF files before they were loaded into the Insight 3G software for cross-correlation.

As for the air flow, the algorithm utilises Fast Fourier Transform (FFT) cross correlation to interrogate the images, which were divided into Interrogation Areas (IA) of 64 x 64 pixels^2. The resulting vector files were loading into and processed in MATLAB 7.1 (Mathworks Inc.) before being displayed. Image analysis algorithms written in MATLAB 7.1 (Mathworks Inc.) were used to calculate particle size and concentration parameters from thresholded images, details of these calculations are given in Appendix D (example codes are displayed in Appendix A).

Two sets of 1000 image pairs (2000 in total) taken at a rate of 500 Hz (4 seconds of footage) were analysed for each experimental point.

3.6 Impact Experiments

In order to investigate the impact behaviour of individual detergent granules an impact rig was used to fire particles into a target. High speed video footage of the impact target was taken so that the impact behaviour of the particles could be observed. This section describes the rig design and its operation and analysis of the images obtained.

3.6.1 Impact Rig, design, Set-up and Operation

This design of impact rig has been used extensively previously: Samimi *et al.* (2003) and Samimi *et al.* (2004) studied the impact breakage of detergent materials, although a slightly

different set-up of the rig was used so that impact debris could be collected and analysed. A schematic of the experimental set-up is shown in Figure 3.7.

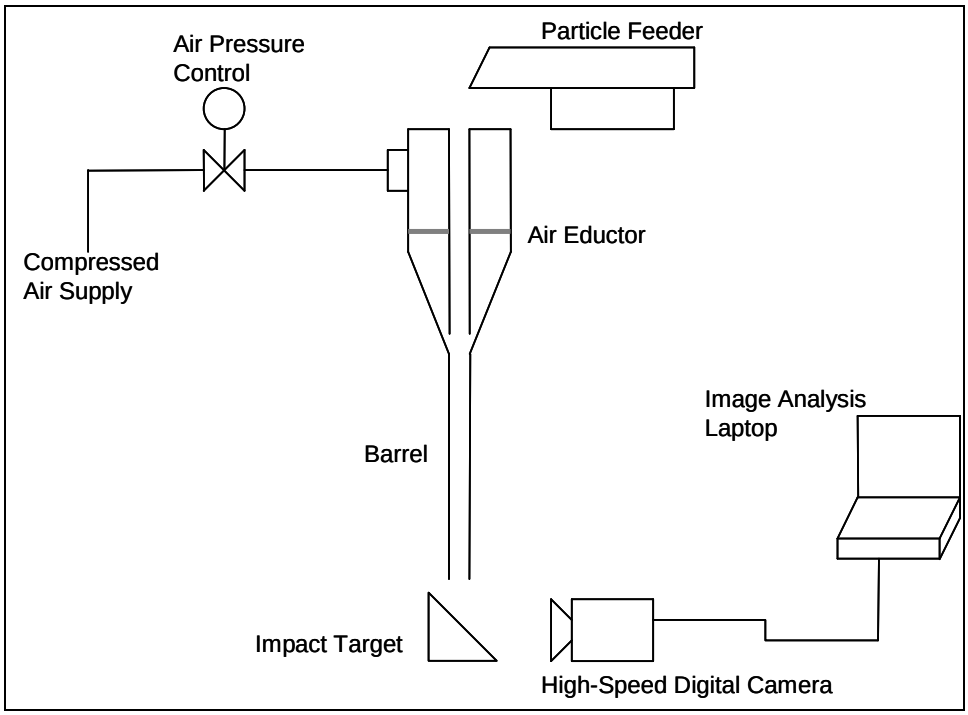

Figure 3.7: Particle Impact Experimental Set-up

The impact rig consisted of an air-eductor which used a compressed air supply to accelerate particles through the barrel of the rig. The barrel was 0.02 m in diameter and 1 metre in length. The air eductor was designed to generate a small vacuum at the inlet to barrel (accelerating tube) so that particles were entrained due to the Venturi effect. Particle velocities were controlled through adjustment of the inlet pressure of the compressed air supply to the eductor. The compressed air supply pressure was controlled by an inlet valve with associated pressure gauge. A porous sintered plate was located above the eductor to help ensure the airflow inside the barrel was straight.

Particles were fed into the rig using a vibratory particle feeder, the rate of particles fed into the rig was controlled by adjusting the oscillations of the particle feed tray. The particle feeder was set so that a constant steady stream of particles was fed into the rig, resulting in regular particle impacts on the target. Due to the nature of the rig these impacts were spread across a 0.01m^2 area of the target and therefore not all particles striking the target are in the field of view or in focus of the high-speed camera.

A series of stainless steel impact targets were positioned at the bottom of the barrel, so that particles accelerated down the rig are directed onto it. These targets were at a range of angles from horizontal, 30°, 45°, 60° and 90°.

3.6.2 Particle Imaging and Analysis

The impact of particles was filmed using a RedLake MotionPro X4 high-speed digital camera. Images were captured at a rate of 10,000 frames per second with a resolution of 256 × 256 pixels using an exposure time of 15 µs. The exposure time of 15 µs was found to minimise blurring of particles (at this exposure, a particle travelling at 20 ms^{-1} will move 0.3 mm), whilst still allowing a sufficient amount of light to be captured to ensure good quality images. Lighting was provided by two carefully positioned 400 W spotlights.

Multiple particle impacts were captured in one sequence of images; typically 2000 to 5000 frames were taken, (time periods of between one fifth and half a second) enough to capture around 50 to 100 particle impacts, depending upon the particle size and feed rate.

A calibration shot (focusing on a scale a set-distance from the lens) was taken at the start of each filming session. This meant the camera was focused on a point at a set distance from

the lens (e.g. the depth of field is used to ensure camera is in focus). The camera was then positioned so that the lens was the same distance from the centre of the impact target as it had been from the calibration scale. The calibration scale was used to calculate the actual distance each pixel on the screen represented by simply taking the number of pixels used to display a set distance on an image of the scale. Each pixel typical represented a distance of 0.05 mm.

Twenty particles were analysed for each experimental condition (constant particle sieve cut, formulation, moisture content, impact velocity and angle) and only particles that were clearly in focus were chosen for analysis. Neglecting particles that were not in focus ensured that all observed breakage could be seen as well as minimising error whilst calculating particle velocities. Particle velocities were obtained by noting the original position of a particle in terms of its *x* and *y* axis pixel values, then moving several frames forward and taking the *x* and *y* pixel values for the particle's final position. This allowed the distance moved in a set time period to be calculated. If breakage of each individual particle was observed it was recorded along with the number of fragments generated. If no breakage was observed the rebound velocity was calculated in the same way as described for impact velocity. The ratio of rebound to impact velocity was calculated to give the restitution coefficient of the particle.

3.6.3 Statistical Analysis

JMP Statistical Discovery Software version 8.02 (SAS Institute, Cary, NC) was used to analyse the relationship between all of the variables studied in the impact experiments. Initially this work involved correlation of the entire dataset to produce values for correlation between

variables, allowing judgement on their interaction. Based on the high correlations seen between some of the variables and impact behaviour responses, surface response models were fitted using the JMP software.

3.7 Particle Characterisation

3.7.1 Particle Size, Shape and Structure

3.7.1.1 Scanning Electron Microscopy (SEM)

Electron microscopy was used to characterise the structure and morphology of samples of detergent powders used in this research. Scanning Electron Microscopy (SEM) has several advantages over optical microscopy, including increased magnification and better topographical information about a materials surface.

All SEM images presented in this thesis were obtained using a Hitachi Tabletop Microscope, quasi-SEM TM-1000 at P&G's Newcastle Technical Centre. This can view samples at magnifications from 20 and 10000 x. It operates with a fixed accelerating Voltage of 15 kV under a vacuum of approximately 0.1 Pa.

3.7.2 Particle Density

3.7.2.1 Envelope Density – GeoPyc

The concept of envelope density is explained previously (§2.9.3). The envelope density of samples in this work was determined using the GeoPyc device supplied by Micrometerics. The GeoPyc determines the envelope density of a sample through a displacement method, which measures the volume of a sample of known mass. This technique relies on DryFlo, a

highly flowable material made-up off a narrow distribution of microspheres. This is used in place of oil or mercury which have been traditionally employed, and has the benefit of not entering pore space or wetting the sample (Webb (2001)).

The GeoPyc consisted of a piston and cylinder arrangement as shown in Figure 3.8. A force is applied to the piston and it moves inside the cylinder and compresses the material present. The amount of force can be adjusted to control the amount of compaction that occurs. A force of 55 N was used throughout this work. The cylinder rotates during the compaction process to ensure the material inside is continuously mixed and does not segment.

The measurement is conducted over two stages, firstly the volume of the DryFlo alone is inserted into the cylinder and a preliminary compaction undertaken to establish a zero-volume baseline (Figure 3.8a). The pre-weighed sample is then inserted into the cylinder with the DryFlo. To ensure that all of the sample is surrounded by DryFlo, the cylinder is gently agitated to mix the sample and DryFlo. The compaction procedure is then repeated to give the volume of the sample (Figure 3.8b), this volume is used to calculate the density of the sample. Five repeats were conducted for both the baseline and sample compaction steps so that an average value could be calculated for increased accuracy (Webb (2001)).

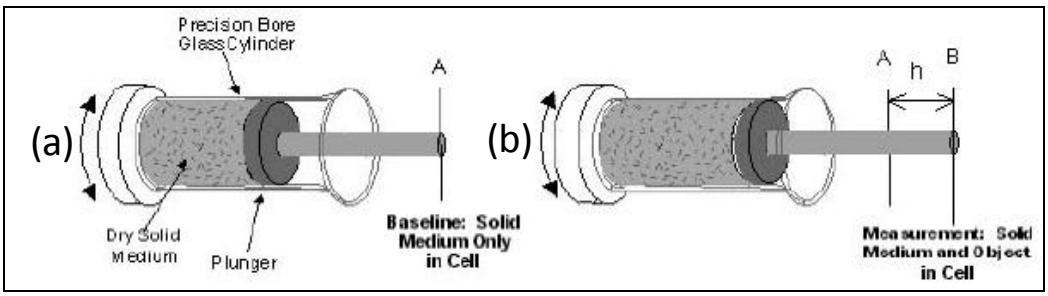

Figure 3.8: Volume determination by displacement of dry solid medium (DryFlo), (Webb (2001))

3.7.2.2 Skeletal Density - AccuPyc

The concept of skeletal density has been explained previously (§2.9.3). The AccuPyc is a helium gas pycnometer. A sample of known mass is sealed inside the sample chamber of known volume (Figure 3.9a), helium is admitted, and then expanded into a reference chamber also of known volume (Figure 3.9b). The difference in pressure from prior to expansion and afterwards is measured and used to calculate the sample volume. Dividing this volume into the sample mass gives the gas displacement density. Helium is the preferred gas medium as it readily diffuses into small pores, (Webb (2001)).

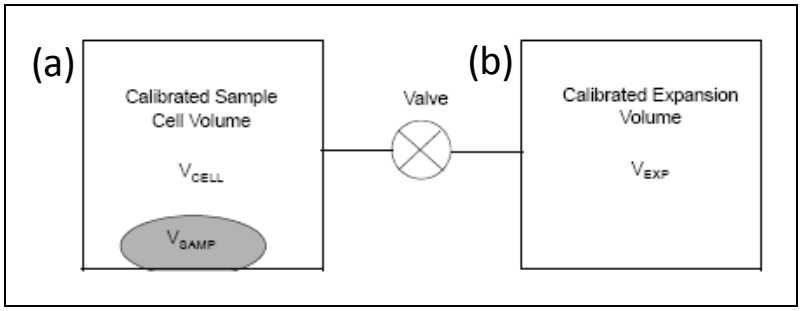

Figure 3.9: Simplified diagram of the AccuPyc (Webb (2001))

3.7.3 Hydroscopic Behaviour

3.7.3.1 Moisture Content

The absolute (§2.9.4) moisture content of samples was measured using an infra-red mass loss method. The standard procedure within P&G is to expose the sample to a temperature of 160°C for a period of 5 minutes and measure the change in mass of the sample as its water evaporates. The standard P&G procedure was used so that the moisture content of powders made and used in this work could be related directly to those made and used in other work within the company. This method has been developed through vast experience

within the company, the temperature of 160 °C is used because it is above that required to evaporate both free and chemical bound moisture within the sample (Bayly (2009)). The time period of 5 minutes is long enough to ensure the entire sample has been heated to 160 °C and therefore that the moisture content has completely evaporated. Two different models of infrared moisture measurement balances were used, both supplied by Mettler Toledo, the HB43-S and the H7.

3.7.3.2 Equilibrium Relative Humidity

Equilibrium Relative Humidities were measured using AW-DIO Water Activity Station probes in conjunction with a Hygrolab 3 bench-top display unit. Both were supplied by Rotonic. To measure the eRH of a powder sample it was placed inside a reusable plastic sample container, which was in turn inserted into a thermally insulated block to prevent temperature changes in the sample during measurement. The sample was covered by the water activity probe which was then activated and left until it reached equilibrium. Once at equilibrium the eRH value was recorded from the bench-top unit.

3.7.4 Mechanical Properties

The importance of mechanical properties to the work presented in this thesis were discussed previously, (§2.8 and 2.9), along with the two principal methods of measuring mechanical parameters, namely confined and unconfined compression tests. Both of these were conducted using an Instron 4469 mechanical tester, which records the force required to apply a certain strain to a sample material. The force recorded can be converted into a stress, allowing a stress versus strain curve to be obtained (§2.8.5). There are many complex methods of operation and experimental set-ups available on the Instron, here only

compression testing was conducted. One key consideration for both confined and unconfined compression work described in this thesis is the rate-dependent behaviour of granular detergent materials. This is expressed as strain rate-dependent since this is the parameter through which this instrument controls compression tests. To account for his behaviour and allow direct comparison between different measurements, a constant strain rate of 1.0 $mm.min^{-1}$ was used for all work, as recommended by Mort (2002).

3.7.4.1 Confined Compression

Uniaxial confined compression tests on powder samples have been investigated by Kawakita and Ludde (1970), Mort *et al.* (1994) and Adams *et al.* (1994) amongst others. Within P&G this type of test has been developed into a standard method for product characterisation, called "Compaction curve analysis" (Mort (2002) and Mort (2004)). The key parameters obtained from compaction curve analysis are the yield stress and join stress of the powder sample. Values of each are calculated from the compaction curve obtained through compression of the powder sample in a die using the Instron. An overview of this experimental set-up is shown in Figure 3.10. The die used in this work was 25.4 mm (1 inch) in diameter.

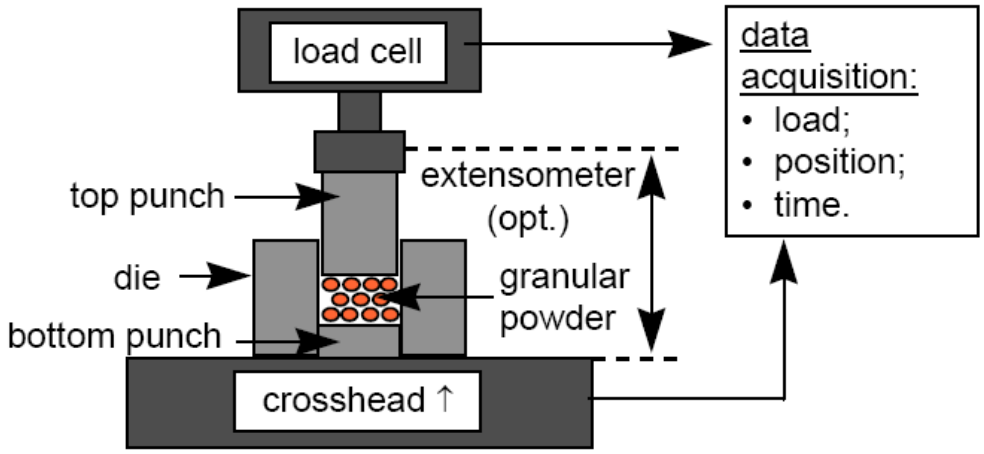

Figure 3.10: Overview of Instron Confined Compaction (Mort (2002))

The force-displacement data obtained from this uniaxial compression is then plotted in a manner referred to as compaction curve analysis and shown in Figure 3.11 (Mort (2002)). The force applied is converted into a pressure (stress) and plotted along the x-axis. The displacement measured is adjusted by subtracting the elastic deformation (both sample and equipment compliance, which is estimated using a mathematical model as described by Mort *et al.* (1994)) at each point to leave the plastic deformation of the sample. This is then converted into relative density (measured density / true density based on the mass of sample entered into the analysis software) and then plotted on the y-axis. The values of this parameter are represented by the bold line on the plot in Figure 3.11. Another parameter plotted on the compaction curve is the "compaction rate", a semi-log relationship between density (Mort *et al.* (1994)).

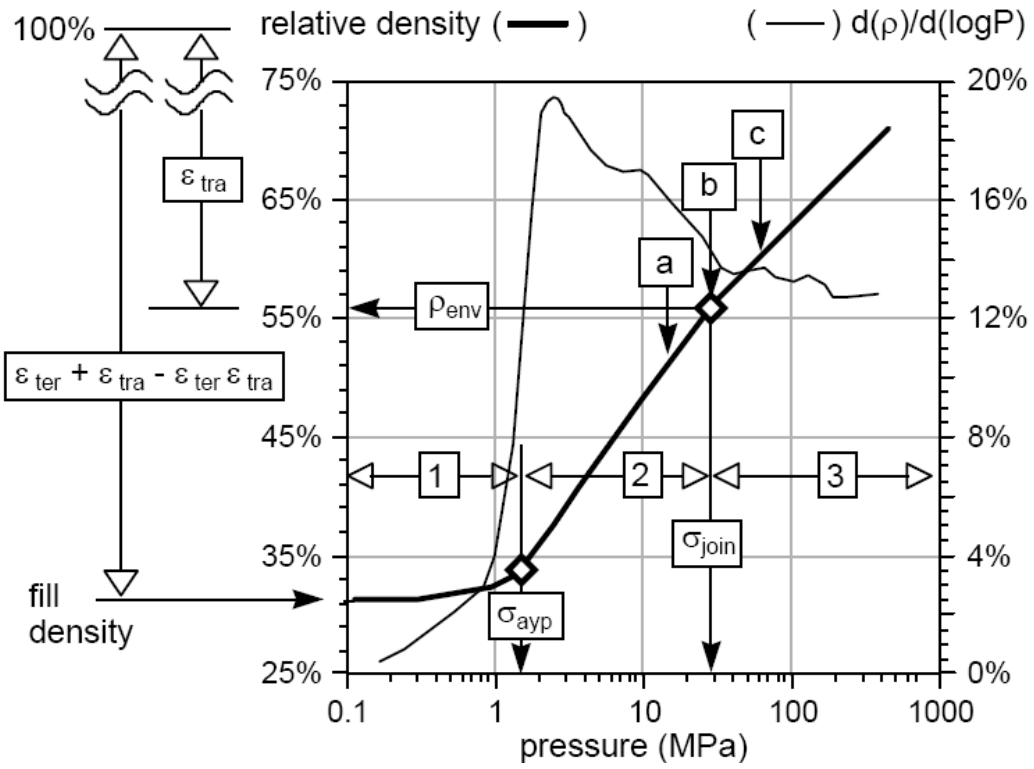

Figure 3.11: Overview of Instron Confined Compaction (Mort (2002))

The compaction curve of granular materials is generally interpreted as having three distinct regions (Mort *et al.* (1994)). These are labelled 1, 2 and 3 on the plot in Figure 3.11. Region 1 is controlled by packing arrangement, as the granules move past each other as bulk density is reduced by the pressure applied. This process is succeeded by plastic deformation of granules in region 2 to fill any remaining interstitial voids in the packing structure. The final stage is the final removal of inter-granular porosity as particles disintegrate and lose their individual structures. The transition between regions 1 and 2 is associated with the onset of plastic deformation in the granular material and is termed the apparent yield stress (σ_{ayp}). The stress at the transition between regions 2 and 3 is termed the join stress (σ_{join}) and indicates the removal of particles individual structure as they break and their surfaces join together, eliminating interstitial voidage. Values for both of these parameters are extracted

through automatic calculations within the analysis software used within P&G as described by Mort (2004).

3.7.4.2 Unconfined Compression

Unconfined compression of tablets of detergent powder is a technique that has been developed to allow the mechanical properties of detergent materials to be studied independently of the effect of particle structure. The tablets compressed were made through similar confined compression in a punch and die arrangement as described for the compaction curve analysis. A force of 45 kN was used to compress the powder to form tablets, this large pressure was used to ensure all porosity was removed from the sample and a solid material formed. In order to check this, SEM images of the tablets were taken and are shown in Figure 3.12, where the tablet's surface can be seen to be solid and continuous on two scales. This is also similar to the appearance of confined compression powder after the compression.

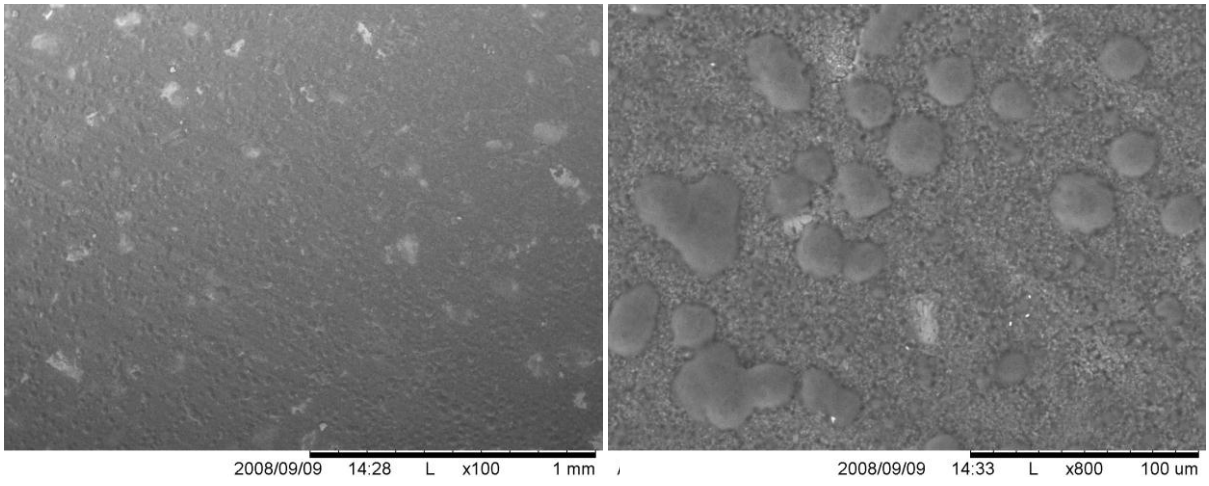

Figure 3.12: SEM Images of unconfined compression tablet before testing

The tablets were then placed between the two anvils and compressed at a strain rate of 1.0 $mm.min^{-1}$ until a force of 45 kN was applied. The stress versus strain curve obtained from this compression was then used to calculate values for the Young's modulus and yield stress.

The Young's modulus of the tablet was calculated as the gradient of the linear deformation region. The yield stress was obtained as the stress relating to the lowest value of the second derivative of stress-strain curve obtained, the point which indicates the end of the linear deformation region.

3.8 Computational Fluid Dynamics Simulations

Computational Fluid Dynamics (CFD) simulations used for aiding understanding of experimental results in Chapters 5 and 6 were performed using the commercially available FLUENT (version 12.0.16) package. This work was conducted by BoonHo Ng who is based in P&G's Beijing Technical Centre.

The geometry of the spray dryer was represented by a three-dimensional mesh, generated from a three dimensional solid model created from engineering drawings of the dryer using the pre-processor GAMBIT 2.4.6. Due to the complexity of the geometry, the meshes were generated through TGrid meshing scheme with Tet/Hybrid elements. The total cell number for the mesh is 4,983,118 cells, with cell refinement for the whole section of ~1.15 m above and below the mirror box, as shown in Figure 3.6. The total mesh size is 4,278,125 cells. An overview of this mesh is shown in Figure 3.13.

The mesh generated was then used in FLUENT to simulate the air flow within the dryer. A pressure-based solver with implicit linearisation was used to solve the mathematical model

in two steps. In the first step, the momentum equations were solved for acquiring velocity profiles. In this study, the second order discretisation model was used for momentum equations. In the second step, an equation for the pressure correction was derived from the continuity equation and the linearised momentum equations. This pressure correction equation was then solved to obtain the necessary corrections to the pressure and velocity fields and the face mass fluxes such that continuity was satisfied. Due to the unsteady-state nature of process, the simulations were done as transient processes with first order implicit temporal formulation, with time step of 0.01 s. The boundary was treated as a non-slip wall in the simulations. A Reynolds stress turbulence model was used to capture the swirls in the spray drying tower. 16 parallel processors were used to run the simulations. Each simulation was run for more than 50 s of process time in order to obtain for reliable results.

The dryer operating conditions used in experiments were replicated in the CFD simulations. The operating temperature was set at 20 °C where the air density was assumed as 1.205 kgm^{-3} and the air flowrate used in experiments was used to set the dryer loading in CFD. To allow simulation results to be compared directly with experimental data, a plane in the location of the lasersheet (0.25 m below mirror box) was created in the CFD simulation, results were plotted for the area of this plane that was covered by PIV images in the experiments.

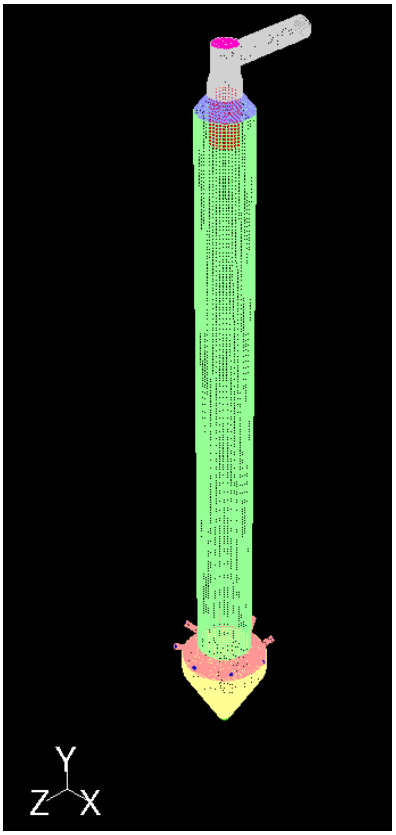

Figure 3.13: CFD Meshing of IPP Spray Dryer

Chapter 4 – Wall Deposition in Detergent Spray Dryers

4.1 Introduction

The principal aim of this research is to develop a detailed understanding of the mechanisms of wall deposition in detergent spray dryers. In this Chapter, this knowledge is developed through experimental studies: qualitative observation of wall deposition from entire periods of dryer operation are presented together with quantitative measurements made for a number of dryer operations with a variety of formulations, dried under different operating conditions. Since wall deposition is known to be a dynamic process, this was investigated with the aim of understanding the governing physics behind the process.

In order to relate this work to previous findings from published studies, a summary of previous work is given in Table 4.1 below. This is referred to throughout the Chapter as a basis for comparison. The process of wall deposition can be broken down into two steps: firstly, the particle must come into contact with the wall and secondly, the particle must stick (adhere) to the wall. The effects of each of these stages on wall deposition are governed by the collision frequency (i.e. how many particles hit the wall) and the collision success rate (i.e. how many particles stick when they hit the wall). The collision frequency of particles is governed by their movement and collision success by their physical and mechanical properties. Table 4.1 summarises existing knowledge on how spray drying variables and parameters affect wall deposition, in terms of collision frequency and collision success rate.

Currently, the influence of dryer operating conditions and formulation upon particle movement and properties inside the dryer, and their consequent effect on wall deposition

are not fully understood, (§2.7). Hence, precise conclusions on how wall deposition is influenced by these interrelating variables cannot be drawn, but their influence on wall deposition can be seen in this Chapter.

Table 4.1: Summary of Effect of Spray Drying Variables and Parameters on Wall Deposition

Variable	Effect on Particle Dynamics: Collision Frequency	Effect on Particle Properties: Collision success rate
Axial position (above nozzle)	Particle concentration is lower than below nozzle, as only a fraction of particles are entrained in the air flow to reach this area (Masters (1991), Kota and Langrish (2006), Bayly (2008) and Woo *et al.* (2008)). ***Collision frequency reduced owing to fewer particles within this part of dryer***	Particle size and moisture content are lower than below nozzle, as entrainment favours smaller particles which dry more rapidly. Dryer particles are less likely to deform and stick to wall on impact (Woo *et al.* (2008), Bayly (2009) and Woo *et al.* (2010)). ***Collision success rate reduced as particles are dryer***
Axial position (below nozzle)	Particle concentration is greater below the nozzle as all particles travel through this area (Masters (1991), Kota and Langrish (2006), Bayly (2008) and Woo *et al.* (2008)). ***Collision frequency increased owing to more particles within this part of dryer***	Particle moisture content peaks close to the nozzle, making particles most likely to stick. Moisture content decreases down the dryer, reducing likelihood of particles sticking (Woo *et al.* (2008), Bayly (2009) and Woo *et al.* (2010)). ***Collision success rate peaks close to nozzle and decreases with distance below the nozzle***
Axial position (dryer cone)	Air flows around air inlets reduce particle-wall collisions in this area. Particles must leave the entrainment in the air and move over the cone walls to leave the dryer (Masters (1991), Kota and Langrish (2006), Bayly (2008) and Woo *et al.* (2008)). ***Collision frequency decreases near to air inlets and increases on cone walls.***	Particle moisture content is low after drying and therefore particles are less likely to deform and stick (Woo *et al.* (2008), Bayly (2009) and Woo *et al.* (2010)). ***Collision success rate reduced as particles are dry***
Slurry flow rate	Particle concentration increases with increasing flow rate as more slurry is present within dryer (Masters (1991) and Bayly (2008)). ***Collision frequency increased owing to more particles within this part of dryer***	Drying decreases, increasing particle moisture content and likelihood of sticking, unless air flow rate or air temperature is increased to counteract increased drying load. (Huntington (2004) and Hecht and Bayly (2009)) ***Collision success rate will increase unless extra drying load is counteracted***

Air flow rate	Increases in air flow rate alter air flow patterns resulting in a stronger vortex forcing particles towards the walls, resulting in more particle-wall collisions (Southwell and Langrish (2001), Harvie *et al.* (2002), Bayly *et al.* (2004) and Woo *et al.* (2008)). ***Collision frequency increased owing to more particles travelling towards the wall.***	Changes in air flow rate and therefore air flow patterns will alter particle residence times and temperature profiles particles experience, altering particle properties and therefore they ability to deform and stick to the wall (Woo *et al.* (2008), Bayly (2009) and Woo *et al.* (2010)). ***Changes in collision success rate are unclear***
Product belt temperature	n/a	Increasing product belt temperature means that particles leaving the dryer are hotter, having experienced more drying and therefore will have a lower moisture content (Woo *et al.* (2008), Bayly (2009) and Woo *et al.* (2010)). ***Collision success rate decreases as particles are dryer***
Slurry moisture content	n/a	Particles contain more moisture (at least initially) and will therefore be more likely to deform and stick ((Woo *et al.* (2008), Bayly (2009) and Woo *et al.* (2010)). ***Collision success rate increases as particles are wetter***
Slurry surfactant content	n/a	Particles contain more surfactant will be more likely to deform and stick to the wall (Huntington (2004), Bayly (2006) and Stewart (2008)). ***Collision success rate increases are particle are stickier***
Powder production moisture	n/a	Particles contain more moisture and will therefore be more likely to deform and stick ((Woo *et al.* (2008), Bayly (2009) and Woo *et al.* (2010)). ***Collision success rate increases as particles are wetter***
Powder product particle size	n/a	Particle size is controlled by several factors, including atomisation and agglomeration. The mechanisms which result in particles stick to each other in agglomeration are the same as particles sticking to the wall. (Hanus and Langrish (2007) and Woo *et al.* (2008)). ***Collision success rate will increase***

4.2 Experimental

All the experiments were conducted on the pilot plant spray dryer (§3.2) for a variety of trials involving changing both formulation and dryer operating conditions. The position and type of spray nozzle (§2.3) used was the same for all trials. A scale diagram of the spray dryer is shown in Figure 4.1, where the experimental positions used during this work are shown. Wherever data is presented, a simplified description of the formulation and operating conditions used are given. Utilising standard pilot plant trials allowed wall deposition from a range of current and future formulations to be observed, enabling this work to be of particular relevance to the business.

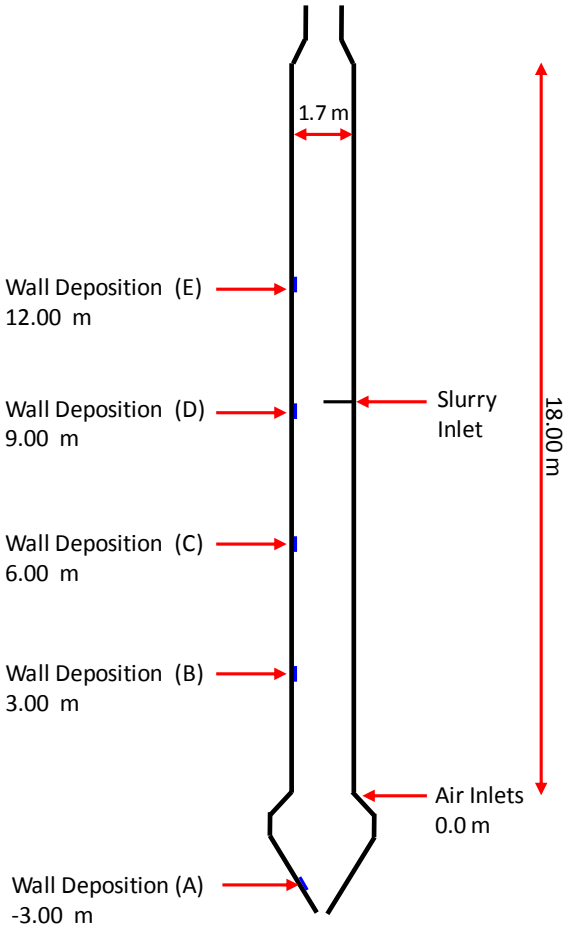

Figure 4.1: Scale Diagram of IPP showing experimental positions

4.3 Qualitative Observation of Wall Deposition

The first step in understanding wall deposition in detergent spray dryers was to observe material deposited on the walls after a period of operation. This was repeated for a large number of operations involving different formulations, operating conditions and spray nozzle positions. These observations were made on two different scales:

Macro-scale – covering the nature of the deposits on a dryer wide basis to highlight the phenomenon as observed in spray drying operations.

Micro-scale – examining the microstructure of wall deposits from various dryer operations and locations within the dryer to understand the mechanisms of deposition, to aid explanation the observations on the macro-scale.

4.3.1 Macro-scale Observations of Wall Deposition

Figure 4.2 (a) shows wall deposition, looking down the dryer from position E (Figure 4.1), which is 3 metres above the spray nozzle used in this work (the other nozzles not used in this work can be seen further down the dryer). The walls at this position can be seen to be covered in a relatively thin and even layer of deposited material. A close-up image of this deposition is shown in Figure 4.2 (b) and reveals patches in the wall build-up, showing the deposition in this position to be variable across areas of the dryer walls.

Figure 4.2: Typical wall deposition as viewed from position E: (a) looking down the dryer and (b) close-up of dryer wall

Figure 4.3 shows wall deposition as viewed from position D (approximately 0.3 metres below the spray nozzle). The layers of deposits on the walls here can be seen to be much thicker and more uneven than were observed above the nozzle. The thickness and unevenness of deposits increases further in Figure 4.4 which shows the area around position C.

Figure 4.3: Typical wall deposition as viewed from position D

The increased amounts of deposition in the area below the nozzle would be expected based Table 4.1, as particle concentration increases and particle moisture content is at its highest. This maximises particle-wall collision frequency and the likelihood of particles being able to deform and stick. In addition, particles close to the nozzle will also be carrying momentum from the nozzle, and will not be fully entrained in the air flow. This results in the particles travelling towards the dryer walls, increasing the number of particles striking the walls and therefore sticking, than in other areas of the dryer (Bayly (2008)). These collisions could also

potentially be at velocities and/or angles, which favour deposition of particles in comparison to impacts in other areas of the dryer (Bayly (2008)). The collision success rate of particles on the dryer walls will be higher close to the nozzle. As particles here are at the start of their journey through the dryer and have experienced minimal drying, hence they are more 'slurry-like' and 'sticky' than solid and therefore potentially more likely to stick when brought into contact with the wall.

Figure 4.4: Typical wall deposition as viewed from position C

Less deposited material is visible in Figure 4.4, and comparison of this with Figure 4.3 shows how deposition decreases with distance from the nozzle, as particles dry and become less likely to stick to the wall, lowing collision success rate, as described in Table 4.1.

Figure 4.5: Typical wall deposition as viewed from position A

The view of deposition around the air inlets and lower section of the drying chamber is shown in Figure 4.5. Less material appears to be deposited in the lower part of the drying chamber and very little around the air inlets. This is likely to be caused by the increased air velocities which have the effect of blowing particles away from the wall, reducing particle collision frequency, and increased air temperatures which reduce collision success rate through extra drying (Table 4.1). The material deposited appears to be patchy and there seems to be evidence of slurry running down the dryer walls and drying to form deposits. This may be an issue from start-up of the dryer where atomisation and air flows have not yet reached steady state, thus allowing wet slurry to run down the walls. An alternative possible source of these streaks is wall deposits washed down by water used to clean the dryer between runs. Another feature revealed in Figure 4.5 is discolouration of some deposited

material that has been exposed to high temperatures for the period of dryer operation. This highlights an important consequence of wall build-up, as charring (oxidation and resulting colour changes) of wall deposits (§2.7.1) is a key quality issue as it can contaminate large amounts of powder with miscoloured (black or brown) particles, thus rendering this product unsuitable for supply to consumers.

4.3.2 Micro-scale Observations of Wall Deposition

To further understand the trends and features of wall deposition observed on the macro-scale, micro-scale investigations of wall deposits were made using SEM (§3.7.1.1). For all SEM images displayed here, the black scale bar represents 1 mm over its entire length, with each sub-division being 100 µm.

Figure 4.6 shows SEM images of deposits collected from position E. These deposits can be seen to be made up of small particles stuck to each other to form a porous deposit where the individual constituent particles can still be clearly defined. These particle diameters are in the range of 10 - 200 µm. This structure of small particles could be the feature which results in the smooth appearance of the deposits in this area of the dryer (Figure 4.2).

Figure 4.7 and Figure 4.8 show SEM images of wall deposits collected from position D. Material deposited on the dryer walls in this area can be split into two categories. Firstly there is a soft fluffy layer of recently deposited material, which can range from a thickness of several millimetres to several centimetres depending on dryer operation. This was removed first, ensuring that the lower layers were not disturbed. Below this top layer is a hard, cement-like layer of material that has been deposited on the wall for a longer period of time,

again this can range in thickness from several millimetres to several centimetres. Figure 4.7 shows two examples of top layer deposits from position D, these images clearly show individual particles that have deposited on lower levels of wall build-up. There appears to be a variety of particle sizes deposited, typically between 100 and 300 μm in diameter, larger than seen higher up the dryer. None of the particles within these deposits appear to have experienced any suffered large deformation on impact.

Figure 4.8 shows hard lower level make-up, collected from below the softer top layer deposits in position D. It can be seen that this material is not formed from individual particles adhered to each other, it is a more uniform material that has clearly undergone a change in structure from when the individual particles were deposited on the wall. This process of build-up aging may possibly be the result of sintering of the particles deposited on the wall as they are exposed to heat over the duration of plant operation. Another possible explanation for this change is that the material making up lower level deposits is in fact material left over from previous trials that has been wetted, but not removed from the wall during washing and cleaning of the dryer. This consideration is important, as even though all efforts were made to clean the dryer walls between trials, it may indicate that trials do not always start with a clean or even layer of deposits on the walls (owing to shortfalls of cleaning techniques). The formation of the two types of deposits shown in Figure 4.7 and Figure 4.8 may therefore explain the increased thickness and unevenness observed previously in Figure 4.3.

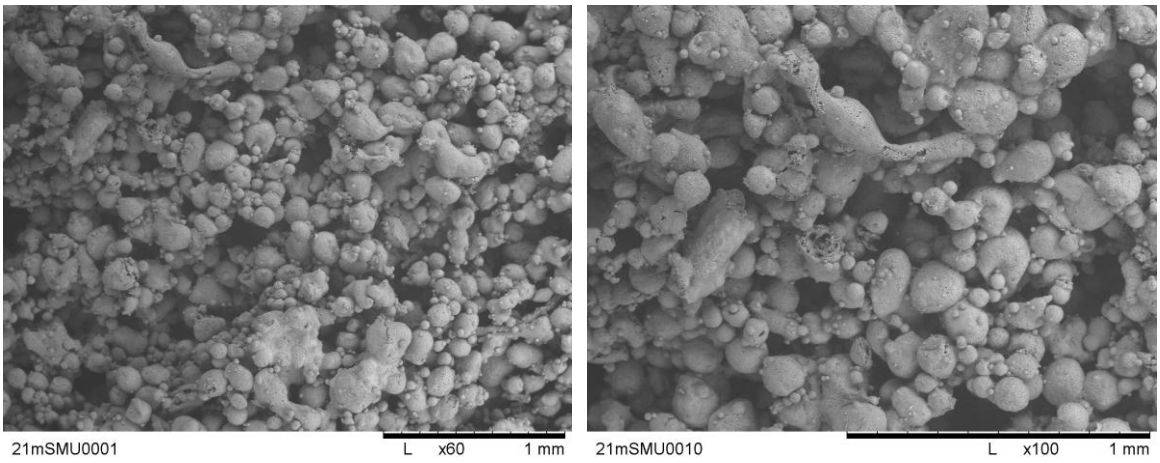

Figure 4.6: SEM Images of Deposits from position E

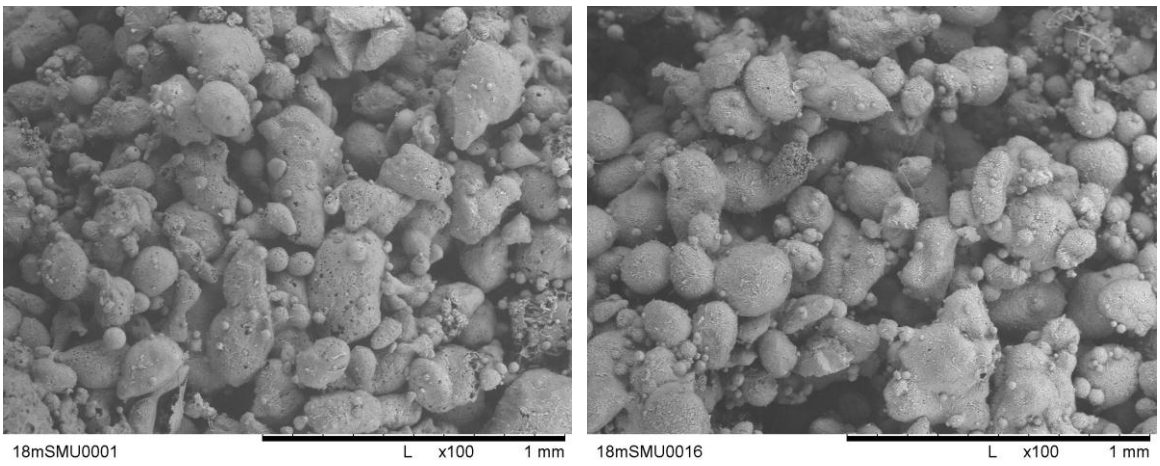

Figure 4.7: SEM Images of Top-layer Deposits from position D

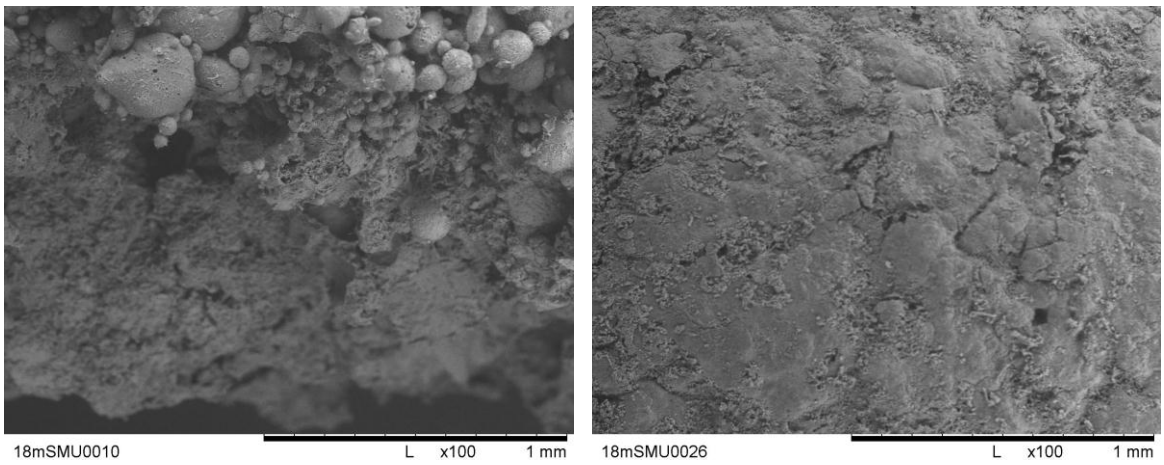

Figure 4.8: SEM Images of Lower-layer Deposits from position D

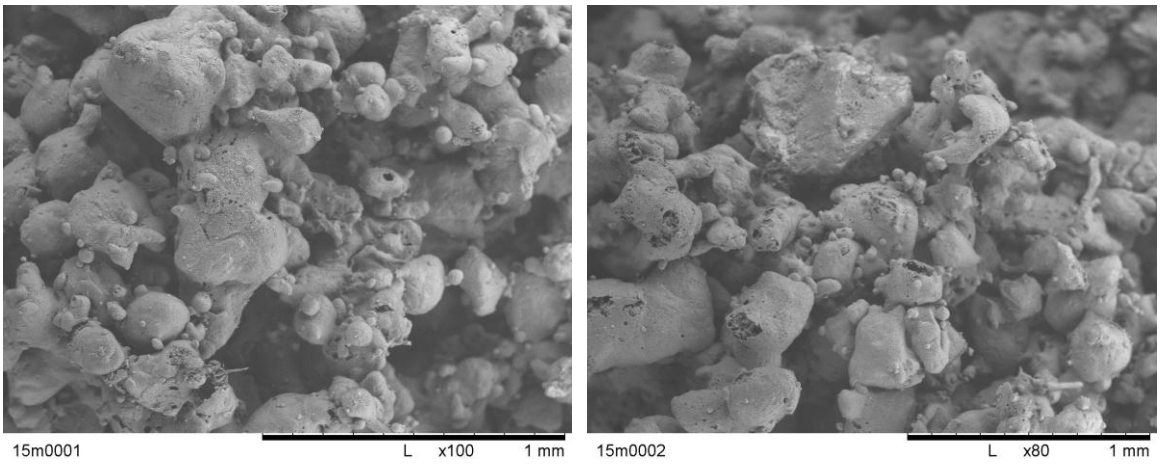

Figure 4.9: SEM Images of Top-layer Deposits from position C

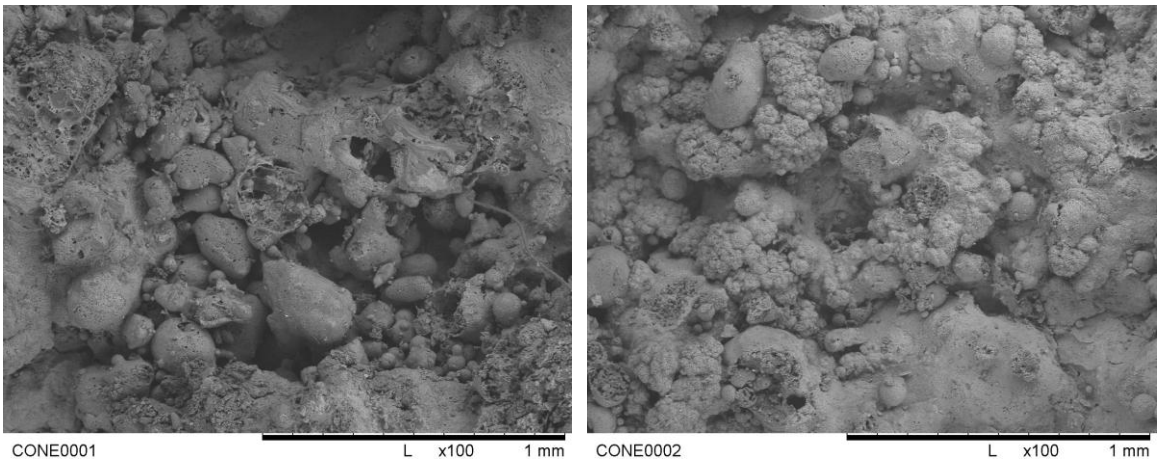

Figure 4.10: SEM Images of Deposits from position A

In contrast to Figure 4.7, Figure 4.9 shows top layer deposits from position C. Particles making up these deposits appear more deformed, suggesting they are softer when they hit the wall because they have experienced less drying, as would be expected in the area closest to the spray cone of the nozzle.

Figure 4.10 shows close up images of deposits collected from position A in the dryer cone. These deposits appear similar to those lower layer level deposits shown in Figure 4.8. The mechanism for this structure forming in the cone is unclear, but as shown in Figure 4.5 it is

possible that during either start up of the dryer or washing out, a mixture of slurry, wetted powder and/or wash water runs down the walls and this may dry and harden over time to give the continuous type of deposit seen mainly in Figure 4.10. The re-entrainment of large pieces of wall deposits during dryer operation may also contribute to this material observed in the cone. These large pieces of material would fall through the dryer quickly, under the influence of gravity, rather than being entrained in the air flow, meaning they reach the cone walls with little drying, thus providing a wet material to stick to the cone walls and seed the deposition of dry particles. Evidence of this may be found in the way that individual particles appear to be stuck onto a layer of more solid material.

4.4 Measurement of Wall Deposition

Quantitative investigations of wall deposition are presented in this section. Measurements of the total amount of deposition over a complete period of operation of the dryer were made for a variety of trials as shown in Table 4.2. This was achieved by collecting the material deposited on the inside of inspection hatches located at different axial positions on the dryer (§3.4.2). The collected material was then weighed to give a mass deposited on each hatch, this value was then translated to an equivalent mass of slurry using the difference in moisture content between the collected deposit and the slurry being sprayed. This mass value for each hatch was then converted into a deposition per unit area, allowing the deposition of material to be studied as a function of position within the dryer.

In order to calculate deposition over the entire area of dryer, it was then split into sections and the deposition per unit area values obtained were extrapolated over these areas to estimate the total amount of material deposited over these sections. By summing the

material deposited in these sections, the total amount of material deposited over the entire dryer was obtained and compared to the total amount of slurry sprayed during the entire period of dryer operation, enabling calculation of a yield value. An example of this calculation is given in Appendix B. This is expressed in terms of the fraction of slurry lost to wall deposition. The effects of dryer operating conditions and slurry and powder product properties on this yield value were then examined, relating the findings to the summary of published knowledge on this shown in Table 4.1.

Table 4.2: Details of Formulations , Operating Conditions, Powder Properties and yields for Trials where Wall Deposition was Measured

Trial	Formulation		Operating Conditions					Powder Properties		Yield
	Relativ Slurry Moisture	Total Surfactant (%mass)	Relative Slurry Flow Rate	Air Flow Rate ($kghr^{-1}$)	Air Inlet Temp (°C)	Product Belt Temp (°C)	Spray Duration (min)	Relative Powder Moisture	Powder mean particle size (by mass) (μm)	Slurry Lost as Deposits (%mass)
1	1.04	14.4	1.00	8500	300	105	108	1.18	600	8.7
2	1.04	14.4	1.00	8500	300	105	137	1.18	550	6.9
3	0.98	14.3	1.02	8250	300	100	147	1.43	600	5.7
4	0.96	14.6	0.97	8500	310	105	153	1.14	650	6.5
5	1.04	14.4	1.00	8500	300	105	101	1.18	550	5.3
6	1.06	13.5	0.92	9000	300	100	186	0.75	510	5.0
7	0.91	12.9	1.01	7000	310	110	260	0.71	490	3.0
8	1.03	13.2	0.96	7500	300	110	187	0.79	520	3.6
9	0.94	9.5	1.14	7500	290	115	230	0.64	450	2.5

4.4.1 The Effect of wall Deposition on Powder Yield

The final column of Table 4.2 shows the yield which ranges between 2.5 and 8.9% by mass of the total sprayed over the 9 trials. This is clearly a significant amount of product lost to wall deposition. The following sections examine these values as a function of location within the dryer, plant operating parameters and slurry/powder properties.

4.4.2 Wall Deposition as a Function of Location within the Dryer

Wall deposition was observed to vary with position within the dryer in terms of both quantity and structure (§ 4.3). To investigate this observation further, the amount of material deposited at various axial positions within the dryer during an entire operation were studied and expressed as mass per unit area. The results of this are shown in Figure 4.11 where the deposition per unit area is plotted as a function of axial position.

Measurements were made in 5 locations (positions A, B, C, D and E, although position B was not available for some trials, due to engineering work on the plant), as plotted on Figure 4.11; the points are joined with lines to highlight the changes between the different locations. An illustration of the dryer layout with matching axial scale to the graph is displayed next to the plot in Figure 4.11

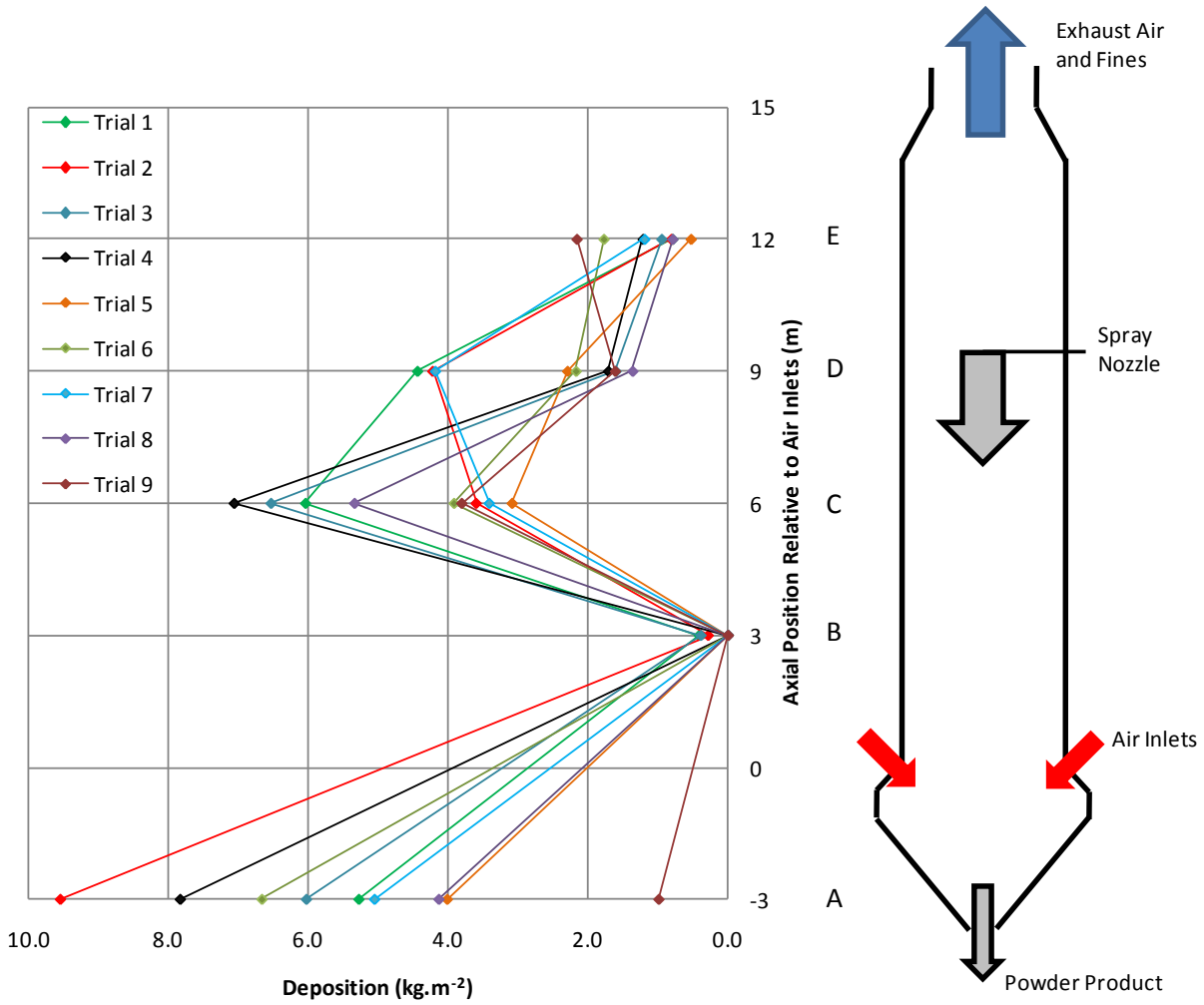

Figure 4.11: Wall Deposition as a function of Axial Position within the Dryer

The Figure shows that the amount of material deposited in various positions within the dryer varies greatly, as would be expected and is in agreement with literature on deposition within all types of spray dryers (Table 4.1) (§2.7). The maximum amount of deposition is observed in two areas, depending on which trial is being examined. The area just below the nozzle, Position C, is expected to show the most deposition (Table 4.1) (§2.7), as the proximity to the nozzle affects both the movement and nature of particles, leading to greater collision frequency and collision success rate, resulting in greater deposition. The dryer cone, position A, is an area where which large amounts of deposition would not be expected, but

may be explained through consideration of how particles move through this area of the dryer (Table 4.1). Particles which have travelled down the dryer will reach a point around the air inlets where they fall onto the walls of the dryer cone, sliding down before exiting the dryer, this leads to a high collision frequency, which could result in more deposition. An additional point is that as shown in Figure 4.5, there is a possibility of slurry running down the dryer walls during start-up, forming deposits in the dryer cone which dry and harden over the period of operation.

Above the nozzle the amount of deposition is seen to decrease with increasing axial distance from the air inlets, this would be expected as particles will be drier and less likely to stick in these locations. The effect of dry particles not sticking is best shown by the low values of deposition in position B (3 m above the air inlets) where the collision frequency of particles will be similar to other areas of the dryer shell, but, in this area particles will be at their driest, and therefore will be least likely to stick and will have the lowest collision success rate.

Figure 4.12 shows the normalised amount of material deposited as a function of axial height inside the dryer, that is the amount of material deposited divided by the dryer-wide average value for the amount of deposition, calculated by divided the total amount of material deposited over the entire dryer by the total wall area of the dryer. Variation in the maximum and relative amounts of material deposited in all locations can be seen in both Figure 4.11 and Figure 4.12 for all of the trials performed. This variation is caused by changes in many parameters between different trials, demonstrating the effect of both dryer operating conditions and slurry/powder properties on wall deposition. These parameters will affect

atomisation and therefore the particle size distribution, concentration and trajectories of particles moving through the dryer, affecting in turn, drying and agglomeration. All of these contribute towards changes in the collision frequency and collision success rate of particle impacting on the dryer walls and therefore wall deposition, as shown by differences between Figure 4.11 and Figure 4.12. The influence of each of these contributing factors is described in the following sections.

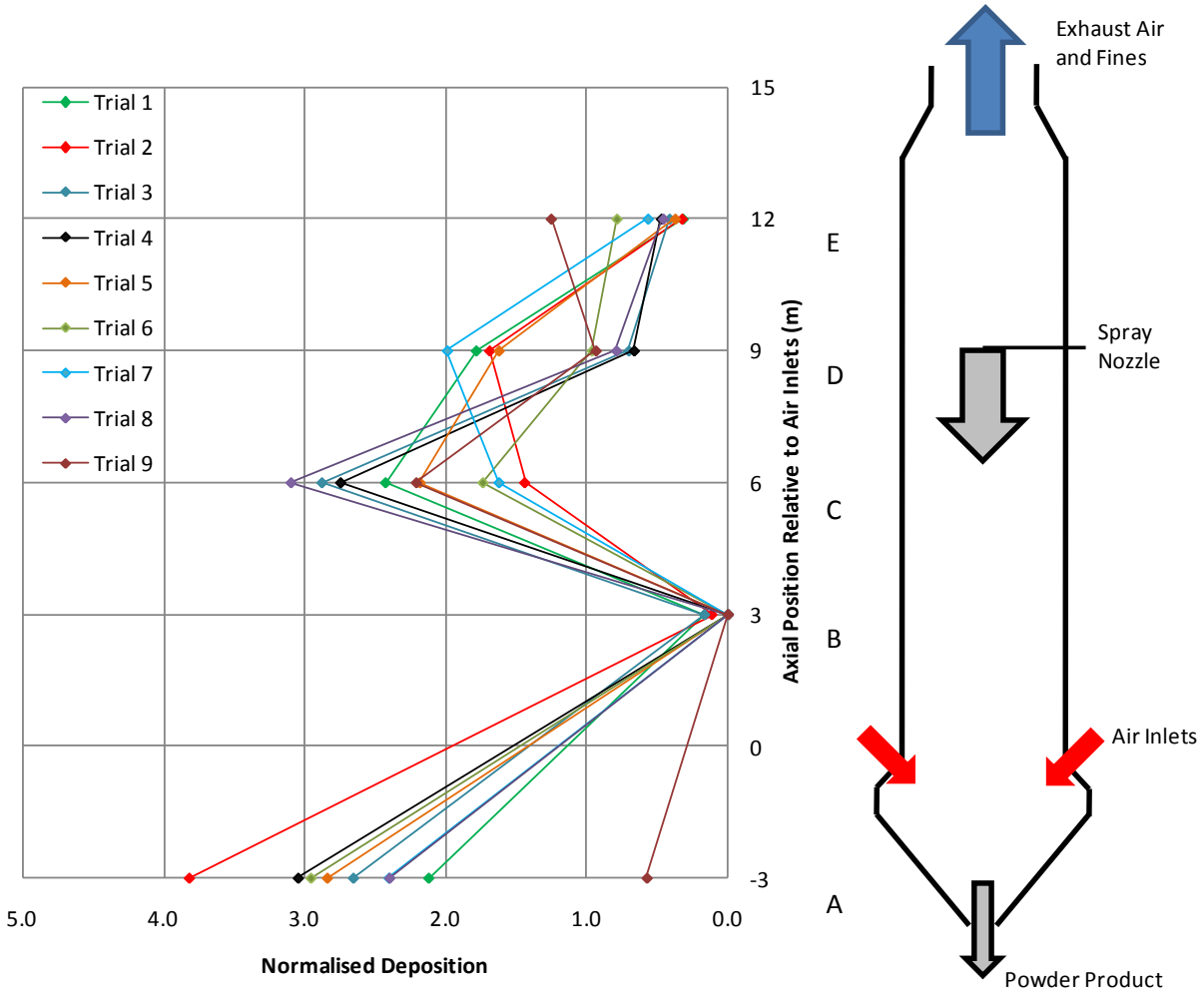

Figure 4.12: Normalised Wall Deposition as a function of Axial Position within the Dryer

4.4.3 The Effect of Dryer Operating Conditions on Wall Deposition

The fraction of slurry lost to deposition is plotted as a function of three key operating parameters, slurry flow rate, air flow rate and powder product belt temperature (the temperature of particles leaving the dryer as they are collected on the product belt). Other operating parameters did not vary enough between the trials used to allow a clear representation of their effect on wall deposition to be established and therefore are not examined.

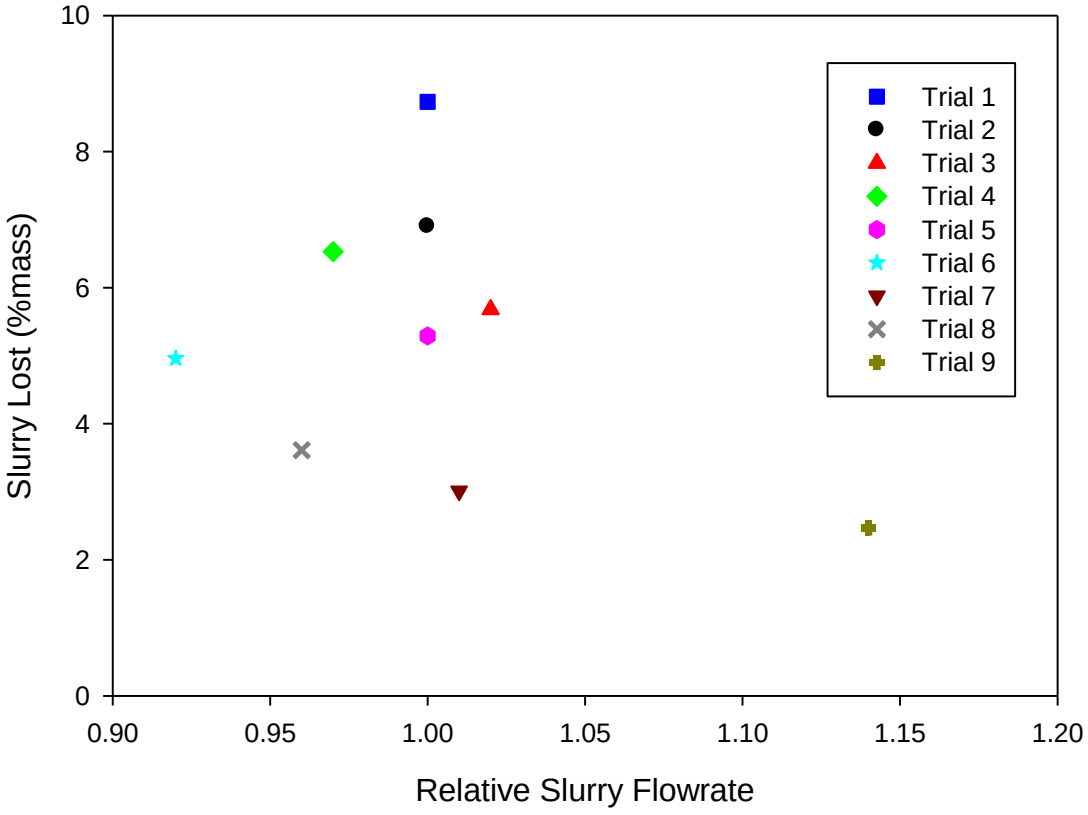

Figure 4.13: Wall Deposition as a function of Slurry Flow

Figure 4.13 shows the effect of variation in the slurry flow rate used in each dryer trial has on the fraction of slurry sprayed which is lost through wall deposition. There appears to be no clear trend in this plot, however, there is an indication that slurry loss decreases (wall

deposition) with decreasing slurry flow rate, particularly with trial 9 as an outliner. This trend is unexpected based on the contents of Table 4.1, as increased slurry flow rate would result in higher particle concentrations within the dryer, meaning more particles are available to hit the dryer walls (increased collision frequency). However this effect may be counteracted by changes in atomisation caused by increasing slurry flow rate, which would be expected to alter particle size and reduce particle drying (Table 4.1), although these effects may be cancelled out through increase in drying air flow rate and/or temperature.

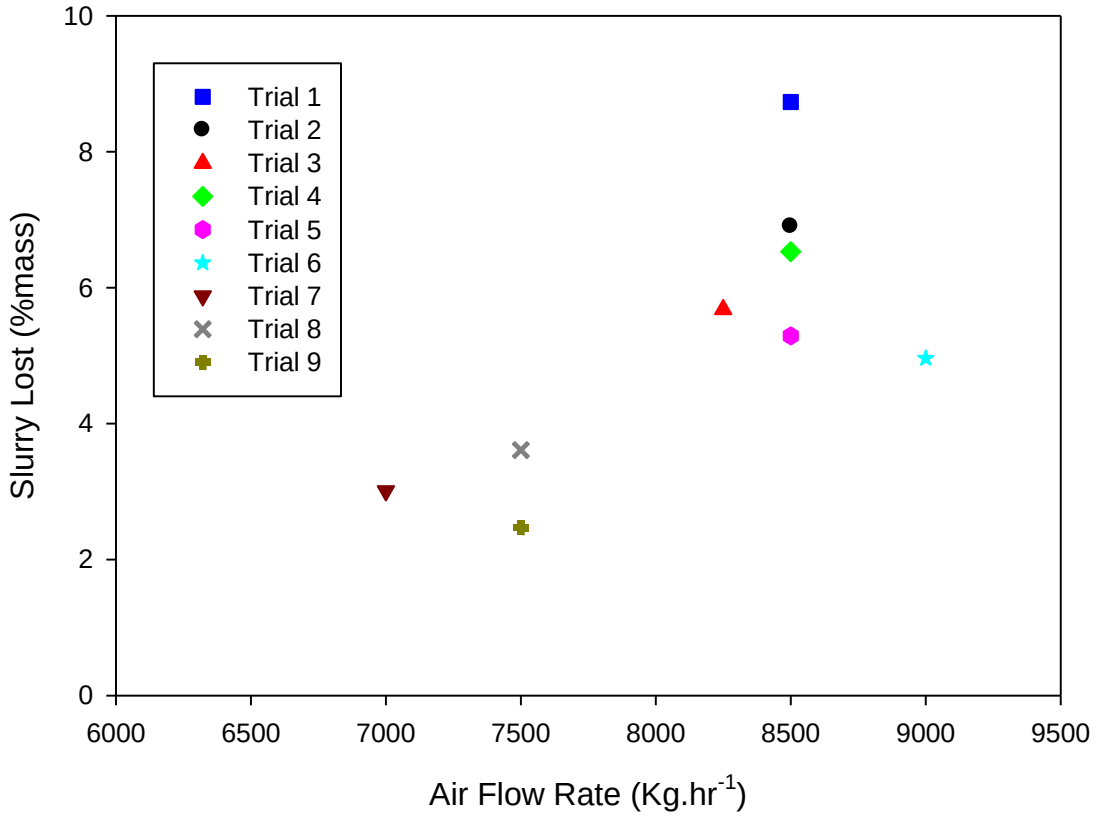

Figure 4.14: Wall Deposition as a function of Air Flow Rate

The change in the amount of slurry lost through wall deposition with increasing air flow rate is shown in Figure 4.14. Increases in the air flow rate through the dryer appear to result in greater amounts of wall deposition, in agreement with previous work (Table 4.1). Changes in

air flow rates through the dryer will alter the air flow patterns inside the dryer, a phenomena that has been linked with wall deposition in the literature (Southwell and Langrish (2000), Harvie *et al.* (2002) and Ozmen and Langrish (2003)) (§2.7). These changes in air flow patterns will affect particle movement, changing collision frequency and velocity between particles and the wall. Furthermore changes in particle movement will affect particle trajectories through the dryer, altering residence times and the temperature profiles particles experience, changing particle drying, thus adjusting collision success rate for particles hitting the dryer walls (Bayly (2008)). There appaears to be two groups of results in Figure 4.14, with trials 7, 8 and 9 showing lower depositon rates than the rest, this may be linked to the general trend of these bing the trials with the lower slurry moisture and surfactant contents.

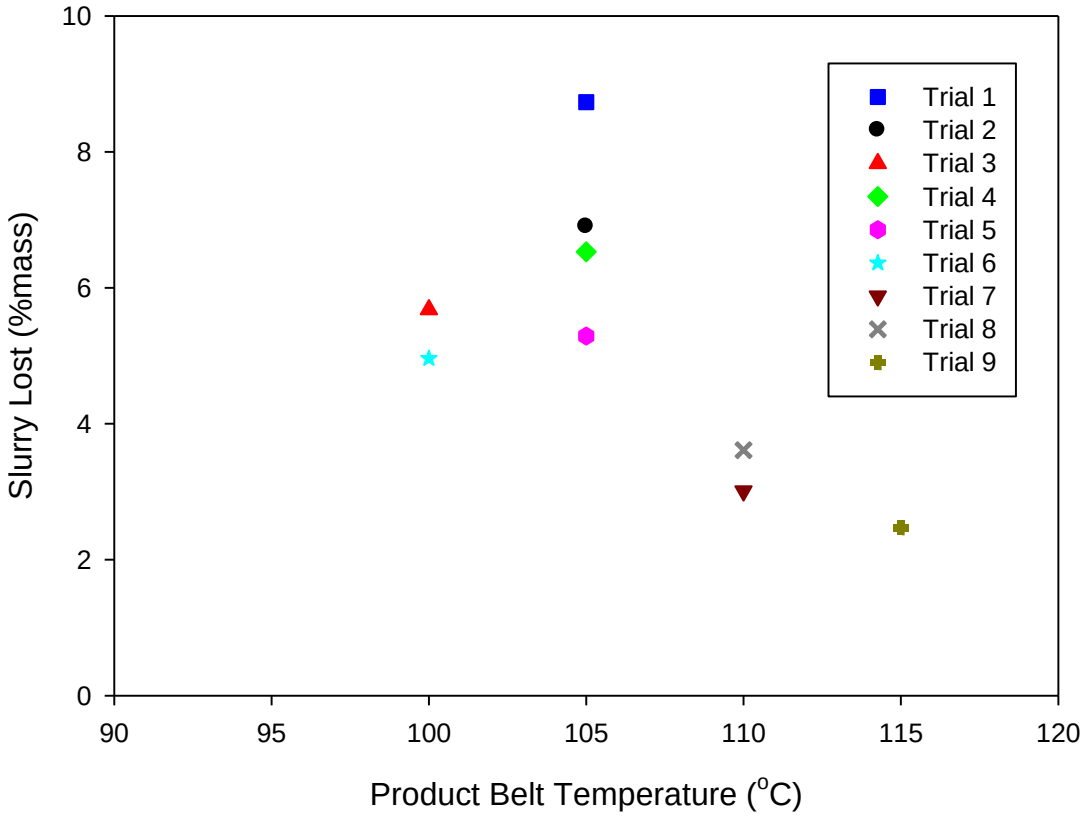

Figure 4.15: Wall Deposition as a function of Product Belt Temperature

The amount of slurry lost through wall deposition can be seen to increase with decreasing product belt temperature in Figure 4.15, in agreement with Table 4.1. The product belt temperature is a measure of the temperature of powder leaving the dryer, and a decrease in this parameter indicates that particles are reaching lower temperatures inside the dryer and therefore possibly experience less drying, making them more likely to stick to the dryer walls, thus increasing the amount of slurry lost through wall deposition. Again trials 7, 8 and 9 appear to be offset from the main bulk of the results and demostrait the highest product belt temperatures.

4.4.4 The Effect of Slurry and Powder Properties on Wall Deposition

Slurry and powder properties change with both formulation and dryer operating conditions, these in turn will change the amount of wall deposition occurring (§2.7). This means that every trial examined here will have droplets/particles of differing properties and morphologies travelling through the dryer. Unfortunately these changes in particle properties with drying and formulation are currently poorly understood (Bayly (2008)), meaning that although their effect can be examined, the exact mechanism by which they influence wall deposition cannot be directly evaluated.

To examine the effect of these properties on wall deposition, several slurry and powder product properties (slurry moisture content, slurry surfactant content, final powder product moisture content and mean particle size) have been plotted as a function of the amount of slurry lost through wall deposition.

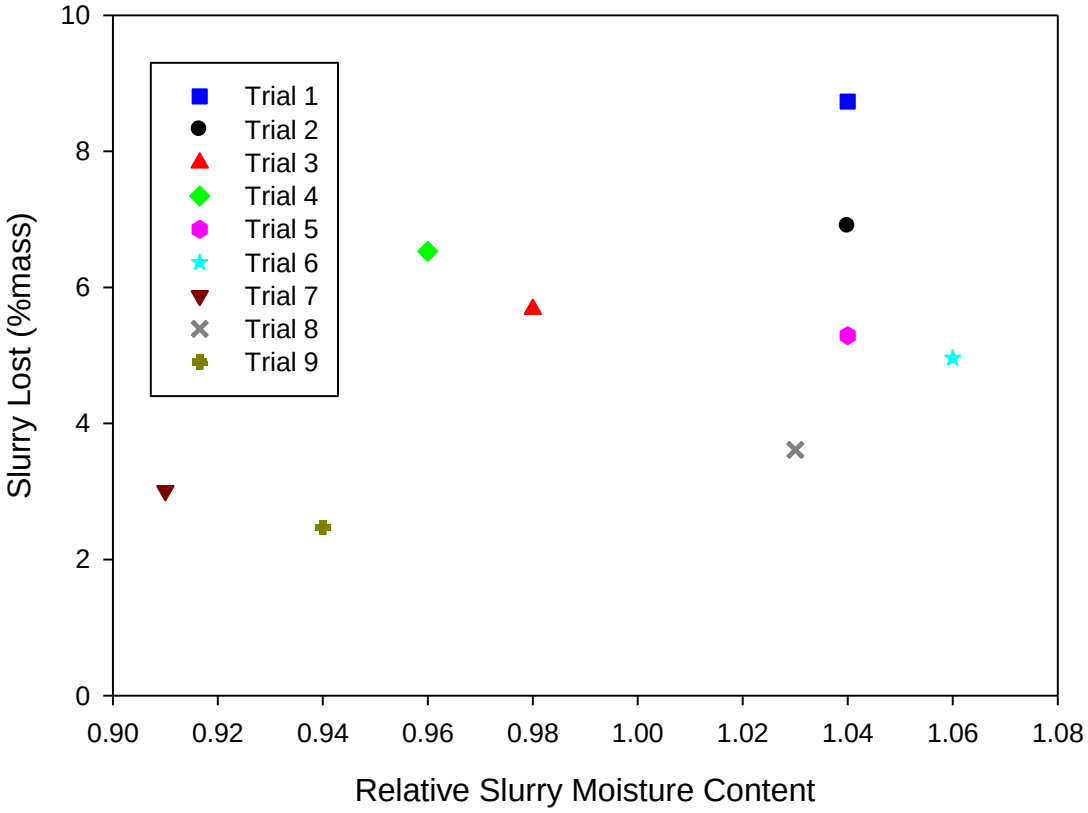

Figure 4.16: Wall Deposition as a function of Slurry Moisture Content

Figure 4.16 shows how changes in the moisture content of slurry being sprayed affects the amount of slurry lost through wall deposition. The trend here appears to be unclear, however, there is an indication that the amount of slurry lost to wall deposition increases with increases slurry moisture content. This would be expected, based on Table 4.1.

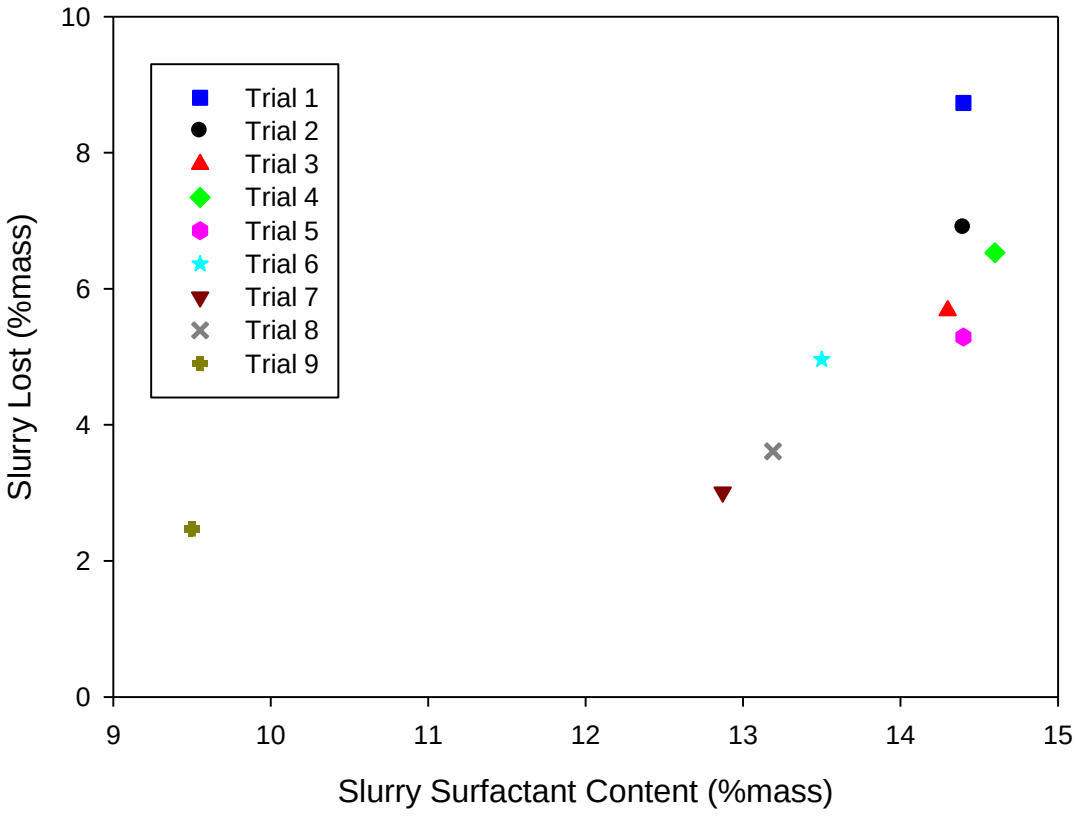

Figure 4.17: Wall Deposition as a function of Slurry Surfactant Content

Detergent formulations contain varying amount of surfactants depending on their end-use and where in the world they are sold (Bayly *et al.* (2008)). Figure 4.17 shows how the amount of slurry lost increases with increasing amount of surfactant in the formulation., with one extreme case in trial 9 which contains a little surfactant. The trends observed would be expected (Table 4.1) as increasing surfactant content is known to change the microstructure and rheology of detergent slurry (Bayly (2006) and Stewart (2008)), such that is becomes more viscous and therefore more likely to stick (§2.7). In addition the presence of more surfactant may lead to more liquid organic phase being present in the granule (Bayly (2006)), resulting in a more sticky surface that can form liquid bridges and become attached the dryer wall and material deposited on it (§2.7).

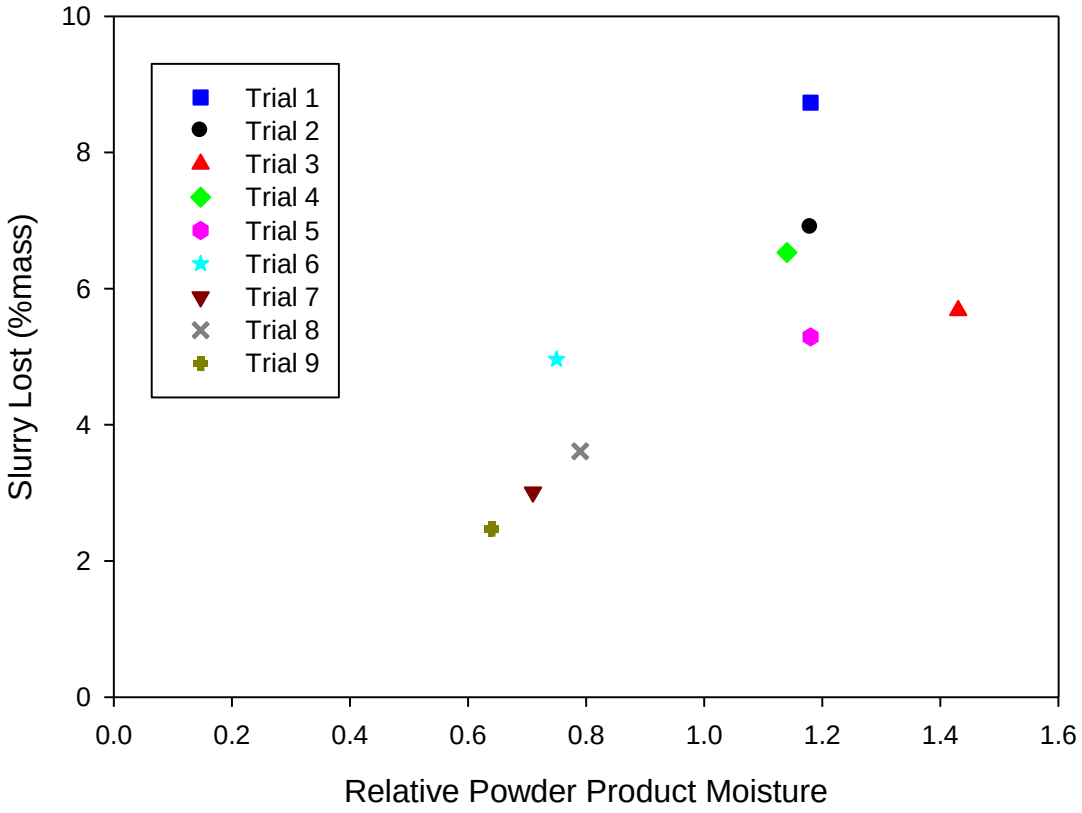

Figure 4.18: Wall Deposition as a function of Powder Product Moisture

A key parameter for controlling the spray drying process and product quality is the moisture content of powder product leaving the dryer. Figure 4.18 shows how the amount of slurry lost through wall deposition increases with increasing powder product moisture content, as would be expected from Table 4.1. This increase in wall deposition can be simply explained by considered that the more moisture particles contain the more likely they are to stick to the dryer walls, in a similar fashion to that explained for the powder product belt temperature. There are two clear groups of results in Figure 4.18, trials 6, 7, 8 and 9 are grouped together with the lower product moisture contents and demostraiting the lowest depositon, these trials also have the lowest product mean particle sizes and use slurries with the lower moisture and slurry contents. This demostraits the interrelation of these

parameters and their effects on deposition. Conversely the other trials have larger product moisture contents, mean particles sizes and slurries which contain more moisture and surfactant and show more depositon, again demostraiting the interrelation and effect of these parameters on deposition.

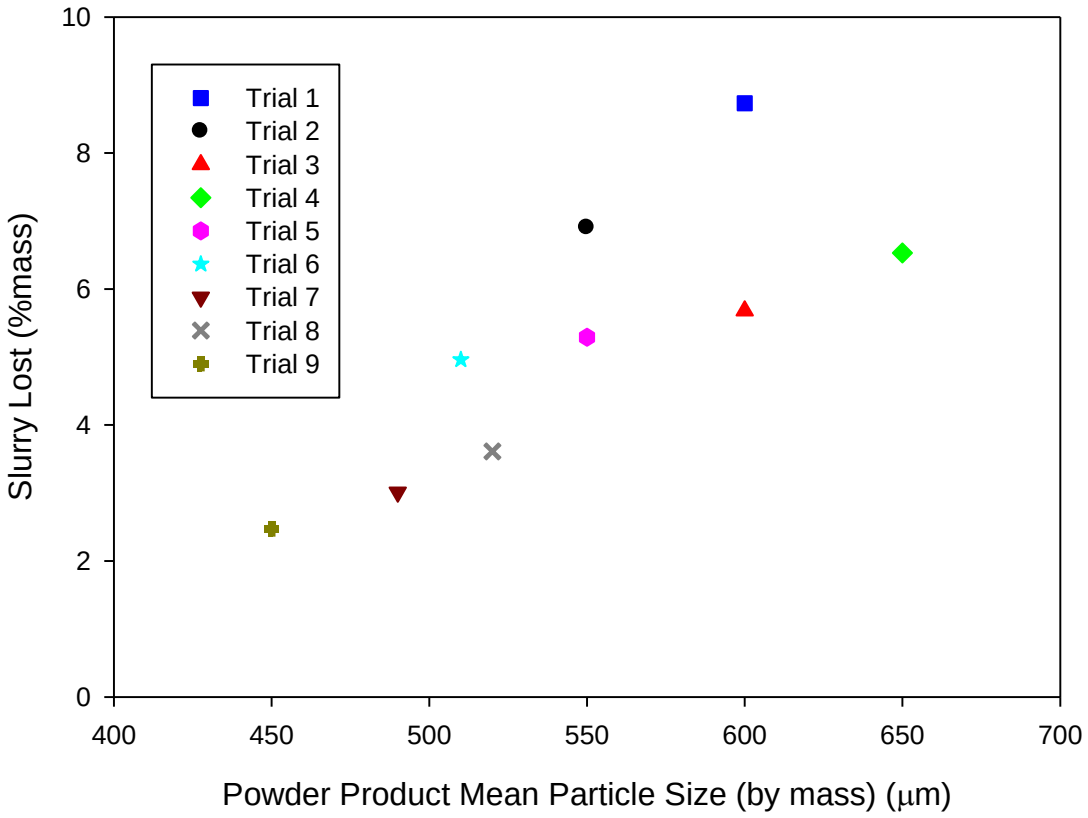

Figure 4.19: Wall Deposition as a function of Powder Product Mean Particle Size

Particle size is another key parameter for controlling product quality when spray drying detergents. Changes in particle size distribution and mean particle size of the powder product are driven by agglomeration inside the spray dryer. A process which can be considered to rely on the same driving forces as wall deposition (particles sticking to each other in the air flow as oppose to on the dryer walls). Therefore, as described in Table 4.1, it would be expected that the mean particle size increases with increasing wall deposition, as

shown in Figure 4.19. An additional consideration of the relationship between wall deposition and powder product particle size is the agglomeration mechanism of re-entrainment of wall deposits into the air flow in pieces larger than the individual particles in the bulk air flow as described by Hanus and Langrish (2007) (§2.7).

4.5 Time-Dependent Studies of Wall Deposition

The time dependent behaviour of wall deposition was investigated to determine the effect of deposition rate on yield. Measurements were made using the collection plate method (§ 3.4.2), in position C (6 m above the air inlets, where most deposition occurs (§4.3)), during steady state operation of the dryer. A representative formulation was sprayed from a nozzle positioned 12 meters above the air inlets.

Measurements with the plates were made for one minute of deposition, such that the plates were exposed in the tower for a total period of 30 minutes of steady-state dryer operation. The mass of the plate and material deposited on it were measured and the mass of material deposited calculated by subtracting the mass of the plate (measured previously). The total mass of material deposited at each measurement point is plotted against time in Figure 4.20, which gives a cumulative count of wall deposition. The relationship is clearly non-linear; and the dependence is close to quadratic, as shown by the second-order polynomial curve which has been added as a line of best fit ($R^2 = 0.94$).

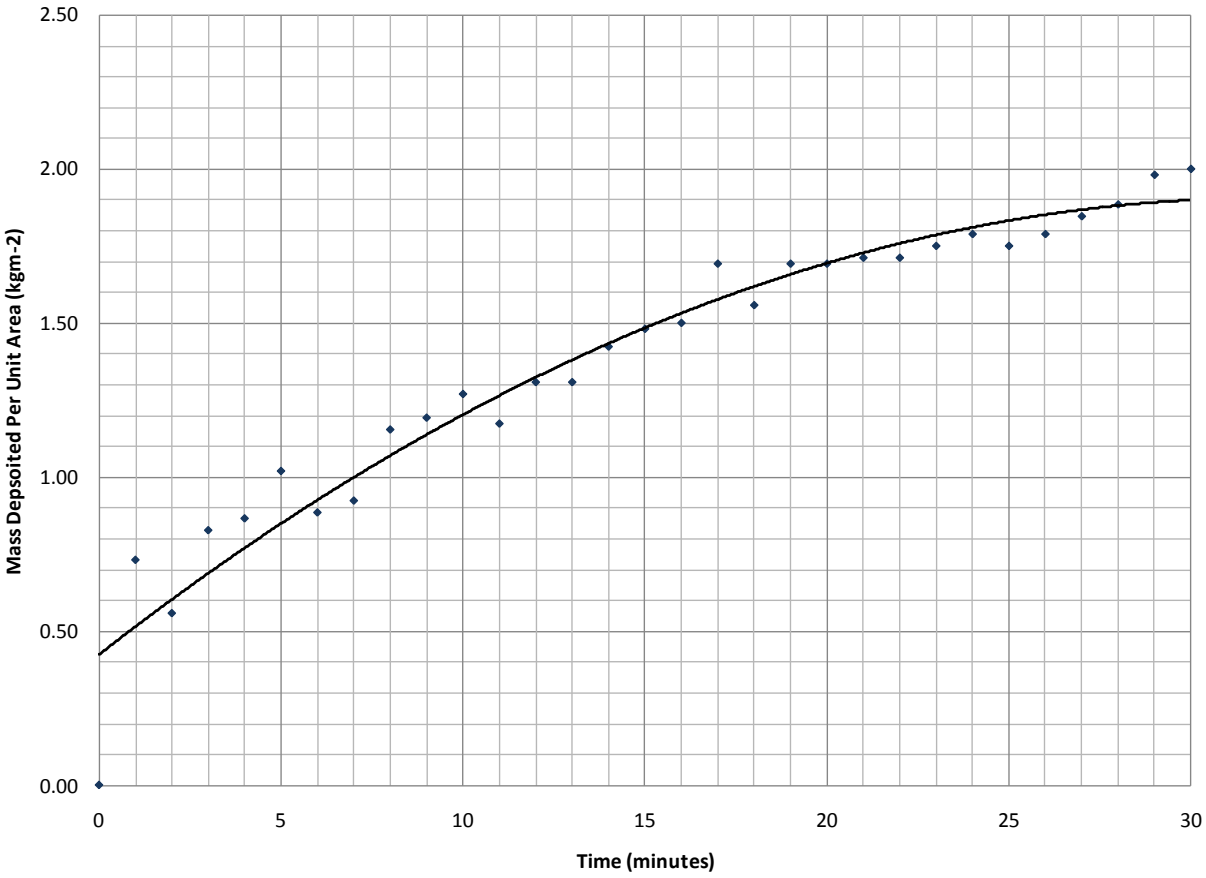

Figure 4.20: Accumulative Wall Deposition

Examining the data points plotted in Figure 4.20 reveals wide variation in deposition rate between measurement points, with values switching between positive and negative. This could possibly be a feature of the measurement technique if material was lost during removal and weighing of the plate, although all efforts were made to keep this to a minimum. Therefore, we can conclude that this feature at least in part is owing to constant changes in the material and amount of it deposited as this is a dynamic process.

Other potential sources of errors in this work include small systemic errors such as inaccuracy of the balance and errors with timing of the period the plate was exposed in dryer.

Another point of interest in Figure 4.20 is that the largest deposition rate is observed for the first period of measurement (time zero to one minute). This is unexpected (§2.7), with most literature reporting that particles becoming deposited on bare steel is the limiting step in deposition (§2.7). To ensure this was a reliable observation and not a freak data point, three repeats of this initial period of deposition were conducted. The results of these repeats are shown in Table 3.4 and the actual deposition shown in Figure 4.21. These show that the amount of material deposited and the inferred rate of deposition is fairly constant between the initial study and the three repeats, demonstrating this as a reliable trend.

Table 4.3: Initial Deposition Rates

Measurement	Amount Deposited (kg)	Deposition (kgm^{-2})	Rate of Deposition ($kgm^{-2}s^{-1}$)
30 minute study	0.038	0.73	0.012
Repeat 1	0.036	0.69	0.012
Repeat 2	0.035	0.67	0.011
Repeat 3	0.035	0.67	0.011

Figure 4.21: Initial (1 minute) Wall Deposition Repeats

When compared with published studies on wall deposition in co-current spray dryers the deposition rates found here are quite large (§2.7). In addition only limited literature

considers the idea of wall deposition reaching an equilibrium state (§2.7). This could potentially be because of the nature of detergent particles and the deposits they form (bigger particles, forming larger, heavier, but more porous deposits) meaning they are more likely to experience re-entrainment back into the air flow than other spray dried materials. This means that wall deposition in detergent spray dryers is more likely to lead to a dynamic equilibrium between entrainment and deposition than for other spray dried materials.

These initial results were produced during one dedicated pilot plant trial to validate the technique used here. This trial allowed measurements to be made which gave the results presented in this section, however, this trial also highlighted problems with the measurement technique. The main issue with making these measurements is that it requires opening inspection hatches on the dryer during operation. This results in large amounts of ambient air flowing through the hatch into the dryer (which is operated under vacuum to ensure no product escapes). This flow of air into the dryer has a significant effect on its operation, affecting the drying air flow rate through the drying chamber (Figure 4.22), disturbing air flow patterns and in turn affecting particle velocities as well as changing the temperature profile experienced by the particles.

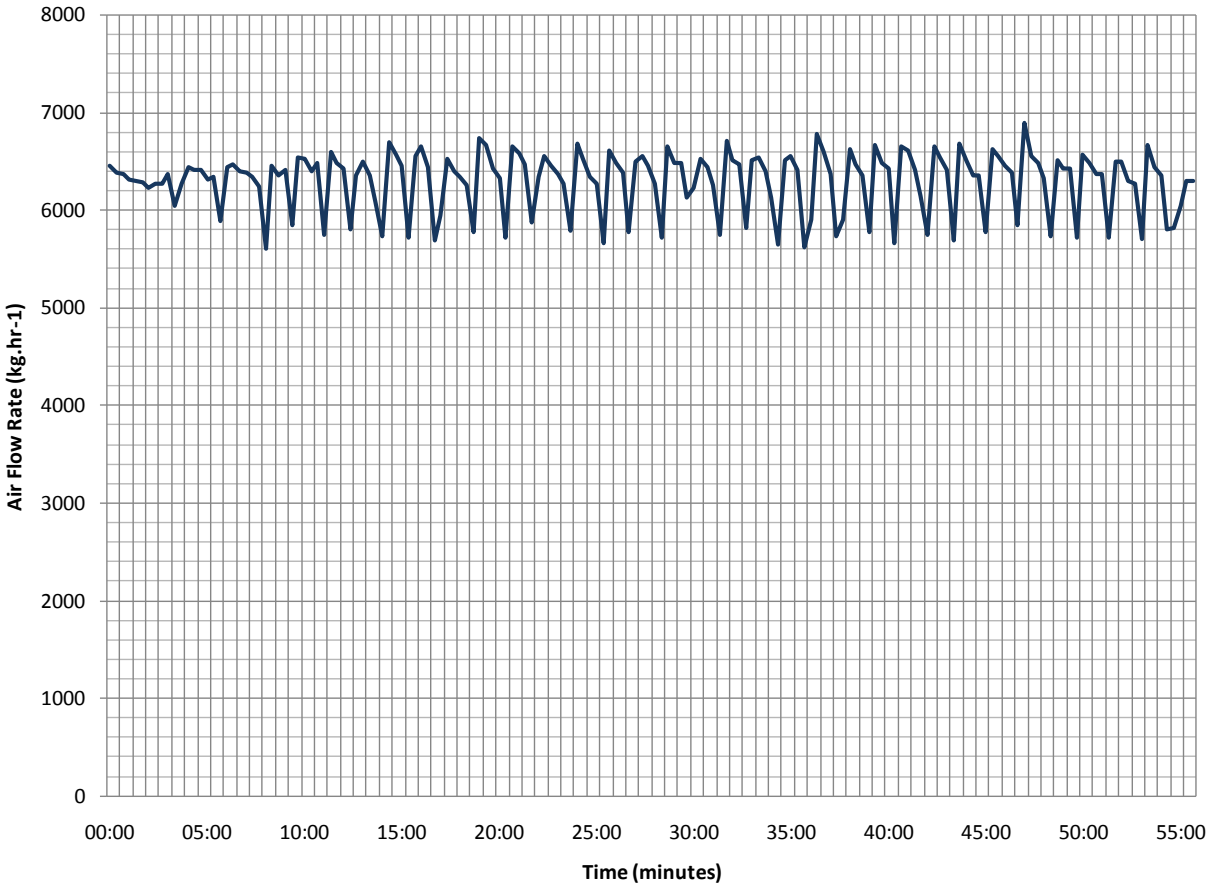

Figure 4.22: Disruption to dryer air flow rate whilst using collection plates

All of these factors affect the drying of particles as well as their movement, influencing product properties such as moisture content as well as affecting wall deposition itself. Therefore, although this technique allowed us to demonstrate the time dependence of wall deposition, it cannot be considered reliable as opening and closing the inspection hatches has a significant effect on dryer operation. This means that steady state operation cannot be achieved whilst using this technique over prolonged periods of time and wall deposition under normal operating conditions cannot be investigated using this technique. This leaves an important area of opportunity of research into wall deposition inside spray dryers using non-intrusive techniques, such as ultrasonics (§8.7).

To complement the time dependent findings reported above, visual observations of wall deposition were made using the PIV set-up utilised in Chapter 6 (§ 3.5). These observations allowed qualitative investigation of both deposition and re-entrainment of material on the dryer walls.

An example of these observations is given in Figure 4.23 where the deposition of material on the dryer wall can be observed for a period of 100 seconds in 20 second increments. The material deposited on the wall is shown by the white area at the top of the images, the white spots in the lower part of the image show particles that are entrained in the air flow travelling past the wall. The scale-bar shown here represents 50 mm over its entire length.

Examining changes in the deposit shown, between frames in Figure 4.23 highlights the dynamic nature of wall deposition. The size of the deposit grows over the period of observation and the whole can be seen to increase from frame to frame. However, certain areas of the deposition can be seen to shrink between frames, showing how some parts of the deposit break off and are re-entrained in the air flow.

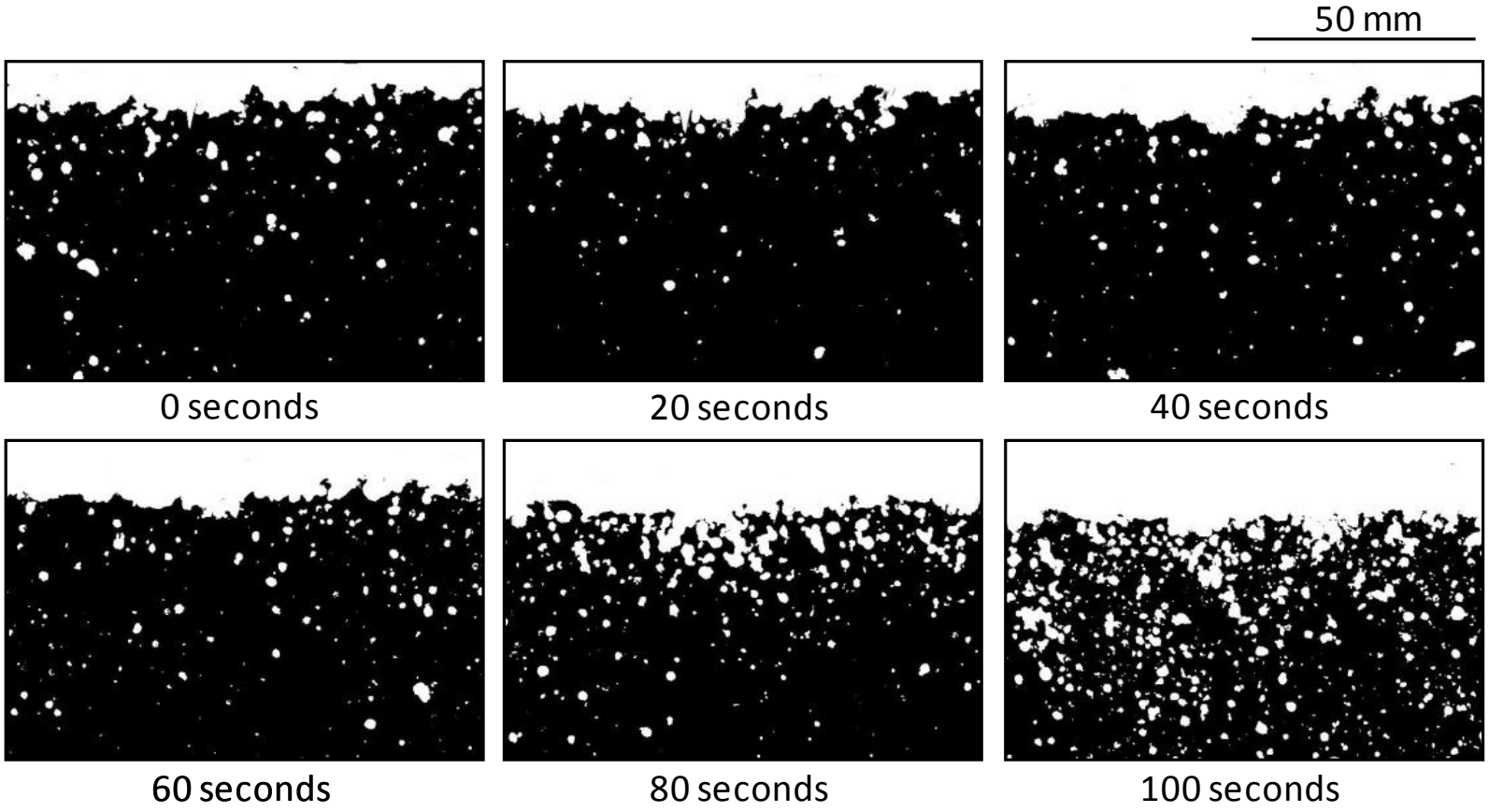

Figure 4.23: Time Dependent Wall Deposition Observed with PIV

4.6 Wall Deposition Conclusions

Wall deposition in a detergent spray dryer has been investigated such that the context of the problem covered in this thesis can be appreciated by the reader. Initially quantitative observations of deposition on both the macro and micro scales were made using photography and electron microscopy. The macro scale observations reveal variation in deposition with location within the dryer in terms of amount and appearance of deposits. The thickest and most uneven deposits were seen closet the spray nozzle, with deposits becoming thinner and smoother moving up the dryer away from the nozzle. In the lower part of the dryer smaller amounts of uneven, and sometime discoloured deposits are seen, with the exception of the dryer cone where large amounts of hard deposits are seen, possible as an artefact of slurry or wash water running down the dryer walls during either start-up or cleaning. Micro scale investigations of deposits from various locations within the dryer reveal variation in their micro-structures, potentially explaining the trends seen on the macro-scale observations.

Qualitative studies of wall deposition have been conducted on both the macro and micro scales. Macro-scale investigation showed how deposition changed with position inside the dryer, with the thickest and most uneven make-up close to the nozzle and the thinner and smoother deposits of smaller diameter particles higher up the dryer. Deposits around the air inlets and cone were shown to be uneven and discoloured in areas exposed to high temperatures of inlet air. Examination of the microstructure of these deposits have shown variation between deposits as function of location in the dryer, which may explain the

appearance of deposition observed on the macro-scale, with a clear link between the wetness of particles striking the walls and the roughness of deposits observed.

Quantitative data on the amount of wall deposits formed during spray drying detergents during a number of operations has been obtained. The amount of deposition was found to vary between different locations in the dryer (expressed as axial position relative to air inlets), with the most deposition seen just below the spray nozzle, in agreement with (§ 4.3) and (§2.7). Large amounts of deposition were also observed in the dryer cone, for some trials. The amount of deposition in all locations was seen to vary between different dryer operations (trials), to limit the effect of this variation, a yield expression in terms of the fraction of the total slurry sprayed that was lost through wall deposition was used.

This yield value was found to vary with dryer operating conditions, with increasing slurry flow rates found to reduce deposition, whilst increasing air flow rates were found to increase deposition, both of these operating parameters will alter collision frequency and success rate. Increasing powder product belt temperature was also found to decrease deposition, this is thought to be caused by changes in drying, and therefore particles properties which influence collision success rate. The influence of slurry and powder product properties on the amount of slurry lost though deposition was also examined. Increasing surfactant content was found to increase deposition, as was increased slurry and final product moisture content, an effect suspected to be caused by moisture and organic components making particles more viscous and therefore more likely to stick and form deposits, thus increasing collision success rate.

Wall deposition has been shown to be time dependent, with a decrease in deposition rate over a period of 30 minutes. This is believed to be caused by a narrowing of the gap between the rate of deposition of material and the rate at which material is re-entrained into the air flow. An interesting feature of the deposition rates measured, was that the initial period of deposition resulted in the largest deposition rate, which is unexpected and goes against reports in literature (§2.7). To ensure this observation was reliable, this initial period of deposition was repeated three times, giving very similar deposition rates, demonstrating this phenomenon is an actual feature of spray drying detergents.

Observations of wall deposition were made using Particle Image Velocimetry and these reveal the mechanisms of both deposition and re-entrainment at work within the spray dryer. Adding strength to the conclusion that wall deposition reaches equilibrium between deposition and re-entrainment, resulting in its growth first slowing and then stopping over time of dryer operation.

During this chapter, wall deposition has been simplified into a phenomena which is governed by two steps, namely collision frequency and collision success rate. The remainder of this thesis examines these two critical steps in wall deposition in spray drying detergents. Firstly, fluid dynamics and particle dynamics inside the dryer, which control collision frequency, are examined in Chapters 5 and 6. Secondly collisions success rate is investigated through work on understanding the physical and mechanical properties of detergent granules, their impact behaviour and linking the two in Chapter 7.

Chapter 5 – Fluid Dynamics in a Detergent Spray Dryer

5.1 Introduction

Airflow patterns inside spray dryers are known to be of critical importance in determining product quality and process operation (§2.5). This Chapter details experimental studies of air flow patterns close to the wall of a counter-current detergent spray dryer. This area has been studied due to its importance as the area in which most particles travel through the spray dryer (as they move outwards due to centripetal force of the swirling air flow). Therefore the air flow patterns in this area determine how particles interact with both each other and the dryer wall, with the potential consequence of creation of wall build-up or production of oversized agglomerated particles.

Particle Image Velocimetry (PIV) was used to measure air velocities inside the dryer (§3.5). The measurements were analysed to investigate turbulent and time-dependent characteristics of these flows. A comparison is conducted between results from this work and published work on similar dryers (§ 2.5.4.1).

5.2 Experimental

PIV measurements were made with air only present inside the spray dyer, i.e. no detergent particles were present. The experiments were conducted in two locations, as shown in Figure 3.3: the higher position (H) is above and the lower (L) is below the usual location of the spray nozzle. This allowed the change in airflow pattern due to distance from the air inlets to be studied. The exact positions, of the areas for which flow fields have been produced are also shown in Figure 5.1.

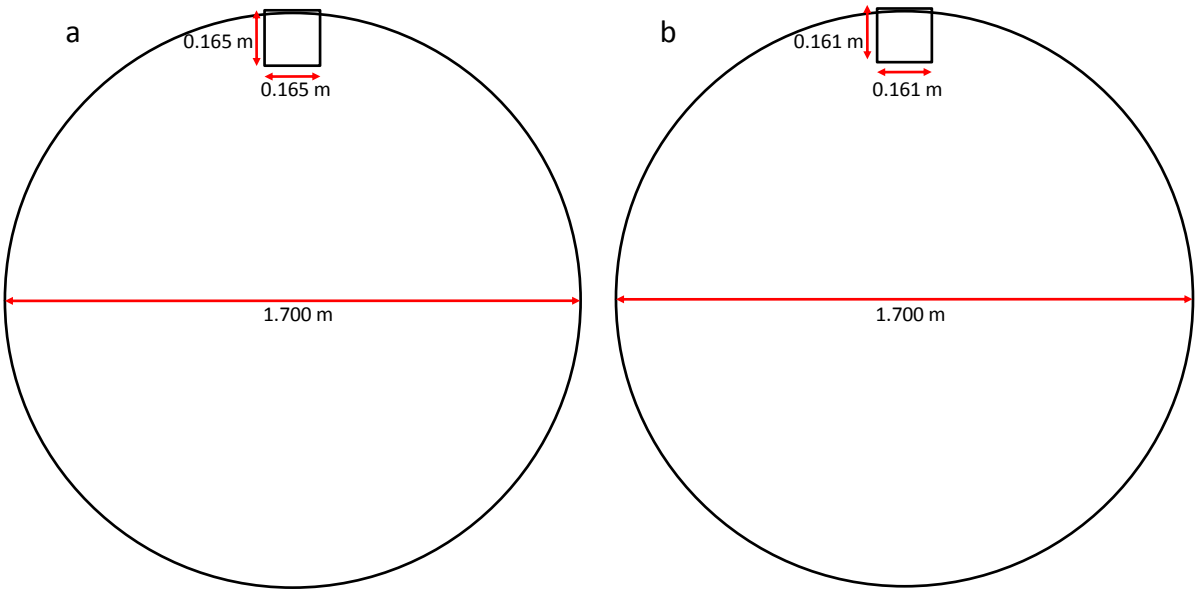

Figure 5.1: Locations of image areas relative to spray dryer (a) position L and (b) position H

To examine the influence of air flowrate, three different flowrates were used for experiments made in position H. This gave four experimental conditions in total, shown below in Table 5.1. Like many spray dryers, detergent dryers are operated under vacuum, this prevents unwanted escape of product through any holes/gaps in the dryer. For the purpose of this work the dryer under-pressure was kept constant at 0.25 kPa.

Table 5.1: Experimental Conditions

Condition	Position	Air flow rate ($kghr^{-1}$)	Air inlet tangential velocity (ms^{-1})
a	Lower (L)	10000 (high)	5.1
b	Higher (H)	6500 (low)	3.3
c	Higher (H)	8000 (medium)	4.1
d	Higher (H)	10000 (high)	5.1

Inserting an object into any flow will alter the movement of the fluid (and therefore the flow patterns observed) as the fluid moves around the object. Installation of the mirror box into the spray dryer (§3.5.1) is no different. To enable the effect of the box on the flow around it

to be studied, CFD simulations of the spray dryer were conducted with and without the mirror box present. These simulations were conducted by BoonHo Ng at P&G's Beijing Technical Centre (§3.8) and the results are shown in Figure 5.2. For each of the scenarios simulated, both contour plots of velocity magnitude and vector plots of the flow field were generated. The area occupied by the mirror box is shown in orange.

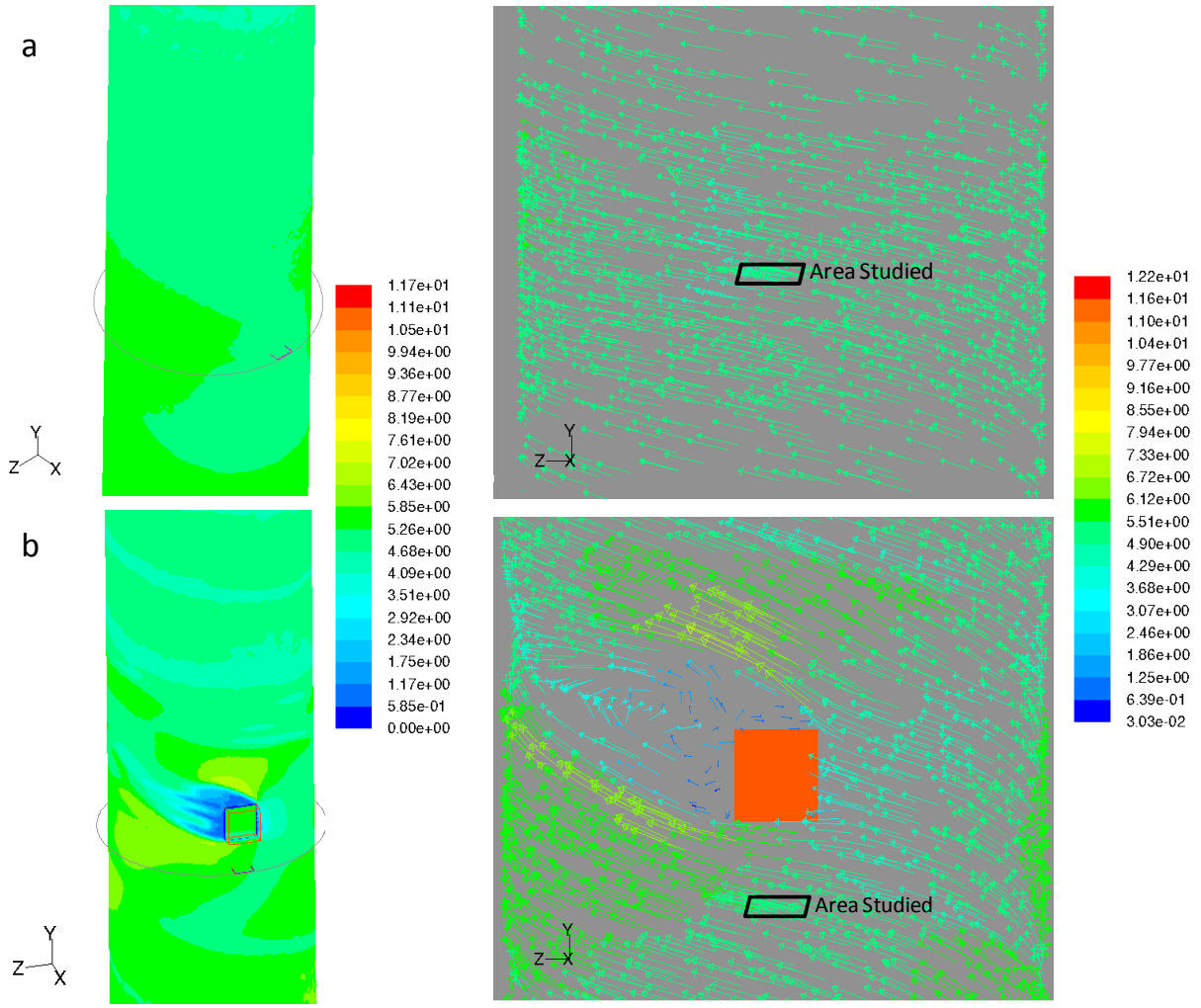

Figure 5.2: CFD Simulation Results of Flow Fields in Dryer Without (a) and With (b) PIV set-up

Comparison of Figure 5.2 a and b clearly show that the present of the mirror box affects the flow within the spray dryer, with a wake effect of the box clearly visible on the contour and vector plots. However, the effect on the flow seems to be most pronounced in areas above

from the imaged area and therefore it can be concluded that although the mirror box affects the flow, the effect should not be pronounced in the area where PIV measurements were made.

The methods used to calculate all parameters displayed as results in this Chapter are given in the literature review (§ 2.5.3).

5.3 Time Average Velocity Studies

To ensure that the results presented here are representative of the flow, it is important to check that a sufficiently large sample size of PIV image pairs has been captured. To prove that this is the case, plots of Root Mean Square (RMS) (§ 2.5.3) and mean velocity magnitude value against the number of PIV image pairs analysed are shown in Figure 5.3 (for the position L, at the highest air flow rate). The mean values converge after 150-200 image pairs and the RMS converges after 200-300 image pairs, showing that the turbulent flow can be taken as steady-on-average and that the sample size of 1000 image pairs is more than sufficient.

In order to demostrait the repeatability of these results, three flow fields produced from different data sets at the same experimental conditions are shown in Figure 5.4. These flow fields show tight agreement with very little difference in either velocity values or flow direction, demostraiting strong repeatability in these experiments.

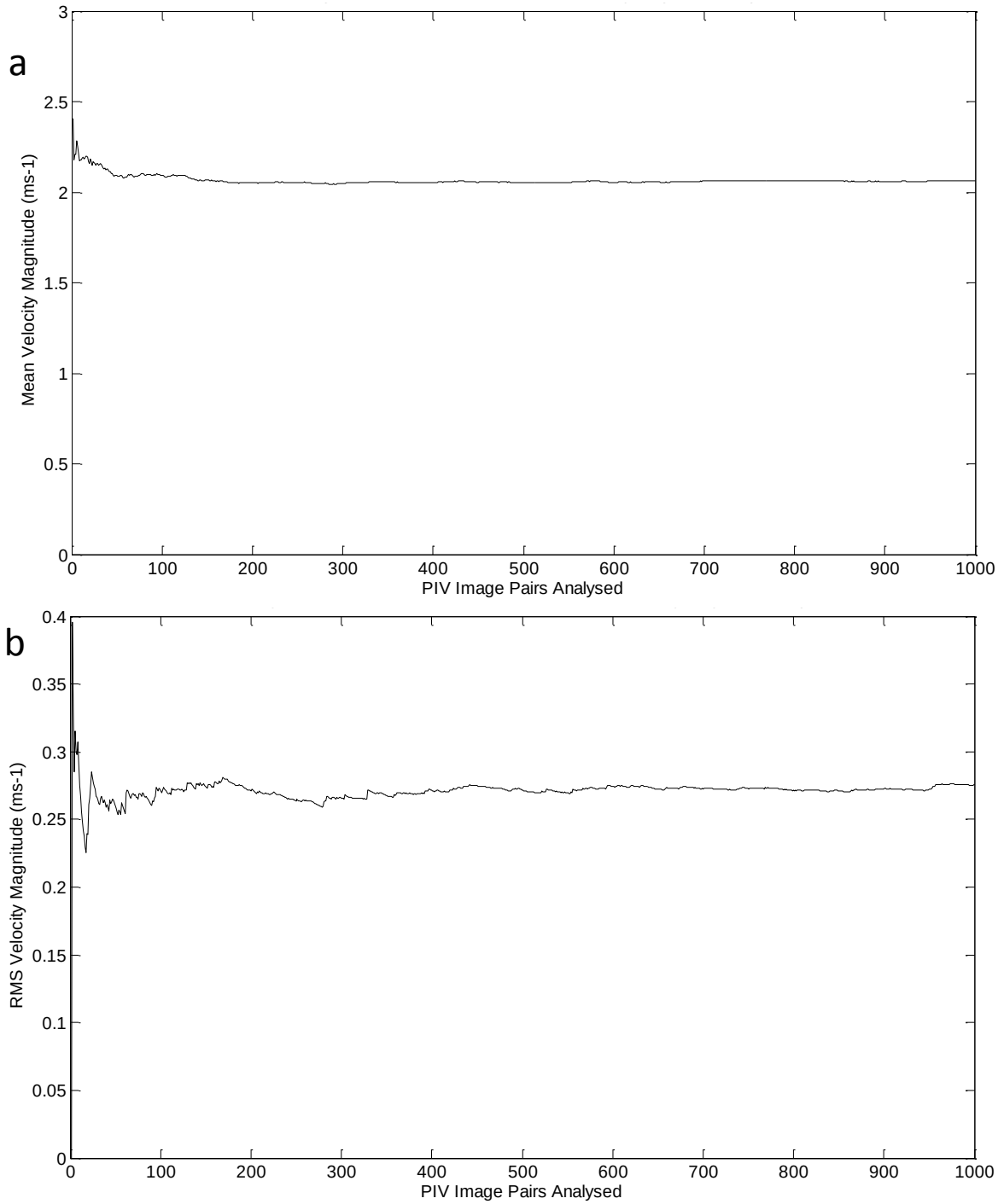

Figure 5.3: Plots of (a) mean velocity magnitude and (b) RMS velocity versus the number of PIV images analysed

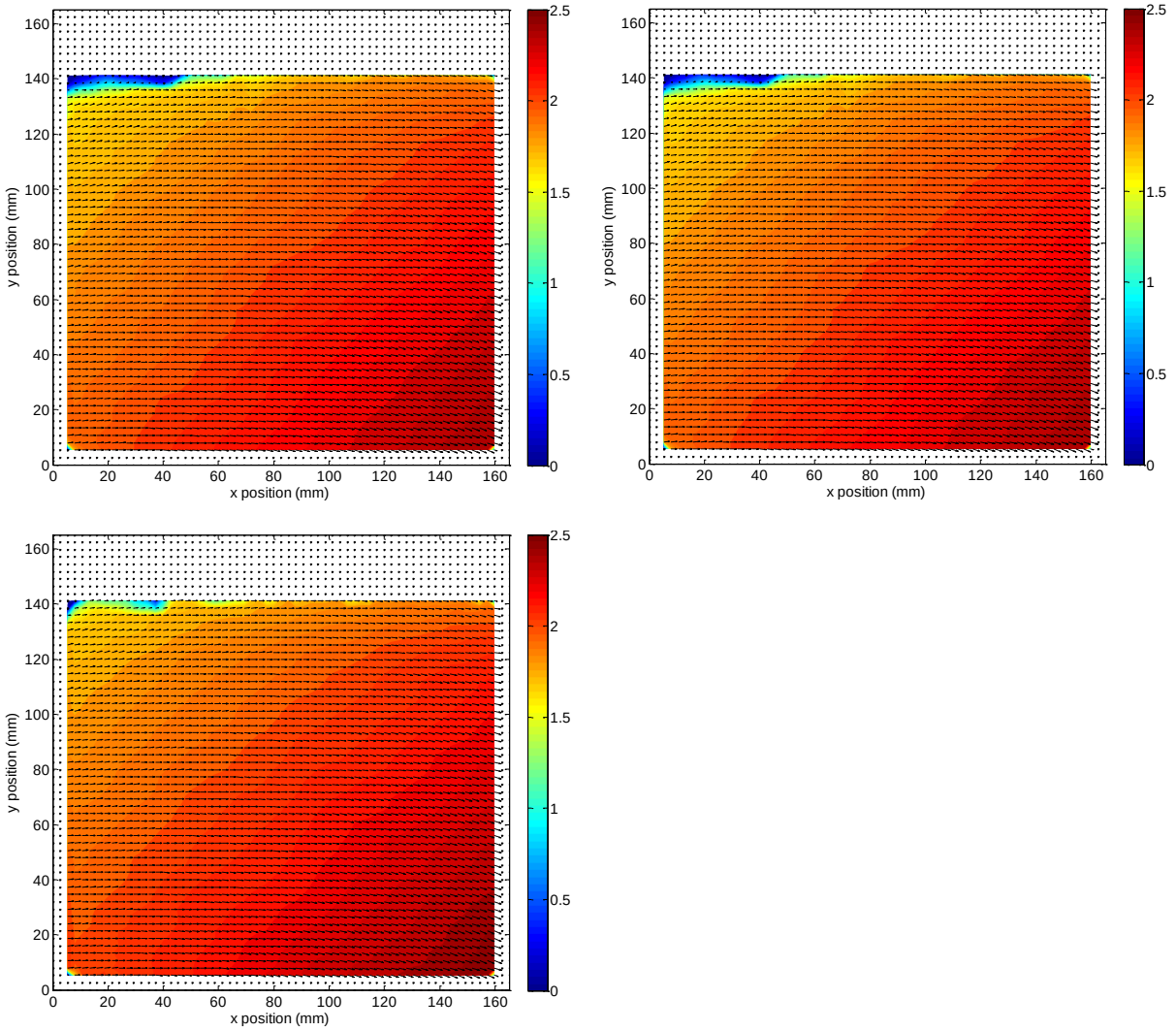

Figure 5.4: Flow Field Plots of Velocity Magnitude Absolute Values (ms^{-1}) (a) position L high flow rate

In the following analysis of the PIV results, the velocity data is displayed as both flow fields and profile plots for velocity magnitude, radial velocity and tangential velocity. The flow fields are shown in plan view, with wall situated in the blank space at the top of the plot and the air flow moving from left to right. Normalised versions of these flow fields are shown in Appendix C.

5.3.1 Velocity Magnitude

Figure 5.5 shows flow fields of velocity magnitude values for each of the experimental conditions studied.

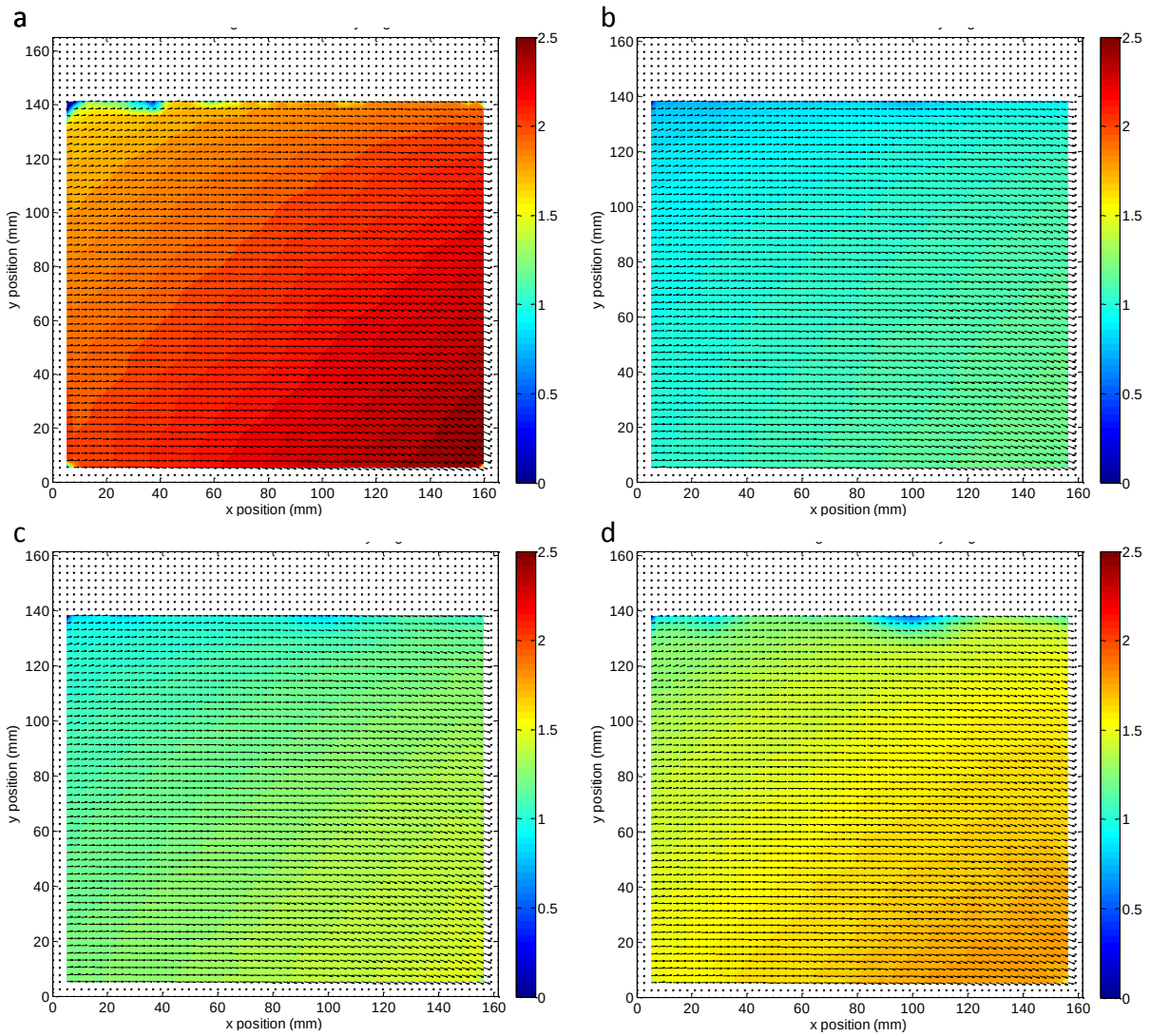

Figure 5.5: Flow Field Plots of Velocity Magnitude Absolute Values (ms^{-1}): (a) position L high flow rate, (b) position H low flow rate, (c) position H medium flow rate and (d) position H high flow rate.

Values of velocity magnitude along the centre of these flow fields are plotted as a function of radial position for all four experimental conditions in Figure 5.6.

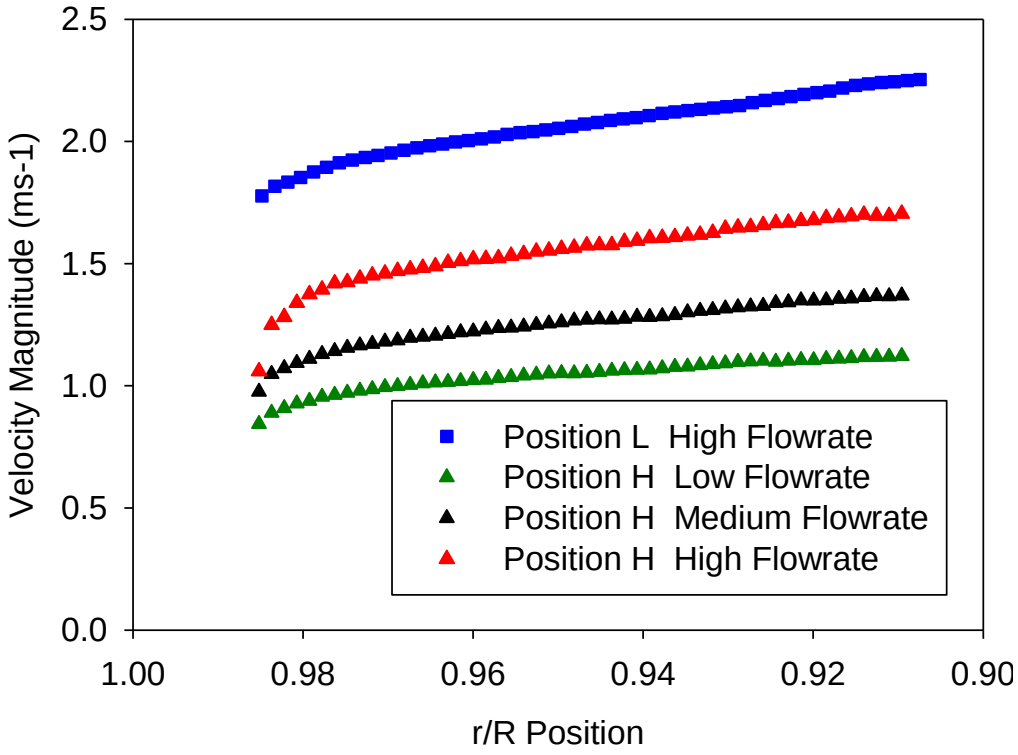

Figure 5.6: Profile Velocity Magnitude plots

The largest velocities are seen for the lower position with high flow rate condition (Figure 5.5 (a) and blue squares Figure 5.6) and the smallest velocities are seen in the higher position with low flow rate (Figure 5.5 (b) and green triangles Figure 5.6). Velocities were found to vary between 0.5 and 2.5 ms^{-1} in the lower position, depending on radial position and between 0.8 and 1.8 ms^{-1} in the higher position, depending on flow rate and radial position.

The observation that velocity was at its highest value in position L at high flow rate and its lowest value in position H at low flow rate can be explained by examining two key factors which affect air velocities inside a counter current spray dryer, namely tower location (height, axial position) and air flow rate (§ 2.5.4).

The effect of axial position (distance from air inlets) can be studied by comparing the two high flow rate experimental conditions, in the lower position, (Figure 5.5 (a) and blue

squares in Figure 5.6) and the higher position, (Figure 5.5 (d) and red triangles in Figure 5.6). This shows that the air velocity (in the horizontal plane) decreases with axial position. This is an example of swirl decay, (§2.5.4), a decrease in the tangential component of fluid velocity in a swirling motion with distance from the initial source of swirl. This would be expected, as described specifically for counter current spray dryers by Bayly *et al.* (2004) and Muller *et al.* (2001), who state that the swirl of the flow decreases as it rises up the tower, as velocity in the horizontal plane (tangential and radial velocities) decreases with increasing velocity in the vertical plane (axial velocity). Direct comparison between these results and the results of previous workers on this phenomenon are given later on in this section.

Comparing the three flow fields displayed for different flow rates of air in the higher experimental position (Figure 5.5b) to (Figure 5.5c) to (Figure 5.5d) shows that the absolute values of air velocity magnitude increase with increasing flow rate, as would be expected in any system where more fluid is passing through the same volume.

Air velocities can be seen to vary across the flow field in both directions, radial and tangential. The largest values of velocity magnitude are seen in the bottom right hand corner of every flow field, and conversely the lowest velocities are seen in the top left hand corner for all flow fields displayed. This is an unanticipated finding as the velocity in the flow fields would be expected to be tangentially symmetrical. This offset in velocity towards the bottom right (and top left) corner may be an effect on the air flow patterns of the mirror boxinserted into the drying chamber (§ 5.2). It would have been anticipated that the velocity would vary with radial distance only. Most literature on airflow patterns in counter current spray dryers reports that air velocity (both velocity magnitude and tangential velocity) increases with

radial distance from the wall at positions close to the wall, as described by the Rankine vortex model (§2.5.4.2). This trend is shown in all flow fields displayed.

5.3.2 Radial Velocity

Figure 5.8 shows plots of values of radial velocity as a flow field for each of the experimental conditions studied, profiles of the radial velocity values along the centre line of these flow fields are shown in Figure 5.7.

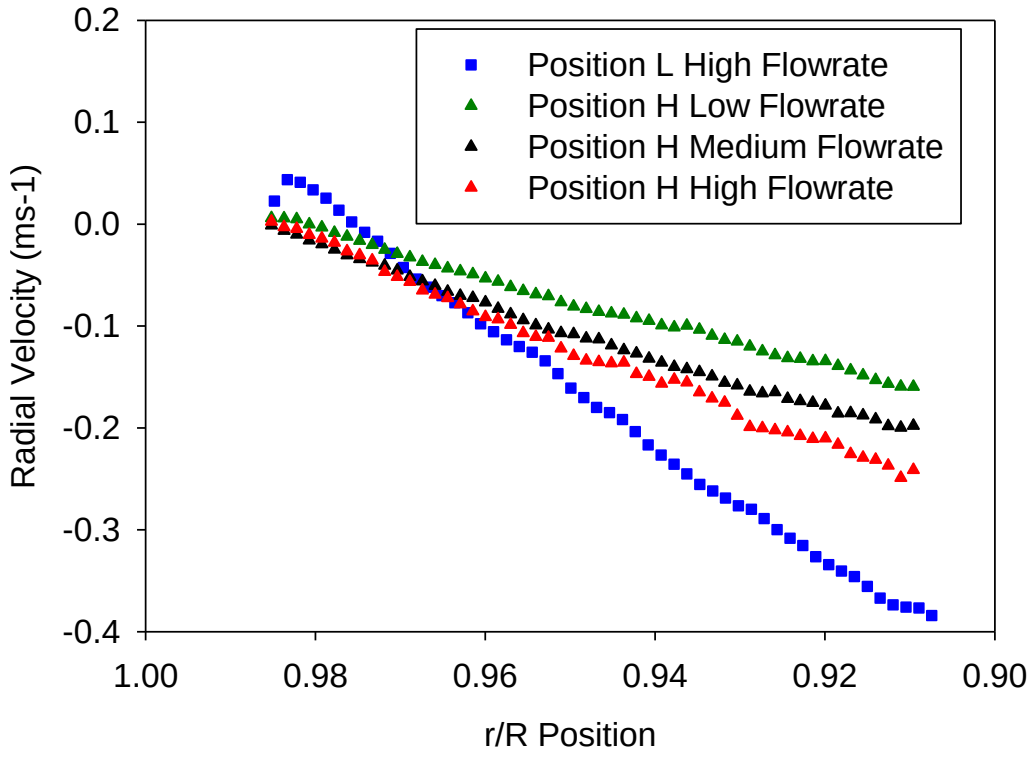

Figure 5.7: Profile Radial Velocity Plots

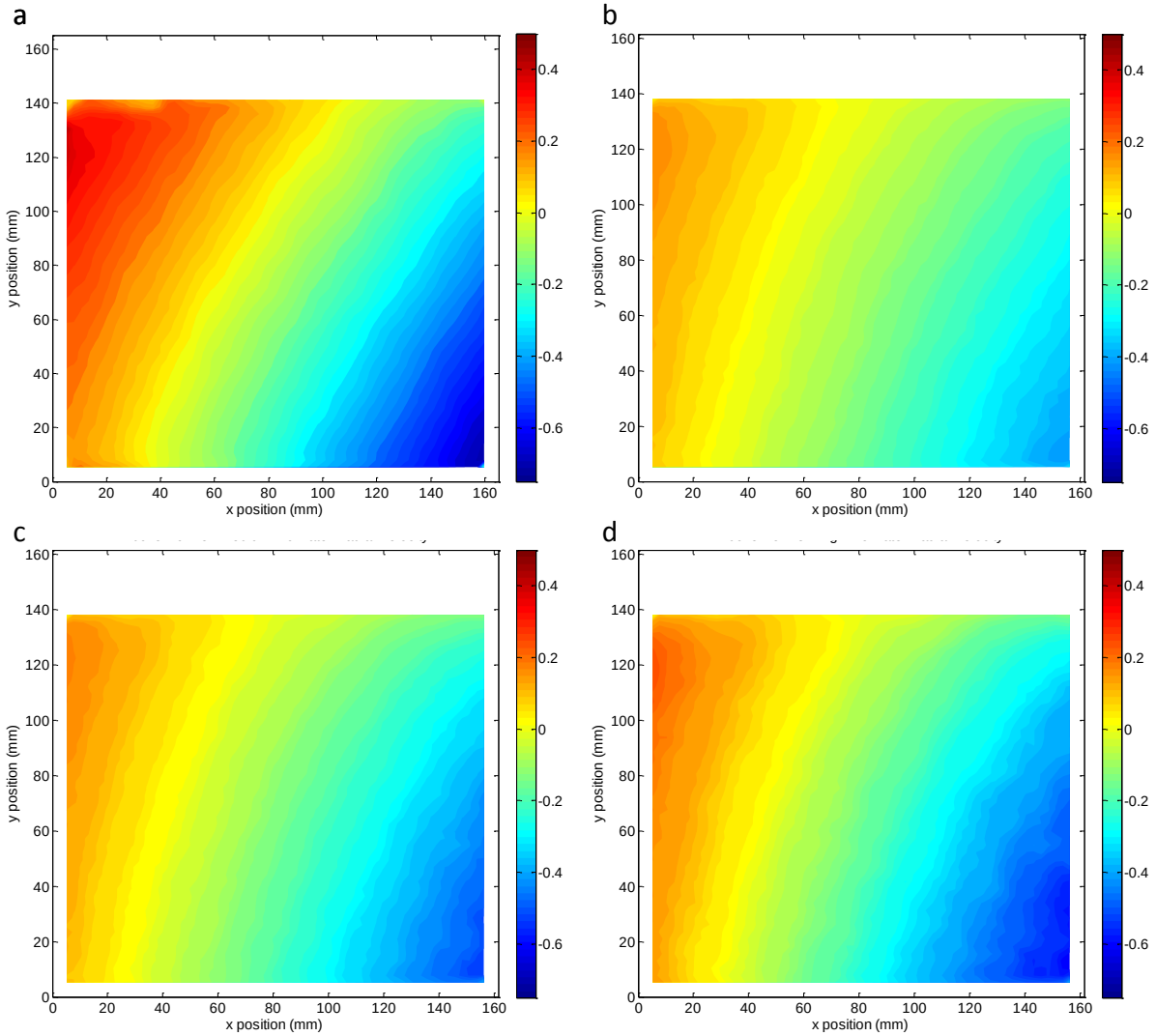

Figure 5.8: Flow Field Plots of Absolute Values of Radial Velocity (ms^{-1}): (a) position L high flow rate, (b) position H low flow rate, (c) position H medium flow rate and (d) position H high flow rate.

The largest velocities are seen in position L with high flowrate condition (Figure 5.8 (a) and blue squares in Figure 5.7) and the smallest velocities are seen in position H at low flowrate (Figure 5.8 (b) and green triangles in Figure 5.7). Velocities were found to vary between -1.0 and 0.5 ms^{-1} in position L and between -0.6 and 0.3 ms^{-1} in position H depending on flowrate. The change in sign of these velocities indicates a change in direction across the flow field, positive velocity values represent movement towards the wall (upwards on the plot) and conversely negative values represent movement away from the wall (downwards on the

plot), which may be an effect of the box as shown in the CFD simulation discussed previously (§ 5.2).

5.3.3 Tangential Velocity

Figure 5.9 shows plots of values of tangential velocity as a flow field for each of the experimental conditions studied. Profiles of tangential velocity values along the centre line of these flow fields are shown in Figure 5.10.

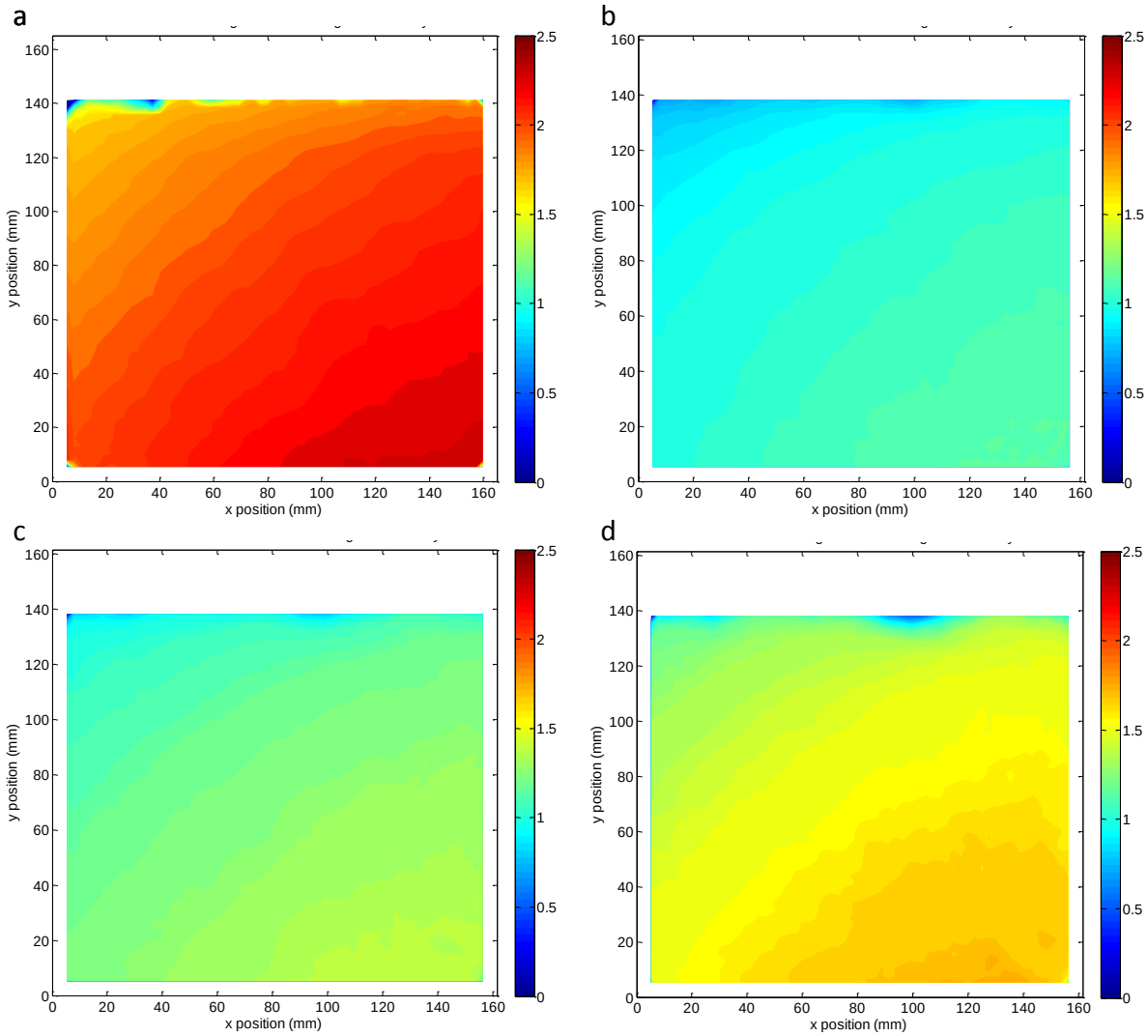

Figure 5.9: Flow Field Plots of Absolute Values of Tangential Velocity: (a) position L high flow rate, (b) position H low flow rate, (c) position H medium flow rate and (d) position H high flow rate.

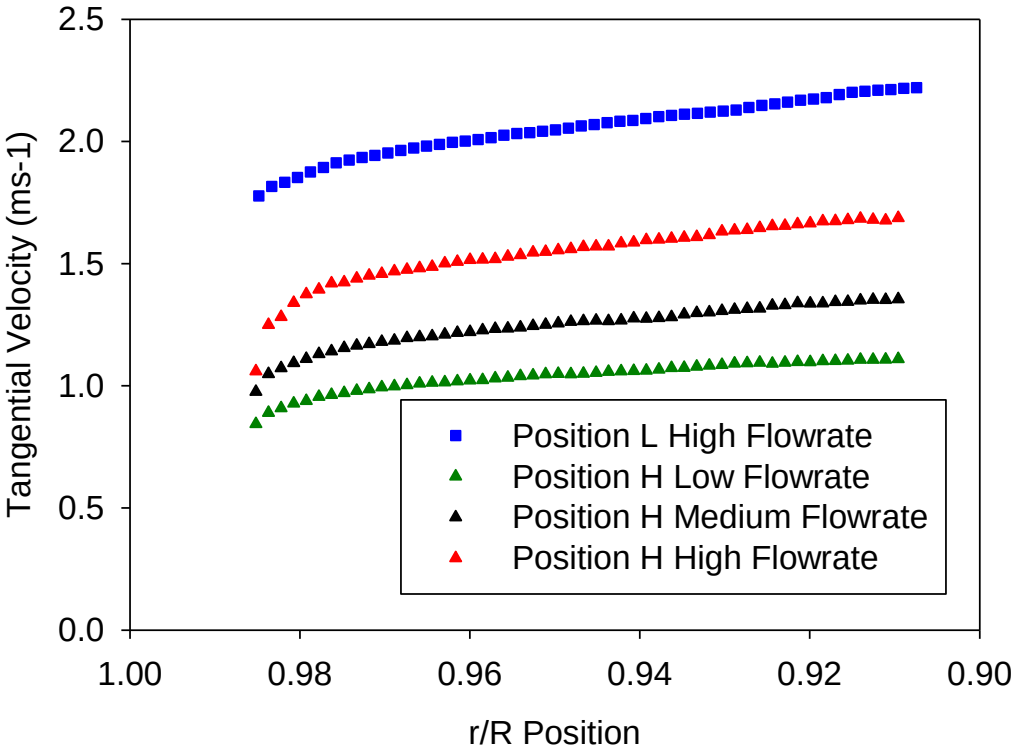

Figure 5.10: Profile Tangential Velocity Plots

The largest velocities are seen in position L high flowrate condition (Figure 5.9 (a) and blue squares in Figure 5.10) and the smallest velocities are seen in position H at low flowrate (Figure 5.9 (b) and green triangles in Figure 5.10). Velocities were found to vary between 0.2 and 2.5 ms^{-1} in position L and between 0.2 and 1.8 ms^{-1} in position H depending on flowrate.

5.3.4 Comparison with Previous Work

Several studies have been published into air flows within comparable detergent spray dryers, these studies involve both experimental measurements and application of Computational Fluid Dynamics (CFD), (§2.5.4). This section presents both qualitative and quantitative comparisons between the experimental work presented here and published studies. This comparison starts by examining the trends and key features seen in these

measurements and relating them to those seen in both measurements and simulations of similar systems.

Several key trends are seen in the flow fields produced from PIV measurements as a function of position within the dryer and air flow rate. These can be summarised as an increase in air velocities in all locations with increasing air flow rate, an obvious trend in consideration of conservation of mass and momentum (§2.5.3) and not surprisingly this is reported in all literature on air flows in comparable spray dryers. Although absolute values of velocities and velocity components are sometime offset in both experiments and simulations, trends in changes in air velocities due to changes in air flow rates are always in agreement with the work presented here.

Changes in air velocity with position inside the dryer are a more complex phenomenon and therefore present more opportunity for disagreement between different studies and also between measurements and CFD results. Through assuming the dryer is tangentially symmetrical, these changes in position can be split into two types, changes in radial positions at a specified axial position and conversely changes in axial position at given radial positions. These are usually expressed as profiles of velocity or velocity components (radial, tangential and axial) as a function of radial position, at various axial positions. Measurements made in this work do not cover the full diameter of the dryer so comparison with full radial velocity profiles is not possible, however, comparison of values from this work, Bayly *et al.* (2004) and Nijdam (2004) are shown in Figure 5.11. Here tangential velocity profiles are presented as a function of radial position and axial position, allowing the trends discussed above to be compared between this work and published work. The

tangential velocities displayed are normalised against the inlet tangential velocities for each experiment in order to allow comparison between work performed for different dryers at different flow rates. The axial position is expressed as a fraction of the height of the dryer, again to enable comparison to be made.

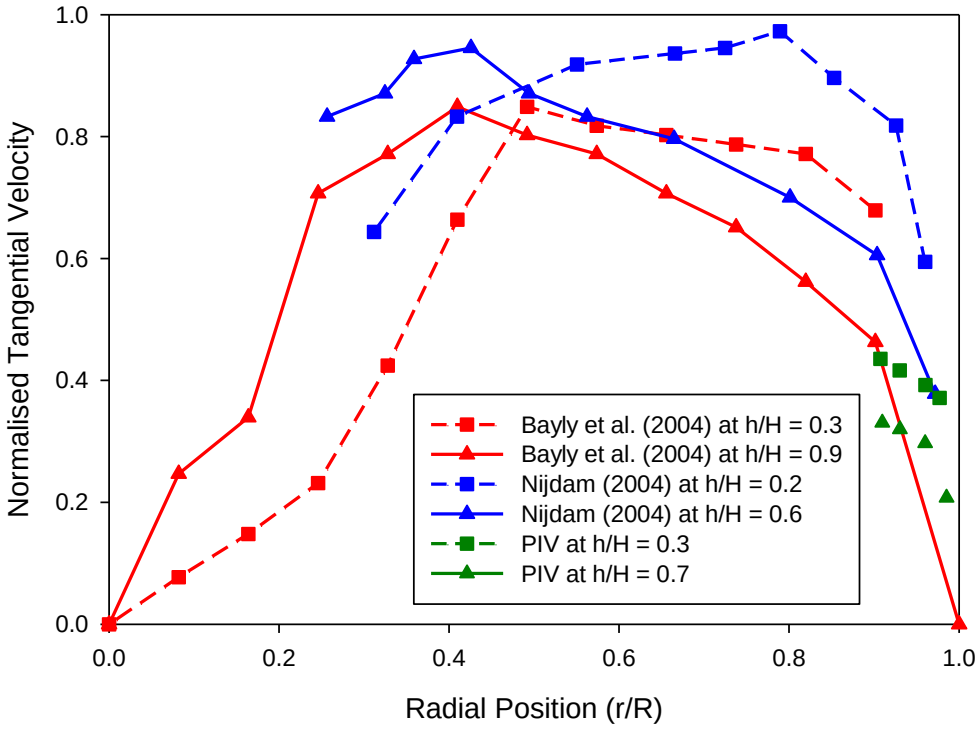

Figure 5.11: Comparison of Tangential Velocity Profile Plots with Published Work

The key trends seen and described for the PIV work presented here can be seen in the published literature complied on Figure 5.11. Changes between the values and shape of profiles of tangential velocities between the different studies can be explained by the small difference in dryer geometries and experimental techniques and conditions used. The PIV data obtained fall on a range of radial positions for which there are few published velocity data, meaning that definitive conclusions on agreement cannot be made. However, any changes in velocity values and velocity profile shapes between this work and published

studies can be explained by changes in dryer geometry, experimental conditions and techniques including the presence of the mirror box in the drying chamber. One aspect of these velocity profiles is the rapid increase in tangential velocity with distance from the wall for the area closest to the wall. This indicates that any boundary layer between the wall and bulk of the flow is very small and that air is moving at considerable velocities close to the wall.

All of tangential velocity profiles plotted here display the characteristics of Rankine vortexes, as report in literature (§2.5.4.2). The changes in the shape of these velocity profiles, as the peak tangential velocity moves towards the centre of the tower with increasing axial position, is described by the phenomena of swirl decay (§2.5.4). This was reported by Bayly *et al.* (2004), Nijdam (2004) and Sharma (1990) (§2.5.4.1). This means that air flow patterns are a function of axial position within the dryer, meaning that particle velocities and trajectories change with axial position, with potential consequences in terms of particle-wall interaction and its effect on wall deposition.

5.4 Time Averaged Turbulent Parameters

5.4.1 Turbulence Intensity

Figure 5.12 shows flow field plots of turbulence intensity, as a percentage of mean velocity magnitude values, (§2.5.3) for all four experimental conditions. Additional turbulent parameters are shown in Appendix C.

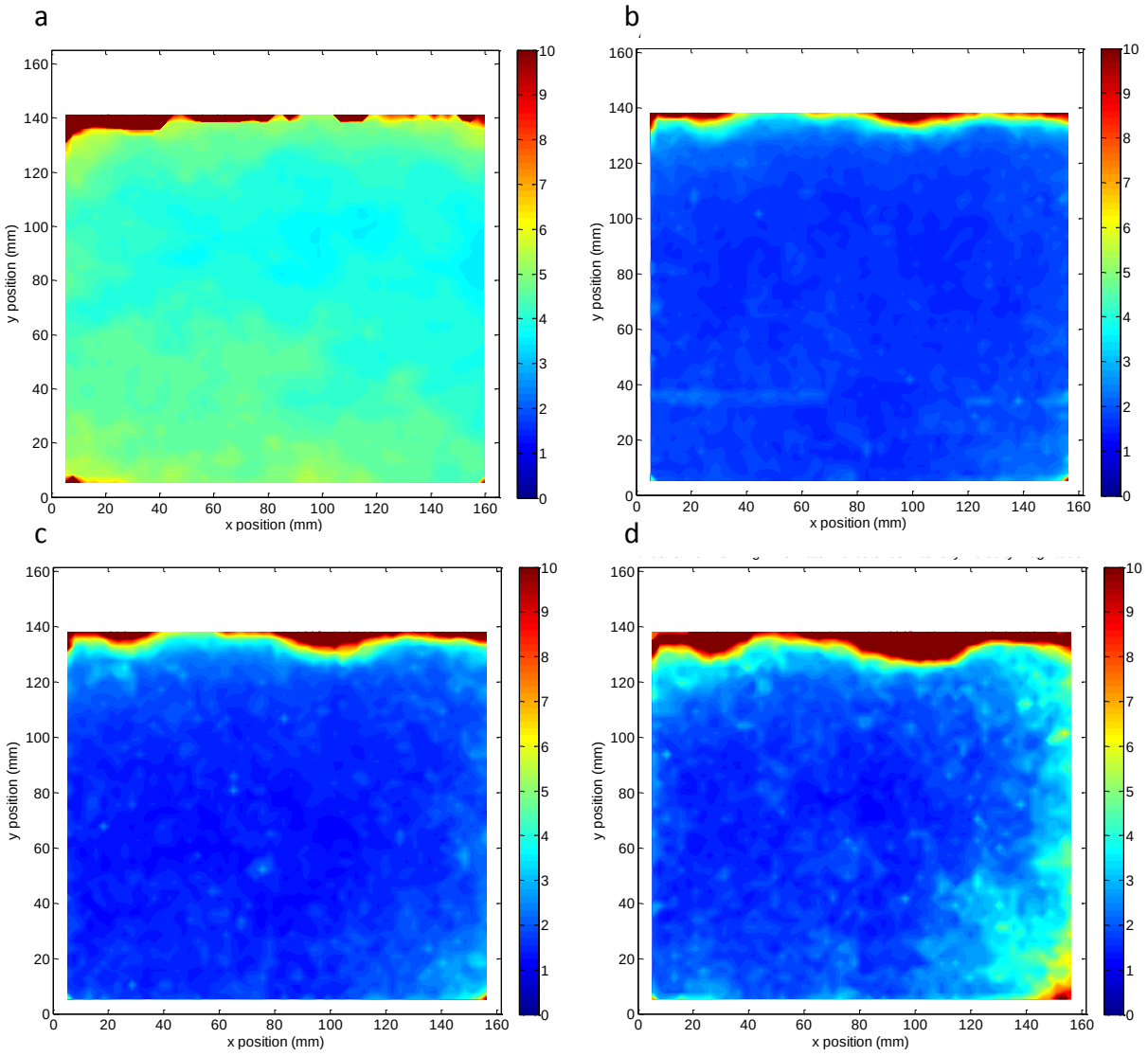

Figure 5.12: Turbulence Intensity Plots (% mean velocity magnitude) : (a) position L high flow rate, (b) position H low flow rate, (c) position H medium flow rate and (d) position H high flow rate.

Values of turbulence intensity for velocity magnitude vary between 2.0 and 10.0% of the mean velocity magnitude value, depending on experimental position and air flow rate. Large values are seen closest to the wall (top of plot) for all experimental conditions, as with the velocity results, it is unclear if these are an artefact of the measurement technique (described below) or if they are caused by the presence of the boundary layer at the dryer wall.

The largest values are seen in position L, ranging from 4.0 to 10%. Smaller values (excluding edge values) of turbulence intensity are observed in position H, these increase from 2.0 - 4.0% at the low flow rate, through to 2.0 – 5.0% for medium flow and finally 2.5 – 7.0% for high flow rate. Overall turbulence intensity is seen to increase towards the air inlets at the bottom of the spray dryer and with increasing flow rate.

An interesting feature present in all four plots is the area of high values of turbulence intensity, shown as dark red areas at the top of each plot, in the area which is closest to the dryer wall. Two possible explanations for the appearance of this feature are available; firstly this is a representation of an area of high turbulence in the boundary layer close to the dryer wall. The second explanation is that this is a feature of the measurement technique applied and this area displays artificial values of turbulence as a result of issues with the PIV images captured and cross-correlation using them, most likely caused by reflection of laser light from the dryer wall. This feature makes it difficult to draw any definite conclusions on the levels of turbulence intensity in this area.

5.5 Time Dependent Velocity Studies

Air flow patterns inside spray dryers are known to be time dependent and this is discussed widely in literature by amongst others, LeBarbier *et al.* (2001), Southwell and Langrish (2001), Muller *et al.* (2001), Langrish (2009) and Gabites *et al.* (2010) (§2.5.4.3). This section examines data obtained from PIV experiments with the aim of detecting time dependence in the air flows studied.

5.5.1 Velocity Signals and Histograms

Velocity signal plots and histograms of velocity values are shown for values of velocity magnitude normalised against the mean value of velocity magnitude, in Figure 5.13. These plots are made for the PIV integration spot (§2.5.2.6) exactly in the centre of the area investigated (the area of PIV images was broken into a grid of 64 by 64 interrogation windows, the spot at 32, 32, *i.e.* in the centre was chosen for this work).

Both signal and histogram plots show how velocity magnitude changes for each of the four experimental conditions studied. Both of these plots represent 1000 data points captured at a rate of 1 Hz. Observing signal plots for velocity magnitude for all four experimental conditions show that the largest amplitude is always seen for position L with high flowrate condition (Figure 5.13a), indicating the increased turbulence within the flow at this condition (as seen for turbulence intensity in Figure 5.12) The corresponding histograms show a wider distribution of velocities than seen for the other three experimental conditions, again highlighting the increased turbulence observed for position L with high flowrate (Figure 5.13a).

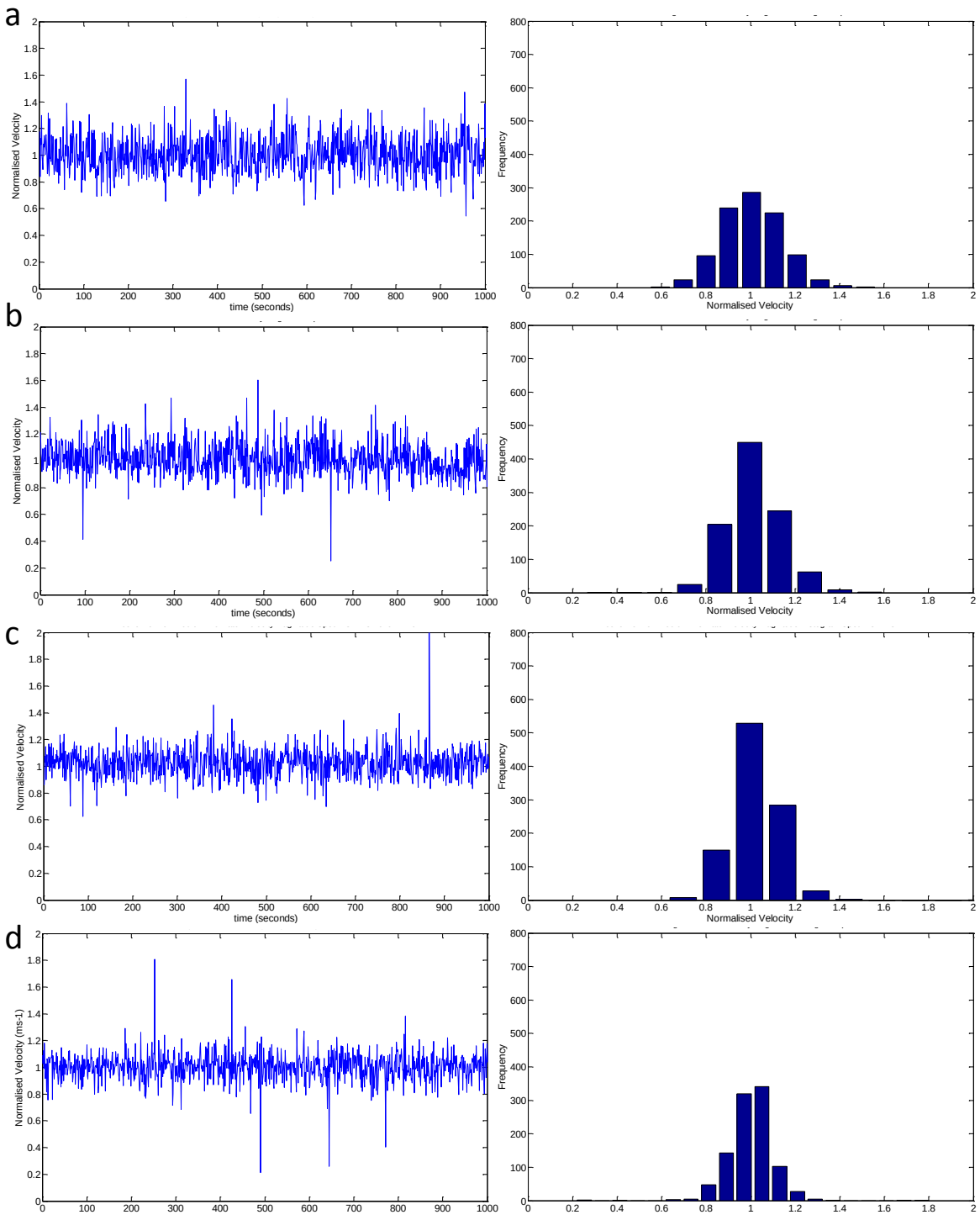

Figure 5.13: Velocity Magnitude Signal Plots and Velocity Histograms: (a) position L high flow rate, (b) position H low flow rate, (c) position H medium flow rate and (d) position H high flow rate.

For in position H experimental conditions (b to c to d), the amplitude of the velocity signal increases, as do the width of distributions on the corresponding velocity histograms. This may indicate increasing levels of turbulence in the flow as velocity increases, possibly owing

to increasing Reynolds number of the flow, or may be caused by changes in time dependent features of the flow with increasing flow rate.

Attempts to observe periodic fluctuations in velocity, caused by oscillation of the vortex due to time-dependent flow characteristics inside the dryer, were made through observation of these signal plots. This did not show any visible evidence of periodicity, therefore further analysis was conducted as described in the next section.

5.5.2 Periodicity

The potential for the presence of time-dependent flow patterns inside spray dryers was introduced previously (§2.5.4.3). Here attempts were made to investigate this phenomenon by processing velocity signal plots, displayed in Figure 5.13, applying Fast Fourier Transform (FFT) analysis using MATLAB 7.1 software (Mathworks Inc.). To enable identification of any frequencies that may have an associated periodic oscillation in velocity, periodograms were produced for the spot at the exact centre of the area investigated for all experimental conditions. These are displayed in Figure 5.14.

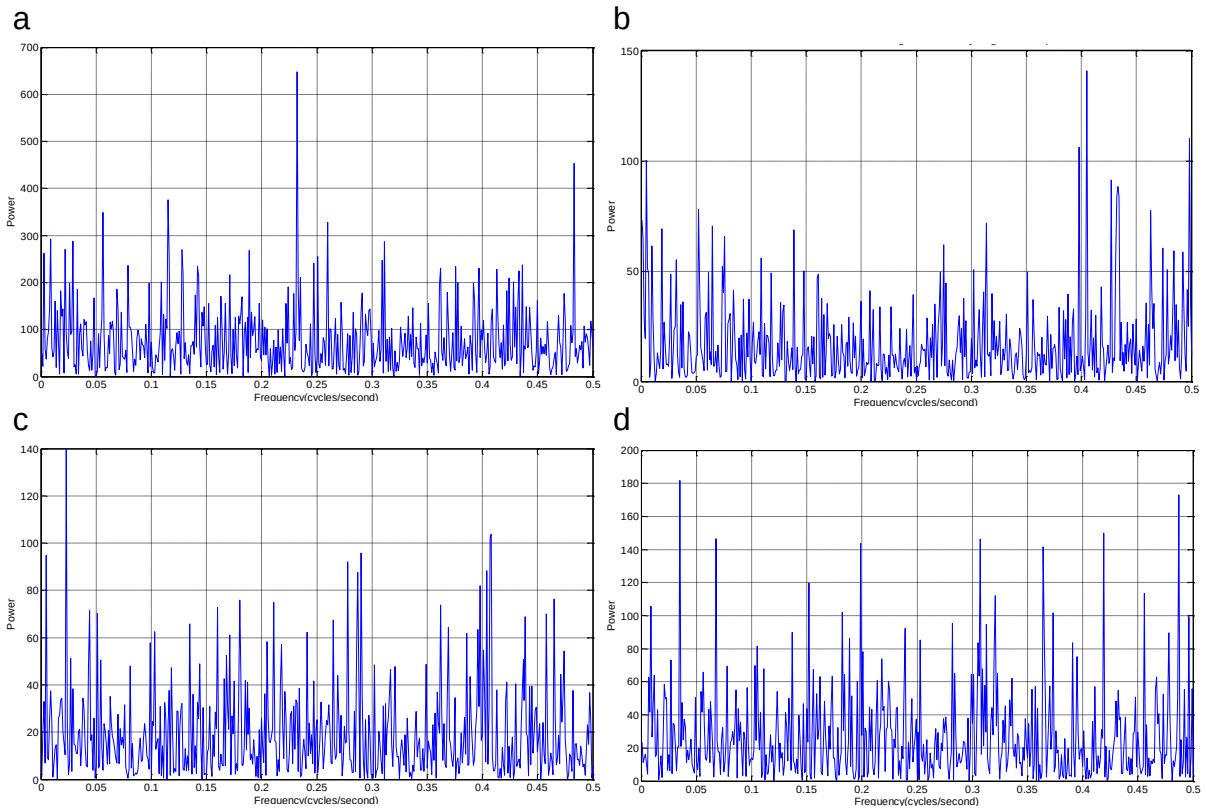

Figure 5.14: Periodogram plots for centre of all experimental conditions: (a) position L high flow rate, (b) position H low flow rate, (c) position H medium flow rate and (d) position H high flow rate.

The clarity of the periodograms shown here varies and the power values for any peaks are much lower than shown for previous studies *e.g.* Muller *et al.* (2001) (§2.5.4.3). However, a weak indication of periodicity is visible in the time frame expected from previous studies, particularly in the plot for position L and high flow rate which shows a distinctive peak at a frequency of approximately 0.23 (cycles/seconds). This gives a period of approximately 4 seconds, which is comparable to the period found by Muller *et al.* (2001).

The lack of clarity from these periodicity studies may be the result of one or a combination of several properties of the velocity measurements made here, namely:

- The position of these measurements is very close to the wall and it is possible that this area is not exposed to such significant changes in velocity, owing to vortex

oscillation, as a position much closer to the centre of the drying chamber, as used by Muller *et al.* (2001).

- Additional turbulence may be generated in the area of measurement by the presence of material deposited on the dryer walls and/or the mirror box, adding extra noise to the velocity signal analysed.

- The use of PIV as a measurement technique may limit the chances of detecting periodicity in terms of the spatial resolution (spot-size area) and the temporal resolution (measurement frequency) being unsuitable to pick-up periodicity in the vortex.

In conclusion these attempts to study periodicity in the air-flow within the spray dryer have given an indication of time-dependent behaviour. The period of these oscillations in vortex have been indicated to be in the range of 4 seconds, which is in agreement with previous studies (§2.5.4.3). This has paved the way for future investigations examining the effect of radial position within the drying chamber on periodicity, these studies could potentially utilise different techniques to avoid the possible effects of using PIV.

5.6 Conclusions

Air flow patterns have been studied inside an industrial scale counter-current detergent spray-dryer. Experiments were conducted in the horizontal plane in an area adjacent to the dryer wall. Two different axial positions on the dryer were used, so that the effect of distance from the air inlets could be studied. Three different air flow rates were used in the higher position to study the effect of flow rates on flow patterns.

Time averaged velocity flow fields have been obtained experimentally for velocity magnitude and the radial and tangential velocity components. These show that the velocity values obtained for tangential velocity are very similar to the velocity magnitude values calculated for all experiment conditions, demonstrating that tangential velocity dominates movement in the horizontal plane. Values of velocity magnitude observed were between 0.5 and 2.5 ms^{-1} in position L and 0.5 and 1.8 ms^{-1} in position H depending on flow rate. Tangential velocity values were almost identical to these. Radial velocities were found to change direction across the area investigated, with flows towards the wall (positive values) in the area closest to the oncoming flow (right side) and flow away from the wall (negative values) in the area furthest from the oncoming flow (left side). The values of radial velocity range from -1.0 and 0.5 ms^{-1} in position L and -0.06 and 0.30 ms^{-1} in position H, depending on flowrate. The change in radial flow direction may be an effect of the presence of the mirror box in the flow.

A comparison has been made between time averaged tangential velocity profiles produced from this work and published studies on similar detergent spray dryers. Common characteristics and features in tangential velocity profiles show the key trends seen for the PIV work presented here. This reinforces the conclusions drawn on flow patterns in spray dryers during this chapter.

Calculations using the experimental velocity data found that, flow in the lower position was found to exhibit the largest amounts of turbulence with turbulence intensity values of 5 to 10% of the mean velocity magnitude. In addition these trends in turbulence are also seen in signal and histogram plots of velocity magnitude, for the centre interrogation spot for each

experimental condition. Attempts to identify periodicity within these velocity signal plots gave an indication of periods in the area of 4 seconds, however, clear periodgrams were not produced.

Chapter 6 – Particle Dynamics in a Detergent Spray Dryer

6.1 Introduction

In Chapter 5, air flow patterns within a counter-current detergent spray dryer were investigated using PIV. In this Chapter, PIV measurements made on detergent particles within the process are reported which are used to determine the particle dynamics. The PIV images were used to obtain particle size, concentration and loading data using bespoke image analysis methods. Cross-correlation of the images was also conducted to obtain particle velocities. All of these parameters were examined as a function of dryer operating conditions and position within the drying chamber.

This chapter begins with a description of the experimental set-up and techniques applied to obtain the images. The development of image analysis techniques to obtain parameters from these images is described in Appendix D, such that the reader can understand and appreciate the principles and assumptions applied to obtain the data. Results displayed here are firstly for time averaged data, then secondly for time dependent results, before conclusions are drawn.

6.2 Experimental

Experiments were conducted in two locations, a high position (position H) above the spray nozzle and a low position (position L) below the spray nozzle; as illustrated in Figure 3.3 (§ 3.5). The exact position of the areas for which flow fields have been produced are shown in Figure 5.1.

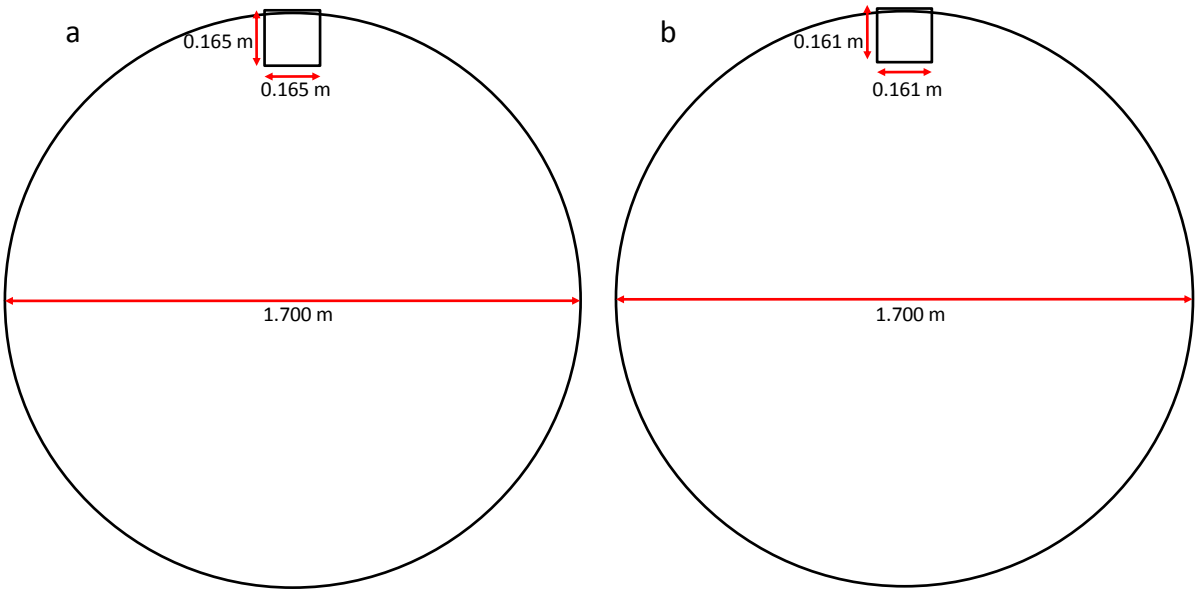

Figure 6.1: Locations of image areas relative to spray dryer (a) position L and (b) position H

Three different combinations of slurry and air flow rates were applied at each position, giving six experimental conditions, shown in Table 6.1.

Table 6.1: Operating parameters used for studying particle dynamics

Relative Slurry Flowrate		Air Flowrate ($kghr^{-1}$)	Air Inlet Temperature (°C)
Position H	1.0	6000	240
	1.2	6000	260
	1.2	8000	220
Position L	1.0	6000	240
	1.2	6000	260
	1.2	8000	220

For all experimental conditions, images were captured for 4 seconds at a rate of 500 Hz, giving 2000 image pairs per condition. These images were then saved as TIFF files for later image analysis. The image analysis methods developed and used during this work are described in Appendix D.

6.3 Results: Time-Averaged Particle Dynamics

Time-averaged results for particle size, loading and concentration inside the spray during operation are discussed in this section. Each of these parameters is displayed as a function of dryer operating conditions (Table 3.4) and radial distance from the dryer wall for both positions L and H. Contour plots for each parameter over the area studied are also shown. Particle velocity flow fields are also shown for each experimental condition, allowing the effect of position within the dryer and operating conditions on particle velocities to be examined.

6.3.1 Particle Size

6.3.1.1 Mean 'Projected Area' Particle Size

The mean particle sizes presented are based on the calculated equivalent diameters of spheres with the same projected area as the irregularly shaped particles in binary images. This calculation was done using the "regionprops" algorithm in MATLAB which uses the quantity, $d_A = \sqrt{4A_P / \pi}$, is used in calculation of the volumetric shape factor, k, proposed by Heywood (1962) (Clift *et al.* (1978)), as $k = V / d_A^3$.

Values of d_A are displayed as a function of dryer operating conditions (experimental conditions) and radial distance from the dryer wall experimental positions L and H in Figure 1.1. The error bars shown here represent an error of one pixel width, at the respective resolutions. The values vary as a function of slurry flow rate and position (H or L) with the largest values of 800 – 1000 μm being observed for position L. This was expected as most particles travel down through the dryer from the nozzle (Bayly (2008)). Smaller values of d_A

were seen at position H as only the minority of smaller particles are sufficiently entrained in the airflow to be carried above the nozzle.

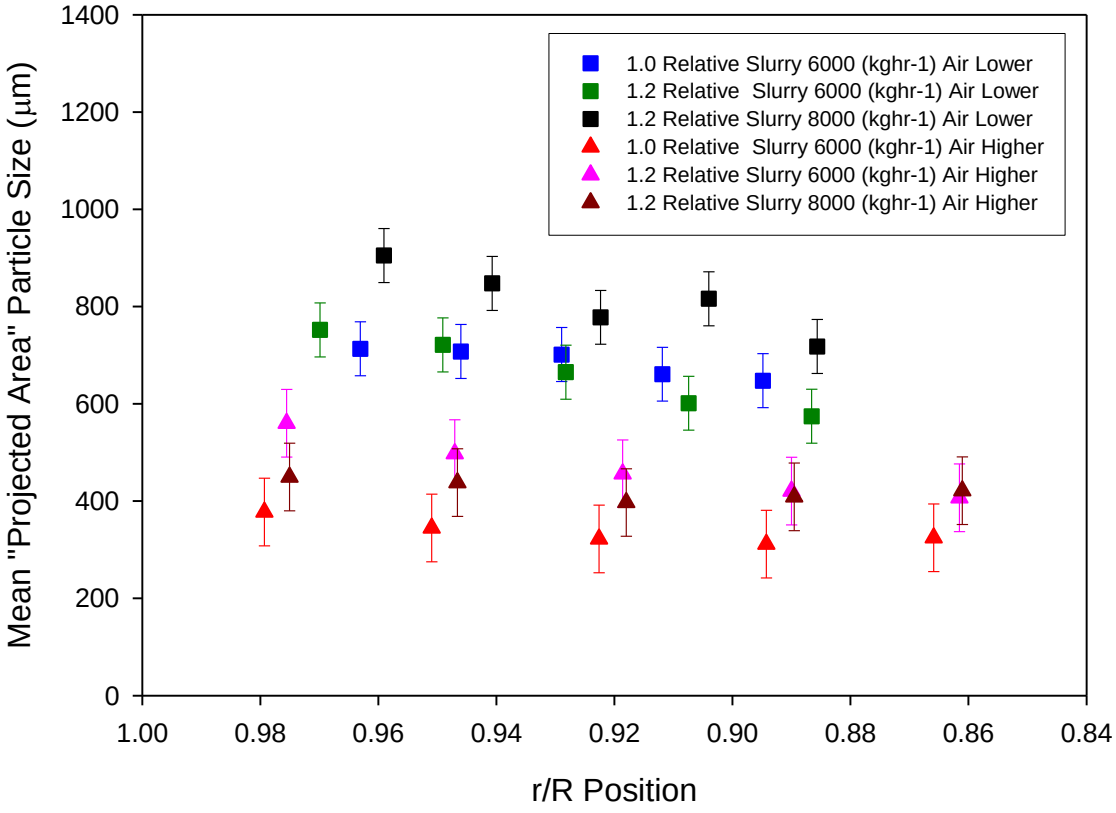

Figure 6.2: Mean projected area diameter, d_A as a Function of Radial Position

Regardless of flow rate or height of measurement, the values of d_A decrease with radial distance from dryer wall both above and below the nozzle, this is may be explained by the effect of the swirling flow inducing centripetal forces on the particles, in effect "throwing" them out towards the wall. This is a process which is preferential to larger particles, as smaller particles are more easily deviated as they have less inertia and are therefore more likely to follow the swirl of the air. Whereas the trajectory of the larger particles is

influenced by the swirl to a lesser extent (due to larger momentum/inertia), meaning that they move more directly through the dryer than moving round closer to the wall.

To explain the above particle sizes and mass results, the process by which the detergent slurry is atomised and then dried to create the final powder product inside a spray dryer needs to be examined. The first step in this process is atomisation, which turns the detergent slurry into discrete droplets, which will eventually form the particles of detergent powder. Therefore the droplet size produced is a critical parameter in determining the particle size within the process and product. Atomisation is achieved through use of a pressure nozzle (§2.3.4), and the size distribution of droplets obtained is highly dependent on the type of nozzle and pressure/flow rate of the slurry. In general the droplet size obtained from atomisation is known to decrease with increasing nozzle pressure, which is a direct function of the slurry flow rate, due to increased shear rates in the nozzle (§2.3.4). This would suggest that a smaller droplet size should be obtained at higher slurry flow rates in the experiments. However, the data shown in Figure 6.8 show the opposite trend, with an increase in d_A with increased slurry flow rate (at constant air flow rate).

This suggests that other phenomena within the dryer are affecting particle size. Both drying and agglomeration have a significant effect (Hecht (2004)) and are heavily influenced by dryer operating conditions. As described in the literature review (§2.3.6) drying occurs due to simultaneous heat and mass transfer, this process involves initial shrinkage as water is lost through drying and is followed by steam puffing (§2.3.6), which leads to expansion in particle size as a porous structure is developed in the drying particle. Since the trajectories

of individual particles are different, it is not possible to determine *a priori* the extent of puffing as a function of position in the dryer.

Agglomeration is known to drive particle size distribution in spray drying operations (§2.3) and requires firstly that particles come into contact with each other, and secondly that these collisions result in the particles sticking to each other, referred to as collision frequency and collision success rate respectively. Collision frequency is a function of the concentration (number and loading) of particles inside the dryer and the velocity and turbulence of the air flow through which the particles are travelling. The collision success rate is affected by moisture content, structure, mechanical and physical properties of particles.

In addition to agglomeration of particles colliding in the flow, particles deposited on the walls will be brought into contact with impacting particles from the bulk. The process of wall deposition is known to be affected by both dryer operating conditions and the duration of operation, as the layers deposited build-up over time (§2.7). This process is dynamic and material is re-entrained into the air flow as well as deposited onto the wall. The material re-entrained will most likely break off in large agglomerated lumps. The rate of re-entrainment and the size of the particles re-joining the air flow will depend on many factors, such as the nature of the particles deposited, dryer operating conditions and the duration for which the dryer has been operated, but in particularly it will depend on the air velocity and turbulence passing over it, as described by Hanus and Langrish (2007) (§2.7.4). This mechanism is only applicable to areas which experience wall deposition, and therefore is most likely to occur below the nozzle, where wall deposition is observed.

The data shown in Figure 6.4 and Figure 6.5 suggest that both agglomeration mechanisms are indeed the driver for the observed particle sizes. In particular they drive the creation of particles which are much bigger than those created by atomisation and puffing of single particles during drying. The size distributions in the Position L contain particles which are up to ten times the diameter of typical atomised droplets (Bayly (2008)). As the air flow rate rises, the collision frequency between the particles would be expected to rise due to the increased air velocities, and thus turbulence, inside the dryer. Comparing the data taken at 1.2 relative slurry flowrate and 8000 $kghr^{-1}$ air flow rate (black squares) with the data at 1.2 relative slurry flowrate and 6000 $kghr^{-1}$ (green squares), there is a noticeable rise in particle size. Reducing the relative slurry flowrate to 1.0 at the lower air flowrate used has a smaller effect and the particle sizes are the same within experimental error. In position H, these trends appear to be less clear, as would be expected, as the particle size distribution above the nozzle depends on entrainment of particles in the air flow rather than agglomeration

Figure 6.3 shows contour plots of d_A over the measured field of view. Whilst at position H, the diameter observed is a strong function of y position and a weak function of x, this is not the case for position L where the distribution is clearly two dimensional.

In order to explain this, two main hypotheses have been put forward as possible reasons for the asymmetrical results in the tangential direction below the nozzle:

1. *Distorted airflow patterns* possibly caused by the mirror box (inserted into the drying chamber) (§ 5.3).

2. *Re-entrainment of material* deposited on the side of the mirror box passing through the field of view.

Distorted airflow patterns. The offset in velocity towards the bottom right (and top left) corner shown in Figure 5.5 (§5.3) may be an effect of the mirror box on the air flow patterns. Air flow patterns in the dryer are known to move in all three dimensions, it is difficult to understand the full extent of these distortions on the flow patterns since PIV cannot be used without the mirror box. However, it is easy to envisage a situation where the distortion in air flow could have the effect of carrying more particles into the region of the image where the radial air flow is towards the wall (left hand side), conversely, where the radial component air flow is moving away from the wall, particles may be carried out or moved away from the image.

Re-entrainment of material. Material was observed to build-up on the mirror box, through the same mechanism as wall-deposition. Therefore it would be expected that material would be re-entrained into the air flow from the mirror box; if this was to move downwards under the influence of gravity it could well pass through the affected area of the image. This could result in a significant amount of large particles passing through a specific area of the image, as observed. In addition the fact this asymmetry is only observed in position L, where wall deposition occurs, is an indicator this is the reason behind the discussed asymmetry.

The likelihood of the situation is that this observation is a combination of both factors which cannot be fully understood with the data available.

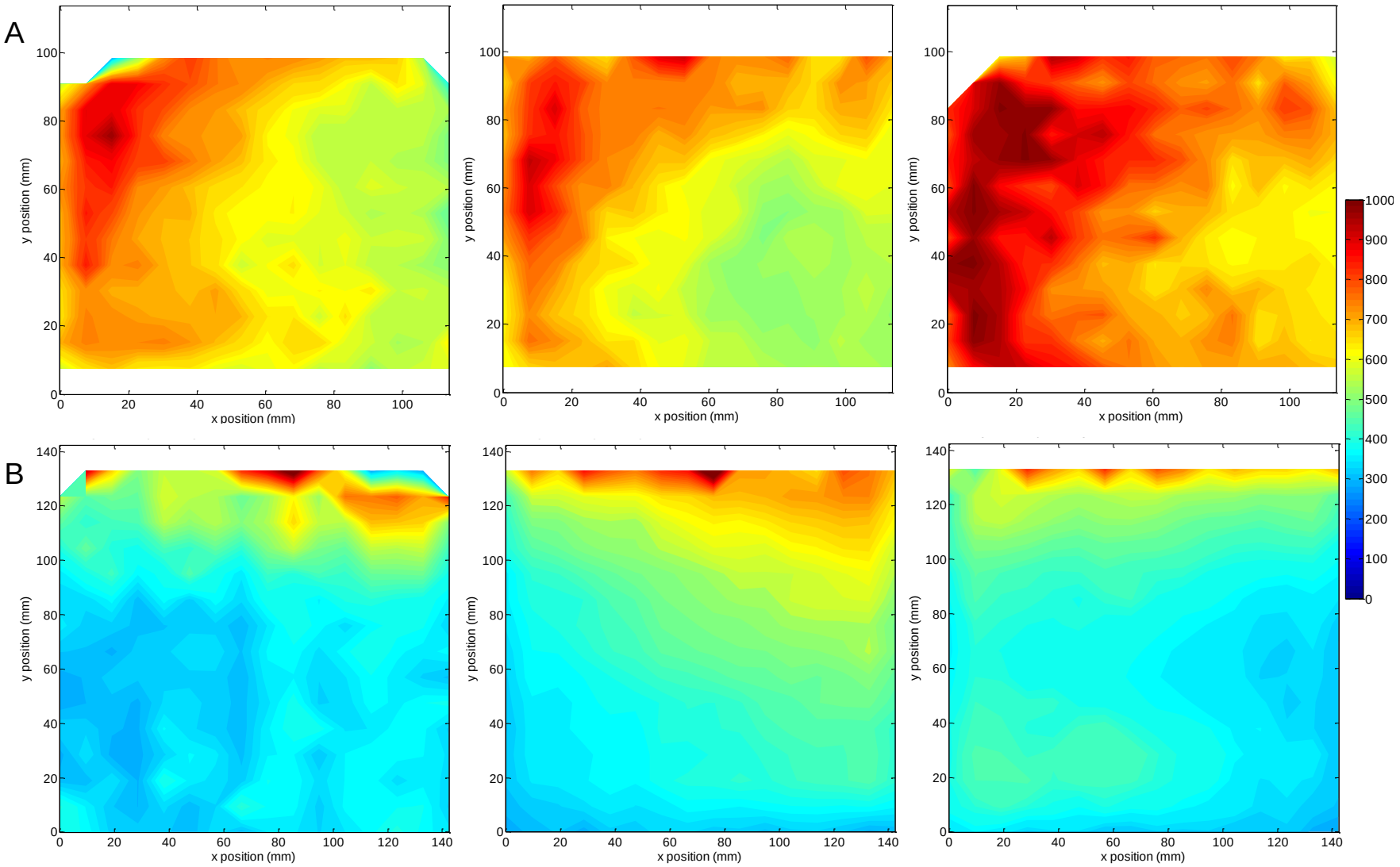

Figure 6.3: Mean Particle Size Contour Plots: (A) Position L and (B) Position H

6.3.1.2 Particle Size Distribution

Particle size distributions for each experimental condition in experimental position L are shown in Figure 6.4, and those for experimental position H in Figure 6.5. These size distributions are taken over the whole field of view and averaged over 4 seconds (2000 images) and presented as both mass fraction and number distributions. The D_{10}, D_{50} and D_{90} values (*i.e.* the percentage less than size), by mass, assuming spherical particles with projected area diameter as diameter of the sphere), are marked on each mass distribution plot. Comparison of the mass and number distribution plots for all experimental conditions show that by number, the smallest particle size possible is clearly the most common. The number of particles present decreases rapidly with increasing particle size for all experimental conditions. Direct comparison of between positions H and L for all experimental conditions show unsurprisingly that larger particle sizes occur more frequently at position L and the distribution of particle size here is much wider. The nature of distribution appears to change between experimental conditions in both locations, demonstrating that slurry and air flow rates influence particle size distribution.

The range of particle sizes in the lower position is much wider than would be expected looking at typical spray dried detergent powder product size distributions, where the maximum particle size is usually in the order of 1000-2000 μm (Huntington (2004), this may indicate that both particle growth through agglomeration and size reduction through attrition/abrasion and breakage occur during the spray drying process.

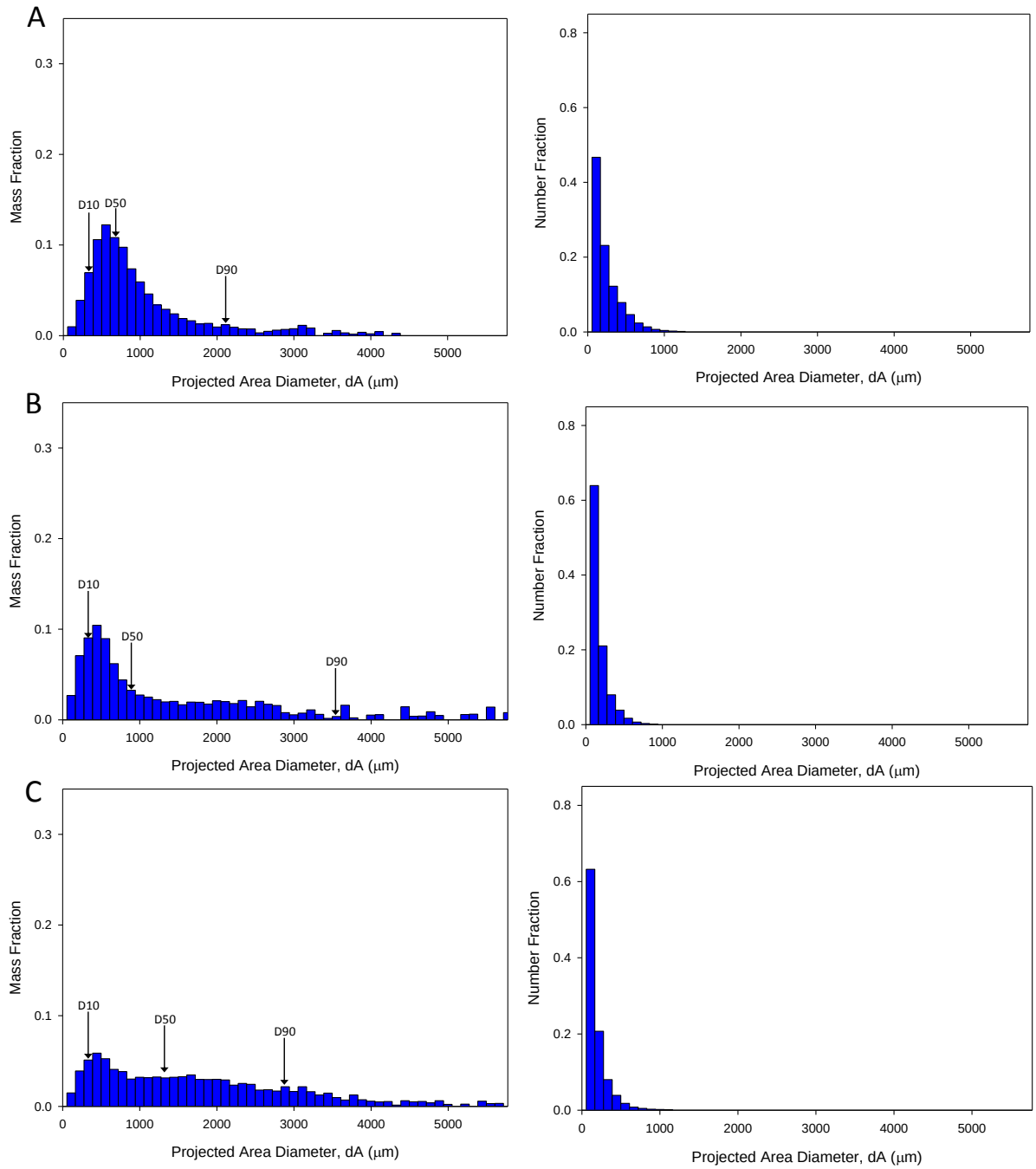

Figure 6.4: Particle size distributions position L (a) 1.0 relative slurry and 6000 kghr^{-1} air; (b) 1.200 relative slurry and 6000 kghr^{-1} air and (C) 1.2 relative slurry and 8000 kghr^{-1} air.

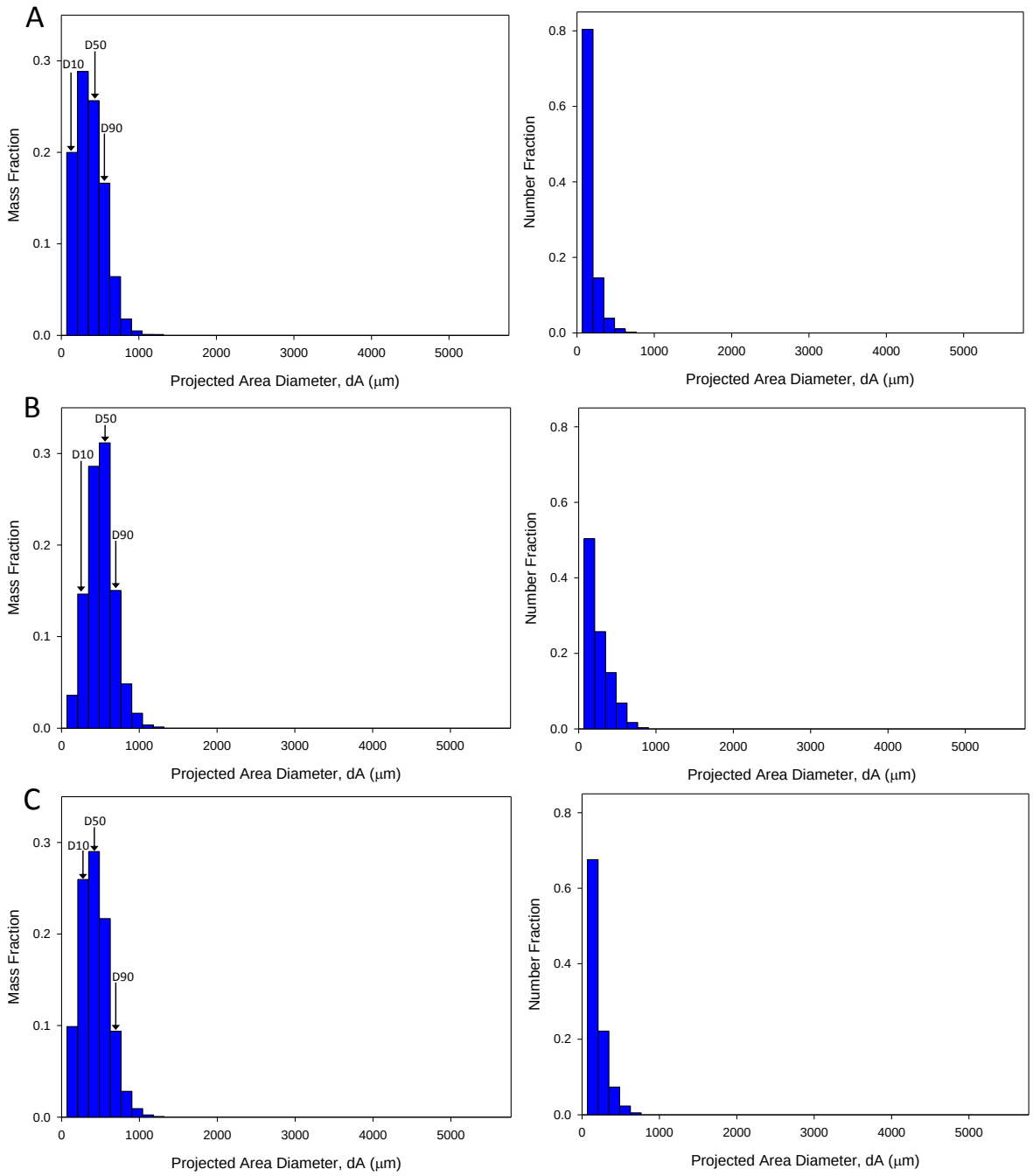

Figure 6.5: Particle size distributions position H (a) 1.0 relative slurry and 6000 kghr^{-1} air; (b) 1.200 relative slurry and 6000 kghr^{-1} air and (C) 1.2 relative slurry and 8000 kghr^{-1} air.

The results shown in Figure 6.4 and Figure 6.5 can also be explained in the context of particle agglomeration. These distributions all appear binominal or multinomial, suggesting that the mechanism that leads to particles forming is not a gradual growth of particles through agglomeration of particles entrained in flow, as would be captured by the "snap-shot" of images, but rather a sudden, discontinuous process of pieces of wall deposited material being re-entrained in the flow.

The amount of material deposited on the dryer walls, and therefore re-entrained in the air flow will increase over the period of dryer operation, and we would expect agglomeration through this mechanism to change accordingly. Therefore the times at which each experiment was done need to be considered. As this mechanism is only possible where wall deposition is observed, it is only applicable to position L, where the experiments were run as follows, 1.0 releative slurry flow rate, 6000 $kghr^{-1}$ air was run on one day, then on the next day, 1.2 releative slurry flow rate, 6000 $kghr^{-1}$ was run first, and then followed by 1.2 releative slurry flowrate, 8000 $kghr^{-1}$. The particle size distributions (Figure 6.4) show that the effect of duration of dryer operation may contribute to the amount of large particles observed in the distributions, as 1.0 releative slurry flow rate, 6000 $kghr^{-1}$ and 1.2 releative slurry flow rate, 6000 $kghr^{-1}$ appear similar, where as 1.2 releative slurry flow rate, 8000 $kghr^{-1}$, which was conducted after the longest period of operation, shows a wider distribution of larger particle sizes.

6.3.2 Particle Number Concentration, C

The number of particles per unit volume, C (calculated based on the volume of the lasersheet, §D.3) displayed as a function of radial position from the dryer wall is shown in

Figure 6.6 and can be seen to vary as a function of slurry and air flow rate and location in the dryer.

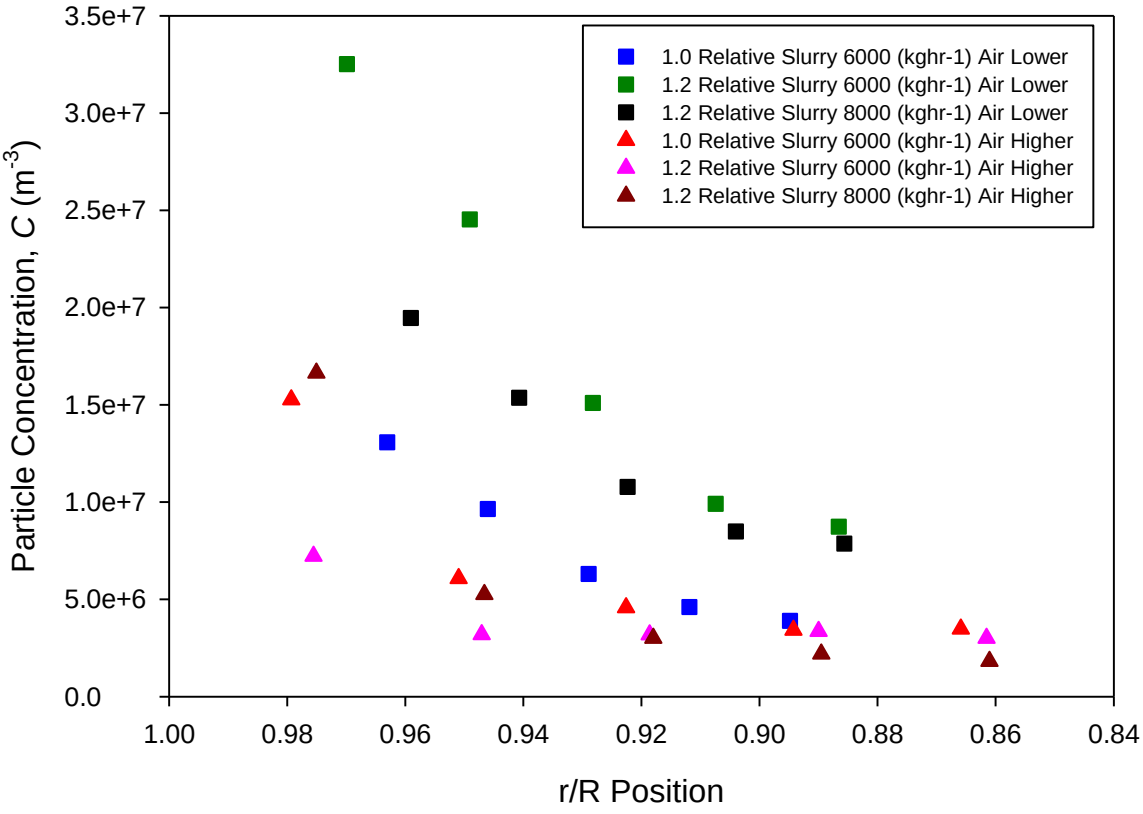

Figure 6.6: Particle Concentration, *C*, as a Function of Radial Position

The largest values of C are, unsurprisingly, observed for the higher slurry flow rates at Position L. The concentration of particles for lower slurry flow rate in the lower position is comparable to the concentrations seen in the higher position. The number of particles present is of course a function of slurry flow rate and particle size (§ 6.3.1), *i.e.* for the lower position the particles are bigger, so there is more slurry contained in a similar number of particles than in the higher position. The concentration of particles decreases with increasing radial distance from the dryer wall, highlighting again the effect of the swirling air flow on particle movement as its centripetal forces "throw" particles out towards the dryer walls.

Figure 6.7 shows contour plots of particle concentration over area studied at each experimental condition in each position. Similarly to Figure 6.9, asymmetrical patterns are seen in position L, as particle concentration changes in both the radial and tangential directions. The hypothesis for this described above also applies here.

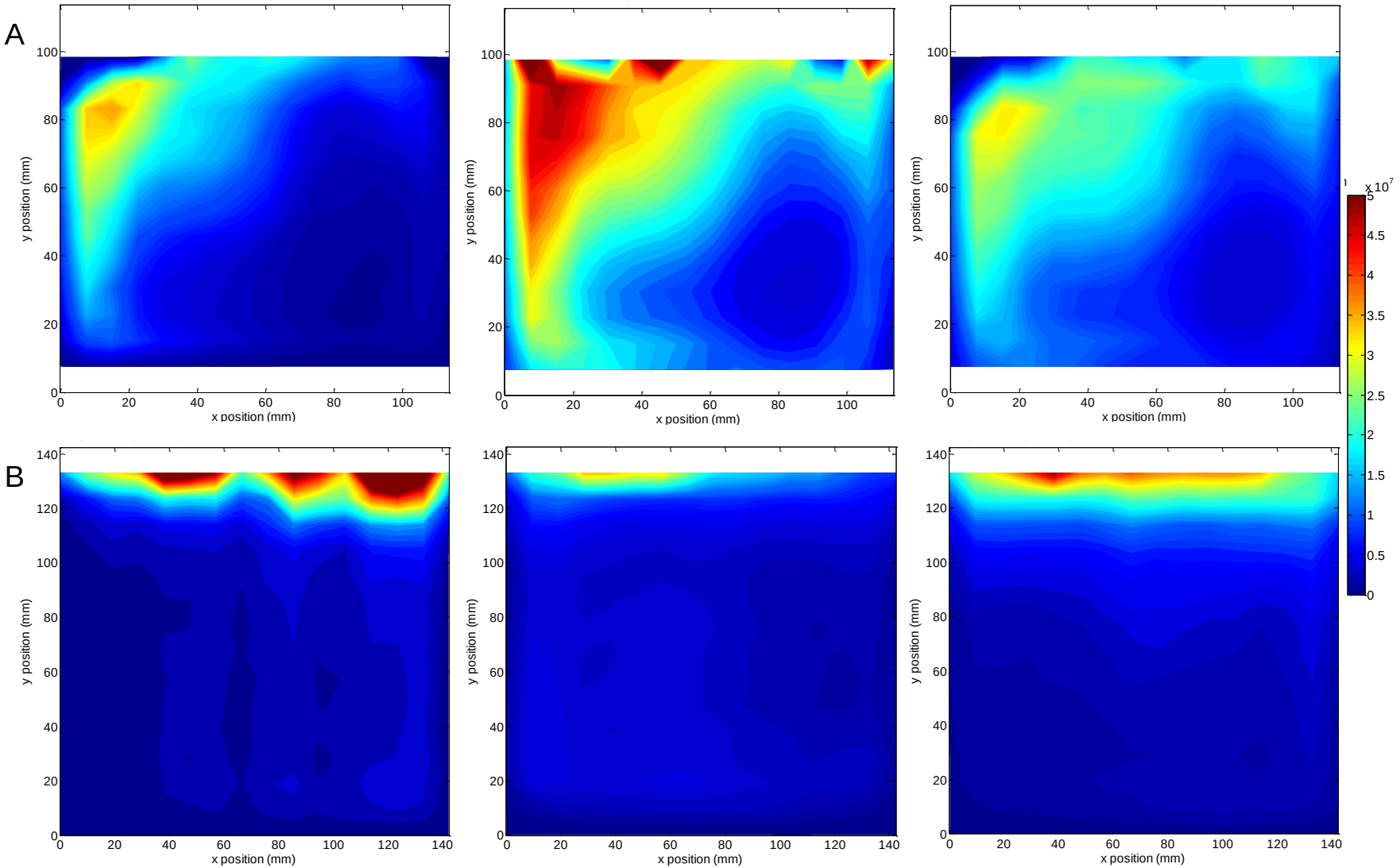

Figure 6.7: Particle Concentration Contour Plots: (A) Position L and (B) Position H

6.3.3 Particle Volume Fraction

Particle volume fractions were calculated by taking the projected area diameter of each particle, d_A to be a spherical equivalent diameter on the basis of volume, d_V, hence $V = \pi d_V^{\,3}/6$. These data were then summed for that area of the image and divided by the volume of the area of the image. This data is shown as a function of radial position from the dryer wall in Figure 6.8.

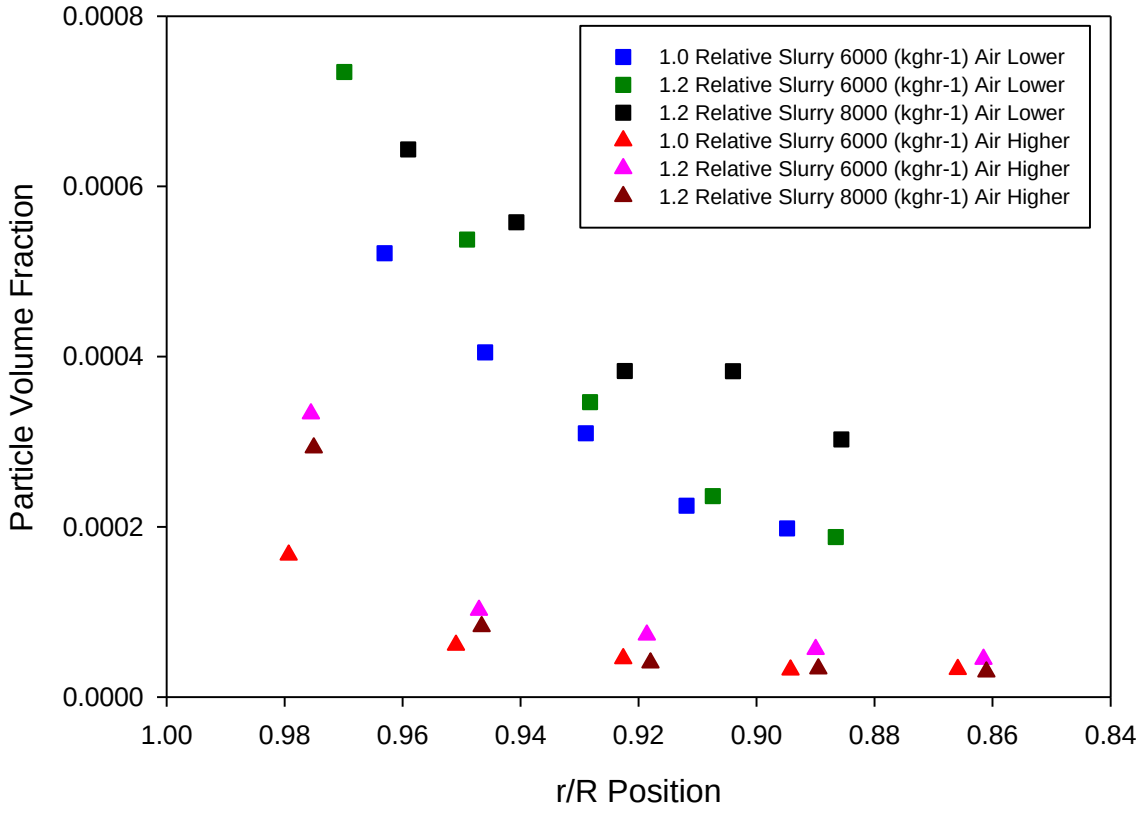

Figure 6.8: Particle Volume Fraction as a Function of Radial Position

Particle volume fraction can be seen to vary as a function of slurry and air flow rate and location in the dryer. The largest particle volume fractions are seen in position L, as would be expected with the majority of particle heading downwards from the nozzle. In this lower

position both slurry and air flow rates appear to affect particle volume fraction, which appears to decrease linearly with distance from the dryer wall.

Lower particle volume fractions are observed in position H (above the nozzle), with less effect of slurry and air flow rates seen apart from in the area closest to the dryer wall, where slurry rate seems to significantly increase particle volume fraction. The decrease in particle volume fraction with distance from the dryer wall seems to be less dramatic than that seen in position L, with a rapid decrease close to the wall before the rate of change slows with increasing distance from the wall.

Contour plots of particle volume fraction over the areas studied are shown in Figure 6.9, which demonstrate all of the trends discussed above and observed in Figure 6.8. As with the previous two particle dynamics parameters, asymmetrical distribution of values in position L can be observed and again the hypothesis for this described above applies here too.

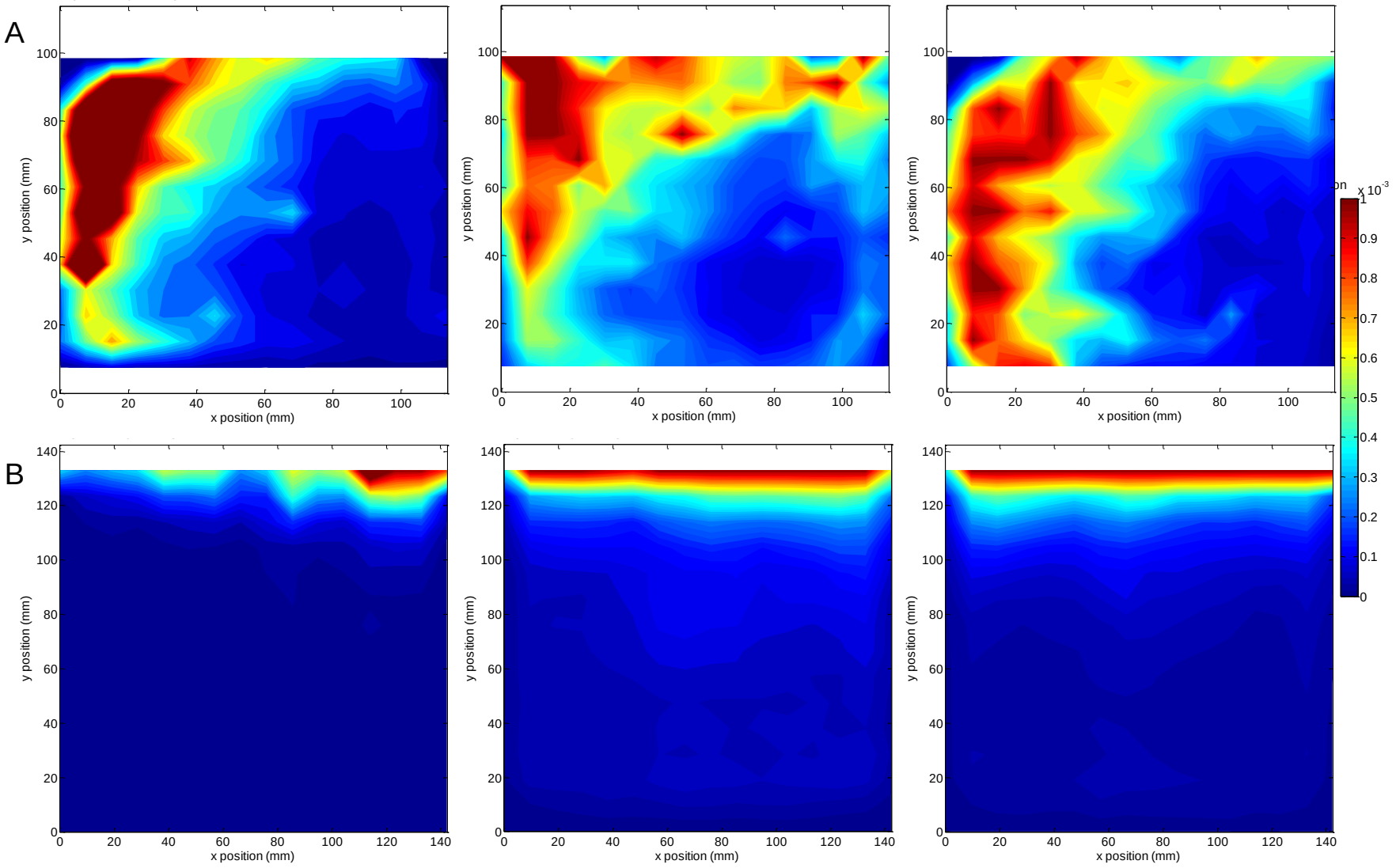

Figure 6.9: Particle Volume Fraction Contour Plots: (A) Position L and (B) Position H

6.3.4 Particle Flow Fields

PIV cross-correlation (§D.3) was used to obtain time-averaged particle velocity fields, which are shown in Figure 6.10. Particle velocities in Position H are much larger than those in Position L. This suggests that two different flow regimes exist within the dryer, depending on position relative to the spray nozzle. Simplistically these two regimes can be described as a flow containing a higher loading of larger particles, which move more slowly in the horizontal plane (as measured here) below the nozzle, and a sparser flow of smaller particles moving faster in the horizontal plane above the nozzle. A further feature distinguishing the two regimes is the direction of flow observed: above the nozzle all particle velocities seem to be tangential, moving parallel to the dryer wall, below the nozzle in position L, the direction of particle velocities appear to be less well defined. Although tangential velocity still seems to dominate here, all three experimental conditions show more deviation from the strictly tangential flow above the nozzle, this could be an indication of more turbulent air flow patterns in this position or an effect of extra turbulence caused by proximity to the nozzle.

In position L velocities are seen to vary between 0.0 and 0.2 ms^{-1}, the effect of slurry and air flow rates appears to be small, with the 1.0 releative slurry flow rate and the 6000 $kghr^{-1}$ air flow rate experimental condition showing slightly larger velocities than the other two experimental conditions. On the whole, all velocities in the horizontal plane, in this region appear to be much lower than those of air flow alone, as shown in Figure 5.5 (§5.3). Although particles would be expected to have lower velocities than air, the fact the velocities differ by an order of magnitude is unexpected and may be explained by considering the motion of particles in the axial direction. The reason behind this discrepancy

may lie in both the nature of the particles and the proximity of the experimental position to the nozzle. Particles which have just left the nozzle will have experienced little drying relative to those which have been inside the dryer for a longer period, and will be contain lots of water in a solid structure, making them much denser than dried and puffed particles. Therefore they are more likely to fall under the influence of gravity before becoming entrained in the swirling air flow. In addition to the nature of the particles, the movement of particles in this area of the dryer may be heavily influenced by momentum they obtain from atomisation through the nozzle, this momentum is likely to result in the velocity in the axial direction, and could therefore explain the lack of velocity observed in the horizontal plane. These observations may be a feature of the location used for the experiment, and if images were captured further away from the nozzle, particles may demonstrate higher velocities in the horizontal plane as particles becoming increasingly entrained in the air flow. This effect appears to be particularly pronounced for the low air flow rate, high slurry flow rate in position L where the particle velocities appear to be the smallest and in the most variety of scattered directions. This could be explained if a point is reached where the amount of air flowing through the dryer isn't sufficient to entrain the amount of slurry atomisied into particles. This could also explain the large standard deviation in particle velocities (Figure 6.12) observed for this condition.

Another possible explanation for the observation of smaller than expected velocities in the horizontal plane could be an artefact of the measurement and analysis technique applied here, PIV only captures average particle velocities and therefore could filter out individual particle velocities and result in a small average velocity (especially if particles in the same

interrogation spot are moving in opposite directions). Issues with special and temporal resolutions could limit the ability of the technique used here to detect changes in direction over time and also filter out the smallest levels of variation in particle direction.

Velocities in both locations can be seen to be constant as a function of radial distance from the wall, with the exception of the area close to the dryer wall (top of plots) which may indicate the presence of a boundary layer in the airflow, which slows particles down. This could also be an artefact of the measurement technique as is seen on a smaller scale around all edges of the plot.

Velocities in position H were found to vary between 0.2 and 0.4 ms^{-1}, depending on dryer operating conditions, showing that in the sparser regime above the nozzle, the effect of air flow and also of slurry flow rate, and therefore particle loading inside the dryer, influence how particles move.

In order to further understand the results presented here, the statistics of the data produced have been examined. Figure 6.11 shows the number of velocity vectors generated during cross correlation, *i.e.* the number of data points used to calculate the time averaged velocity in each interrogation spot. The number of vectors is plotted as the colour fill on the contour, where blue represents zero, *i.e.* no velocity vectors were successfully generated through cross-correlation and where red represents 2000, *i.e.* a velocity vector was suitably generated for that spot with every pair of images processed. The velocity vectors of the particle flow field are plotted over this to allow comparison between the number of vectors generated and the velocity calculated in each spot. Examining the number of velocity vectors

generated in each integration spot (Figure 6.11) reveals that there is a close link between the number of vectors generated and particle number concentration (Figure 6.7).

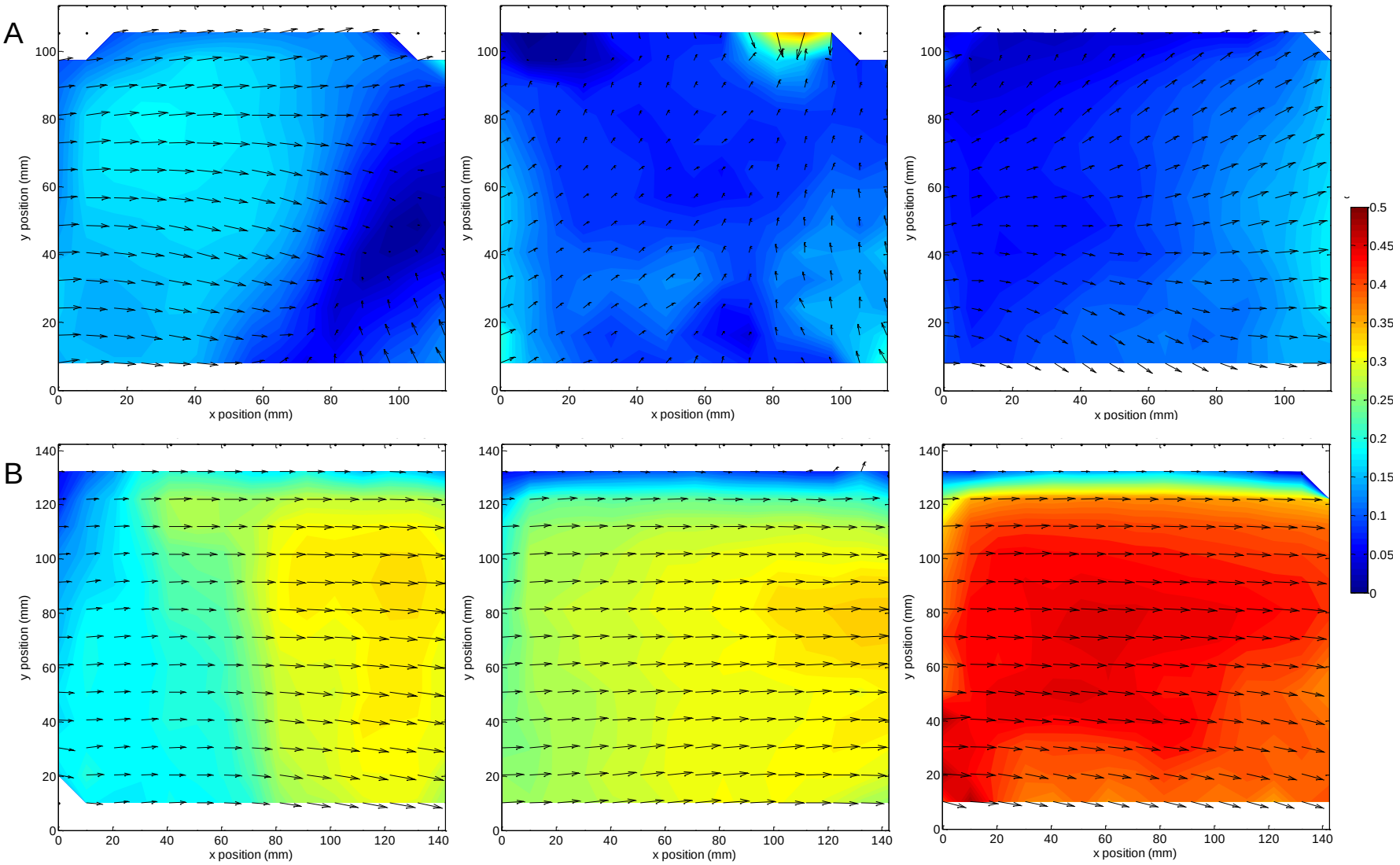

Figure 6.10: Time Average Particle Flow Fields (ms^{-1}): (A) Position L and (B) Position H

This pattern is highlighted in position L where both particle number concentration and the number of velocity vectors generated are at a maximum close to the wall and in an asymmetric fashion towards the left hand side of the image and in position H where the number of vectors and particle number concentration are at a maximum close to the wall. The link between the number of vectors generated and the velocity calculated for each spot appears to be unclear, with one dataset showing a clear link between maximum velocities and the highest number of vectors generated (position L (below the nozzle) the 1.0 releative slurry flow rate and 6000 $kghr^{-1}$ air), and all other data sets display velocities which appear independent of the number of vectors generated. The apparent independence of velocities from the number of vectors generated allows confidence in the data generated as it demonstrates the velocities calculated here are not a function of the technique and analysis applied. Although results produced in areas with more vectors generated are more likely to be reliable than those produced in areas with fewer vectors generated, as would be expected. This leads to the conclusion that, as a general point, velocity data plotted in areas closer to the wall are more reliable than those further away from the wall.

To further understand the results presented here, the standard deviation of the time averaged particle velocities are plotted with the actual velocity vectors over them in Figure 6.12. The standard deviations presented here are in ms^{-1} and show values similar to the velocity magnitude in Figure 6.10, indicating that there is large variation in particle velocities over the period of measurement, particularly for position L (below the nozzle) the 1.2 releative slurry flow rate and 6000 $kghr^{-1}$ air conditions.

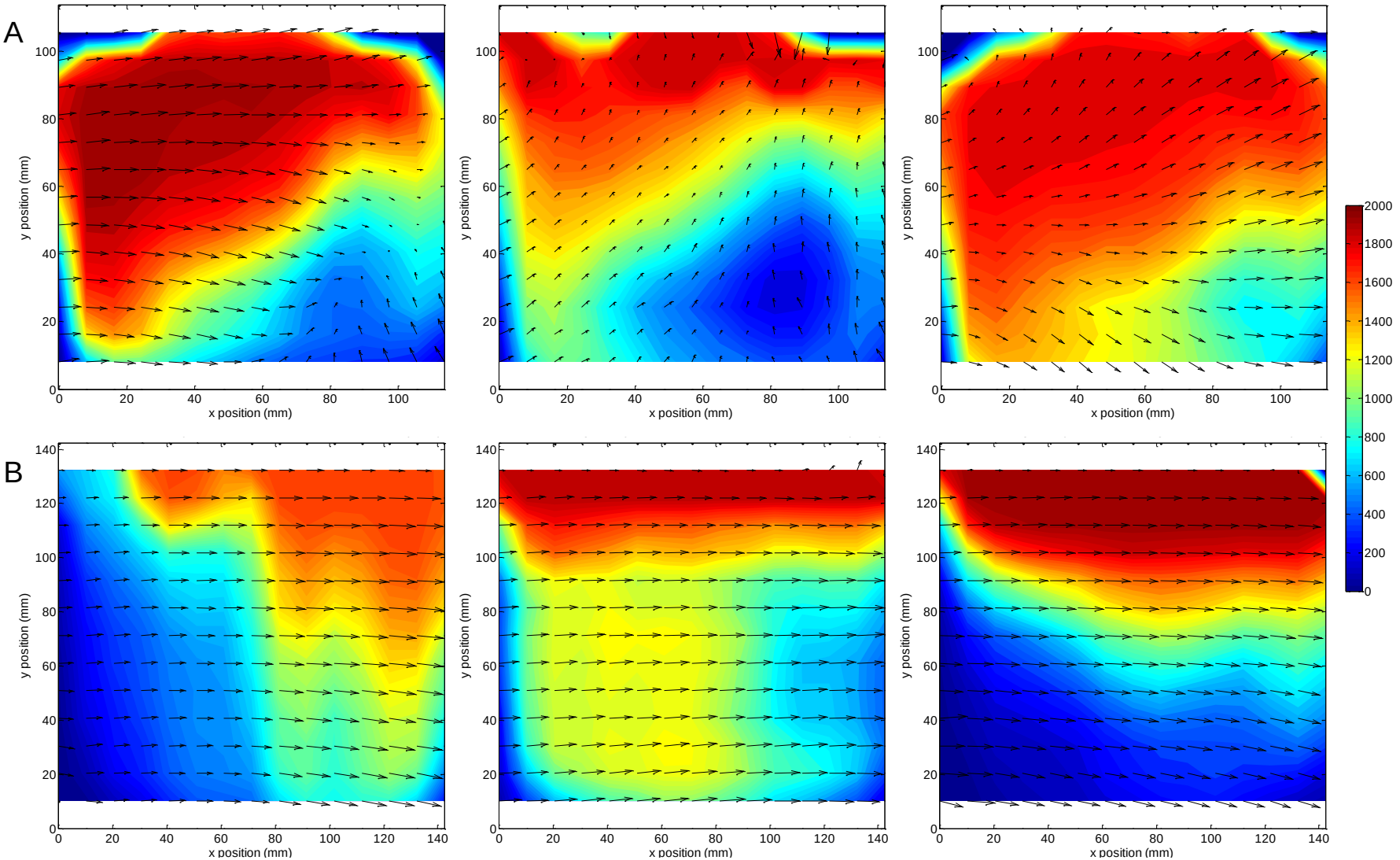

Figure 6.11: Velocity Vectors Generated per Interrogation Spot for Particle Flow Fields: (A) Position L and (B) Position

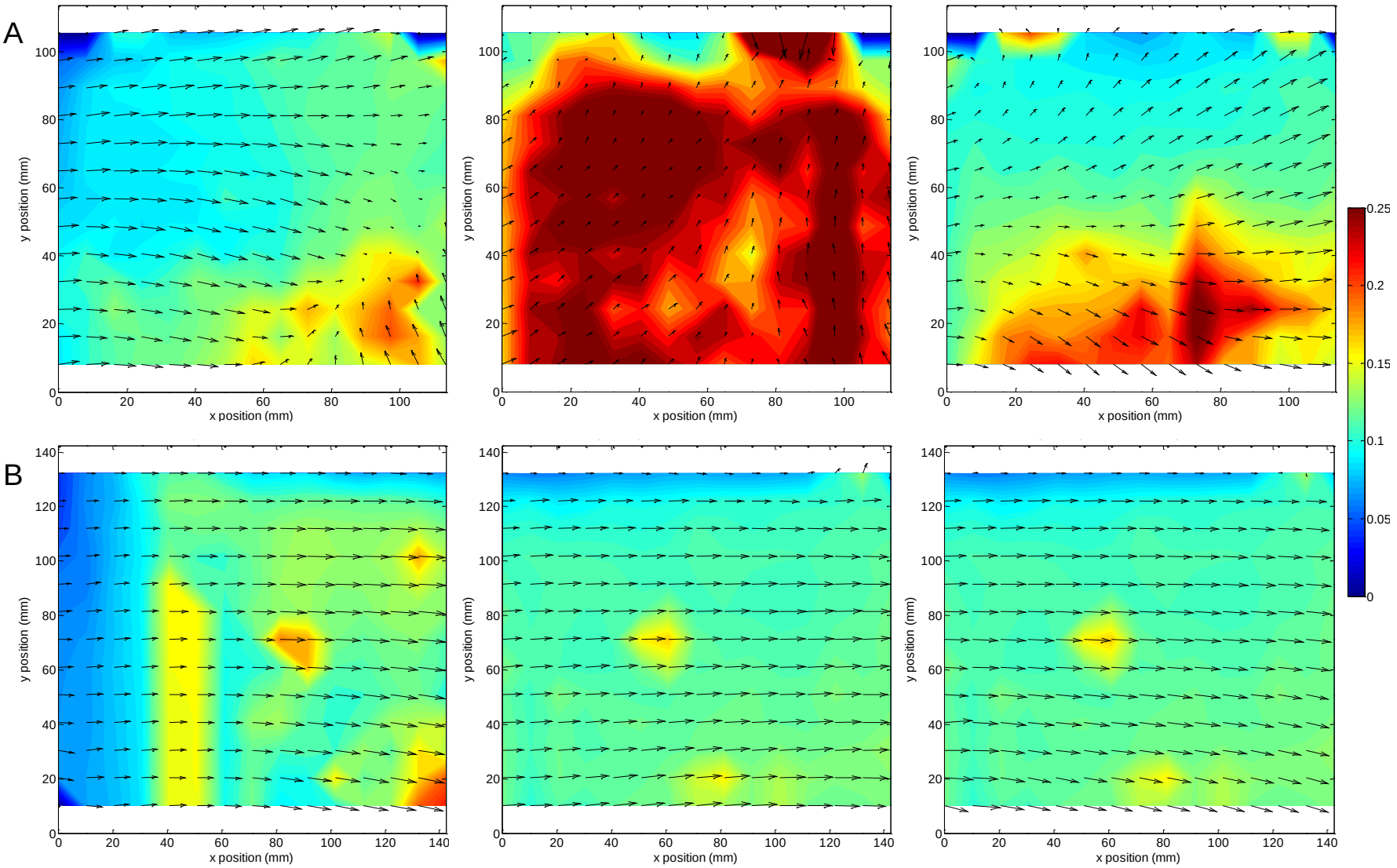

Figure 6.12: Velocity Magnitude Standard Deviation for Particle Flow Fields (ms^{-1}): (A) Position L and (B) Position H

6.4 Results: Time Dependent Particle Dynamics

Air flows inside spray dryers are widely reported to be time-dependent (§2.5.4.3). As air flow patterns are known to largely determine particle movement inside spray dryers, it can therefore be assumed that particle dynamics inside spray dryers undergo changes on similar time scales. The dynamics of the flows are investigated by plotting mean particle size, particle number concentration and particle volume fraction as a function of time. Particle velocity flow fields are also plotted as a function of time.

6.4.1 Time Dependent Particle Size, Number Concentration and Volume Fraction

Mean particle diameter (blue), number concentration (red) and particle volume fraction (green) are plotted as a function of time for a period of 4 seconds for the 1.0 releative slurry flowrate, 6000 $kghr^{-1}$ air experimental conditions for both experimental positions in Figure 6.13 and Figure 6.14. These plots reveal the time dependent behaviour of all particle parameters in the two different flow regimes inside the dryer. As would be expected, the values of mean particle diameter and particle volume fraction are much larger in position L and display much more variation. The number concentration of particles is more comparable between the two experimental positions, although the lower position shows slightly larger values and more frequent variation.

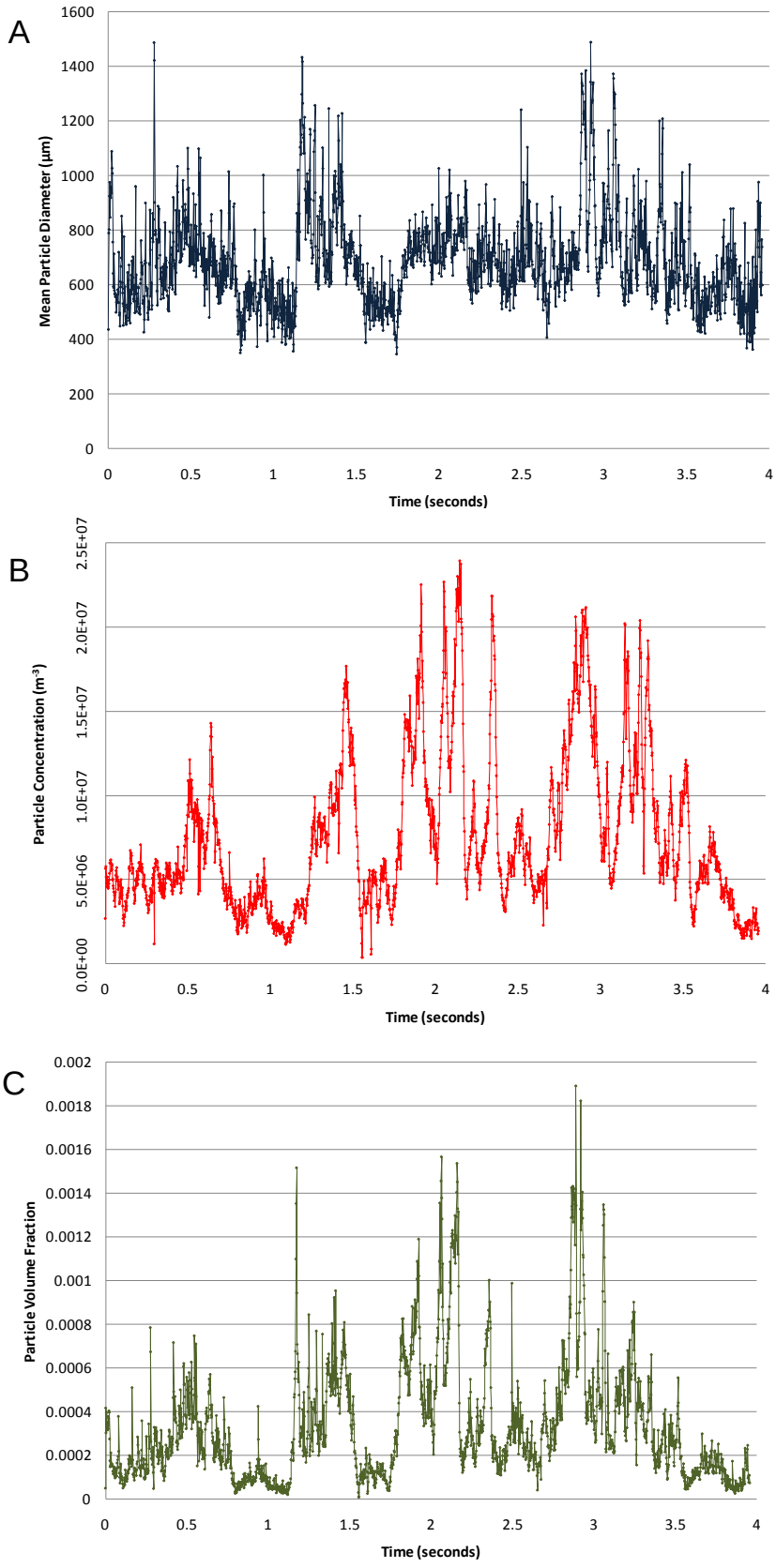

Figure 6.13: Time Dependent Particle Size (A), Concentration (B) and Volume Fraction (C): Position L

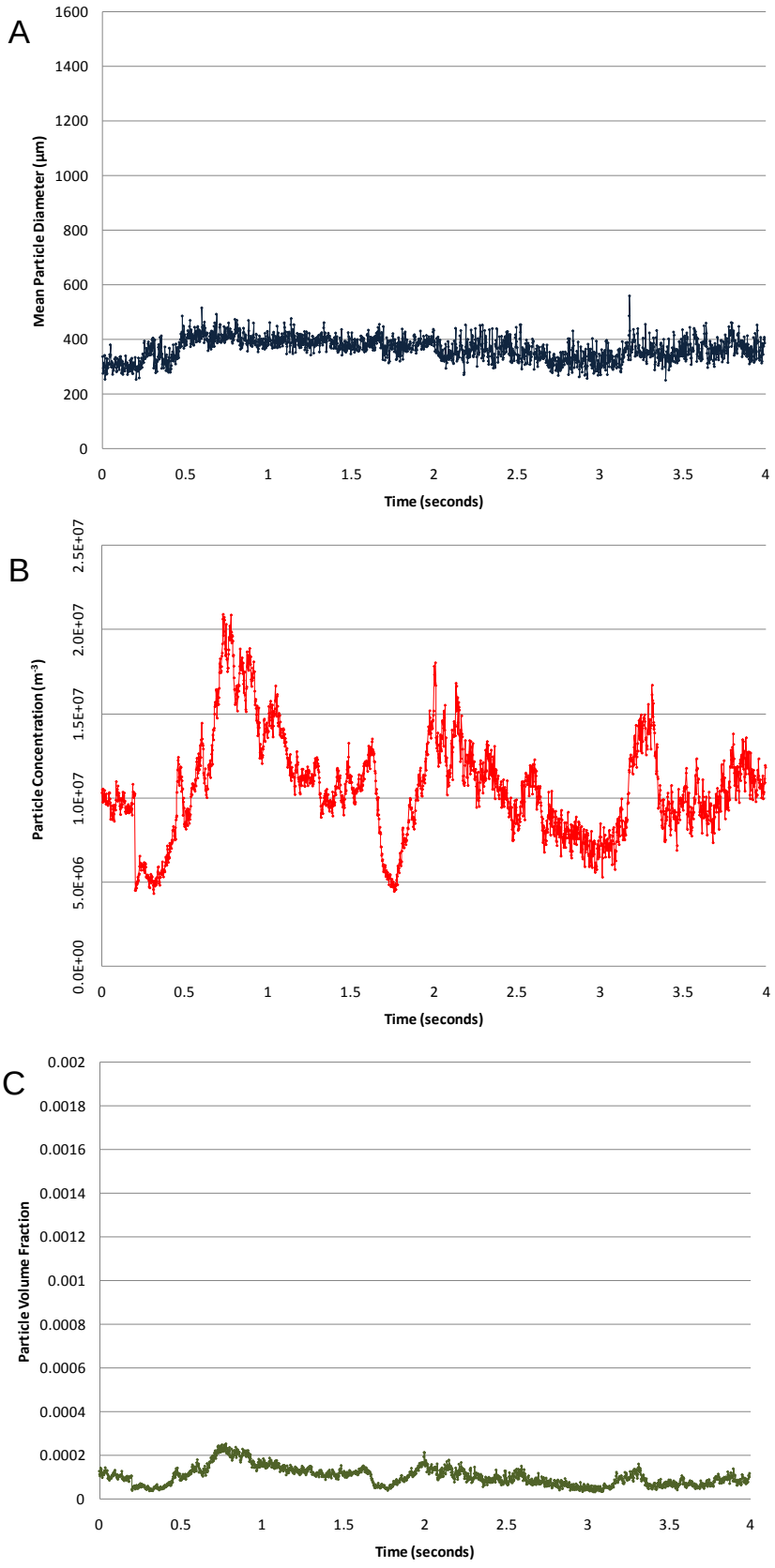

Figure 6.14: Time Dependent Particle Size (A), Concentration (B) and Volume Fraction (C): Position H

6.4.2 Time Dependent Particle Flow Fields

In order to examine particle velocity flow fields as a function of time, a series of flow fields have been produced for small increments of the time period observed in these experiments. The data sets presented in this chapter are for measurements over a period of 4 seconds, which was divided into 10 periods of 0.4 seconds. The sampling rate was 500 Hz, giving 200 image pairs per increment. This kind of analysis greatly reduces number of vectors used to calculate each velocity and therefore brings in some statistical error, but allows time dependent behaviour over time scales of less than a second to be visualised.

Figure 6.15 shows velocity flow fields for increments of 0.4 seconds which allows the variation in velocity magnitude and direction to be observed throughout the 4 second measurement period. The largest values of velocity magnitude seen here appear for small areas of the image for one or two increments of the data and are much larger than the time averaged velocity (Figure 6.10). This variation in velocity magnitude and direction indicates a flow which is constantly changing, and can therefore assumed to be linked to turbulent air flow, and possibly transient behaviour, which would be expected to vary over a time scale of several seconds (§5.5.2). The flow fields shown for position H in Figure 6.16 reveal smaller variations in velocity direction with time, and a gradual increase in values of velocity magnitude over the final 5 increments (2 seconds) in the right hand side of the plot. This gradual increase indicates variation of particle velocities on a longer time scale than seen for position L. The lack of variation in particle velocity direction shows a flow which changes a lot less than position L and this could either be a function of particle dynamics or of the less turbulent air flow observed in position H (§5.4). These differences again indicate the

presence of two particle flow regimes within detergent spray dryers, depending on axial position in relation to the nozzle.

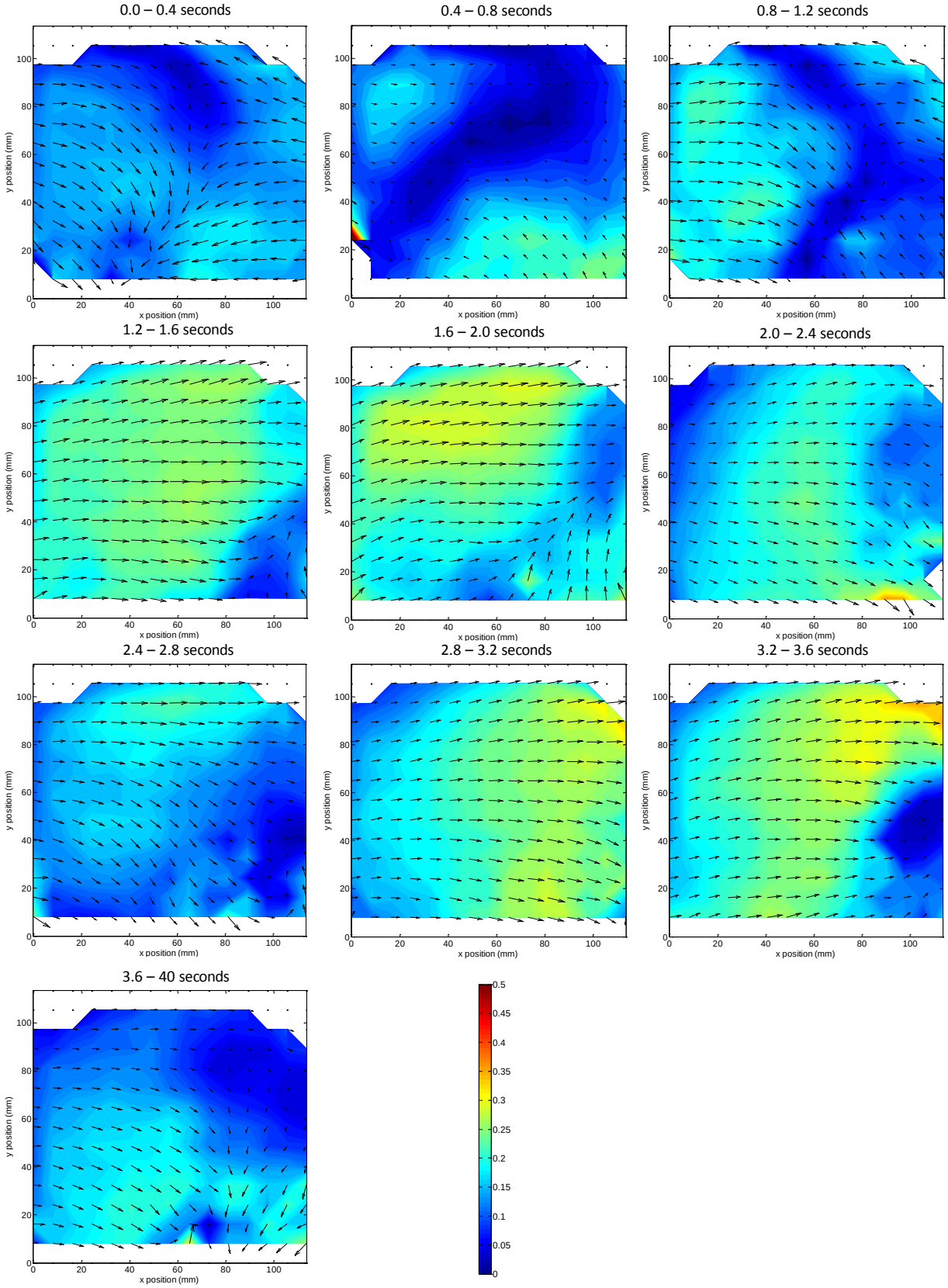

Figure 6.15: Time Dependent Particle Velocity Fields (ms^{-1}): Position L

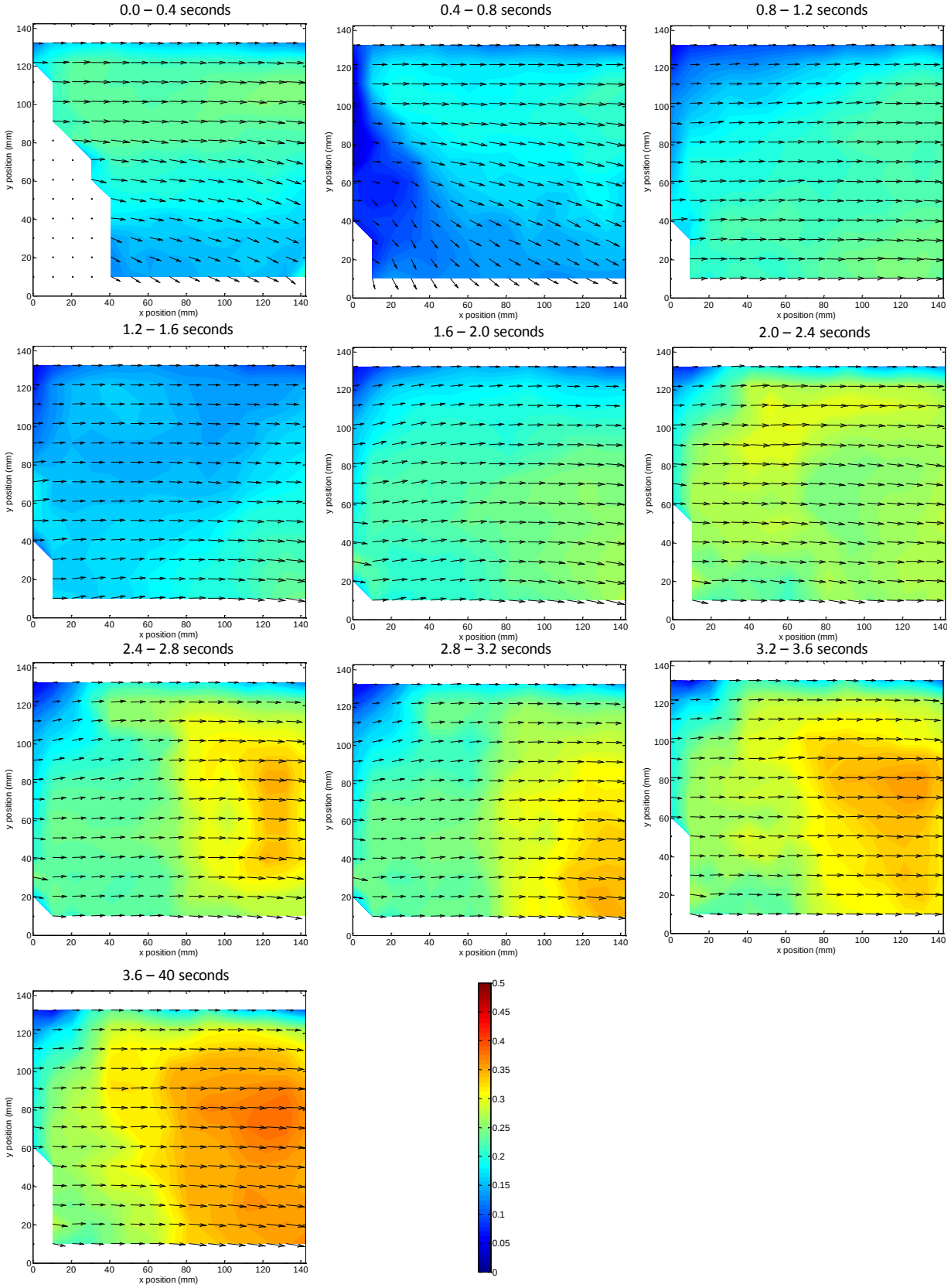

Figure 6.16: Time Dependent Particle Velocity Fields (ms^{-1}): Position H

6.5 Conclusions

Particle dynamics inside the spray dryer were studied through the use of PIV to capture images. A method for thresholding images was developed (Appendix D), such that binary images could be obtained containing only particles contained with the laser sheet. Image analysis and PIV cross-correlation were used to obtain data on particle size, concentration and volume fraction as a function of position within the dryer (both axial and radial) and of slurry and air flow rates, on both a time averaged and time-dependent basis.

Particle size, concentration, volume fraction and velocity magnitude and directions all vary with dryer operating conditions and position within the dryer. Two different flow regimes exist inside the dryer, below the nozzle the flow contains a higher loading of larger particles, which move more slowly in the horizontal plane (as measured here), in a wide range of directions, below the nozzle, whilst above the nozzle there is a sparser flow of smaller particles moving faster in the horizontal plane, consistently parallel to the wall.

The effect of slurry flow rate on particle size, concentration and volume fraction has been linked to changes in atomisation, agglomeration and the distribution of particles inside the dryer. These effects are more pronounced in position L, below the nozzle, where the majority of particles travel. In the higher position, above the nozzle, only particles sufficiently entrained in the air flow to be carried upwards in the dryer are observed, meaning the effect of atomisation and agglomeration are less prominent. One feature of these results is an unexpected asymmetric distribution of particle size, concentration and volume fraction in the tangential direction observed in experiments in position L. Two

possible reasons are; disruption in air flows caused by the mirror box and re-entrainment of deposited material on the mirror box.

Flow fields of particle velocities show variation in both velocity magnitude and direction with slurry and air flow rates and position within the dryer. The largest velocities are seen in position H, where increases in slurry and air flow rates result in larger velocity magnitude values, with velocity direction remaining constant, parallel to the wall. In position L velocity magnitude values are lower and change less much less with slurry and air flow rates, the direction of particle velocities appear to be more variable in this position.

In both flow regimes, above and below the nozzle, particle size, concentration and volume fraction have all been shown to vary with time. Flow fields produced from particle velocities have also been shown to vary with time, with velocity magnitude varying more above the nozzle and velocity direction varying more below the nozzle.

One key conclusion into time dependence is to highlight the need to select the correct temporal resolution for all experiments involving particle dynamics in. This has to be considered when reviewing the results presented in this chapter, and could explain some of the variation seen in results.

Chapter 7 – Particle Characterisation and Impact Behaviour

7.1 Introduction

The impact behaviour leading to particle breakage, restitution or more critically, in the context of this work, deposition of particles, is greatly affected by their physical and mechanical properties. The purpose of this Chapter is to present the results of experiments conducted to characterise the physical and mechanical properties of detergent granules/powders and also their impact behaviour. Variation in physical and mechanical properties was achieved by using four different detergent formulations. The first part of the Chapter presents characterisation of the physical and mechanical properties of these formulations. This allows their effect to be interpreted in the second part of the Chapter where the impact behaviour of the four formulations is examined. The effect of both particle (particle size and formulation, *i.e.* changing physical and mechanical properties) and impact properties (impact velocity and impact angle) on particle breakage and restitution, were studied.

7.2 Experimental

7.2.1 Particle Characterisation Experiments

Values of the properties listed in Table 7.1 were obtained through a wide range of techniques, some from standard measurements and others from methods developed during this project (§3.7). For the techniques which were either developed during this work, or are exclusive to the company, a detailed description of the principles behind them is given.

Table 7.1: Physical and Mechanical Particle Properties Measured

Property		Technique
Particle Shape and Structure		Scanning Electron Microscope (SEM)
Hydroscopic Behaviour	Moisture Content	Infrared mass loss
	Equilibrium Relative Humidty (eRH)	Water activity equilibrium
Density	Envelope Density	Quasi- fluid diaplacement
	Skeletal Density	Helium gas pycnometer
Mechanical Properties	Confined Yield Stress	Confined compression
	Confined Join Stress	
	Unconfined Young's Modulus	Unconfined compression
	Unconfined Yield Stress	

The effect of particle size and formulation were studied for the properties listed in Table 7.1. The formulations studied here are summarised in Table 3.2 and identified as 'HH', 'HL', 'LH', and 'LL' depending on the relative levels of SiO_2 and LAS in the formulation. Changing the levels of these components would be expected to cause the following effects (§2.2 and §3.3.3): according to Bayly (2006), particles with a high level of LAS will be paste-like, sticky, soft and therefore easily deformable. Sodium silicate increases the strength of particles, such that particles high in silicate will be strong yet brittle. Samples of each of these powders were sieved into five different particle size ranges, namely, 150-250, 250-425, 425-710, 710-1180 and 1180-1800 micrometres (§ 3.3.3).

Table 7.2: Formulations Overview

Component Function	Component	Fraction by mass (wt)			
		High SiO_2 High LAS (HH)	**High SiO_2 Low LAS (HL)**	**Low SiO_2 High LAS (LH)**	**Low SiO_2 Low LAS (LL)**
Surfactant	LAS (linear Alkylbenzene-Sulphonate)	23.0%	5.0%	30.0%	5.0%
Polymer	polycarboxylate	2.0%	2.0%	2.0%	2.0%
Builders	Phosphate	20.0%	20.0%	20.0%	20.0%
	Sodium Silicate	14.4%	20.0%	0.0%	0.0%
	Sodium Sulphate	30.4%	42.8%	37.8%	62.8%
Others (minor components)		3.2%	3.2%	3.2%	3.2%
Additional Water (processing aid)		7.0%	7.0%	7.0%	7.0%

7.2.2 Particle Impacts Experiments

Particles were fired into a steel target to mimic their impact on the dryer walls using a Ghadiri design (Ahmadian (2008) and Samimi *et al.* (2003)) particle impact rig (§3.6.1). The impact velocity of particles was controlled by adjusting the air pressure used to accelerate particles in the impact rig (§3.6.1). Four different impact targets (90°, 60°, 45° and 30°) were used to allow the impact angle of particles to be changed. High speed video footage of the target was taken so that the impact behaviour of the particles could be observed. The images captured were analysed to obtain particle velocities and breakage details so that impact behaviour could be expressed quantitatively.

To enable the effect of formulation (and the resulting physical and mechanical properties of granules) on impact behaviour to be studied, the four different formulations summarised in Table 3.2 were used and as before, samples of each of these powders were sieved into five different particle size ranges, namely, 150-250, 250-425, 425-710, 710-1180 and 1180-1800 micrometres (§3.3.3), so that the effect of particle size could be also be studied. Statisitcal analysis of these results was conducted using JMP software (§3.6.3). Both correlation and response modelling was undertaken to aid understanding of the results from these experiments. The results from this analysis are presented in Appendix E.

7.3 Particle Characterisation Results

The results from experiments to characterise the physical and mechanical properties of the four formulations are shown in this section.

7.3.1 Effect of Formulation on Particle Shape and Structure

The sieved samples were examined using the Hitachi TM-1000 table top electron microscope (§3.7.1.1). Images of each sieve cut for each formulation are displayed in Figure 7.1 (HH), Figure 7.2 (HL), Figure 7.3 (LH) and Figure 4.2 (LL). All of these images were taken with a magnification of x 80. The images were selected from extensive range to ensure they were representative.

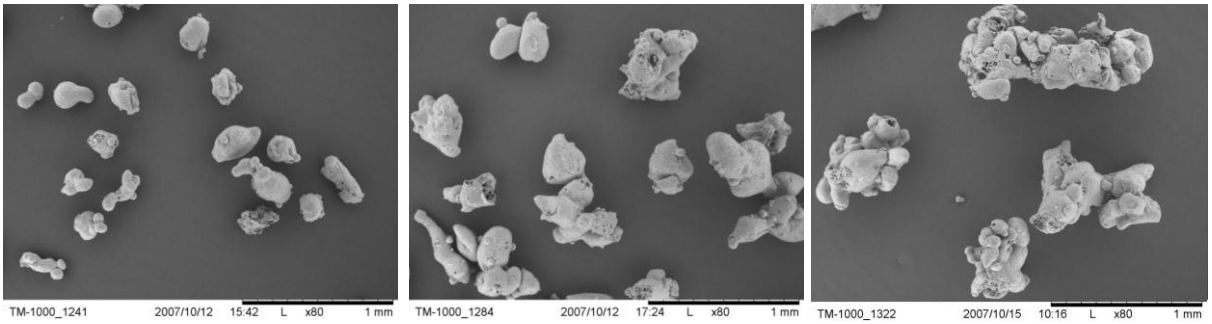

150-250 microns 250-425 microns 425-710 microns

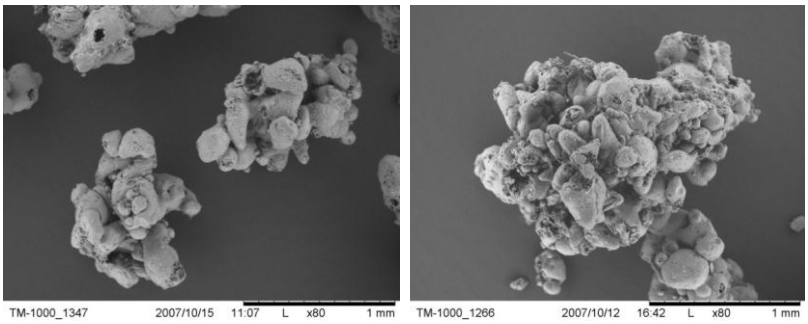

710-1180 microns 1180-1800 microns

Figure 7.1: SEM images of HH formulation for each sieve cut

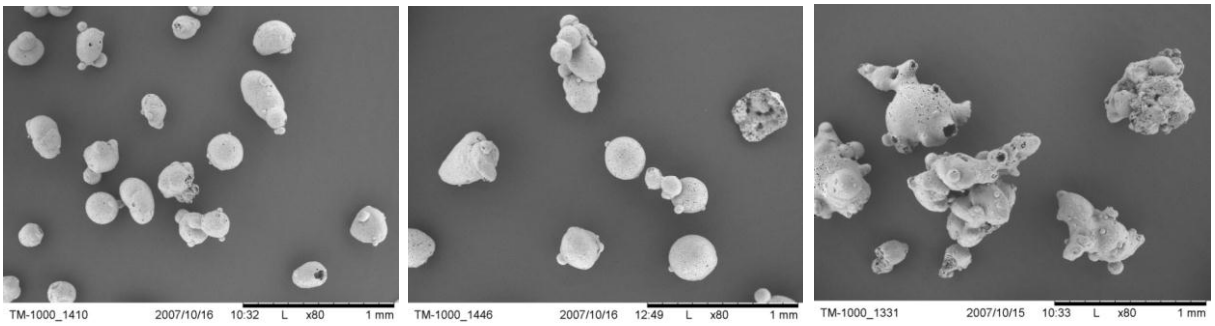

150-250 microns 250-425 microns 425-710 microns

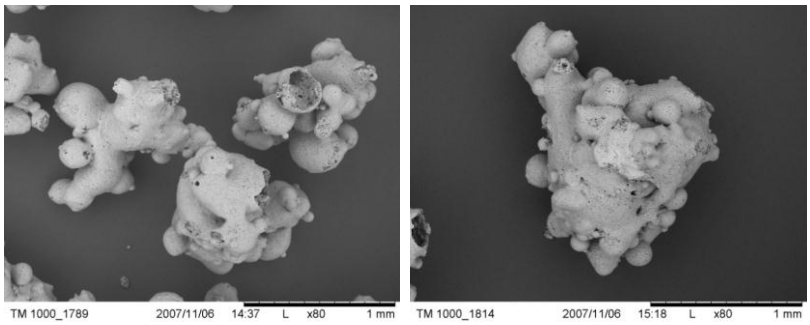

710-1180 microns 1180-1800 microns

Figure 7.2: SEM images of HL formulation for each sieve cut

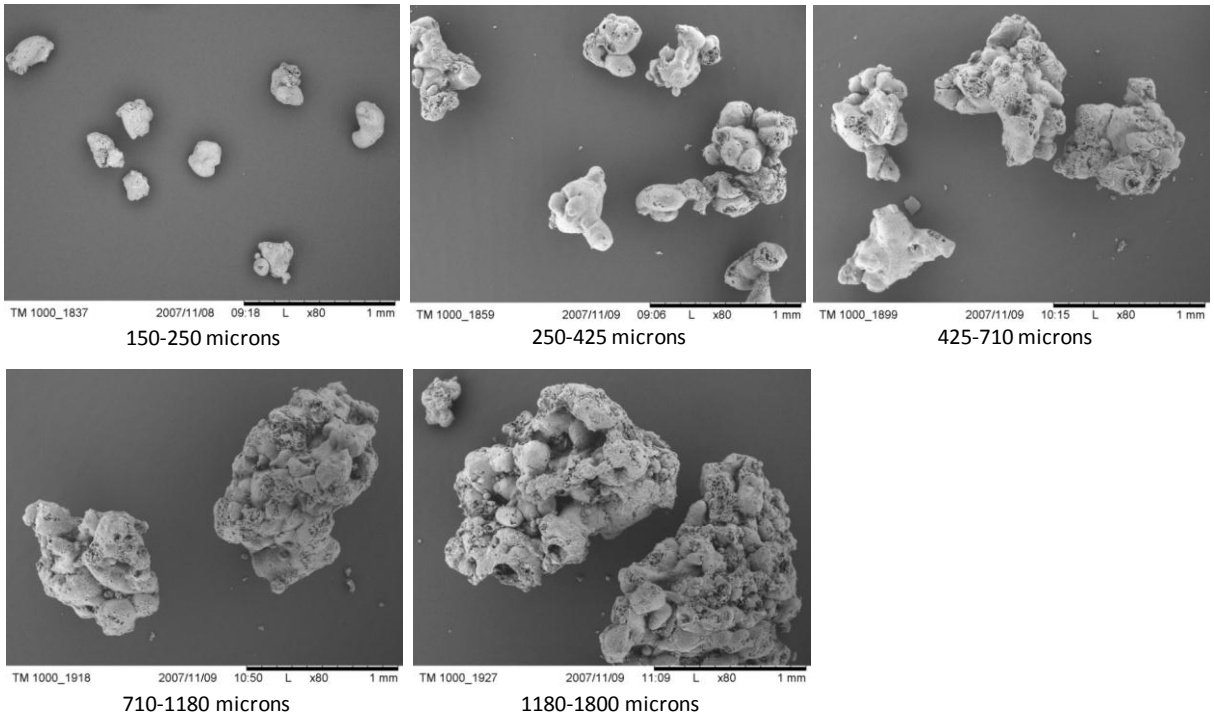

Figure 7.3: SEM images of LH formulation for each sieve cut

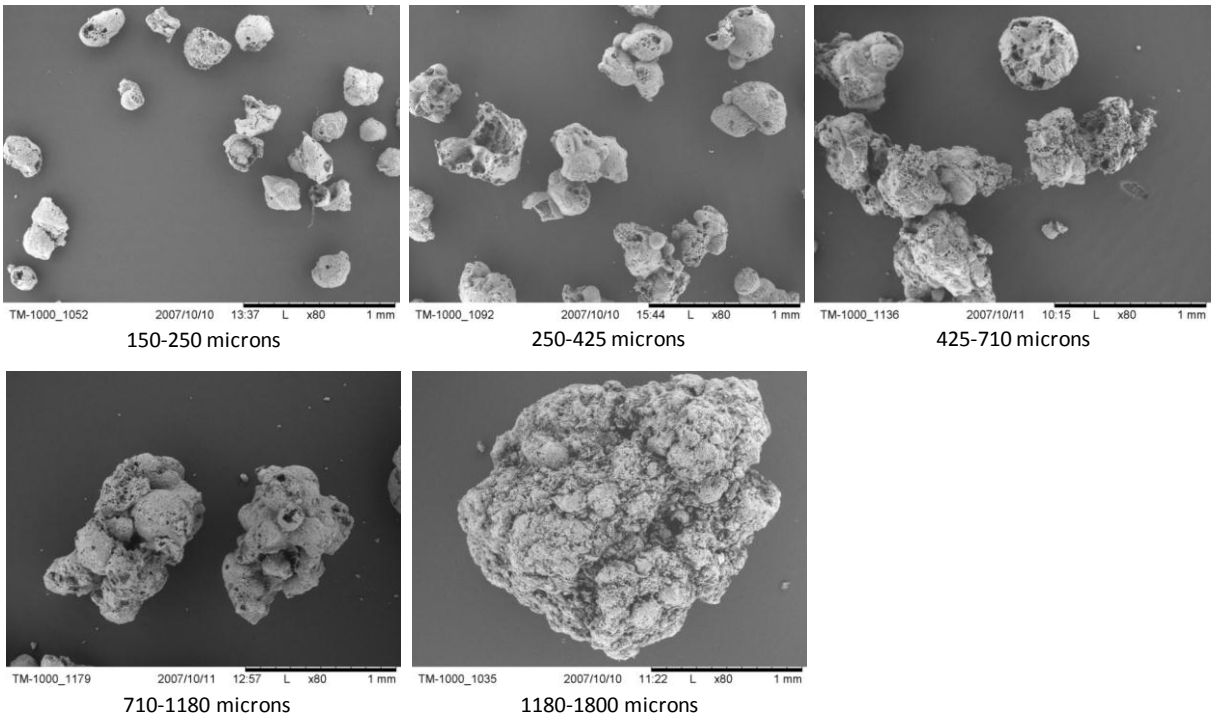

Figure 7.4: SEM images of LL formulation for each sieve cut

These figures illustrate common themes for all of the formulations and particle sizes. Notably most particles show signs of damage from abrasion and attrition, this could occur during either processing and/or sieving. The following observations can be made on how particle size is linked to particle structure:

- For particles in the 150-250 µm size range the vast majority are single entities, either single puffed droplet or debris from large broken particle.
- Some agglomerates are present along with single entities in the 250-425 µm range.
- All particles above 425 µm feature some kind of agglomeration. As particles get bigger they become agglomerates with increasing numbers of primary particles.

These observations can be attributed to the range of droplet sizes created during atomisation, which is usually around 200 to 400 µm according to Bayly *et al.* (2008) and therefore any particle larger than this can be assumed to be formed from agglomerated smaller particles.

Variation in appearance and structure between particles of different formulations is also noted. Particles from the LL formulation tend to have the most porous surfaces (Figure 4.2) and seem to suffer the most damage from abrasion/attrition. The formulas containing the higher levels of silicate (HH, HL) tend to have the smoothest surface appearance (Figure 7.1 and Figure 7.2) and suffer least damage, they also seem to have the roundest shape. This change in appearance in surface texture and shape maybe a function of changes in atomisation, caused by variation in slurry viscosity as discussed by Stewart (2008) (§2.3.4), and the drying mechanism described by Hecht (2004) (§2.3.6) taking place for each formulation.

7.3.2 Hydroscopic Behaviour

In this section, the moisture content and equilibrium relative humidity values of the powders used in this research are examined.

7.3.2.1 Moisture Content

The moisture content of a detergent powder refers to the sum of both the bound and free moisture contained within the particles. This was measured using an infrared mass loss method (§3.7.3.1). The results obtained from these measurements are plotted as a function of particle size for four formulations in Figure 7.5. These data points represent the average of five repeats. Moisture contents were found to vary between 3 and 12 % by mass, depending on both formulation and particle size. All of the formulations were manufactured from slurry with the same moisture content and dried under the same conditions, therefore the variation seen is caused by changes in the drying behaviour of different formulations. This might be caused by changes in the split between bound and free moisture in the formulation and also variation in droplet/particle size changes between formulations, caused by both atomisation and agglomeration.

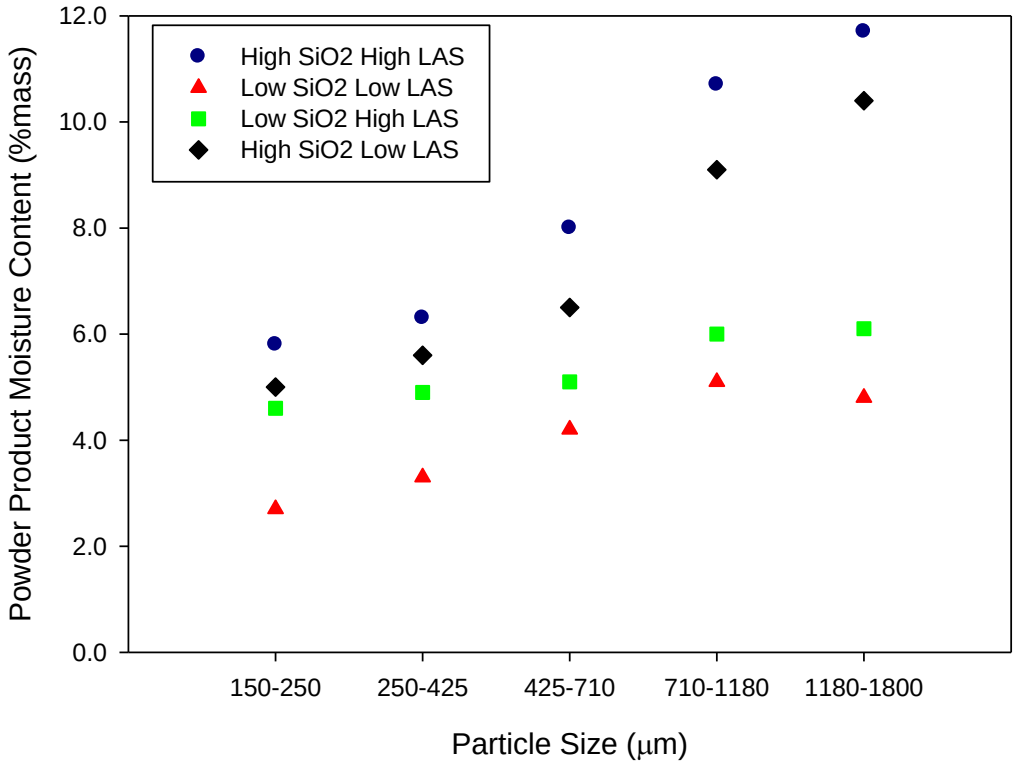

Figure 7.5: Powder moisture contents for each formulation as a function of particle sieve cut

Figure 7.5 shows a clear effect of particle size on moisture content for all formulations, and shows a general increase with increasing size. The degree of increase is not consistent for each formulation, again a possible indicator of different drying behaviour. An overall increase in moisture content with particle size is expected as big particles will dry more slowly than smaller ones as described by Hecht (2004), due to heat and mass transfer limitations within the particle structure and also in the boundary layer around the particle, as widely reported in literature (§2.3.6). An additional consideration is the possibility of variation in chemical composition between different sizes, which in turn would lead to differing balance of free and bound moisture according to Bayly (2006).

7.3.2.2 Equilibrium Relative Humidity

Free moisture is known to be key in determining detergent powder properties as this water is free to move into the organic phase of the granule, altering the phase of the surfactant in the granule and thus changing its mechanical properties, and covered by Bayly (2006) and Stewart (2008). The values of eRH for all four formulas are displayed in Figure 7.6, as a function of particle size.

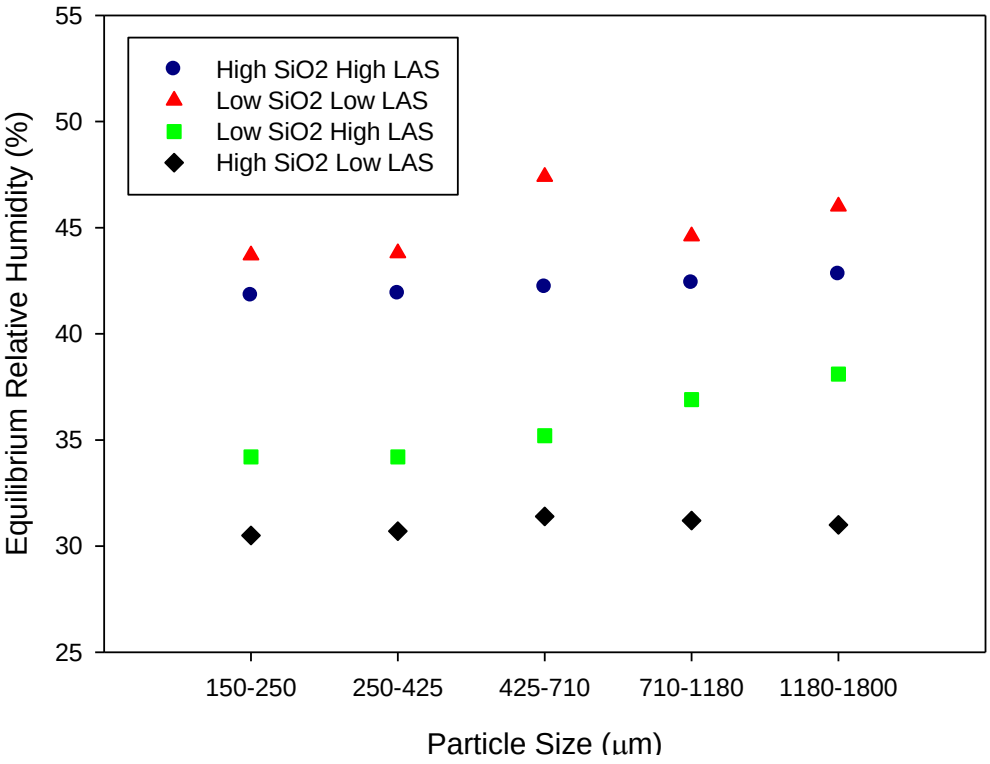

Figure 7.6: Powder Equilibrium Relative Humidities

Clear variation in eRH values for all of the formulations can be seen, with the LL formulation having the largest values of between 42% and 48%. The lowest values are seen for the HL formulation, at around 30%, for all particle sizes. This variation gives a clear indication of different amounts of free moisture contained within each, as a result of different levels of

key components. This in turn affects the balance between free and bound moisture in the slurry and powder product.

The trend in eRH with changes in particle size appears to be small for some formulations, namely the two formulations containing large amounts of sodium silicate; HH and HL. The LL formulation shows an unclear trend, where the middle particle size exhibits the largest value of eRH, for all samples measured at around 48%. The LH formulation demonstrates the clearest trend, with values eRH increasing with particle size, from approximately 34% to 38% over the range of particle sizes, as would be expected as larger particles dry less due to heat and mass transfer limitations as they travel through the spray dryer covered by Hecht (2004).

7.3.3 Particle Density

This section of the chapter covers results for the envelope and apparent (skeletal) density as a function of formulation and particle size.

7.3.3.1 Envelope Density

The principle of envelope density is discussed in section (§2.8.3) and Figure 7.7 shows values of this for the four formulations used in this work as a function of particle size. Envelope density varies between values of 500 and 1400 kgm^{-3} as a function of particle size and formulation. The LL formula displays the largest values for envelope density for all particle sizes, varying from 0.7 to 1.4 kgm^{-3}, whilst the high silicate formulation displays the smallest values for all but the largest particle size, varying from 0.5 to 0.9 kgm^{-3}. The changes in envelope density, with particle size (for each individual formulation), show the effect of

particle structure on density (§ 7.3.1), with items such as porosity and agglomeration influencing envelope density, as well as the density of the detergent material itself. Smaller particles could also actually be undissolved solids from the slurry which pass through the entire spray drying process unchanged; possibly solid lumps of sulphate and such as would have much higher densities than normal granules and therefore the presence of just a few could influence the envelope density of a sample as suggested by Bayly (2006).

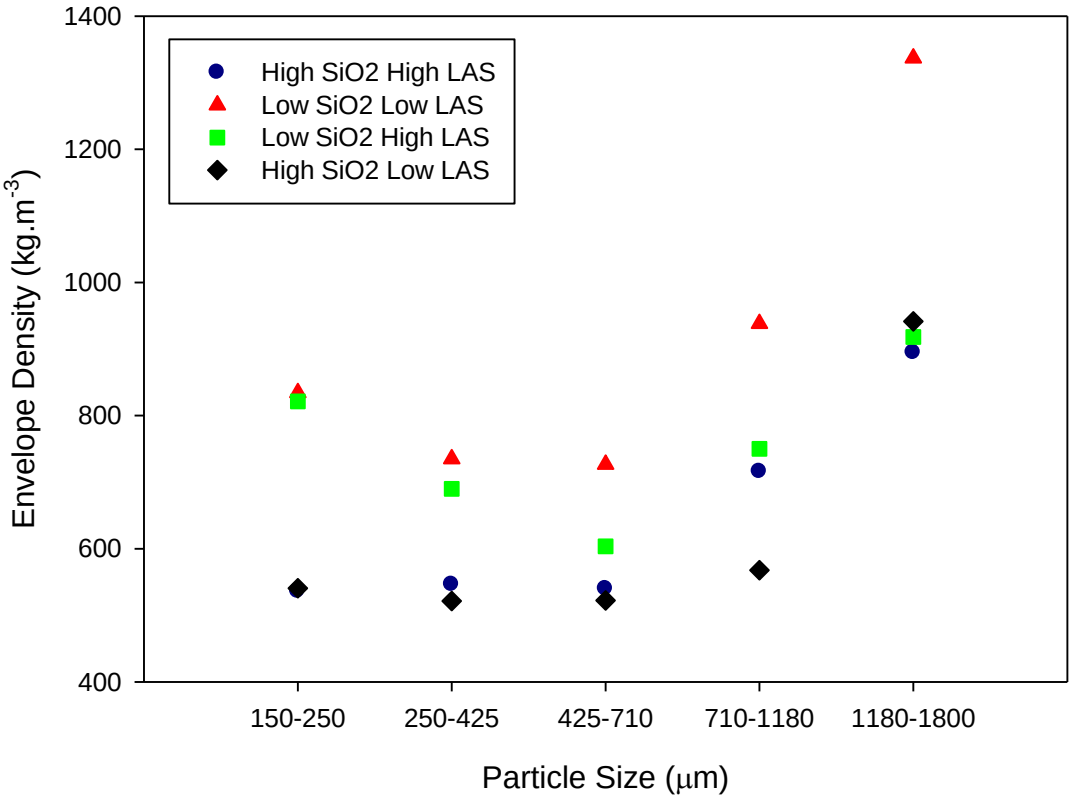

Figure 7.7: Particle Envelope Densities

Another issue to be considered on how particle size influences envelope density is the accuracy of the technique employed with respect to particle size. The method used employs a quasi-fluid fine powder, 'dry-flo', which is packed around the particles in the sample during the compression, thus allowing the envelope volume to be measured. The size distribution of the dry-flo powder heavily influences its ability to pack tightly around the sample

granules, with the packing value decreasing as the particle size in the sample approaches that of the dry-flo. This may partially explain the trend of increasing envelope density at small particle sizes, as this is the region in which sample particles and dry-flo particles approach the same size, thus reducing packing and in accurately measuring the envelope volume of the sample. The lower size limit of particles that can be measured using this technique is not stated by the manufacturer or any workers on this device, so definite conclusions on this cannot be drawn.

The variation in envelope densities observed for the smallest particles sizes shows interesting trends in terms of the effect of formulation, and specifically the level of sodium silicate builder. The two formulations which contain no sodium silicate appear to have almost identical envelope densities for the smaller particle sizes, as do the two formulas which contain sodium silicate, with the zero silicate powders having the largest envelope densities. This behaviour seems less well defined at larger particle sizes, where the LL formula shows much higher values than the other three formulas. These changes with formulation may be partly explained by changes in porosity and also by variation in the skeletal density of each formulation described in the next section.

7.3.3.2 Apparent Density

Figure 7.8 shows values of apparent density (§2.8.3) for the four formulations as a function of particle size.

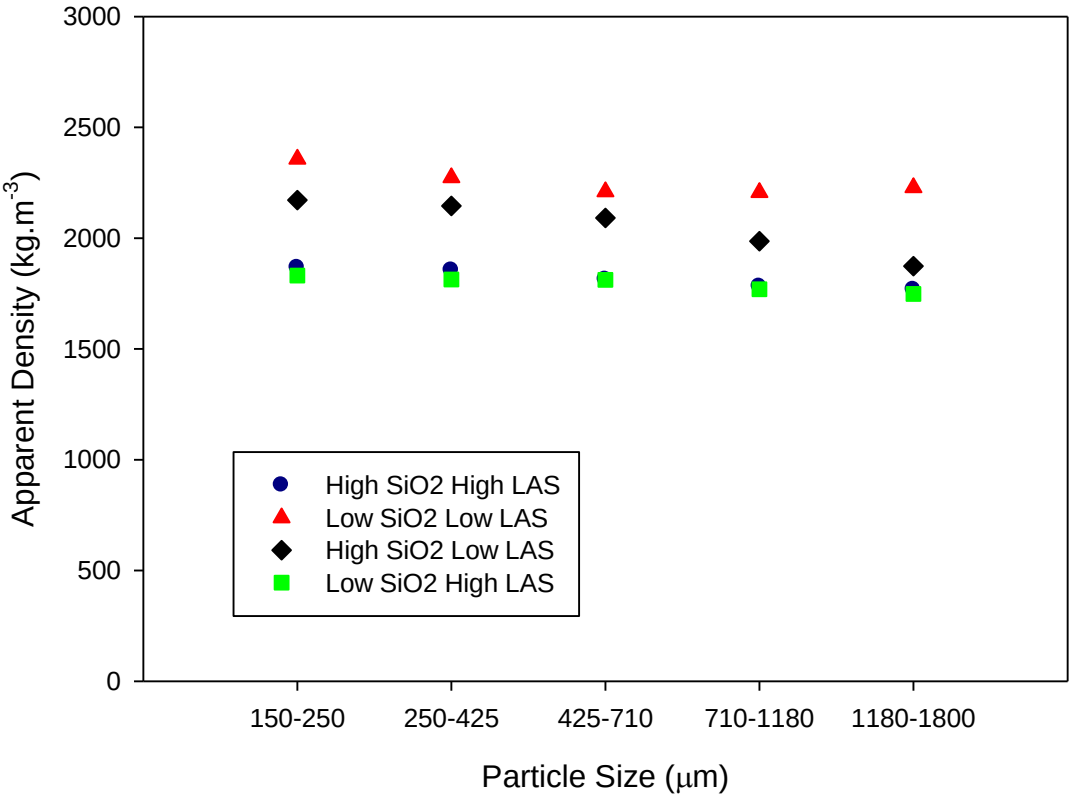

Figure 7.8: Particle apparent densities

Values of apparent density can be seen to vary between 1.7 and 2.4 kg.m^{-3}. The effect of formulation on apparent density appears to be greater than that of particle size.

As with the envelope density data, the LL formulation shows the largest apparent density values for all particle sizes, between 2.3 and 2.4 kgm^{-3}. The next highest values are for the HL formulation, varying between 2.3 and 1.9 kgm^{-3}. Increasing particle size appears to slightly decrease the skeletal density for all formulations. This change is a function of increasing moisture content with particle size or an increase in the amount of closed pores in larger particles.

Comparison of envelope and skeletal densities reveal that the inclusion of open pores within the sample reduces its density by between two and three times. This indicates that between half and two-thirds of the volume of a detergent particle can be accounted for by

considering open pores. The effect of formulation and particle parameters on these two density parameters shows no clear links, therefore it can be determined that formulation and particle size influence envelope density of detergent granules through changes in microstructure (porosity) rather than actually density of the solid detergent material in the granule.

7.3.4 Mechanical Properties

The mechanical properties of the particles are key to understanding the impact behaviour of particles, in terms of their deformation and therefore energy dissipation on impact and also the contact area created between the particle and the impacted surface. This in turn controls restitution and deposition, which determines the collision success rate of particles on the dryer walls, and is therefore of great importance to this work. Presented here are the results for characterisation of the mechanical properties of the detergent powders, with two main techniques being employed: confined compression, and unconfined compression (§2.8.5). The former gives the mechanical properties of the formulation independent of particle structure, whilst the latter gives mechanical properties of the formulation including particle structure which enables the effects of material properties and particle structure to be decoupled.

7.3.4.1 Confined Yield Stress

The confined yield stress is defined as an interpretation of the point at which the granules in a powder sample, being compressed within a die begin to plastically deform. This a useful value when investigating the impact behaviour of particles, as it is the point at which plastic deformation begins and therefore energy dissipation through deformation, which will

control restitution and ultimately deposition, through the size of the contact area made through deformation. Therefore the changes in confined yield stress with formulation and particle size will allow understanding of how impact behaviour changes with these variables. Values for confined yield stress of all formulas as a function of particle size are plotted in Figure 7.9.

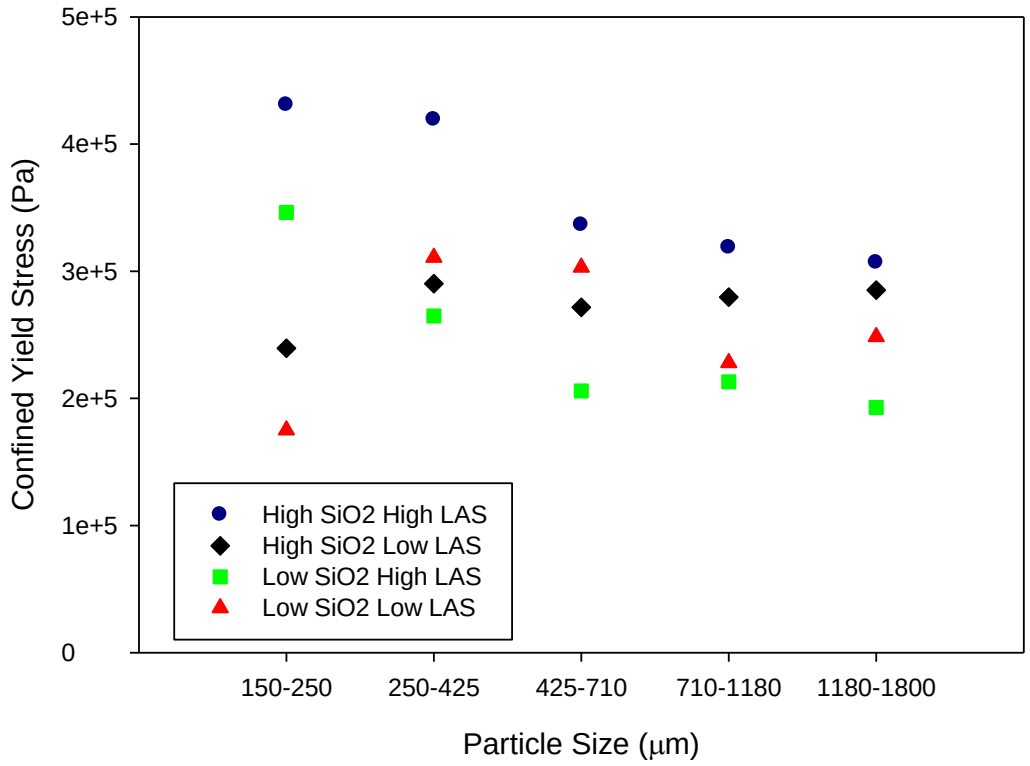

Figure 7.9: Confined yield stresses for the four formulations as a function of particle sieve cut

Values of confined yield stress can be seen to vary with both formulation and particle size. The highest yield stresses across all particle sizes can be seen for the HH formulation, this is despite this formula having the largest moisture content of the four, which would be expected to reduce yield stress, as stated by Bayly (2006). This leads to the conclusion that addition of silicate and LAS strengthens granules enabling them to resist plastic deformation; examining the microstructure of these granules, as shown in Figure 7.1 to 7.4 shows that

they appear to have solid structures in comparison with the other formulas, with the exception of the HL formula.

The trends for the effect of formulation for the other three formulas become less clear. The LH formula has the largest yield stress for the smallest particle size, whilst the LL formula has the second largest values for the two middle particle sizes. The HL formulation has the second highest values for the biggest two particle sizes.

The effect of particle size on yield stress appears to be different for each formulation, however, the formulations containing large amounts of LAS surfactant (HH and LH) show similar trends. For these formulations, the largest values of yield stress are seen for the smallest particle sizes, and then yield stress decreases with increasing particle size, almost reaching a plateau for final three particle sizes, this may be an effect of particle structure, as the morphology of granules is known to change between the 250-425 µm and 425-710 µm size group (§7.3.1). The effect of particle size for the formulations containing low levels of LAS surfactant appear to go the other way, with the smallest particles having the lowest yield stress values, and then an increase with particle size, although the trends are less clear. All of this indicates that particle morphology and structure, which varies with particle size (§ 7.3.1), has a significant effect on yield stress of samples of detergent powders, this effect appears to also depend on formulation, which also controls particle morphology (§ 7.3.1)

7.3.4.2 Confined Join Stress

The confined join stress is defined as an interpretation of the point at which the granules in a powder sample (compressed within a die) begin to physically lose their structure under the stress being applied. This is useful for investigating the impact behaviour of particles, as it is

an indication of the point at which particle will break. Therefore the changes in confined yield stress with formulation and particle size will allow understanding of how particle breakage changes with these variables. Values are plotted in Figure 7.10.

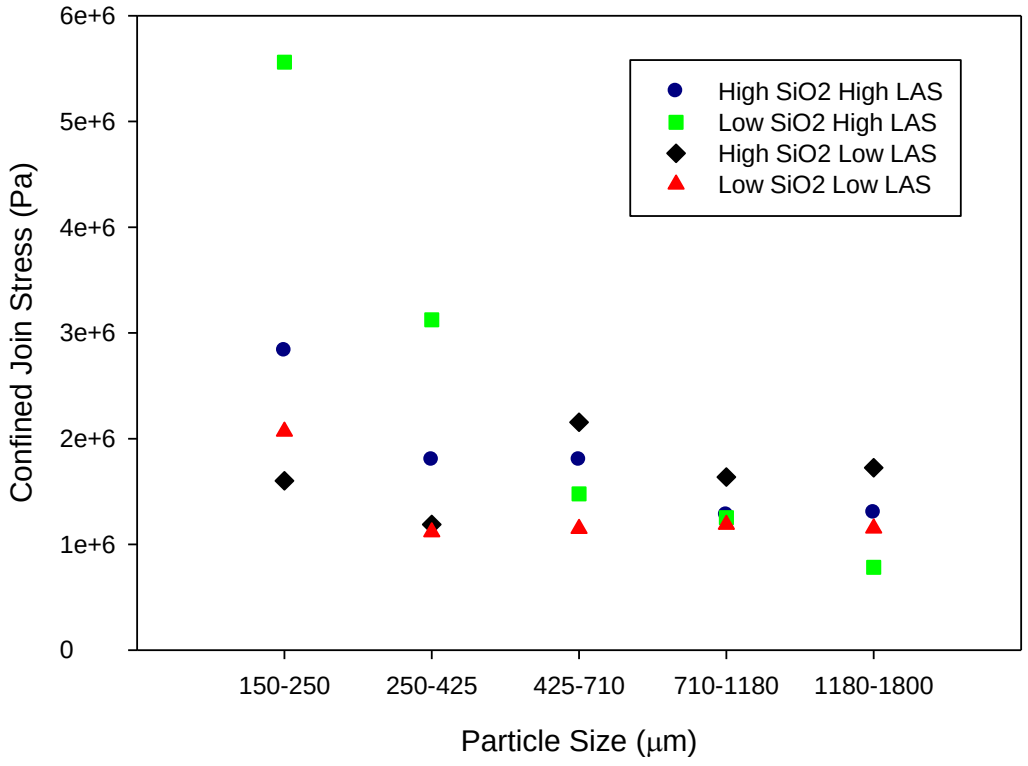

Figure 7.10: Confined compression join stresses as a function of particle size for the four formulations

The join stress of granules can be seen to vary between 6×10^{6} and 8×10^{5} Pa. Examining Figure 7.10 reveals a general trend of decreasing join stress with particle size, with the exception of the HL formulation. The largest values for join stress are displayed by the LH formula at small particle sizes (6×10^{6} Pa), indicating these granules offer the most resistance to applied stresses before they lose their individual structures.

All formulas appear to reach a plateau of constant join stress values for larger particle sizes, this may be a feature of the agglomerated nature of particles above 425 (μm) (§ 7.3.1). This is assuming that the agglomerated granules are most likely to break through splitting into

their constituent particles, thus the same stress is required to do this regardless of the number of constituent particles in the original agglomerate.

7.3.4.3 Unconfined Young's Modulus

The unconfined Young's modulus is the measure of the amount of elastic deformation a tablet of detergent material will undergo at an applied level of stress. This value is important in the impact behaviour of particles as it controls the amount of deformation a particle suffers up to the yield stress, this parameter was used to explain adhesion (deposition) of particles by Johnson *et al.* (1971), in their famous JKR theory. Therefore Young's modulus can be used to aid understanding of collision success rate of particles on the dryer walls. The values of Young's modulus displayed in Figure 7.11 are expressed in units of Pascal, as the strain in this work was described as a fraction of the tablets original thickness.

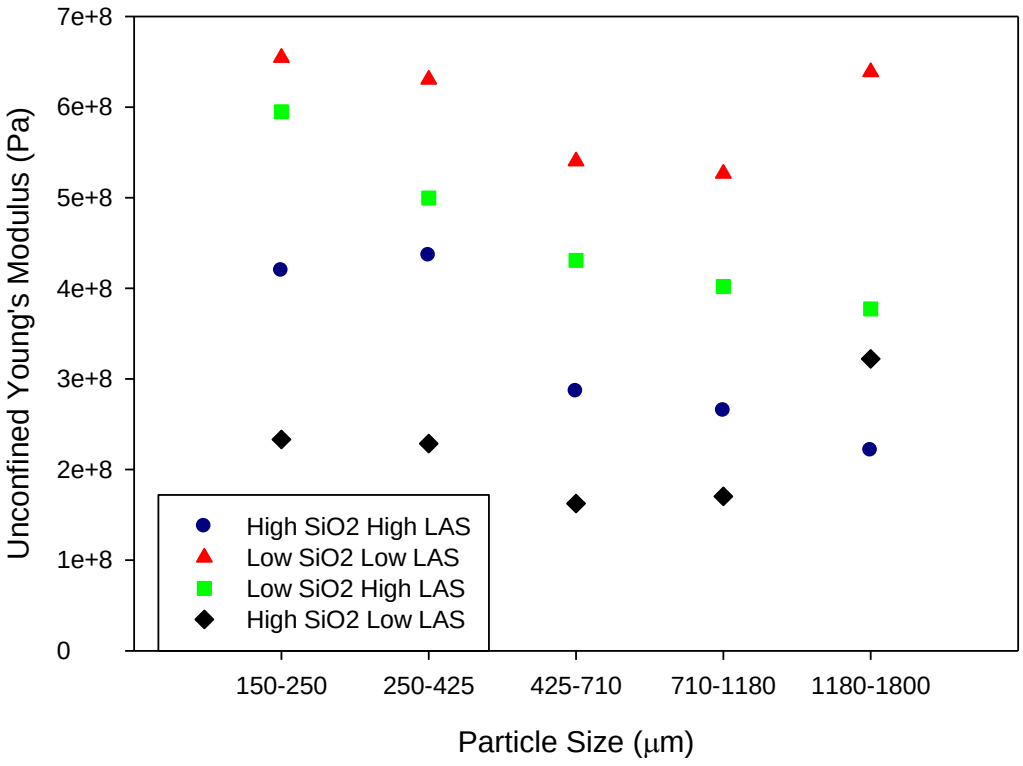

Figure 7.11: Unconfined Compression Young's Modulus

Clear trends in Young's Modulus with formulation can be seen in Figure 7.11, with the LL formula, shows the largest values at all particle sizes, ranging between 5.2×10^{8} and 6.2×10^{8} Pa. The lowest values are exhibited for the HL formula, with the exception of the largest particle size where the HH formula shows the smallest values. The effect of particle size on Young's modulus varies between formulations, however, the trends seen in the two formulas containing large amounts of LAS appear to be similar, a steady decline with increasing particle size, as do the two formulas containing small amounts of LAS, which show the smallest values for the mid-sized particles.

7.3.4.4 Unconfined Yield Stress

The unconfined yield stress is defined as an interpretation of the point at which the tablet of detergent material in a powder sample being compressed begins to plastically deform. Having an understanding of how the yield stress of the solid detergent material compares to that of particles of the same material allows the effect of particle structure to be accounted for, thus helping understand the importance of the microstructure of detergent granules in their impact behaviour. Values for unconfined yield stress of all four formulas as a function of particle size are plotted in Figure 7.12.

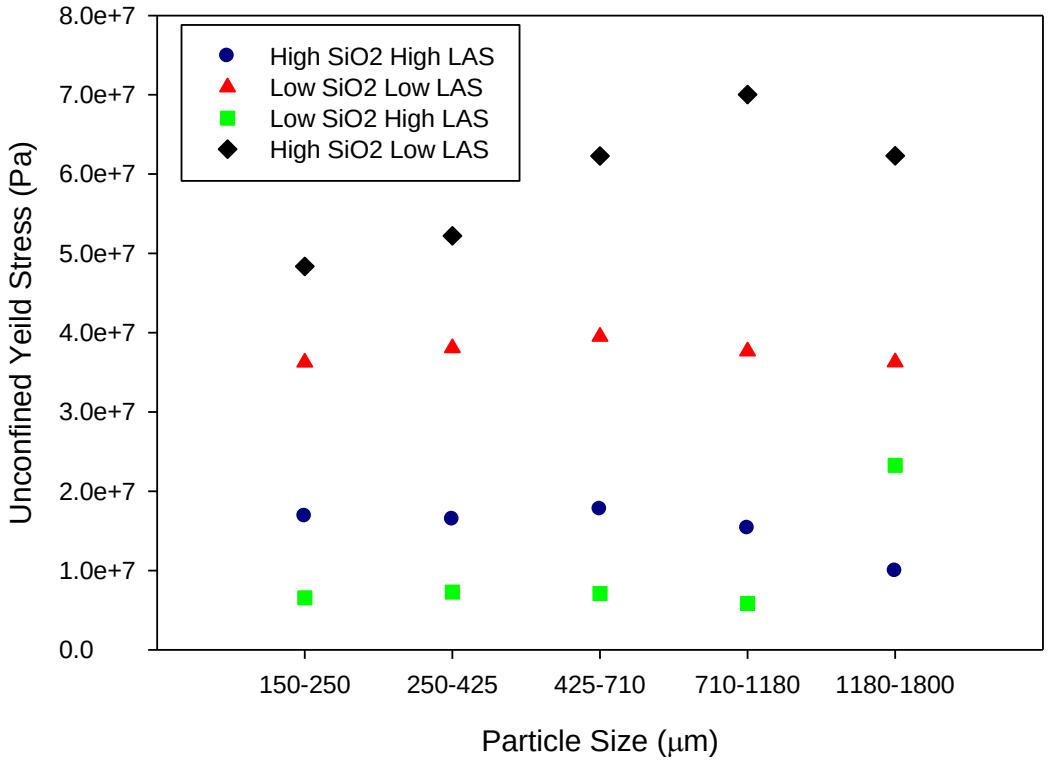

Figure 7.12: Unconfined Compression Yield Stresses

Clear effects of formulation on unconfined yield stress can be seen in Figure 7.12 (with the one exception of the LH formula at the largest particle size). The largest values of unconfined yield stress, varying between 5×10^7 and 7×10^7 Pa are shown by the HL formula across all particle sizes. The smallest values of yield stress are shown by the LH formula, which has yield stresses approximately one order of magnitude lower than those of the HL formula. The fact that the two formulas which contain low levels of LAS have significantly larger values of yield stress than the formulas containing large amounts of LAS indicate that addition of this component has a key role in controlling yield stress of detergent material, this is also evident when considering the small difference in the LAS content between the HH formula and the LH formula. This trend would be expected based on the conclusions of Yangxin *et al.* (2008). Unexpectedly the effect of moisture content on yield stress, explained

by Bayly (2009), does not appear in this data, this is possibly because it is over shadowed by large changes in component levels between the formulas used.

Particle size seems to influence the yield stress values of the HL formula much more than any of the other formulas, particularly the LL formula where the yield stress is almost constant across all particle sizes.

Comparison of the values of unconfined yield stress with those of confined compression, show that the later have yield stress values of one or two orders of magnitudes lower than the former, showing that including particle structure reduces the yield stress of detergent granules. The effect of formulation and particle size also varies greatly between the two sets of yield stress data. All of these changes highlight the importance of granule microstructure on mechanical properties.

7.3.5 Particle Characterisation Conclusions

The physical and mechanical properties of particles are key to determining their impact behaviour, in terms of restitution, breakage, deposition, or a combination of these, and therefore determine the collision success rate of particles impact on the dryer walls. Physical and mechanical parameters of a range of formulations of detergent powders have been studied as a function of particle size. This has revealed a mutual dependence of all properties on both formulation and particle size. It is clear that most, if not all physical and mechanical properties are interlinked.

The microstructure, morphology and structure and appearance of granules was found to vary with both particle size and formulation. These changes in microstructure have been

linked to the formation of granule characteristics through agglomeration and drying mechanisms in the spray drying process.

The hydroscopic behaviour of the detergent formulations studied have been characterised in terms of total moisture content and equilibrium relative humidity. Both of these parameters were found to vary with particle size and formulation, with the largest particles having the largest total moisture contents. The density of the powders was studied through measurement of both the envelope and skeletal density of samples, again both were found to vary with formulation and particle size.

Confined and unconfined compression tests were used to examine the mechanical properties of the detergent powders, with and without the effects of particle structure. The mechanical properties of powders were found to vary greatly with formulation but less so with particle size. The influence of particle structure was found to reduce the yield stress values obtained by one or two orders of magnitude. This change also highlighted the effect of formulation and particle sizes on the yield stress of detergent granules, through their influence on the microstructure developed during spray drying.

This section has shown the effect of formulation and particle size on microstructure, physical and mechanical properties of detergent powders. These parameters are known to be important in controlling particle impact behaviour and therefore particle collision success rate. The impact behaviour of these detergent powders are examined in the next section.

7.4 Particle Impact Behaviour Results

7.4.1 Particle Breakage

Breakage of detergent particles during spray drying and processing will have a significant effect of product quality (§2.2) and therefore understanding this aspect of impact behaviour is of considerable interest. Both particle and impact properties studied are reported to affect particle breakage (§2.9.2), therefore it is expected that all will affected the results presented in this section.

The fraction of particles that broke under each experimental condition was recorded, along with the number of fragments generated by each particle that broke. This data is presented in terms of the fraction of particles that broke at each experimental condition and the average number for fragments from breakage at each condition. Before this quantitative data, examples of the three types of breakage mechanisms observed are shown and discussed qualitatively.

7.4.1.1 Breakage Mechanisms

Examples of the three types of particle failure mechanisms (§2.9.2) observed are shown in the following figures. These allow the reader to gain an appreciation of the types of breakage of detergent granules observed upon impact with a steel surface. Additionally, these observations help to give an indication of the link between the granules microstructure and its breakage, as examined by Mullier *et al.* (1987) and Samimi *et al.* (2003).

The microstructure of detergent granules was previously examined (§ 7.3.1). It was found to change greatly with particle size, smaller particles tend to be single entities with larger particles (typically above 425 µm) being agglomerates. This needs to be kept in mind when trying to understand breakage mechanisms of detergent granules. Therefore the hypothesis behind the breakage of larger particles and possibly some smaller particles is that the particle is an agglomerated structure and the kinetic energy dissipated at the point of impact breaks the bonds holding these particles together.

Figure 7.13 and Figure 7.14 show HL formulation particles being chipped (attrition and abrasion) at 5 and 10 ms^{-1} respectively. The main characteristic of attrition and abrasion is that some small amount of material is released whilst the main body of the particle remains intact. The weakest bonds in these cases appear to be positioned such that individual or agglomerates of small numbers of constituent particles, resulting in the main bulk of the particle staying together with a number of smaller pieces removed from it as shown in Figure 7.13 and Figure 7.14.

Figure 7.13: Chipping of a 1180-1800 µm HL particle at 5 ms^{-1}

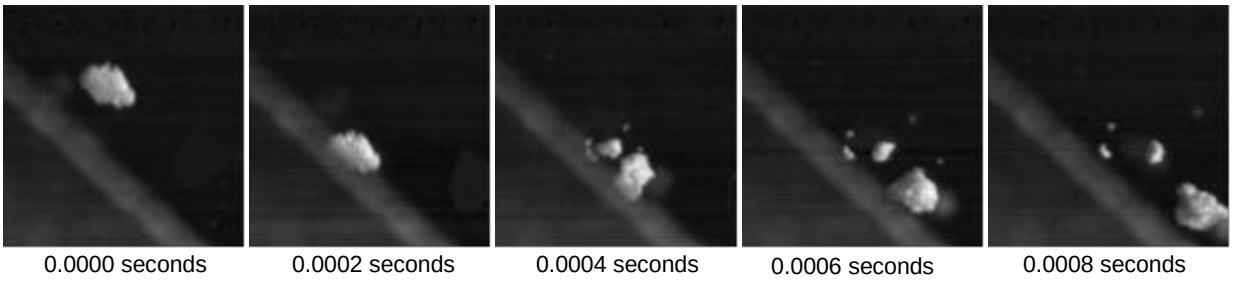

Figure 7.14: Chipping of a 1180-1800 µm HL particle at 10 ms^{-1}

Figure 7.15 and Figure 7.16 show particles splitting, involving the particle breaking into smaller particles of reasonably equal size. In this kind of breakage, the weakest bonds in the granule are those between large parts of the granule, meaning the granule breaks apart to leave large fragments. Figure 7.15 shows one particle splitting into two particles with some smaller fragments also being created. Figure 7.16 shows a particle splitting into 3 equally sized pieces along with some smaller fragments.

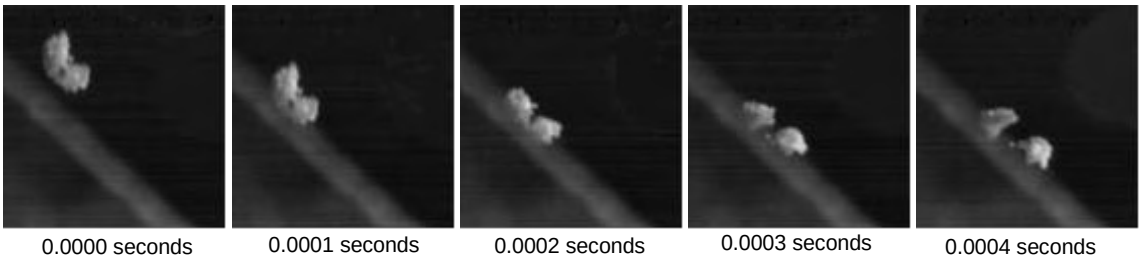

Figure 7.15: A HL particle of 1180-1800 µm splitting at 10 ms^{-1}

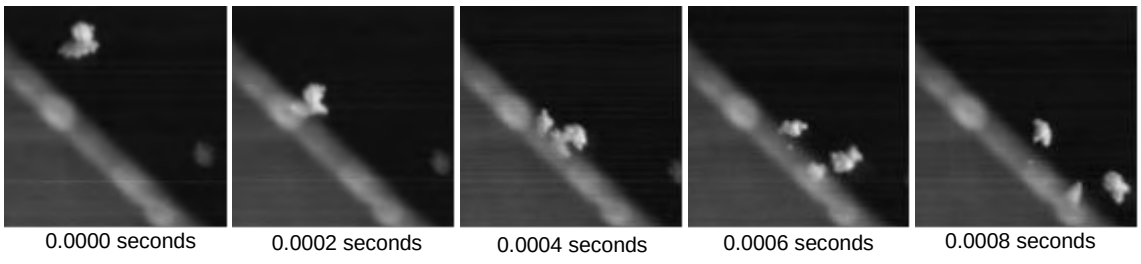

Figure 7.16: A HL particle of 1180-1800 µm splitting at 10 ms^{-1}

The complete destruction of the particle's original structure, through either breaking of large number of bonds between constituent particles and even breaking constituent particles,

during smashing is shown in Figure 7.17 and Figure 7.18. Smashing is characterised by the large amount of fragments created and the way in which these fragments are scattered in all directions.

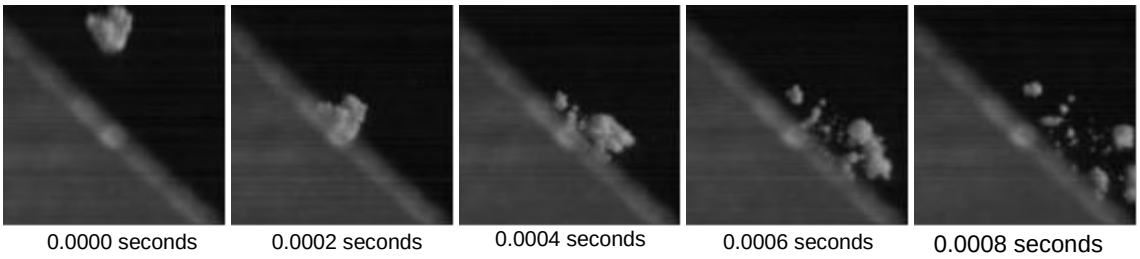

Figure 7.17: A HL particle of 1180-1800 µm smashing at 15 ms^{-1}

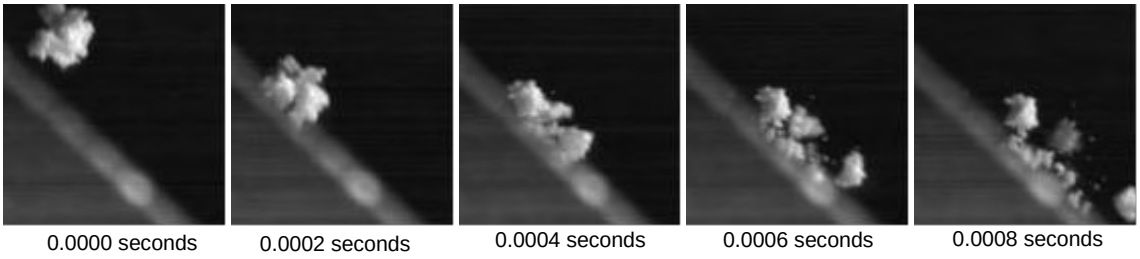

Figure 7.18: A HL particle of 1180-1800 µm smashing at 10 ms^{-1}

These examples of breakage mechanisms highlight the importance of detergent granule microstructure in breakage and therefore how parameters such a formulation and drying conditions will affect the processability of detergent powders in terms of size reduction through breakage.

7.4.1.2 Breakage Fractions

Figures 7.19-7.22 show the effect of formulation, particle size, impact kinetic energy and impact angle on the fraction of particles that suffer breakage. The most striking trend in these plots is that the fraction of particles suffering breakage increases with impact kinetic energy and particle size for all four formulations, at all impact angles. These trends are also shown in the statistical analysis in Appendix E, and would be expected as increasing kinetic

energy (linked to particle size) means more energy is available to deform and then eventually break both bonds between constituent particles and the structure of individual constituent particles within the particle. Higher kinetic energy increases the loading (force) on the particle as it impacts. This will increase the impact stress and therefore deformation. If the force is great enough the deformation will continue through the elastic regime into the plastic regime and possibly to the point of failure, for both bonds between constituent particles and the structure of individual constituent particles. The models shown in Appendix E highlight how these trends are most pronounced at lower to mid values of these parameters and their effect decreases at higher values, particularly for particle size.

Larger detergent particles are constructed from agglomerated smaller particles (§ 7.3.1). These changes in particle morphology appear to be closely linked with the breakage behaviour of detergent powders studied in this work. Evidence for this can be seen as the breakage fraction for particles increases with the number of consistent particles making up particles in each size range. Moreover, there is a fairly consistent change in breakage fraction with impact velocity, across all angles and formulations, as particle size increases. This is a clear indication of the role of particle morphology, in terms of agglomerated versus single particle granules (§ 7.3.1), in particle breakage.

The effect on angle on breakage fraction is that increasing angles towards the normal increases breakage fraction, potentially due to the increasing normal impact velocity component. This effect appears to be most significant for the smallest impact angles, as shown by the models in (§E.2.3). However, this effect appears to be smaller in this work than in comparison to the findings of workers such as Samimi *et al.* (2003) found that impact

angle heavily influenced breakage, this discrepancy might be linked to the structure of spray dried detergents.

The effect of formulation and resulting particle properties on breakage fraction appears to be complex. The response modelling (§E.2) shows that SiO_2 content has a significant effect on breakage, with mid levels of this parameter producing the smallest breakage fraction. The effect of LAS levels on breakage fraction was found to not be significant. In terms of resulting particle properties, both types of particle density measured in this work have a strong positive correclation, showing that increasing density leads to more breakage, this could be caused by the increased kinetic energy carried by heavier particles upon impact. Moisture content also has a positive correlation, however, eRH does not, suggesting the effect of free moisture is not as important as described by Bayly (2009). The mechanical poroperties measured show a range of correlations, with all being negative apart from the unconfined yield stress, decreasing meachanical strength would be expected to increase breakage and this may explain the moisture content correlation. The unconfined yield stress may be an outlier and its effect may be cancelled out by the effect of granular structure on mechanical behaviour upon impact.

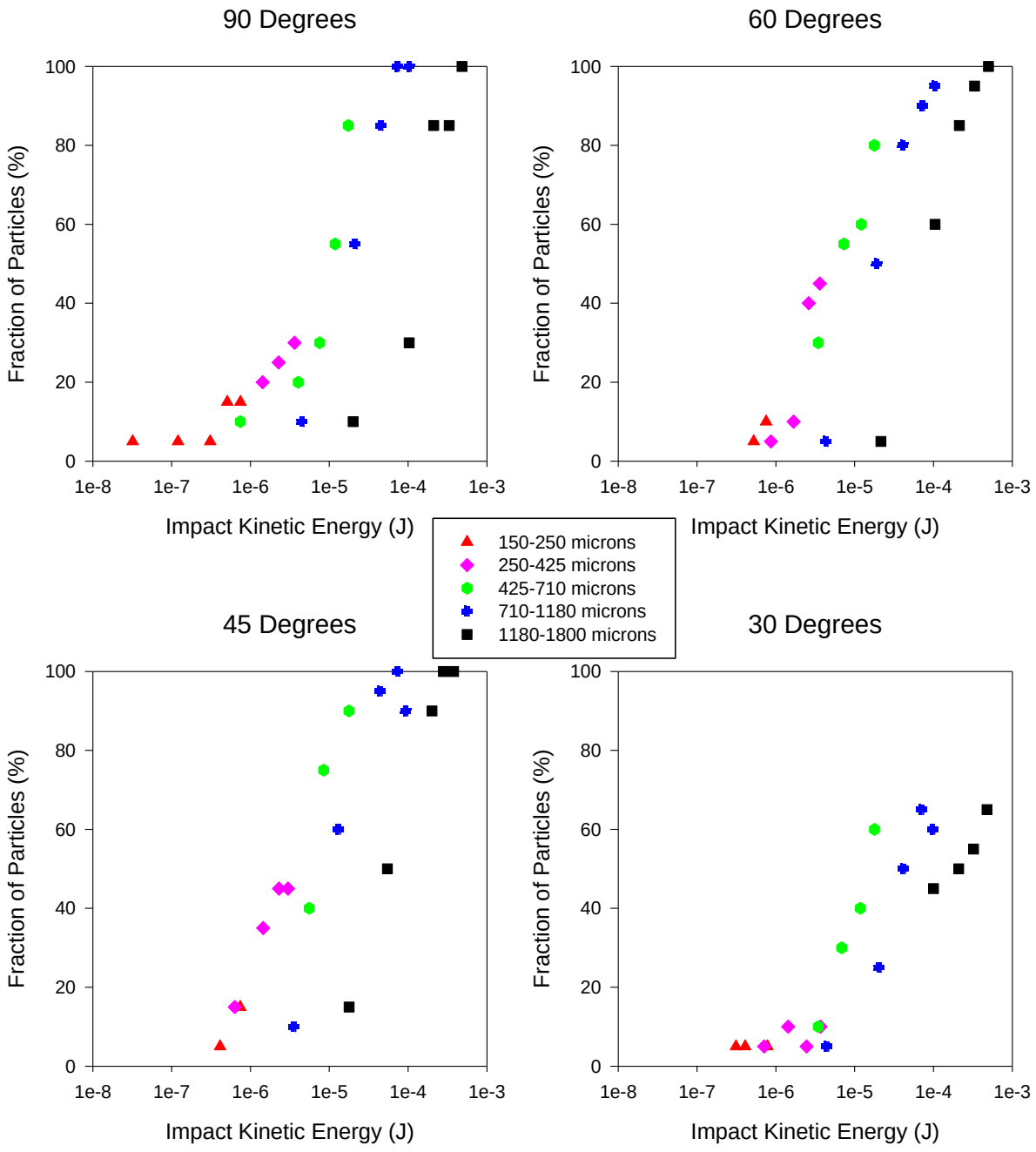

Figure 7.19: Breakage Fraction: HH Formulation

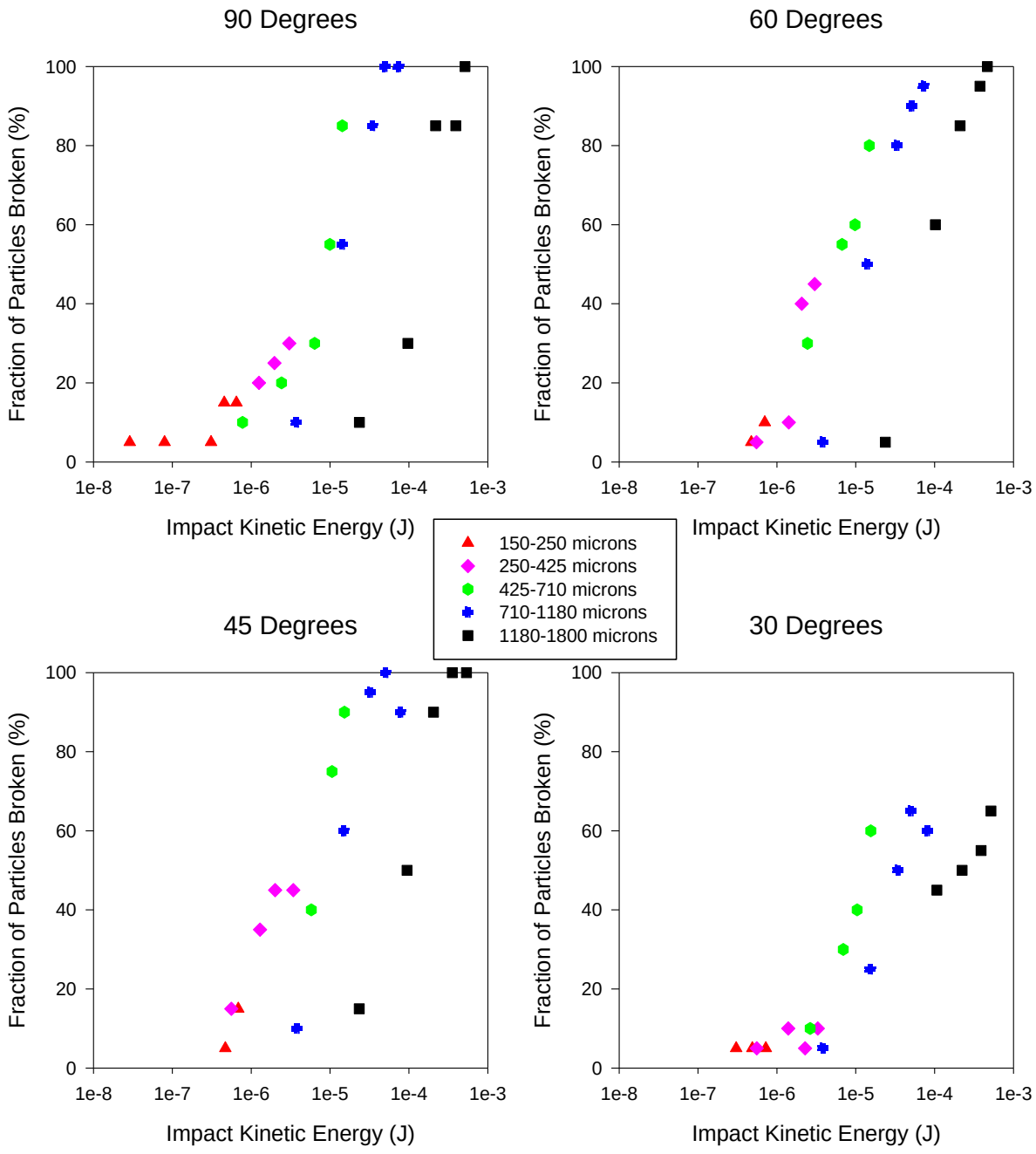

Figure 7.20: Breakage Fraction: HL Formulation

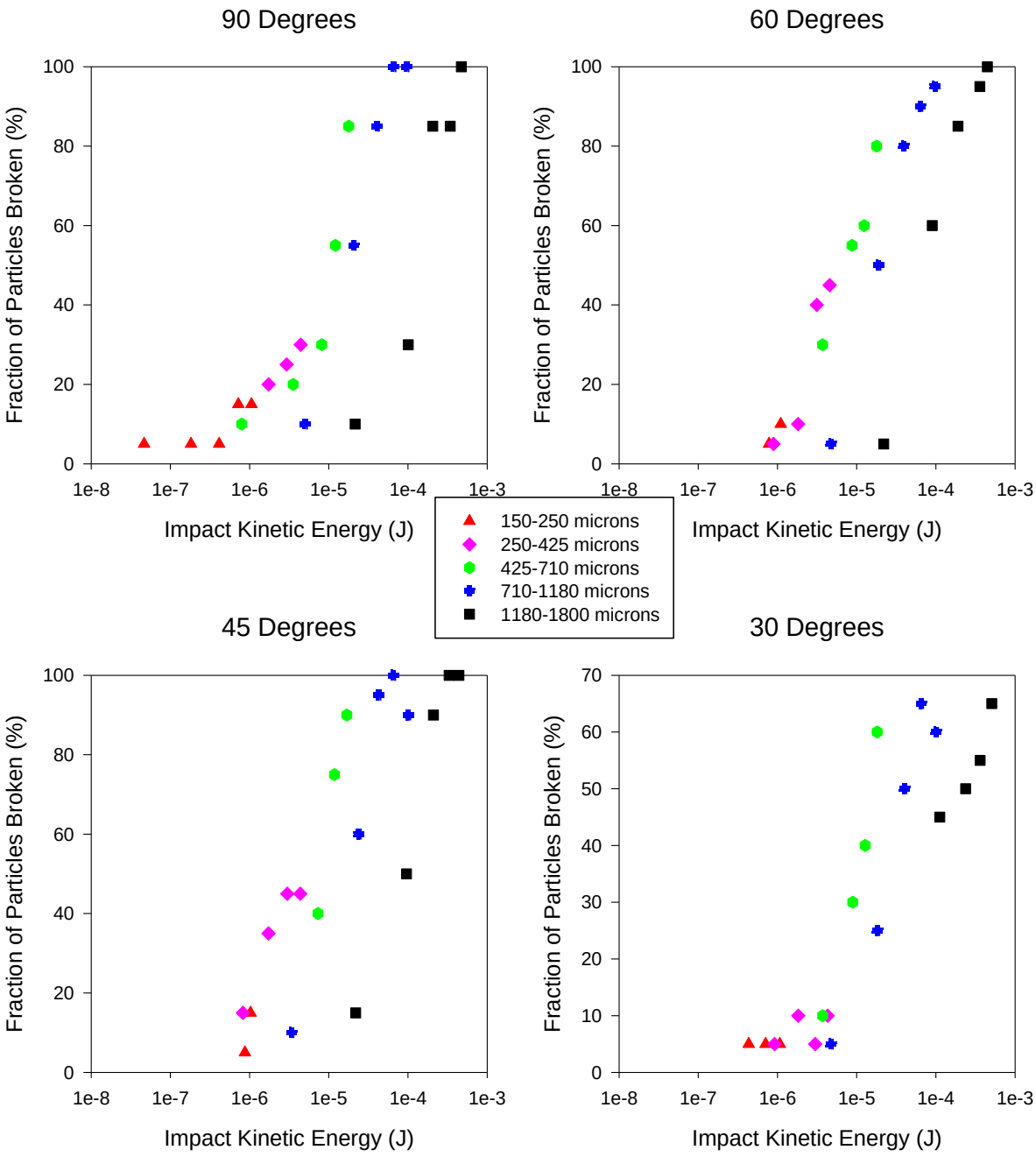

Figure 7.21: Breakage Fraction: LH Formulation

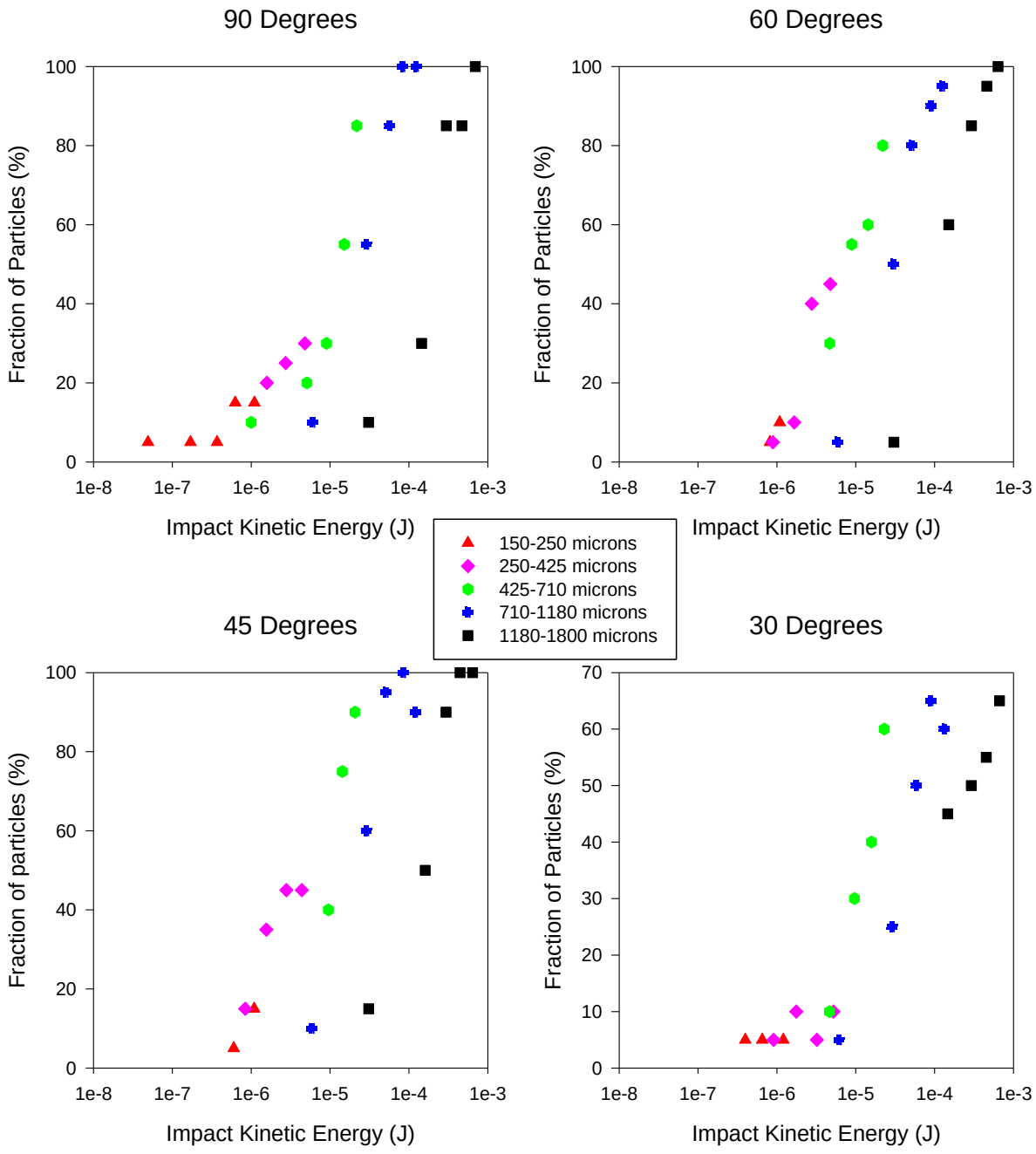

Figure 7.22: Breakage Fraction: LL Formulation

7.4.1.3 Number of Fragments Generated

The number of fragments generated from each particle that suffered breakage are examined here as a function of impact velocity, impact angle, formulation and particle size. Figures

7.23-7.26 show average number of fragments generated, at each impact angle as a function of impact velocity, formulation and particle size. The number of fragments formed from each break increases with both impact velocity and particle size, as would be expected from the breakage fraction results. There appears to be an approximately linear relationship between the number of fragments formed and impact velocity, for the majority of particle sizes across the four formulations and four impact angles.

The relationship between the number of fragments generated and particle size shows a clear trend across all formulations and impact angles, that increasing particle size increases the average number of fragments generated from each particle breaking. This would be expected based upon the literature (§2.9.2.3) and the findings on particle structure (§7.3.1). The smallest particles clearly break into the fewest fragments (often no more than 2).

The statistical analysis of these results showed very similar correlations to breakage fractions, as would be expected (§2.9.2.3). Therefore, particle density and mechanical properties are the key particle properties in determining the number of fragments generated aside from particle size.

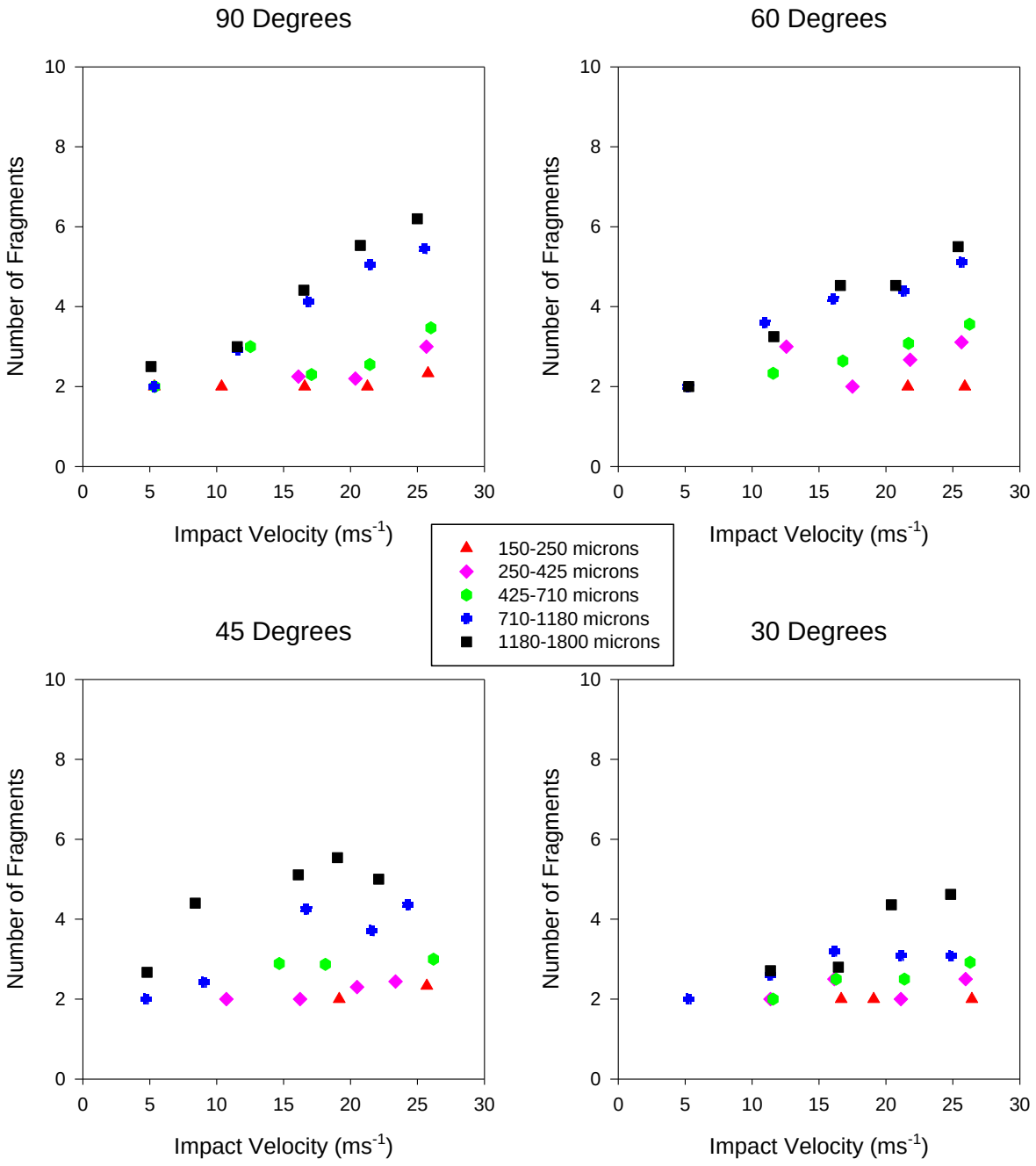

Figure 7.23: Number of Fragments: HH Formulation

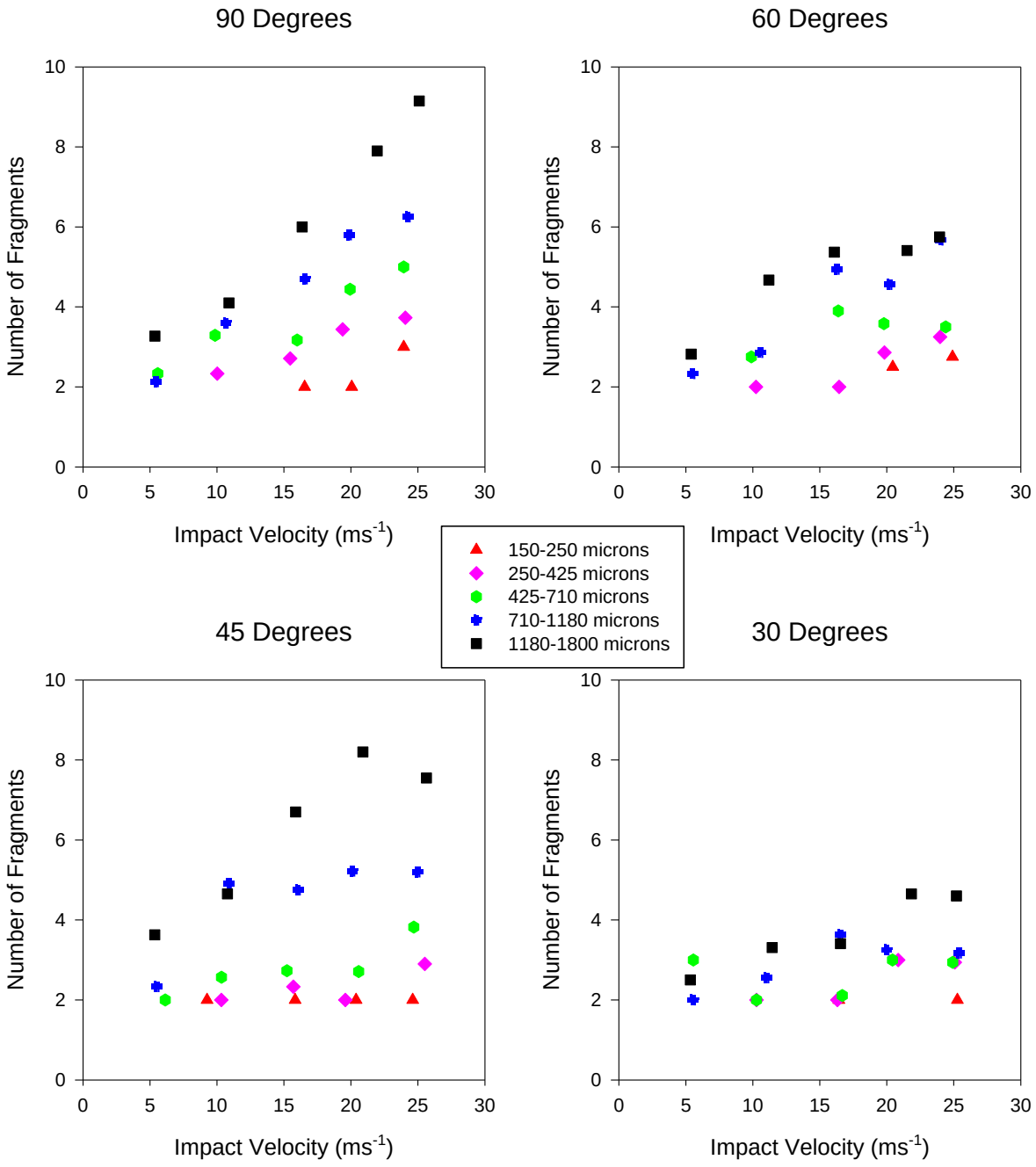

Figure 7.24: Number of Fragments: HL Formulation

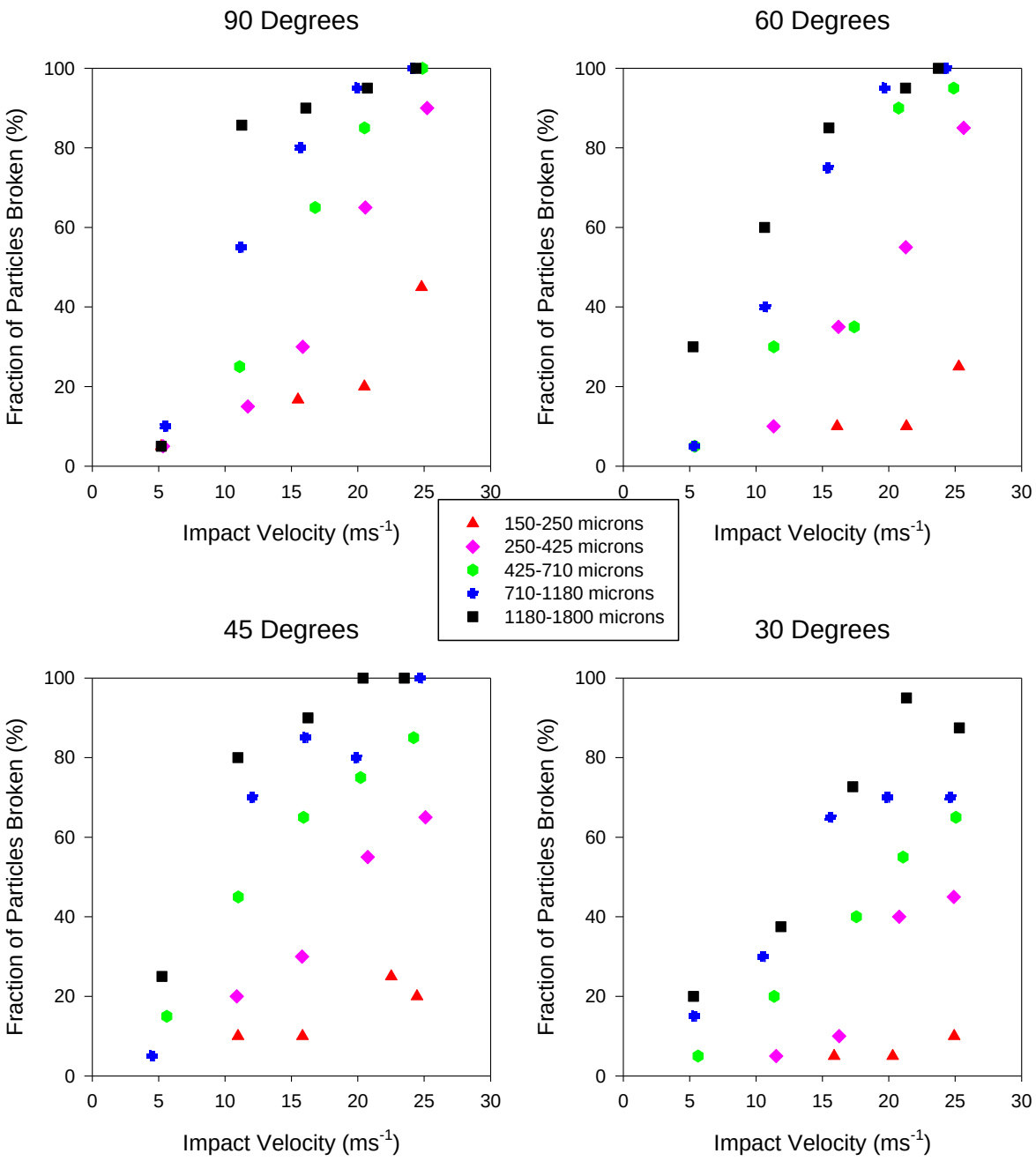

Figure 7.25: Number of Fragments: LH Formulation

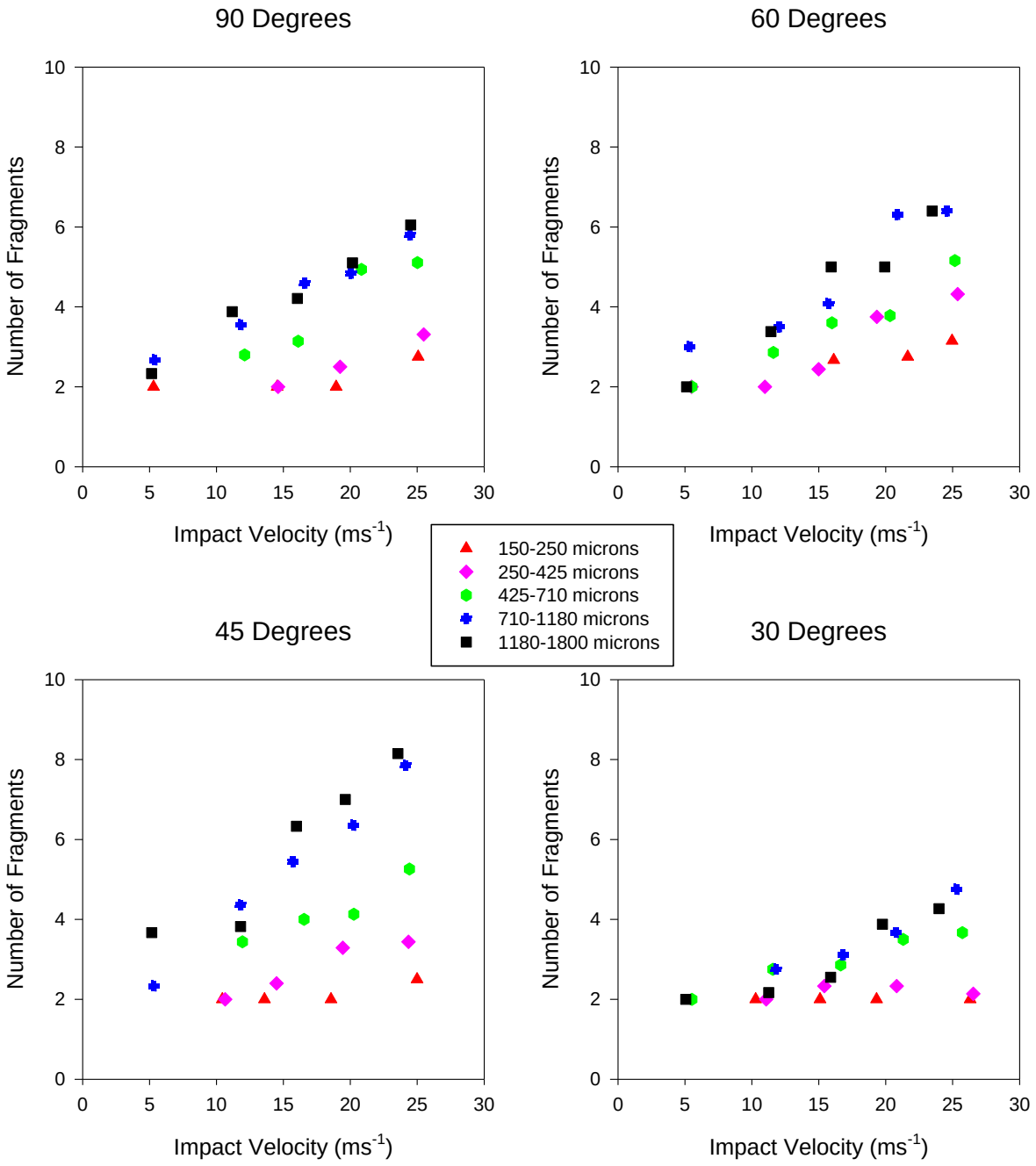

Figure 7.26: Number of Fragments: LL Formulation

7.4.2 Rebound Behaviour

The rebound behaviour of particles that did not break upon impact was examined in terms of restitution coefficient and rebound angle. Owing to the fact that several impact angles were studied, the restitution coefficient was expressed in both its standard form and also as a normal restitution coefficient, that is the ratio of the normal velocity component for rebound to the normal component of the impact velocity. In addition the rebound angle of particles was described in two ways, as an angle from the impact vector (where deviation in either direction was taken as positive) and as an angle from the surface (taken clockwise).

7.4.2.1 Restitution Coefficient

The rebound velocity of any particles not suffering breakage was calculated in the same way as is described for the impact velocities (§3.6.2), this meant the ratio of impact and rebound velocities for each individual particle could be calculated to give the restitution coefficient for all unbroken particles. Figures 7.27-7.29 show plots of the restitution coefficient and Figures 7.31-7.34 show the normal restitution coefficient measured for 5 particle sizes at varying impact velocities and angles for all four formulations.

From these plots impact angle appears to have the greatest affect on values of restitution coefficient, as it increases with increasing obliqueness of the impact angle, as shown by the strong negative correlation (§E.1) and the response models (§E.2). For normal restitution coefficient the effect of angle is also shown, although not as strongly, potentially showing the effect of impact angle on contact mechanics and energy dissipation during impact. The effect of impact angle is also seen in the negative correlation between normal impact velocity and restitution coefficient, there appears to be little correlation between impact

velocity and restitution coefficient, showing that the normal velocity component is driver for changes in restitution with impact velocity. Particle size, LAS and SiO_2 content were all included in the response models (§E.2), but show only a small influence on restitution coefficient compared to impact angle. Literature, including Thornton and Ning (1998) and Fu *et al.* (2004), suggests that two properties that change with formulation, namely hardness and Young's modulus would be expected to have an effect on restitution coefficient. However, the effect of youngs modulus on these results can be seen to not that great in the the response models (§E.2). This may be because the Young's modulus of compressed powder tablets was measured rather than that of actual particles. The hardness of the material was not measured during this work and therefore can not be linked to the restitution results here.

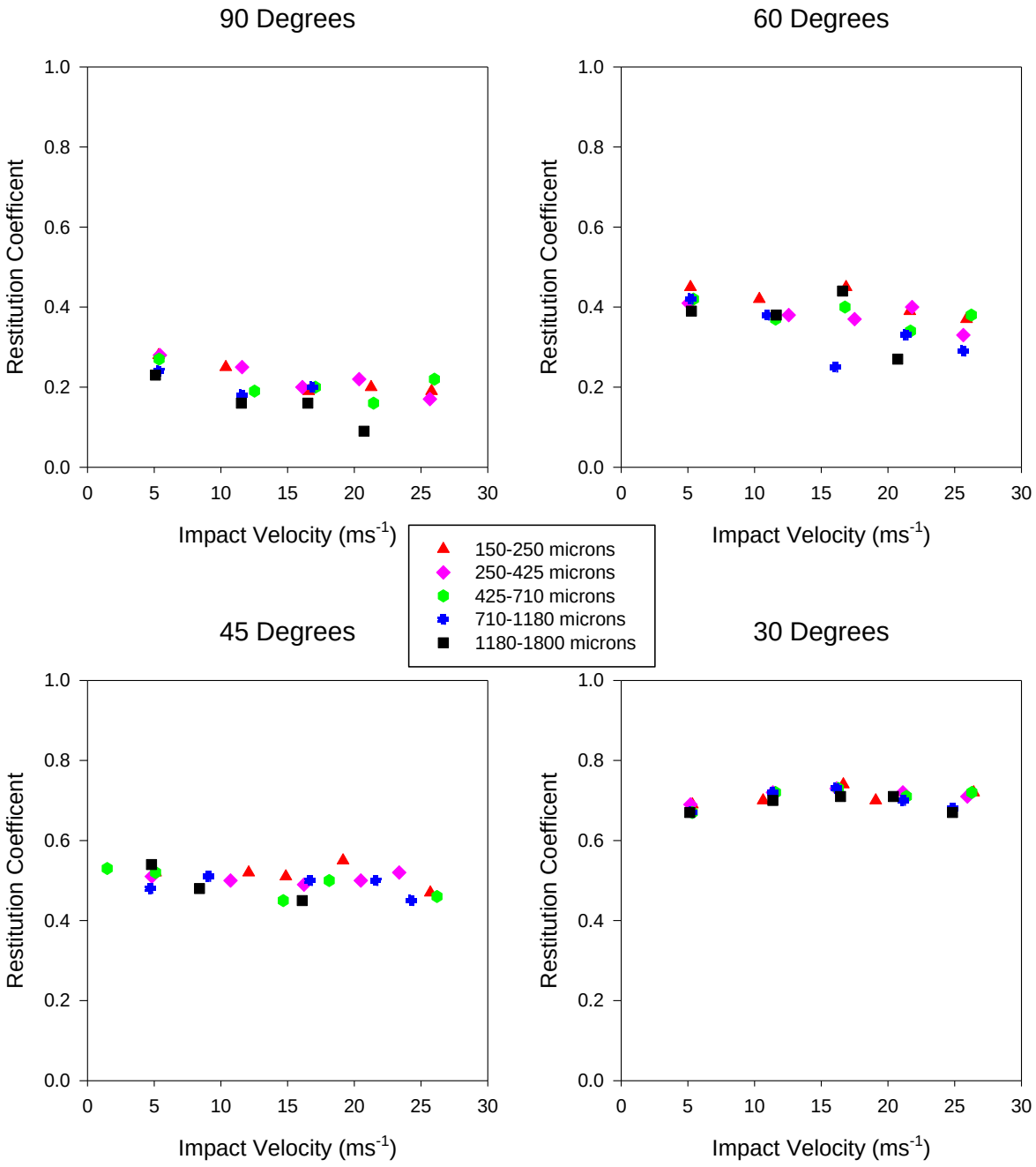

Figure 7.27: Restitution Coefficient: HH Formulation

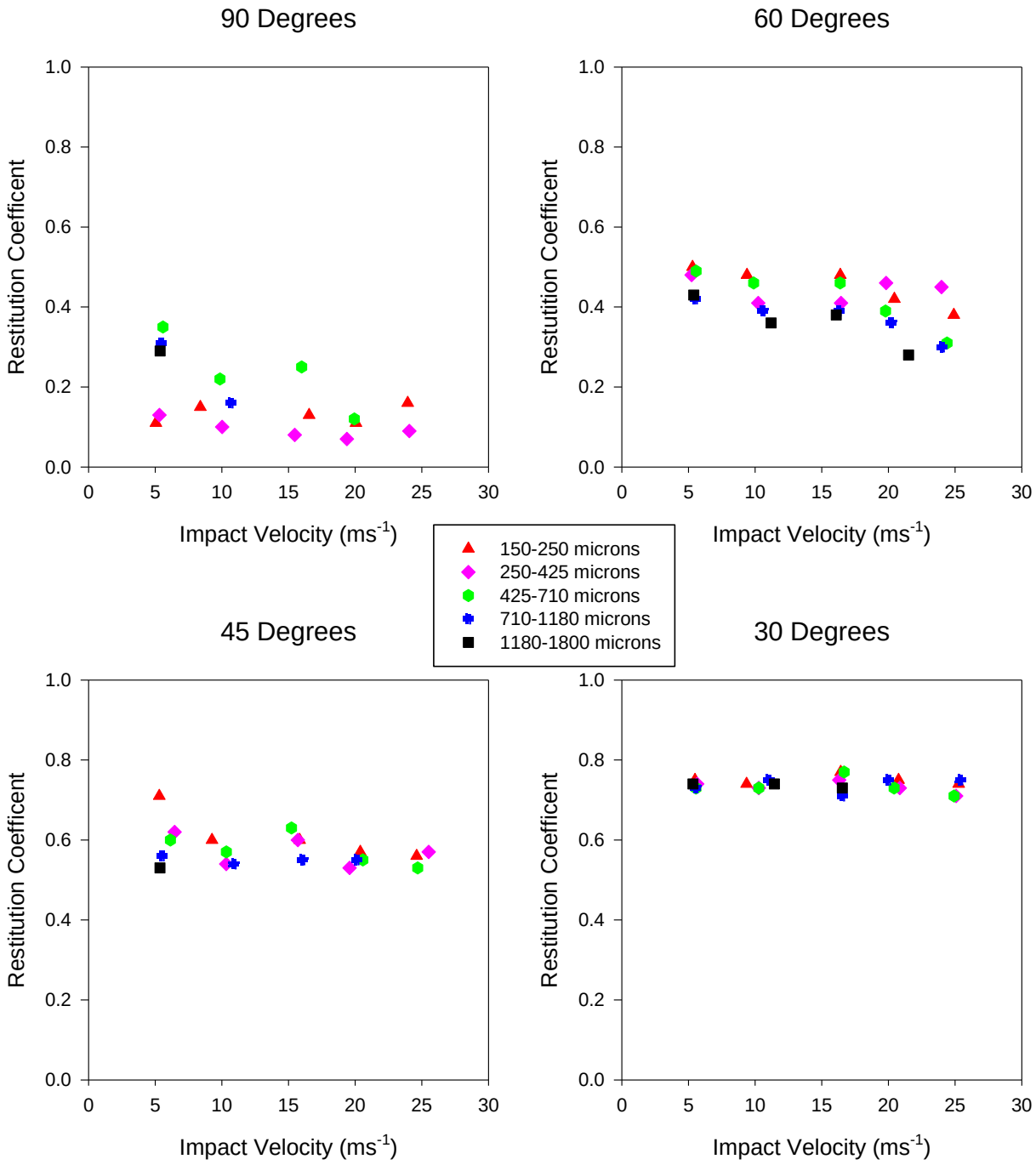

Figure 7.28: Restitution Coefficient: HL Formulation

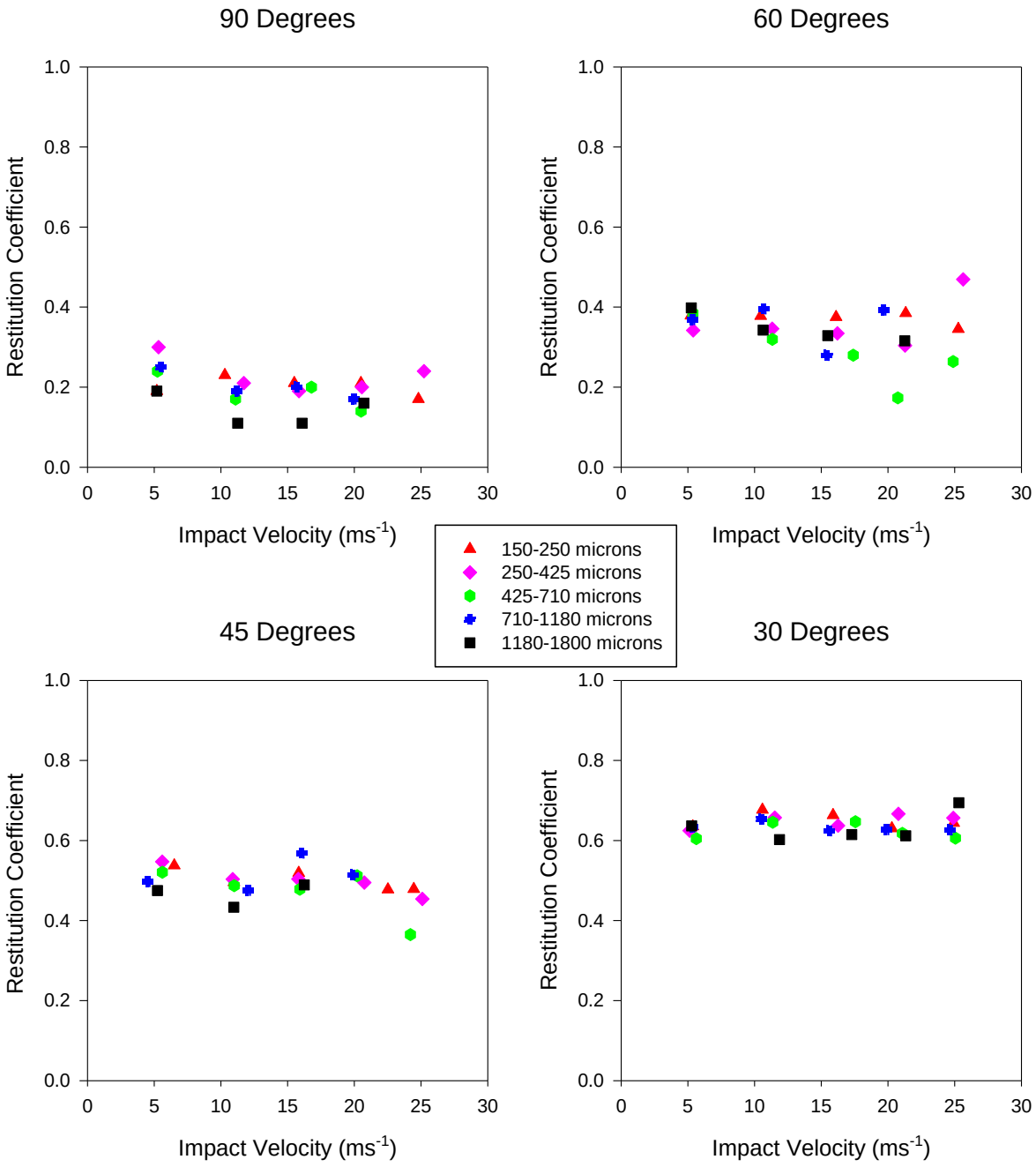

Figure 7.29: Restitution Coefficient: LH Formulation

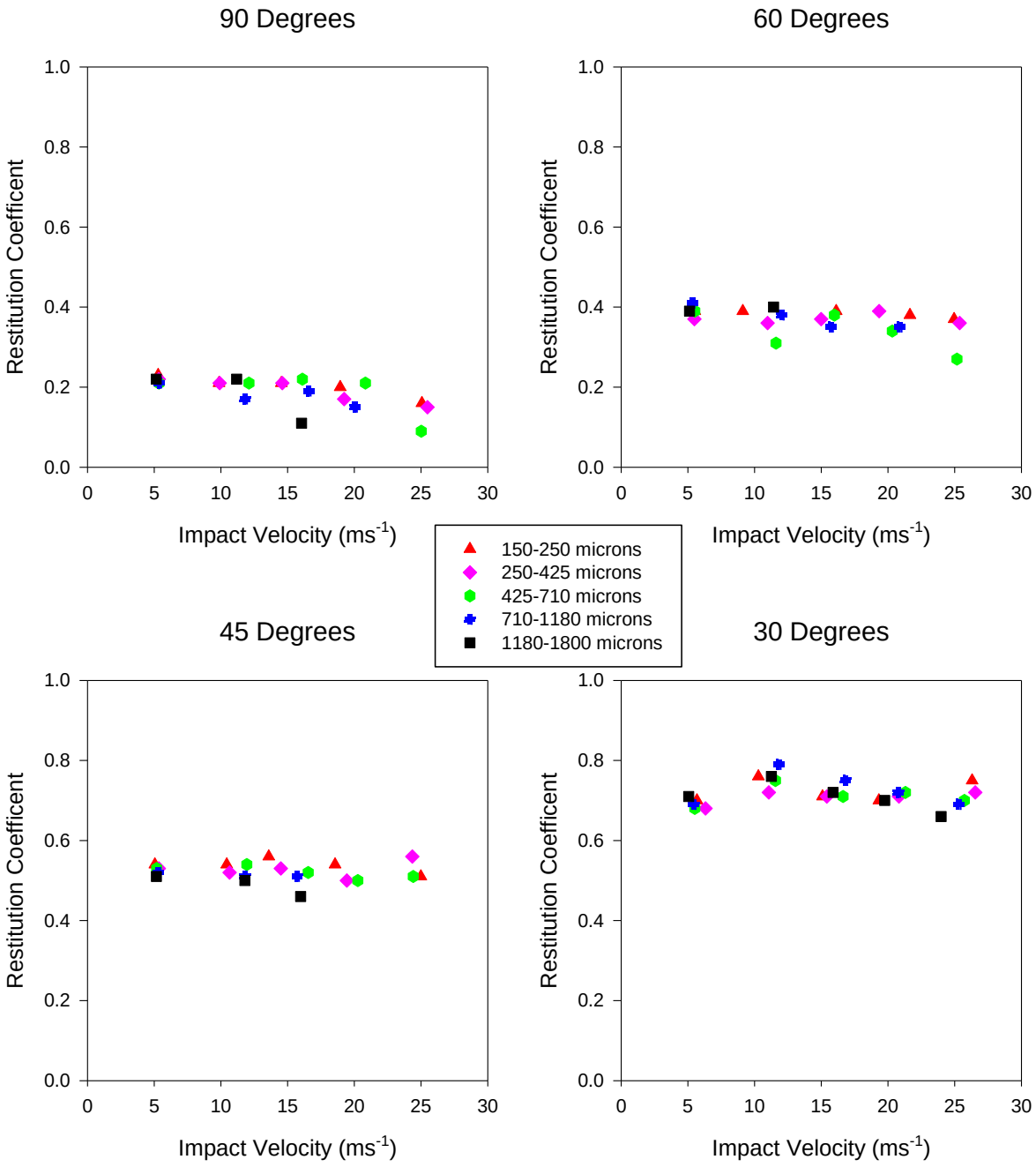

Figure 7.30: Restitution Coefficient: LL Formulation

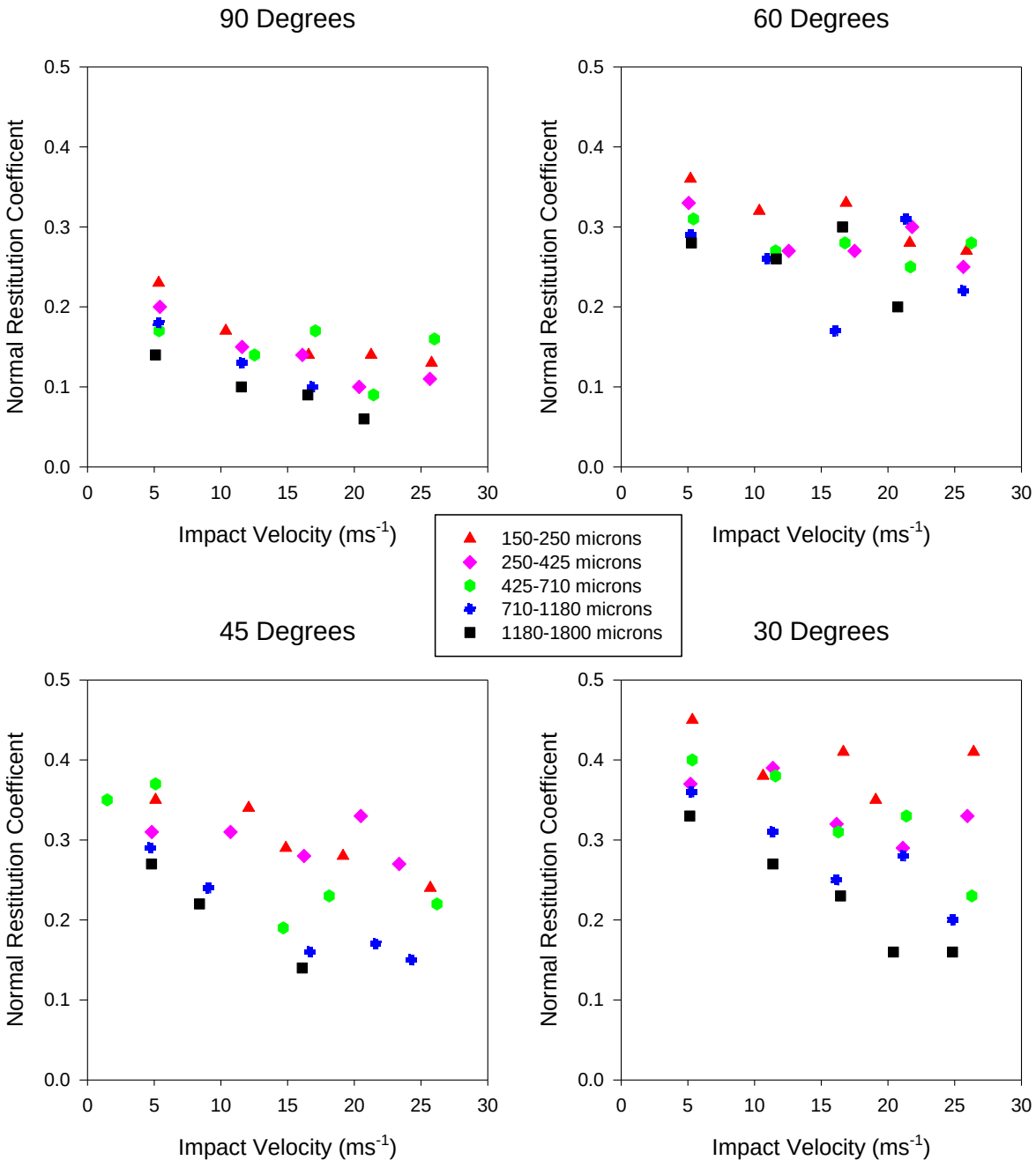

Figure 7.31: Normal Restitution Coefficient: HH Formulation

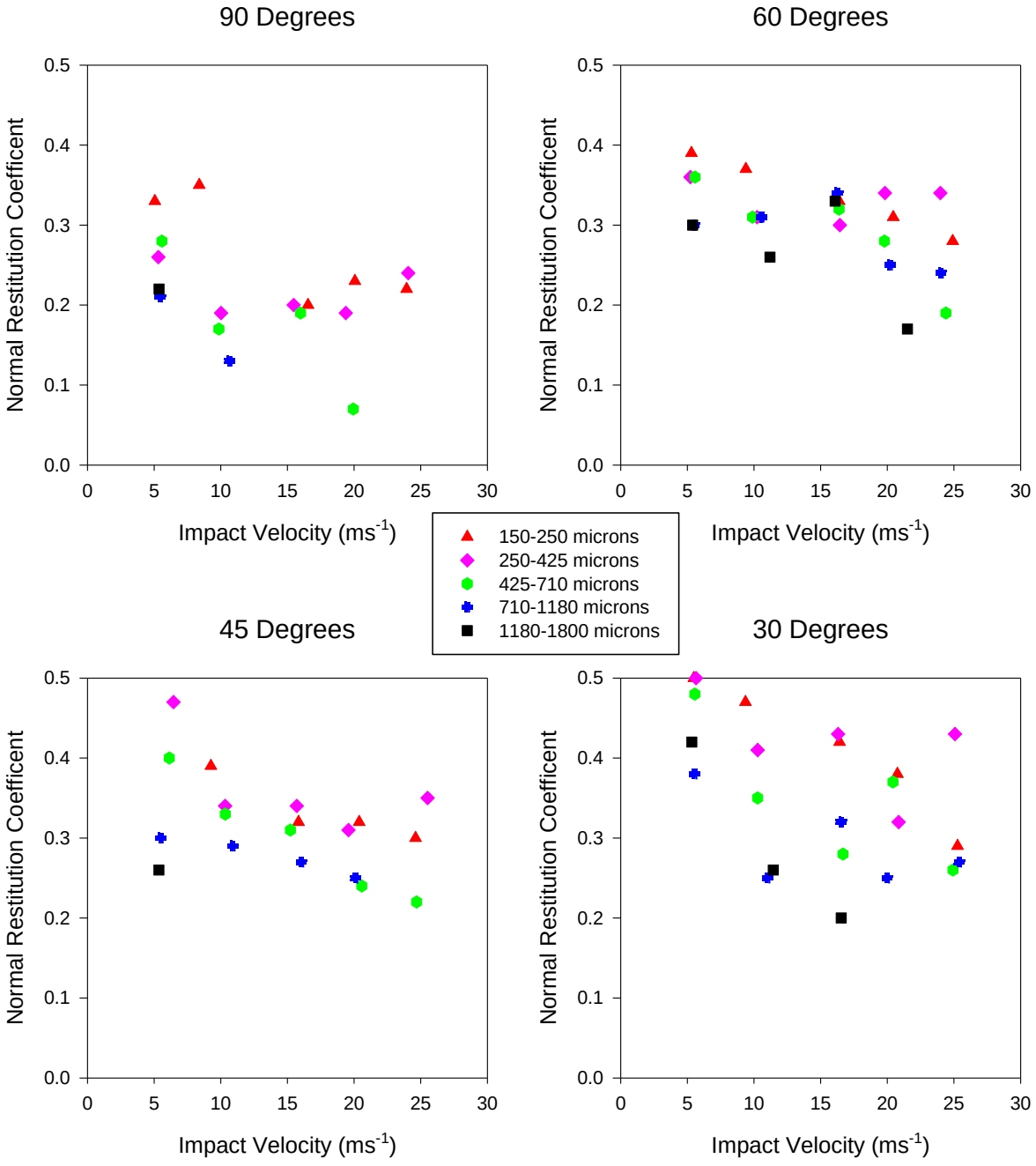

Figure 7.32: Normal Restitution Coefficient: HL Formulation

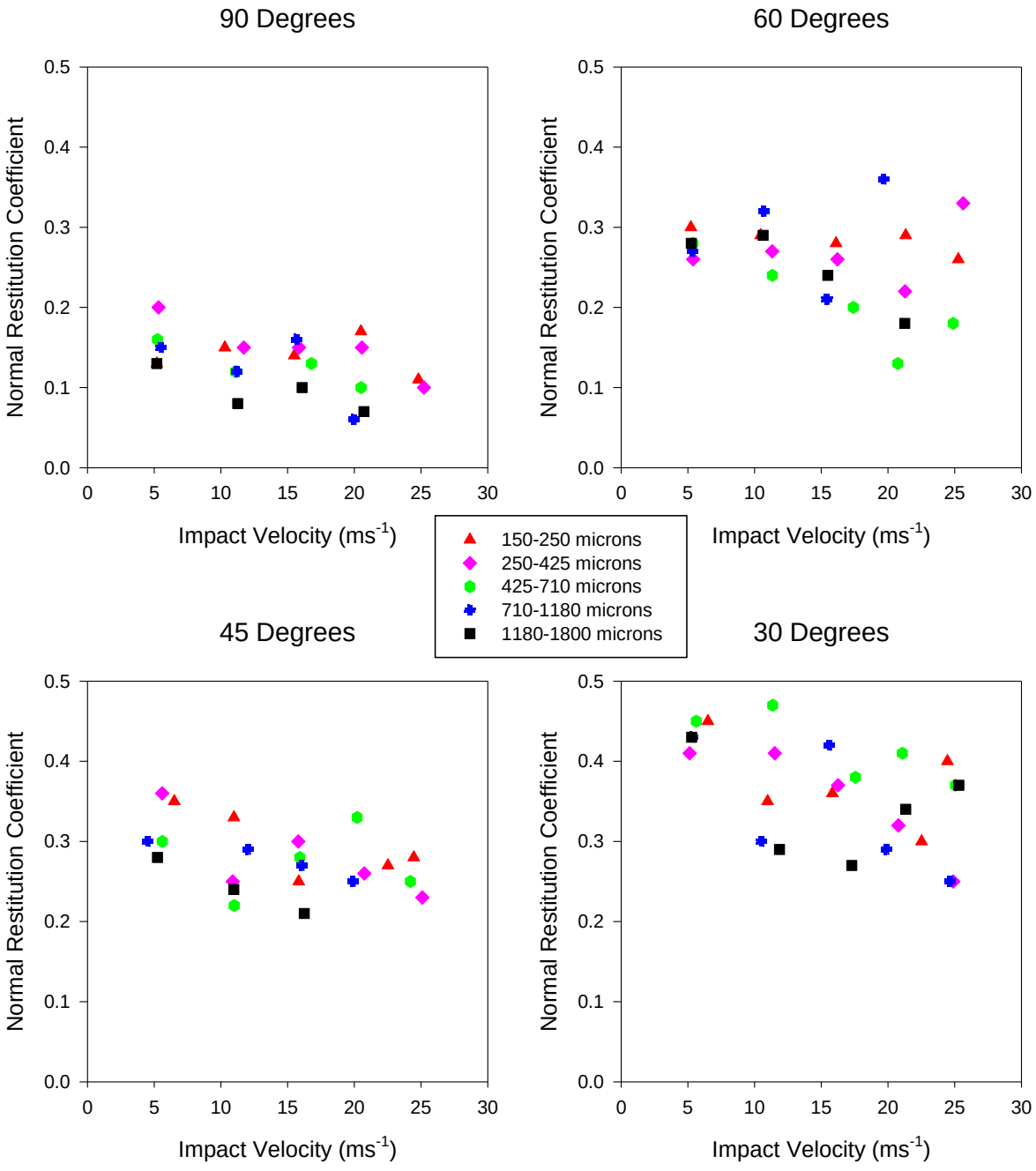

Figure 7.33: Normal Restitution Coefficient: LH Formulation

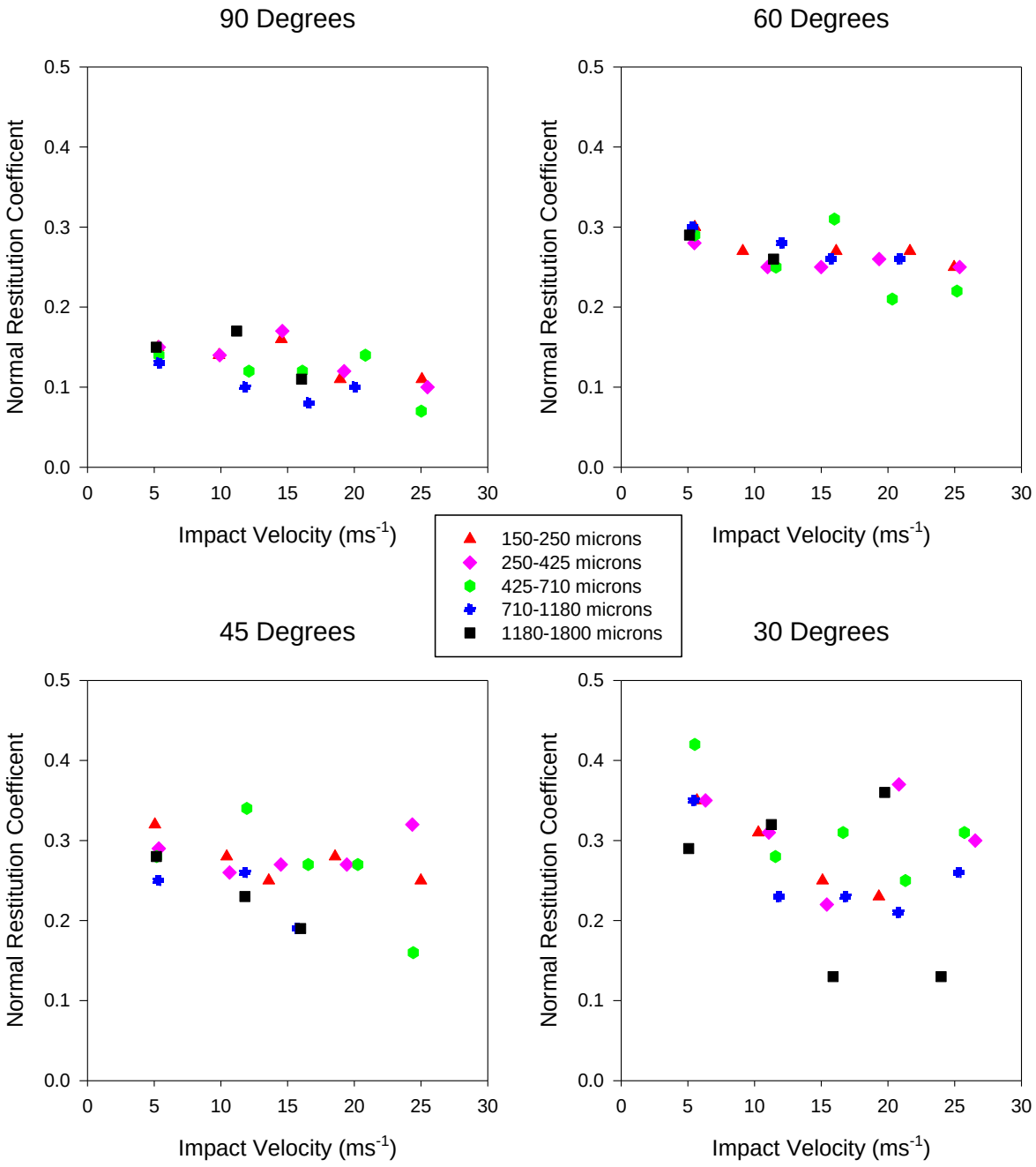

Figure 7.34: Normal Restitution Coefficient: LL Formulation

7.4.2.2 Rebound Angle

Figures 7.35-7.38 show the angle between the impact and rebound vectors of particles changes with formulation, particle size, impact velocity and impact angle. Figures 7.39-7.42

show how the angle between the surface and rebound vector change with the same parameters.

The angle between the impact and rebound vectors seems to be largely determined by the impact angle, with the increasing obliqueness of the impact increasing this angle, this is shown in the statistical analysis (§E.1 and E.2). The angle between the rebound vector and the surface also increases with increasing obliqueness of the impact angle. The only other parameter to play any kind of significant role is normal impact component, which appears to decrease rebound angle as it increases. As with restitution particle properties were found to have little effect, particle size, LAS and SiO_2 content were all included in the response models (§E.2), but show a little influence on rebound angle.

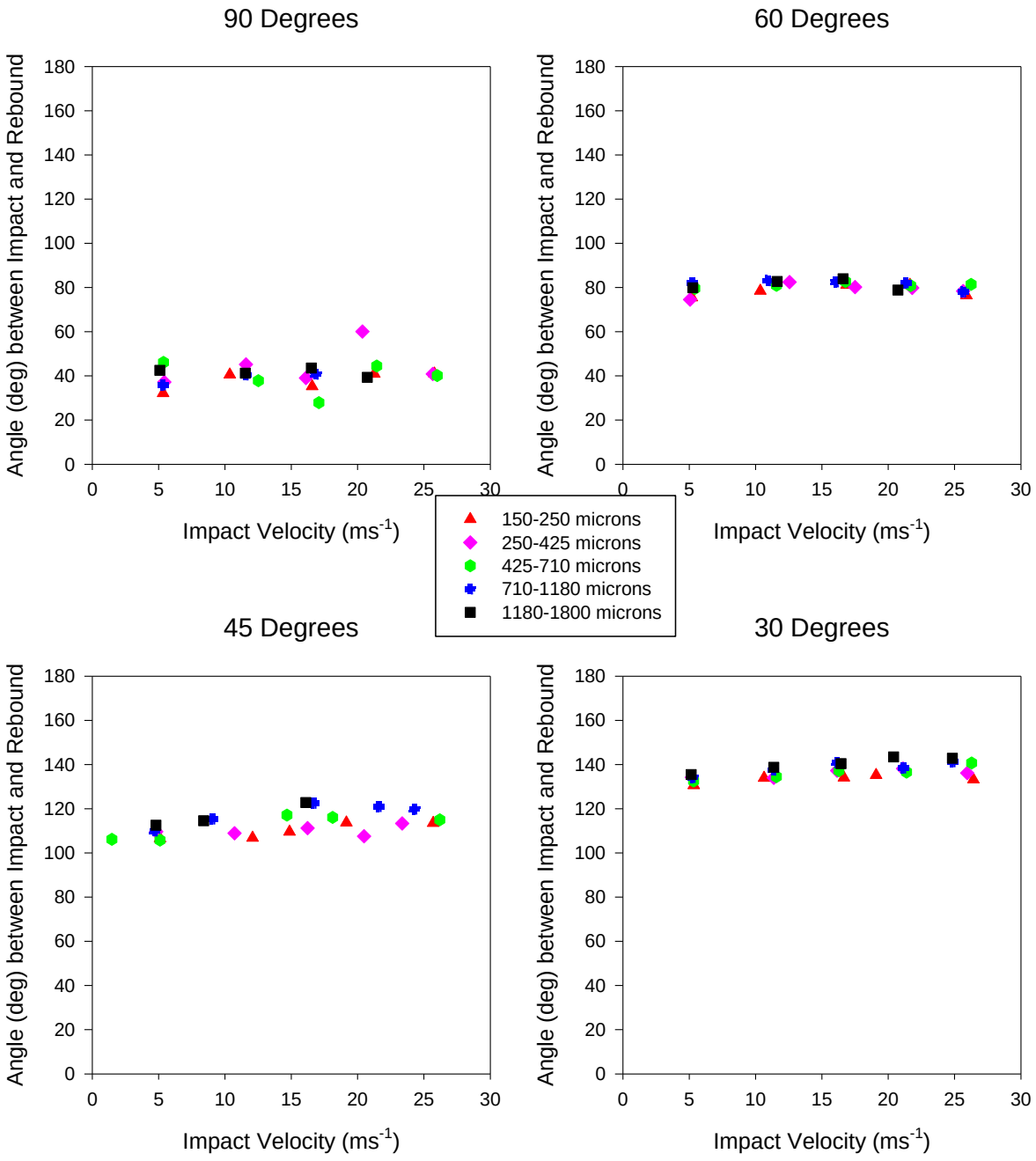

Figure 7.35: Angle between Impact and Rebound Vectors: HH Formulation

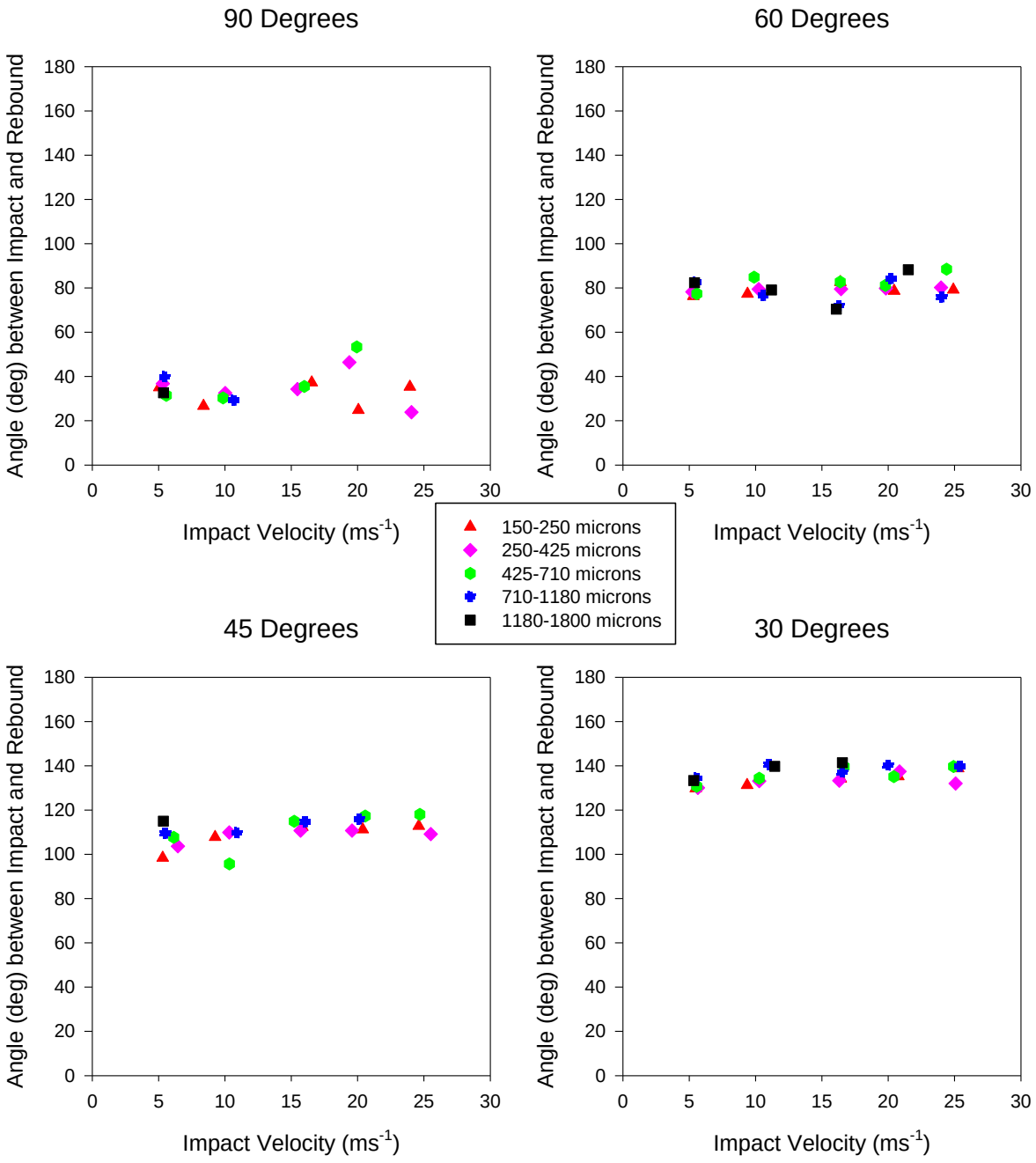

Figure 7.36: Angle between Impact and Rebound Vectors: HL Formulation

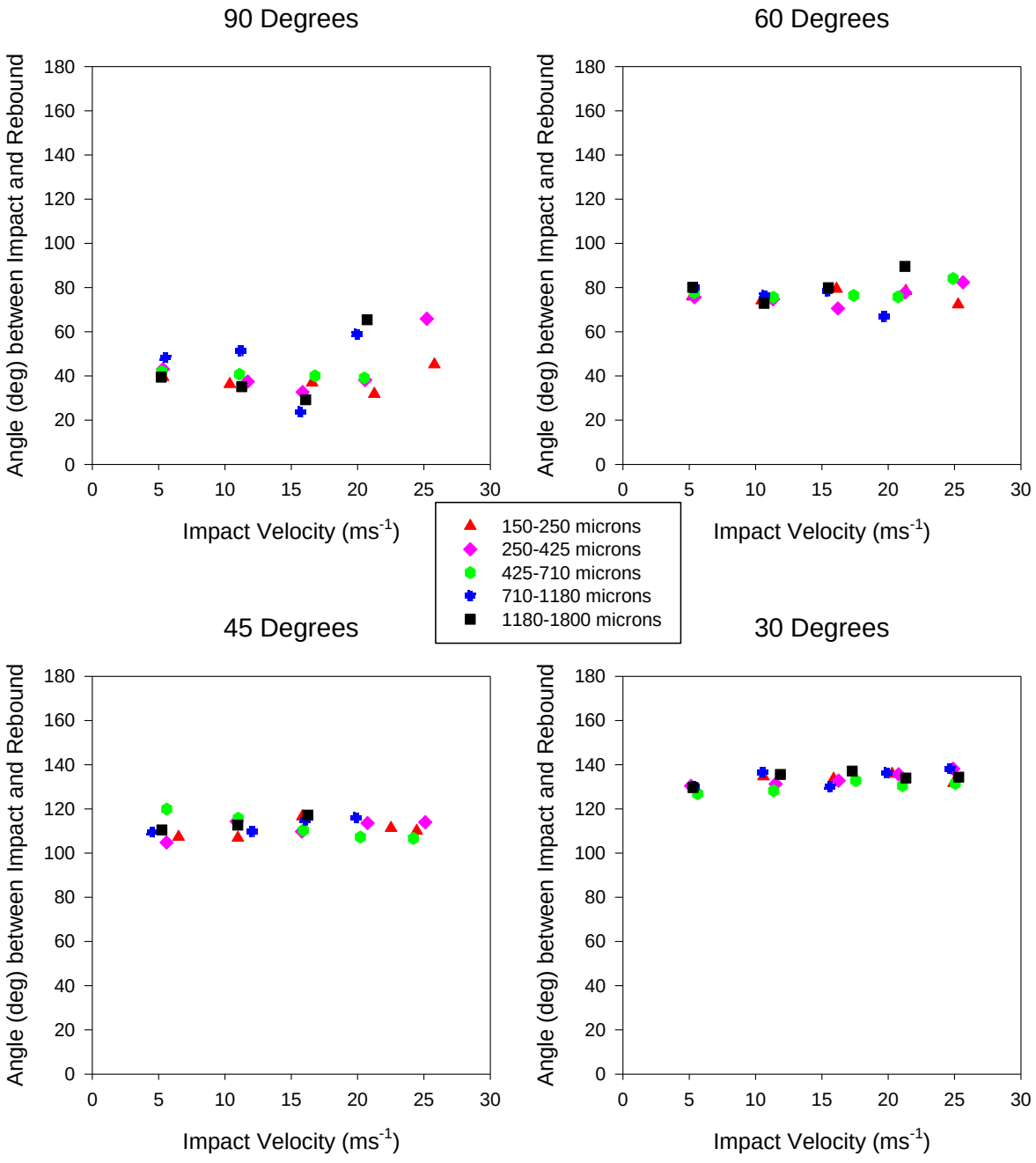

Figure 7.37: Angle between Impact and Rebound Vectors: LH Formulation

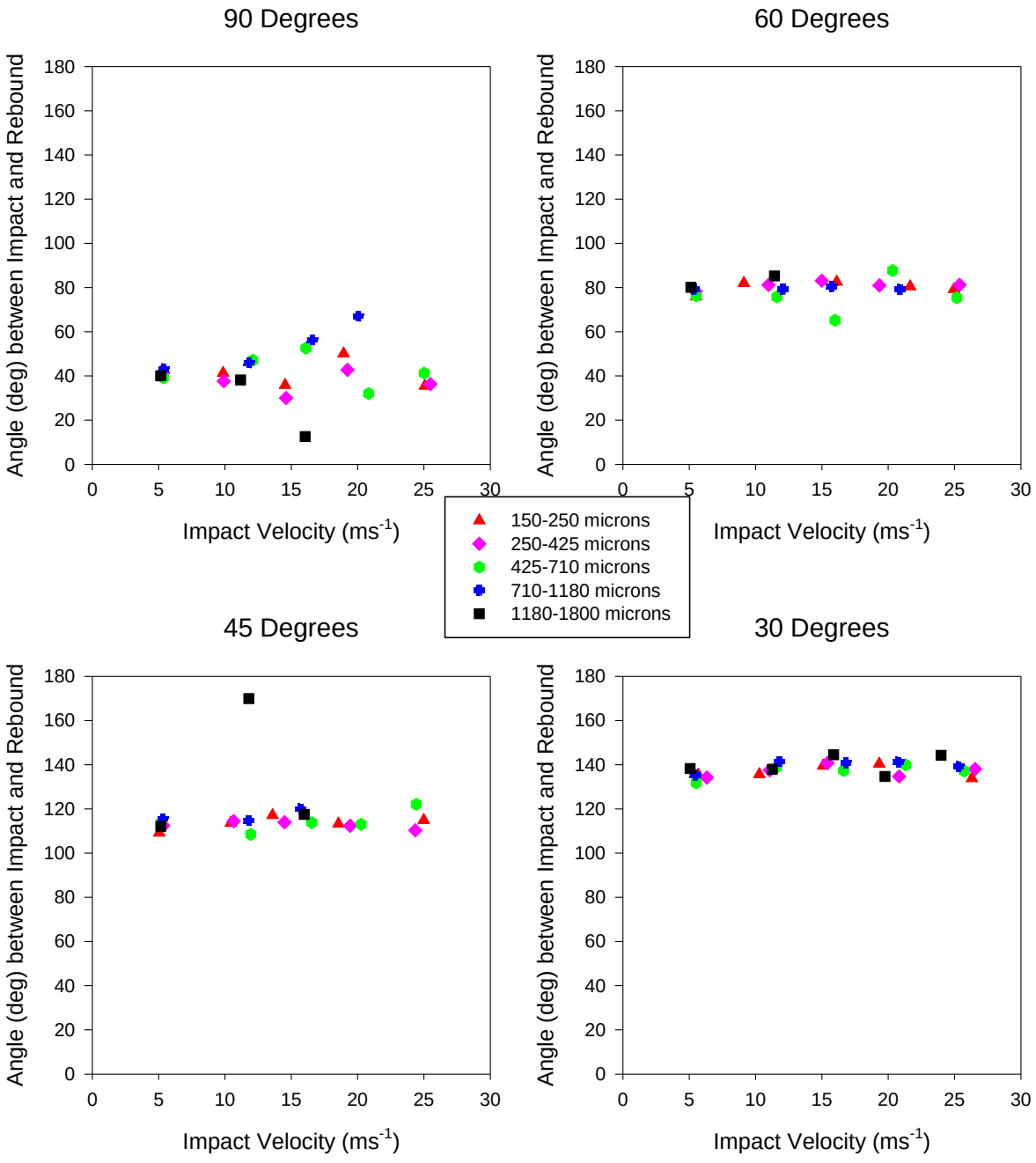

Figure 7.38: Angle between Impact and Rebound Vectors: LL Formulation

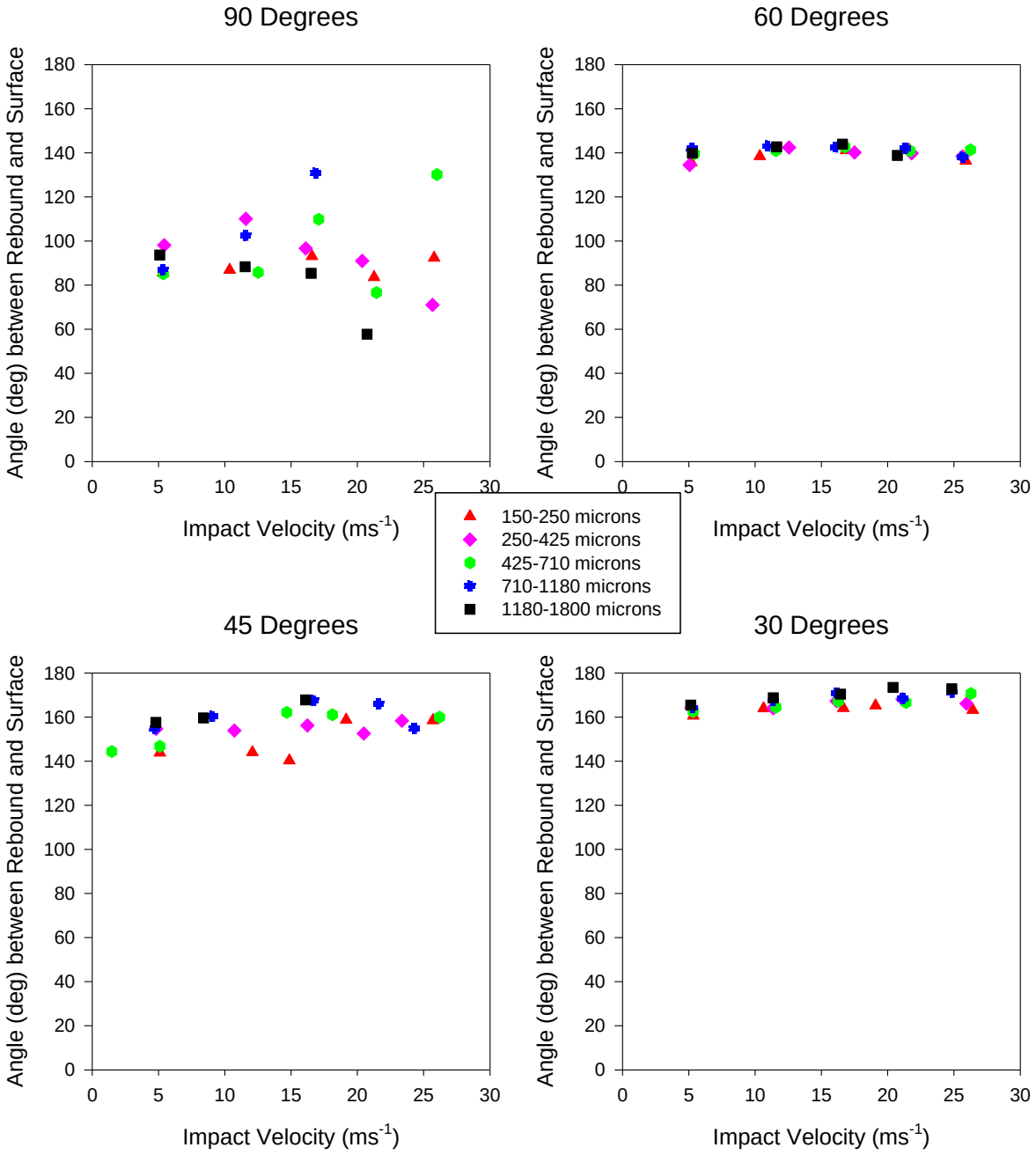

Figure 7.39: Angle between Surface and Rebound Vector: HH Formulation

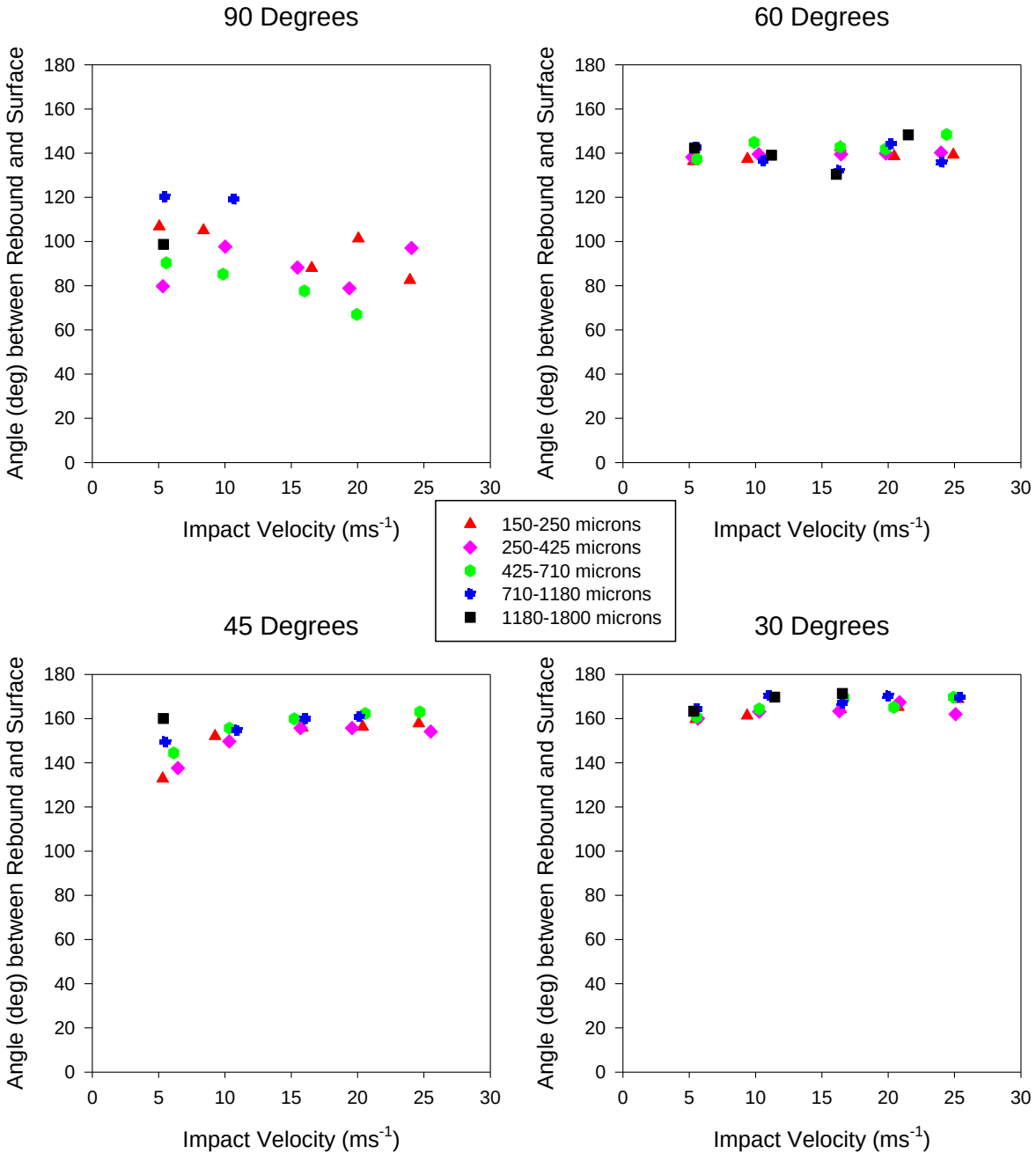

Figure 7.40: Angle between Surface and Rebound Vector: HL Formulation

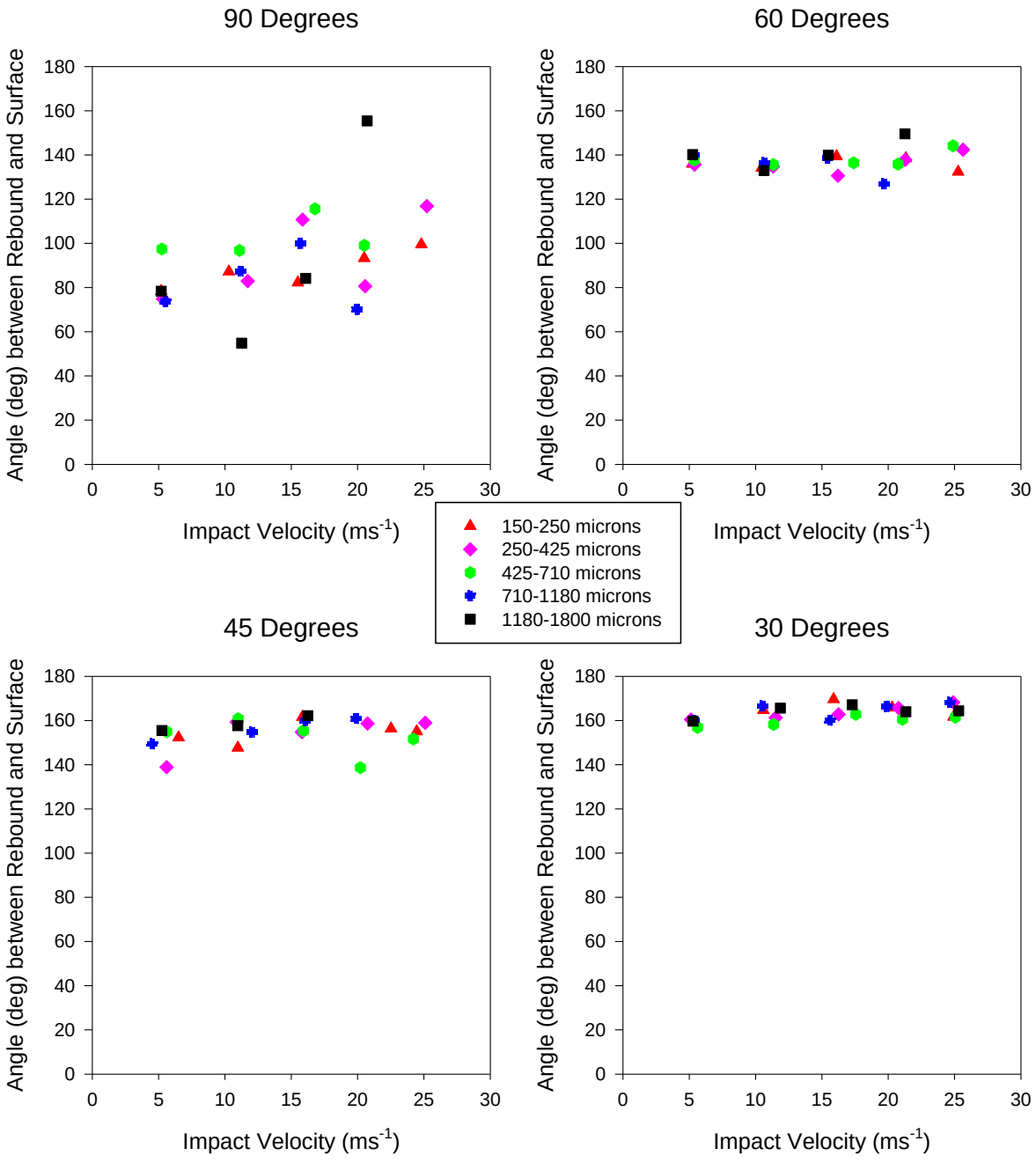

Figure 7.41: Angle between Surface and Rebound Vector: LH Formulation

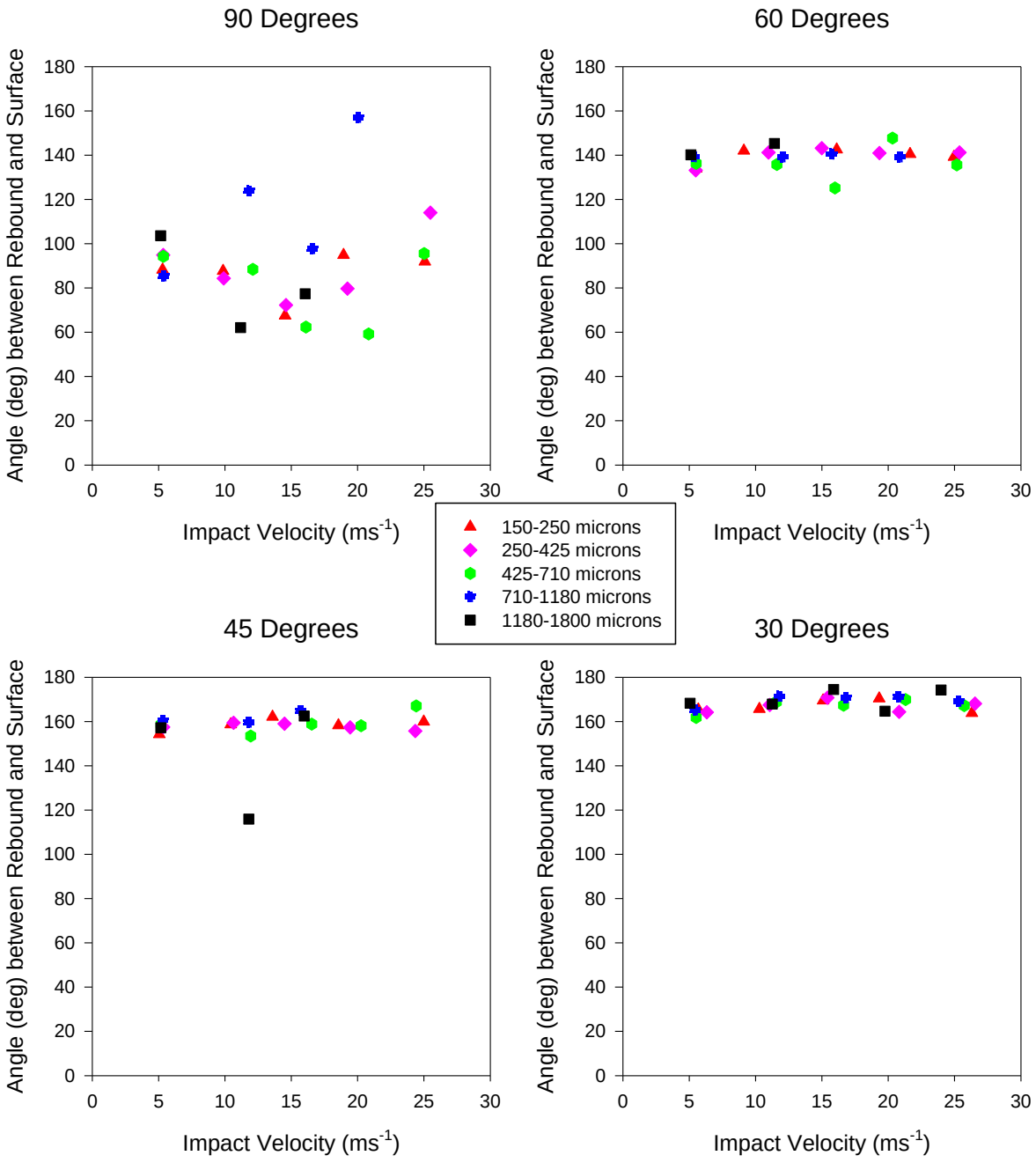

Figure 7.42: Angle between Surface and Rebound Vector: LL Formulation

7.5 Conclusions

The physical and mechanical properties of particles are key to determining their impact behaviour, in terms of restitution, breakage, deposition, or a combination of these, and therefore determine the collision success rate of particles impact on the dryer walls. Physical and mechanical parameters of a range of formulations of detergent powders were studied as a function of particle size. This has revealed a mutual dependence of all properties on both formulation and particle size. It is clear that most, if not all physical and mechanical properties are interlinked.

The microstructure, morphology and structure and appearance of granules was found to vary with both particle size and formulation, with all particles above 425 μm being formed of two or more agglomerated particles and those below this size being a mixture of single dried droplets, fragments of broken particles and smaller agglomerates. The total moisture content and equilibrium Relative humidity, both were found to vary with particle size and formulation, with the largest particles having the largest total moisture contents. Similarly the density of the powders were found to vary with formulation and particle size.

The mechanical properties of powders were found to vary greatly with formulation but less so with particle size. The influence of particle structure was found to reduce the yield stress values obtained by one or two orders of magnitude. This change also highlighted the effect of formulation and particle sizes on the yield stress of detergent granules, through their influence on the microstructure developed during spray drying.

The fraction of particles suffering breakage was seen to vary from zero to 100%. Increasing particle size and impact velocity was found to increase the fraction of particles suffering

breakage for all formulations. The number of fragments formed when a particle broke also increased with both particle size and impact velocity. The relationship between the number of fragments from each breakage and impact velocity was considered to be roughly linear for each particle size. The SiO_2 content was found to have a significant effect on particle breakage, with mid levels of this parameter producing the smallest amount of breakage.

Restitution coefficient was influenced greatly by impact angle, with normal velocity component being the only other significant influence. The effect of formulation and resulting particle properties appears to be minial for the restitution coefficient. Rebound angle was also found to be influenced by impact angle and normal velocity component only.

This work has investigated the physical and mechanical properties and their effect on the impact behaviour of spray dried detergent powders generating data on how breakage and restitution coefficients are affected by impact velocity, impact angle particle size and formulation. However no visible deformation of particles was observed and no particles were found to stick to the target.

Chapter 8 – Conclusions

8.1 Summary of Research

The thesis aim was to develop a detailed understanding of wall deposition during the spray drying of detergent powders and the influence of both process and product parameters upon it. The phenomena was broken down into two stages, firstly the movement of particles striking the wall and secondly what occurs during the impact with the wall. Particle and fluid dynamics were utilised in the first stage, whilst the second stage was investigated by examining the physical and mechanical characteristics of detergent particles and their effect on impact behaviour.

8.2 Wall Deposition

Macro scale observations revealed a variation in deposition with location within the dryer in terms of amount and appearance of deposits. The thickest and most uneven deposits were seen closest to the spray nozzle, with deposits becoming thinner and smoother moving away from the nozzle. Micro scale investigations of deposits revealed a variation in their micro-structures, potentially explaining the trends seen on the macro-scale observations.

Quantitative studies of wall deposits showed that amounts of between 1.0 and 10.0 kgm^{-2} were deposited. This was translated into a yield value, with the amount of slurry lost to wall deposition calculated by extrapolating deposition rates for different parts of the dryer to form a total amount of deposition over the whole dryer. This yield value was estimated to vary between 2.0 and 10.0% of the slurry sprayed.

Wall deposition was also shown to be time dependent, with a decrease in deposition rate over a period of 30 minutes, from a peak initial rate of around 0.01 $kgm^{-2}s^{-1}$. This is believed to be caused by a narrowing of the gap between the rate of deposition of material and the rate at which material is re-entrained into the air flow. Particle Image Velocimetry observations revealed the mechanisms of both deposition and re-entrainment at work.

8.3 Fluid Dynamics

Air flow patterns were studied at two different axial positions and three different air flow rates. Time averaged velocity flow fields obtained for velocity magnitude and the radial and tangential velocity components, show that the velocity values obtained for tangential velocity are very similar to the velocity magnitude values calculated for all experiment conditions, demonstrating that tangential velocity dominates movement in the horizontal plane. Values of velocity magnitude observed were between 0.5 and 2.5 ms^{-1} in the lower position and 0.5 and 1.8 ms^{-1} in the higher position. Tangential velocity values were almost identical to these. Radial velocities were found to change direction across the area investigated, with flows towards the wall (positive values) in the area closest to the oncoming flow (right side) and flow away from the wall (negative values) in the area furthest from the oncoming flow (left side). The values of radial velocity range from between -1.0 and 0.5 ms^{-1} in the lower position and -0.06 and 0.30 ms^{-1} in the higher position. The change in radial flow direction may be an effect of the presence of the mirror box in the flow. The resulting velocity profiles compared well to literature results.

Flow in the lower position was found to exhibit the largest amounts of turbulence with turbulence intensity values of 4 to 10% of the mean velocity magnitude, compared to

between 2 and 7% in the higher position. Attempts to identify periodicity within these velocity signal plots gave an indication of periods in the area of 4 seconds, however, clear periodgrams were not produced.

8.4 Particle Dynamics

Particle dynamics were studied through the use of PIV to capture images. A method for thresholding images was developed, such that binary images could be obtained containing only particles contained with the lasersheet, allowing image analysis and PIV cross-correlation to obtain data on particle characteristics and dynamics.

Particle size (mean projected area diameter) was found to vary between 200 and 900 μm, particle concentration between 1.5×10^6 and 3.5×10^7 particles.m^3, volume fraction between 2×10^5 and 7×10^4 and mean velocity magnitude between 0.05 and 0.5 ms^{-1}. The observation of how these parameters change with axial position relative to the spray nozzle led to the conclusion that two different flow regimes exist inside the dryer. Below the nozzle the flow contains a higher loading of larger particles, which move more slowly in the horizontal plane, in a wide range of directions. Above the nozzle a sparser flow of smaller particles moving faster in the horizontal plane, consistently parallel to the wall, was observed. An unexpected asymmetric distribution of particle size, concentration and volume fraction in the tangential direction was observed in experiments below the nozzle. Two reasons were hypothesised, disruption in air flows caused by the mirror box and re-entrainment of deposited material on the mirror box.

Flow fields of particle velocities showed variation in both velocity magnitude and direction with slurry and air flow rates and position within the dryer. The largest velocities seen were

above the nozzle, where increases in slurry and air flow rates resulted in larger velocity magnitude values, with velocity direction remaining constant, parallel to the wall. Below the nozzle, velocity magnitude values were smaller and changed less much less with slurry and air flow rates, the direction of particle velocities appeared to be more variable in this position.

In both flow regimes, above and below the nozzle, particle size, concentration and volume fraction were all shown to vary with time. Flow fields produced from particle velocities were also shown to vary with time, with velocity magnitude varying more above the nozzle and velocity direction varying more below the nozzle. One key conclusion is the importance of selecting the correct temporal resolution for all experiments involving particle dynamics in detergent spray dryers.

8.5 Particle Characterisation and Impact Behaviour

Physical and mechanical parameters of a range of formulations were studied, which revealed a mutual dependence of all properties on both formulation and particle size. It is clear that most, if not all physical and mechanical properties are interlinked. The same formulations and particle sizes were impacted at a range of velocities and angles, results revealed that the fraction of particles suffering breakage ranged from 0 to 100%, with impact kinetic energy and particle size the largest effects and SiO_2 content and impact angle having significant influence. Restitution coefficients ranged from 0.1 to 0.8, mainly influenced by impact angle, but with signicant effects caused by impact velocity, particle size and formulation.

8.6 Implications of this research for the sponsoring company (Procter & Gamble)

This thesis represents the first study into wall deposition in the spray drying of detergents and as such has implications and potential applications for P&G during manufacture of current products and when developing new products.

The development of techniques has enabled the company to systematically study the effect of formulation (slurry/powder properties) and dryer operator conditions on wall deposition. The observation of discoloured deposits around the air inlets aids understanding of charring, aiding the reduction of this issue. The finding that wall deposition is time-dependent has implications in terms of production scheduling as the majority of deposition appears to happen in the initial period of operation, meaning that prolonged periods of operation will lose a lower proportion of slurry sprayed to deposition than short periods of operation between cleaning out of the dryer. Another point of note is the possibility of washout water being a cause or seed for deposition within the dryer.

The study of fluid and particle dynamics has demonstrated the complex and time dependent nature of each of these as well as their interaction. These factors stress the complexity of modelling techniques, such as CFD, required to conduct accurate simulations of detergent spray dryers. The observation that airflow patterns are heavily influenced by the air flow rate through the dryer is of importance in the selection of operating conditions for spray dryers. It is common for air flow rates and air temperatures to be changed to accommodate different amounts of drying required with different slurry flow rates, however it is clear that changing air flow rates affects particle movement, changing residence times and wall collision frequency which affects particle formation and thus product morphology and

properties. In addition the change of air flow patterns with axial position in highlights the need for more detailed thought on the location of spray nozzles. The observation of deposition and re-entrainment highlights the complex nature of particle-wall interaction and how this influences product morphology and properties, meaning simulations of spray drying cannot neglect this if they are accurately predict product properties.

Investigation of particle physical and mechanical properties has shown how these change with particle size and formulation and that they are largely interdependent. The impact behaviour of powder product influences processability of powder, affecting product quality and process reliability. The effect of particle size on these highlights the need to understand atomisation and the mechanics such as wall deposition (and re-entrainment) which affect particle size, and thus particle properties, allowing optimisation of particle size to improve product quality and process reliability. The values of particle properties and impact behaviour parameters will enable the application of modelling techniques such as DEM in the development of simulations of post-dryer powder handling systems to again improve product quality and process reliability.

8.7 Future Work

Development of a non-intrusive method for measuring wall deposition is a crucial next step in understanding this phenomenon. Ultrasonics is the most likely technique to achieve this as described by Hassall (2008). Further observations of wall deposition via PIV or another imaging system would allow the mechanisms of deposition and re-entrainment to be further understood.

This work has developed an understanding of particle-wall interaction and how this is influenced by air flow patterns and dryer operating conditions, however this needs to be expanded to cover the whole area of the dryer. An improvement would be to utilise a non-intrusive technique, such as LDV, thus ruling out the possibility of the measurement affecting the fluid and/or particle dynamics being observed. The temporal and spatial resolution used for these measurements needs to be carefully selected in order to capture the time dependence of both fluid and particle dynamics within the dryer. Improved understanding of fluid and particle dynamics would aid development of more accurate CFD simulations.

The missing piece of work on understanding wall deposition in spray dryers is to understand how the physical and mechanical properties of detergent particles change as they dry whilst travelling through the dryer. Generating droplets of detergent slurry without using a pressure nozzle is difficult, and therefore so is obtaining small amounts of droplets or semi dry particles to characterise and impact in a controlled environment. To overcome this difficulty several different approaches can be suggested:

- Thermal analysis, using DMA and DSC, of dry granules with varying moisture contents to understand their mechanical properties and changes which go on during drying as proposed and initiated by Veryaeva *et al.* (2009) and Hassall *et al.* (2008).

- Studying the impact behaviour of semi-dry particles extracted directly from the dryer.

- Drying of slurry “cakes” in controlled conditions to allow its properties to be characterised independently of having to atomise it to form particles.

Chapter 9 – References

Adams, M. J., M. A. Mullier and J. P. K. Seville (1994). "Agglomerate Strength Measurement using a Uniaxial Confined Compression Test." Powder Technology 78: 5-13.

AdeJohn, A. O. and G. V. Jeffreys (1978). "Flow Visualisation and Residence Time Studies in a Spray Dryer." Trans IChemE 56: 36-42.

Adhikari, B., T. Howes, B. Bhandari and V. Truong (2003). "In Situ Characterisation of Stickiness of Sugar-Rich Foods Using a Linear Actuator Driven Stickiness Testing Device." Journal of Food Engineering 58(11-22): 11.

Adhikari, B., T. Howes, D. Lecomte and B. Bhandari (2005). "A Glass Transistion Temperature Approach for the Prediction of the Surface Stickiness of a Drying Dropplet During Spray Drying." Powder Technology 149: 168-179.

Adrian, R. J. (1991). "Particle-Imaging Techniques for Experimental Fluid Mechanics." Annual Review of Fluid Mechanics 23: 261-304.

Adrian, R. J. (2005). "Twenty years of Particle Image Velocimetry." Experiments in Fluids 39: 10.

Adrian, R. J. (2005). "Twenty Years of Particle Image Velocimetry." Experiments in Fluids 39: 159-169.

Ahmadian, H. (2008). Analysis of Enzyme Dust Formation in Detergent Manufacturing Plant. School of Process, Enviromental and Materials Engineering. Leeds, The University of Leeds. PhD.

Amador, C. (2009). Discussion on particle residence times. G. Hassall. Newcastle-Upon-Tyne.

Bajpai, D. and V. K. Tyagi (2007). "Laundry Detergents: An Overview." Journal of Oleo Science 56(7): 327-341.

Bayly, A. E. (2004). Introduction to detergent spray drying within P&G. P&G Internal Training. A. E. Bayly. Newcastle Upon Tyne, Procter and Gamble.

Bayly, A. E. (2005). EngD Project Proposal: Wall Build-up in Spray Dryers, Procter and Gamble.

Bayly, A. E. (2006). Discussion on the effect of formulation on detergent particle properties. G. J. Hassall. Newcastle-Upon-Tyne.

Bayly, A. E. (2008). Discussion on particle movement through spray dryers. G. Hassall. Newcastle-Upon-Tyne.

Bayly, A. E. (2009). Water - The most important ingredent in dry laundry. Beijing, Procter and Gamble.

Bayly, A. E., P. Jukes, M. Groombridge and C. McNally (2004). Airflow Patterns in a Counter-Current Spray Drying Tower - Simulation and Measurement. International Drying Symposium 2004. Sao Paulo. B: 775-781.

Bayly, A. E., D. J. Smith, N. S. Roberts, D. W. York and S. Capeci (2008). Handbook of Detergents: Part F - Production. London, CRC Press.

Bemrose, C. R. and J. Bridgwater (1987). "A Review of Attrition and Attrition Test Methods." Powder Technology 49: 97-126.

Berggren, J., G. Frenning and G. Alderborn (2004). "Compression Behaviour and Tablet-Forming Ability of Spray Dried Amorphous Composite Particles." European Journal of Pharmaceutical Sciences 22: 191-200.

Black, D. L., M. Q. McQuay and M. P. Bonin (1996). "Laser-Based Technqiues for Particle Size Measurement: A Review of Sizing Methods and Their Industrial Applications." Progress in Energy and Combustion Science 22: 267-306.

Boerefijn, R., Z. Ning and M. Ghadiri (1998). "Disintegration of Weak Lactose Agglomerates for Inhalation Applications." International Journal of Pharmaceutics 172: 199-209.

Boonyai, P., B. Bhandari and T. Howes (2004). "Stickiness Measurement Techniques for Food Powders: A Review." Powder Technology 145: 34-46.

Bryanston-Cross, P., M. Burnett, B. Timmerman, W. K. Lee and P. Dunkley (2000). "Intelligent Diagnostic Optics for Flow Visualisation." Optics and Laser Technology 32: 641-654.

Chaloud, J. H., J. B. Martin and J. S. Baker (1957). "Fundamentals of Spray Drying Deteregents." Chemical Engineering Progress 53(12): 593-596.

Charlesworth, D. H. and W. R. Marshall (1960). "Evaporation from Drops Containing Containing Dissolved Solids." American Institute of Chemical Engineers Journal 6(1): 9-23.

Chen, X. D., R. Lake and S. Jebson (1993). "Study of Milk Powder Deposition on a Large Industrial Dryer." Trans IChemE 71(C): 180-186.

Chen, X. D., L. Rutherford and R. J. LLoyd (1994). "Preliminary Results of Milk Powder Deposition at Room Temperature on a Stainless Steel Surface Mimicking the Ceiling of a Spray Dryer." Trans IChemE 72(C): 170-175.

Chung, K. H. K., M. J. H. Simmons and M. Barigou (2009). "Local gas and liquid phase velocity measurement in a miniature stirred vessel using PIV combined with a new image processing algorithm." Experimental Thermal and Fluid Science 33(4): 743-753.

Chung, T. J. (2002). Compuational Fluid Dynamics. Cambridge, Cambridge University Press.

Cleaver, J. (2008). Powder Caking: A Review for IFPRI, International Fine Particles Research Institute

Clift, R., J. R. Grace and M. E. Weber (1978). Bubbles, Drops and Particles. New York, Academic Press.

Crowe, C. T. (2006). Multiphase Flow Handbook. London, CRC.

Crowe, C. T., M. Sommerfeld and Y. Tsuji (1998). Multiphase Flows with Droplets and Particles. London, CRC Press.

de Groot, W. H., I. Adami and G. F. Moretti (1995). The Manufacture of Modern Detergent Powders.

Dong, H. and M. H. Moys (2006). "Experimental Stduy of Oblique Impacts with Initial Spin." Powder Technology 161: 22-31.

Durst, F. (1990). "Optical Techniques for Fluid Flow and Heat Transfer." Experimental Thermal and Fluid Science 3: 33-51.

Dyer, D., F. Dalzell and R. Olegario (2004). Rising Tide. Boston, Massachusetts, Harvard Business School Press.

Ennis, B. J. and G. Sunshine (1993). "On Wear as a Mechanism of Granule Attrition." Tribology International 26(5): 319-327.

Fletcher, D. F., B. Guo, D. J. E. Harvie, T. A. G. Langrish, J. J. Nijdam and J. Williams (2006). "What is Important in the Simulation of Spray Dryer Performance and how do Current CFD Models Perform?" Applied Mathematical Modelling 30: 1281-1292.

Fletcher, D. F. and T. A. G. Langrish (2009). "Scale-Adaptive Simu;ation (SAS) Modelling of Pilot-Scale Spray Dryer." Chemical Engineering Research and Design 87: 1371-1378.

Fu, J., M. J. adams, G. K. Reynolds, A. D. Salman and M. J. Hounslow (2004). "Impact Deformation and Rebound of Wet Granules." Powder Technology 140: 248-257.

Fu, J., G. K. Reynolds, M. J. adams, A. D. salman and M. J. Hounslow (2004). "An Experimental Study of the variability in the Properties and Quality of Wet Granules." Powder Technology 140: 209-216.

Gabites, J. R., J. Abrahamson and J. A. Winchester (2010). "Air Flow Patterns in an Industrial Milk Powder Spray Dryer." Chemical Engineering Research and Design.

Ghadiri, M. (1997). Particle Impact and Attrition. Powder Technology Handbook. K. Gotoh, H. Masada and K. Higshitani. New York, Marcel Dekker: 183-191.

Ghadiri, M. and Z. Zhang (2002). "Impact Attrition of Particulate Solids. Part 1: A Theorectical Model of Chipping." Chemical Engineering Science 57: 3659-3669.

Goder, D., H. Kalman and A. Ullmann (2002). "Fatigue characteristics of granular materials." Powder Technology 122: 19-25.

Godridge, R. K. (2009). Predictive Storage Stability of Granular Laundry Detergents. Center for Formulation Engineering. Birmingham, The University of Birmingham.

Gorham, D. A. and A. H. Kharaz (2000). "The Measurement of Particle Rebound Characteristics." Powder Technology 112: 193-202.

Grant, I. (1997). "Particle Image Velocimetry: A Review." Proceedings Institution of Mechanical Engineers 211(C): 55-76.

Guo, B., T. A. G. Langrish and D. F. Fletcher (2003). "Simulation of Gas Flow Instability in a Spray Dryer." Trans IChemE 81(A): 631-638.

Hanus, M. J. and T. A. G. Langrish (2007). "Resuspension of Wall Deposits in Spray Dryers." Journal of Zhejiang University Science A 8(11): 1762-1774.

Harvie, D. J. E., T. A. G. Langrish and D. F. Fletcher (2001). "Numerical Simulations of Gas Flow Patterns within a Tall-form Spray Dryer." Trans IChemE 79(A): 12.

Harvie, D. J. E., T. A. G. Langrish and D. F. Fletcher (2002). "A Computational Fluid Dynamics Study of a Tall-Form Spray Dryer." Trans IChemE 80(C): 12.

Hassall, G. (2008). Preliminary Experiments in the use of Ultrasound and Acoustics to Measure Wall Deposition in Spray Dryers. Newcastle-Upon-Tyne, Procter and Gamble.

Hassall, G., C. Amador and A. E. Bayly (2008). Understanding the effect of temperature and moisture content on the deformability of blown powder through analysis of its organic components. Newcastle-Upon-Tyne, Procter and Gamble.

Hecht, J. P. (2004). Mathematical Model of a Drying Drop of Laundry Detergent Slurry Including Puffing Cincinnati, USA, Procter and Gamble.

Hecht, J. P. (2005). Key Challanges in Atomisation in Consumer Product Manufacturing. Instittue of Liquid Atomisation and Spray Systems. Irvine, California, USA.

Hecht, J. P. and A. E. Bayly (2009). Atomisation for Spra Drying: Unanswered Questions and Industrial Needs. 11th Triennial International Annual Conference on Liquid Atomisation and Spray Systems. Vail, Colorado, USA.

Hecht, J. P. and C. J. King (2000). "Spray Drying: Influence of Developing Drop Morphology on Drying Rates and Retention of Volatile Substances. 1. Single Drop Experiments." Industrial and Engineering Chemistry Research 39: 1756-1765.

Hecht, J. P. and C. J. King (2000). "Spray Drying: Influence of Developing Drop Morphology on Drying Rates and Retention of Volatile Substances. 2. Modelling." Industrial and Engineering Chemistry Research 39: 1766-1774.

Herbst, J. A. and A. V. Potapov (2004). "Making a Discrete Grain Breakage Model Practical for Comminution Equpiment Performnce and Simulation." Powder Technology 143-144: 144-150.

Huang, L., K. Kumar and A. S. Mujumdar (2003). "Use of Computational Fluid Dynamics to Evaluate Alternative Spray Dryer Chamber Configuurations." Drying Technology 21(3): 385-412.

Huang, L., K. Kumar and A. S. Mujumdar (2004). "Simulation of a Spray Dryer Fitted with a Rotary Disk Atmoiser using a Three-Dimensional Computational Fluid Dynamics Model." Drying Technology 22(6): 1489-1515.

Huntington, D. (2004). "The Influence of the Spray Drying Process on Product Porperties." Drying Technology 22(6): 1261-1287.

Hutchinsons, I. M. (1993). "Mechanisms of Wear in Powder Technology: A Review." Powder Technology 76: 3-13.

Iveson, S. M. and J. D. Litster (1998). "Liquid-bound Granule Impact Deformation and Coefficent of Restitution." Powder Technology 99: 234-242.

Iveson, S. M. and N. W. Page (2005). "Dynamic Strength of Liquid-Bound Granular Materials: The Effect of Particle Size and Shape." Powder Technology 152: 79-89.

Johnson, K. L., K. Kendall and A. D. Roberts (1971). "Surface Energy and the Contact of Elastic Solids." Proceeding of the Royal Society of London 324: 301-313.

Kawakita, K. and K. H. Ludde (1970). "Some Considerations on Powder Compression Equations." Powder Technology 4: 61-68.

Keey, R. B. and Q. T. Pham (1976). "Residence-Time Distribution of Air in a Tall-Form Spray Chamber." Chemical Engineering Science 32: 1219-1226.

Kharaz, A. H., D. A. Gorham and A. D. Salman (2001). "An Experiemntal Study of the Elastic Rebound of Spheres." Powder Technology 120(281-291): 281.

Kieviet, F. G. and P. J. A. M. Kerkhof (1995). "Measurements of Particle Residence Time Distributions in a Co-Current Spray Dryer." Drying Technology 13(5): 1241-1248.

Kieviet, F. G. and P. J. A. M. Kerkhof (1996). Using Compuataional Fluid Dynamics to Model Product Quality in Spray Drying: Air Flow, Temperature and Humidity Patterns. International Drying Symposium 1996. Krakow, Poland: 259-265.

Kieviet, F. G., J. VanRaaij, P. P. E. A. DeMoor and P. J. A. M. Kerkhof (1997). "Measurement and Modelling of the Air Flow Pattern in a Pilot-Plant Spray Dryer." Trans IChemE 75(A): 321-328.

Kim, E. H. J., X. D. Chen and D. Pearce (2005). "Melting Characteristics of Fat Present on the Surface of Industrial Spray-Dried Dairy products." Colloids and Surfaces B: Biointerfaces 42: 1-8.

Kota, K. and T. A. G. Langrish (2006). "Fluxes and Patterns of Wall Deposits for Skim Milk in a Pilot-Scale Spray Dryer." Drying Technology 24(8): 993-1001.

Kudra, T. (2003). "Sticky Region in Drying—Definition and Identification." Drying Technology 21(8): 1457-1469.

Kurada, S., G. W. Rankin and K. Sridhar (1993). "Particle-Imaging Techniques for quantitative Flow Visualisation: a Review." Optics and Laser Technology 25(4): 219-233.

Langrish, T. A. G. (2009). "Multi-Scale Mathematical Modelling of Spray Dryer." Journal of Food Engineering 93: 10.

Langrish, T. A. G., W. C. Chan and K. Kota (2007). "Comparison of Maltodextrin and Skim Milk Wall Deposition rates in a Pilot-Scale Spray Dryer." Powder Technology 179(1-2): 84-89.

Langrish, T. A. G. and D. F. Fletcher (2003). "Prospects for the Modelling and Design of Spray Dryers in the 21st Century." Drying Technology 21(2): 197-215.

Langrish, T. A. G., R. B. Keey and C. A. Hutchinson (1992). "Flow Visualisation in a Spray Dryer Fitted with a Vaned-wheel Atmoiser: Photography and Prediciton." Trans IChemE 70(A): 385-394.

Langrish, T. A. G., D. E. Oakley, R. B. Keey, R. E. Bahu and C. A. Hutchinson (1993). "Time-Dependent Flow Patterns in Spray Dryers." Trans IChemE 71(A): 355-360.

Langrish, T. A. G., J. Williams and D. F. Fletcher (2004). "Simulation of the Effects of Inlet Swirl on Gas Flow Patterns in a Pilot-Scale Spray Dryer." Trans IChemE 82(A7): 821-833.

Langrish, T. A. G. and I. Zbicinski (1994). "The Effects of Air Inlet Geometry and Spray Cone Angle on the Wall Deposition Rate in Spray Dryers." Trans IChemE 72(A): 420-430.

LeBarbier, C., T. K. Kockel, D. F. Fletcher and T. A. G. Langrish (2001). "Experimental Measurement and Numerical Simulation of the Effect of Swirl on Flow Stability in Spray Dryers." Chemical Engineering Research and Design 79(A3): 260-268.

Li, T., J. Zhang and W. Ge (2004). "Simple Measurement of Restitution Coefficient of Irregular Particles." China Particuology 2(6): 274-275.

Li, X. and B. Bhushan (2002). "A Review of Nanoindentation Continuous Stiffness Measurement Technique and its Applications." Materials Characterization 48(1): 11-36.

Livesley, D. M., D. E. Oakley, R. F. Gillespie, B. Elhaus, C. K. Ranpuria, T. Taylor, W. Wood and M. L. Yeoman (1992). Development and Validation of a Computational Model for Spray-Gas Mixing in Spray Dryers. International Drying Symposium 1994. A. S. Mujumdar. Montreal, Canada. 3: 407-416.

Mangwandi, C., Y. S. Cheong, M. J. Adams, M. J. Hounslow and A. D. Salman (2007). "The Coefficent of Restitution of Different Representative Types of Granules." chemical Engineering Science 62(437-450): 437.

Masters, K. (1991). Spray Drying Handbook. London, Longman.

Maury, M., K. Murphy, S. Kumar, L. Shi and G. Lee (2004). "Effects of Process Variables on the Powder Yield of Spray-Dried Trehalose on a Laboratory Spray-Dryer." European Journal of Pharmaceutics and Biopharmaceutics 59: 565-573.

Mavros, P. (2001). "Flow Visualisation in Stirred Tanks: A Review of Experimental Techniques." Trans IChemE 79(A): 113-125.

Melling, A. (1997). "Tracer Particles and Seeding for Particle Image Velocimetry." Measurement Science and Technology 12(8): 1406-1416.

Montazer-Rahmati, M. M. and S. H. Ghafele-Bashi (2007). "Improved Differential Modelling and Performance Simulation of Slurry Spray Dryers as Verified by Industrial Data." Drying Technology 25: 1451-1462.

Mort, P. (2002). Analysis and Application of Powder Compaction Diagrams. Cincinnati, Procter and Gamble.

Mort, P. (2004). Automated Generation and Analysis of Powder Compaction Diagrams. Cincinnati, Procter and Gamble.

Mort, P., R. Sabia, D. Niesz and R. Riman (1994). "Automated Generation and Analysis of Powder Compaction Diagrams." Powder Technology 79: 111-119.

Muller, J., A. E. Bayly and D. Huntington (2001). Flow Patterns in Spray Dryers. Procter and Gamble Internal Report. A. E. Bayly, Procter and Gamble.

Nesic, S. and J. Vodnik (1991). "Kinetics of Droplet Evaporation." Chemical Engineering Science 46(2): 527-537.

Ng, B. H. (2009). A CFD Tool to Investigate Wall make-up. Newcastle-Upon-Tyne, Procter and Gamble.

Ng, B. H. and C. Amador (2008). Evaluation of New Tubular Guard Designs in London Tower. Newcastle-Upon-Tyne, Procter and Gamble.

Ng, B. H. and C. Amador (2008). Modelling Slurry Injection in a Spray Drying Tower - Validation and Modification. Newcastle-Upon-Tyne, Procter and Gamble.

Niederkorn, T. (2000). Global Scalable Tower: Pilot Plant Development and Design. T. Niederkorn. Newcastle-Upon-Tyne, Procter and Gamble.

Nijdam, J. J. (2004). Experimental Investigation of Air Flows in IPP Spray Dryer. Newcastle-Upon-Tyne, Procter and Gamble.

Nijdam, J. J. and T. A. G. Langrish (2006). "The Effect of Surface Composition of the Functional Properties of Milk Powders." Journal of Food Engineering 77(919-925): 919-925.

Nordstorm, J., K. Welch, G. Frenning and G. Alderborn (2008). "On the Physical Interpretation of the Kawakita and Adams Parameters Derived from Confined Compression of Granular Solids." Powder Technology 182: 424-435.

Oakley, D. E. (1994). "Scale-up of Spray Dryers with the Aid of Computational Fluid Dynamics." Drying Technology 12(1&2): 217-233.

Oakley, D. E. (2004). "Spray Dryer Modelling in Theory and Practice." Drying Technology 22(6): 1371-3937.

Oakley, D. E. and R. E. Bahu (1992). Computational Modelling of Spray Dryers. European Symposium on Computer Aided Process Engineering - 2. Toulouse (France).

Ozmen, L. and T. A. G. Langrish (2003). "An experimental Investigation of the Wall Deposition of Milk Powder in a Pilot-Scale Spray Dryer." Drying Technology 21(7): 1253-1272.

Paris, J. R., N. P. Ross, S. P. Dastur and R. L. Morris (1971). "Modelling of the Air Flow Pattern in a Countercurrent Spray Drying Tower." Industrial and Engineering Chemistry Process Design and Development 10(2): 157-164.

Parti, M. and B. Palancz (1974). "Mathematical Model for Spray Drying." chemical Engineering Science 29: 355-362.

Pasley, H. and P. Haloulos (1995). "Stickiness - A Comparison of Test Methods and Characterisation Parameters." Drying Technology 13(5/7): 165-172.

Perez-Correa, J. R. and F. Farias (1995). "Modelling and Control of a Spray Dryer: a Simulation Study." Food Control 6(4): 219-227.

Peukert, W. and L. Vogel (2001). "Comminution of Polymers - An Example of Product Engineering." Chemical Engineering and Technology 9: 945-950.

Pitchumani, R., G. M. H. Meesters and B. Scarlett (2003). "Breakage Behaviour of Enzyme Granules in a Repeated Impact Test." Powder Technology 130: 421-427.

Pitchumani, R., O. Zhupanska, G. M. H. Meesters and B. Scarlett (2004). "Measurement and Characterisation of Particle Strength using a New Robotic Compression Tester." Powder Technology 143-144: 56-64.

Place, G., K. Ridgway and P. V. Danckwerts (1959). "Investigation of Air-Flow in a Spray Dryer by Tracer and Model Techniques." Trans IChemE 37: 268-276.

Raffel, M., C. E. Willert, S. T. Wereley and J. Kompenhans (2007). Particle Image Velocimetry - A Practical Guide. New York, Springer.

Rennie, P. R., X. D. Chen, C. Hargreaves and A. R. Mackereth (1999). "A Study of the Cohesion of Dairy Powders." Journal of Food Engineering 39: 277-284.

Reynolds, G. K., J. S. Fu, Y. S. Cheong, M. J. Hounslow and A. D. Salman (2005). "Breakage in Granulation: A Review." Chemical Engineering Science 60: 3969-3992.

Rhodes, M. (1997). Introduction to Particle Technology Chichester, Wiley.

Rumpf, H. (1990). Particle Technology. London, Chapman and Hall.

Saareninne, P., M. Piirto and H. Eloranta (2001). "Experiences of Turbulence Measurement With PIV." Measurement Science and Technology 12(11): 1904-1910.

Salman, A. D., C. A. Biggs, J. Fu, I. Angyal, M. Szabo and M. J. Hounslow (2002). "An Experimental Investigation of Particle Fragmentation using Single Particle Impact Studies." Powder Technology 128: 36-46.

Salman, A. D., D. A. Gorham and A. Verba (1995). "A Study of Solid Particle Failure under Normal and Oblique Impact." Wear 186-187: 92-98.

Salman, A. D., G. K. Reynolds, J. S. Fu, Y. S. Cheong, C. A. Biggs, M. J. Adams, D. A. Gorham, J. Lukenics and M. J. Hounslow (2004). "Descriptive Classification of the Impact Failure Modes of Spherical Particles." Powder Technology 143-144: 19-30.

Samimi, A., M. Ghadiri, R. Boerefijn, A. Groot and R. Kohlus (2003). "Effect of Structural Characteristics on Impact Breakage of Agglomerates." Powder Technology 130: 428-435.

Samimi, A., A. Hassanpour and M. Ghadiri (2005). "Single and Bulk Compressions of Soft Granules: Experimental Study and DEM Evaluation." Chemical Engineering Science 60: 3993-4004.

Samimi, A., R. Moreno and M. Ghadiri (2004). "Analysis of Impact Damage of Agglomerates: Effect of Impact Angle." Powder Technology 143-144: 97-109.

Sano, Y. and R. B. Keey (1982). "The Drying of Spherical Particle Containing Colloidal Material into a Hollow Sphere." Chemical Engineering Science 37(6): 881-889.

Schonert, K. (2004). "Breakage of Spheres and Circular Discs." Powder Technology 143-144: 2-18.

Seville, J. P. K., U. Tuzun and R. Clift (1997). Processing of Particulate Solids. London, Chapman and Hall.

Sharma, S. (1990). Spray Dryer Simulation and Air Flow Pattern Studies. Chemical Engineering. Birmingham, University of Aston. Ph.D.

Sheng, J., H. Meng and R. O. Fox (2000). "A Large Eddy PIV Method for Turbulence Dissipation Rate Estimation." Chemical Engineering Science 55: 4423-4434.

Southwell, D. B. and T. A. G. Langrish (2000). "Observations of Flow Patterns in a Spray Dryer." Drying Technology 18(3): 661-685.

Southwell, D. B. and T. A. G. Langrish (2001). "The Effect of Swirl on Flow Stability in Spray Dryers." Chemical Engineering Research and Design 79(A3): 222-234.

Southwell, D. B., T. A. G. Langrish and D. F. Fletcher (1999). "Process Intensification in Spray Dryers by Turbulence Enhancement." Trans IChemE 77(A): 189-205.

Stafford, R. A., O. Fauroux and D. H. Glass (1997). "Flow Visualisation and Instanteous Velocity Measurements of Spray Dryer Gas and Spray Flows Using Particle Image Velocimetry." Drying Technology 15(6-8): 1661-1671.

Stanislas, M. and J. C. Monnier (1997). "Practical Aspects of Image Recording in Particle Image Velocimetry." Measurement Science and Technology 8: 1417-1426.

Stewart, J. A. (2008). Engineering the Properties of Spray-Dried Deteregent Granules. Engineering in the Faculty of Engineering and Physical Sciences. Manchester, University of Manchester. Doctor of Engineering.

Straatsma, J., G. Van Houwelingen, A. E. Steenbergen and P. De Jong (1999). "Spray Drying Food Products: 1. Simulation Model." Journal of Food Engineering 42: 67-72.

Tayali, N. E. and C. J. Bates (1990). "Particle Sizing Techniques in Multiphase Flows: A Review." Flow Measurement and Instrumentation 1: 77-105.

Taylor, T. (1994). Powder and Air Residence Time Distributions in Countercurrent Spray Driers. International Drying Symposium 1994. Gold Coast, Australia: 463-470.

Taylor, T. (1998). Particle Residence Time Distribution in Con and Counter Current Spray Drying Towers. 11th International Drying Symposium (IDS '98). Halkidiki, Greece. A: 533-540.

Thornton, C. and Z. Ning (1998). "A Theoretical Model for the Stick/Bounce Behaviour of Adhesive, Elastic-Plastic Spheres." Powder Technology 99: 154-162.

Velic, D., M. Bilic, S. Tomas and M. Planinic (2003). "Simulation, Calculation and Possibilities of Energy Saving in Spray Drying Process." Applied Thermal Engineering 23: 2119-2131.

Veryaeva, L., G. Hassall and C. Amador (2009). Investigating the mechanical properties of phosphate, nil-phosphate and nil-silicate formulations using confined and unconfined compression. newcastle-Upon-Tyne, Procter and Gamble.

Walton, D. E. (2000). "The Morphology of Spray-Dried Particles: A Qualitative View." Drying Technology 18(9): 1943-1986.

Walton, D. E. and C. J. Mumford (1999). "The Morphology of Spray Dried Particles: The Effect of Process Variables upon the Morphology of Spray-Dried Particles." Trans IChemE 77(A): 442-460.

Walton, D. E. and C. J. Mumford (1999). "Spray Dried Products - Characterisation of Particle Morphology." Trans IChemE 77(A): 21-38.

Webb, P. A. (2001). Volume and Density Determinations for Particle Technologists, Micromeritics Instrument Corp.

Weir, G. and S. Tallon (2005). "The Coefficent of Restitution for Normal Incident, Low Velocity Particle Impacts." Chemical Engineering Science 60: 3637-3647.

Woo, M. W., W. R. W. Daud, A. S. Mujumdar, S. M. Tasirin and M. Z. M. Talib (2010). "Role of Rheological Characterisitics in Amorphous Food Particle-Wall Collisions in Spray Drying." Powder Technology 198: 251-257.

Woo, M. W., W. R. W. Daud, S. M. Tasirin and M. Z. M. Talib (2008). "Amorphous Particle Deposition and Product Quality under different Conditions in a Spray Dryer." Particuology 6: 265-270.

Woo, M. W., W. R. W. Daud, S. M. Tasirin and M. Z. M. Talib (2009). "Controlling Food Powder Deposition in Spray-Dryers: Wall Surface Energy Manipulation as an Alternative." Journal of Food Engineering 94: 192-198.

Woo, M. W., W. R. Wan Daud, A. S. Mujumdar, M. Z. M. Talib, W. Z. Hua and S. M. Tasirin (2008). "Comparative Study of Droplet Drying Models for CFD Modelling." Chemical Engineering Research and Design 86: 1038-1048.

Yangxin, Y. U., J. Zhao and A. E. Bayly (2008). "Development of Surfactants and Builder in Detergent Formulations." Chinese Journal of Chemical Engineering 16(4): 517-528.

Yap, S. F., M. J. Adams, J. P. K. Seville and Z. Zhang (2007). "Single and Bulk Compression of Pharamceutical Excipients: Evaluation of Mechnical Properties." Powder Technology 185(1): 1-10.

Zbicinski, I., S. Grabowski, C. Strumillo, L. Kiraly and W. Krzanowski (1988). "Mathematical Modelling of Spray Drying." Computers and Chemical Engineering 12(2/3): 209-214.

Zbicinski, I., M. Piatkowski and C. Strumillo (2004). Experimental Analysis of the Mechanism of Counter-Current Spray Drying Process. 14th International Drying Symposium (IDS 2004). Sao Paulo, Brazil. A: 161-168.

Zbicinski, I., C. Strumillo and A. Delag (2002). "Drying Kinetics and Particle Residence Time in Spray Drying." Drying Technology 20(9): 1751-1768.

Appendix A – PIV MATLAB Codes

This appendix displays the MATLAB codes written to calculate the results shown in Chapter 5 and Chapter 6, from the raw PIV data obtained from experiments.

A.1 Fluid Dynamics Codes (Chapter Five)

Chapter Five presents results from PIV studies of seeded air flows within the spray dryer. This section of the appendix displays the MATLAB codes that were written to calculate the results shown in Chapter Five from the vector files produced by the PIV software.

A.1.1 Vector file loading and 3D matrix construction

The first step in these calculations was to load up individual vector files (one per measurement point, *i.e.* 1000 vector files for each experimental point), which form the output from PIV cross-correlation with TSI PIV software. The vector files contain a list of 5 columns with X and Y coordinates, giving the location of the spot of information, with U (X) and V (Y) velocity values along with a value indicating the type of velocity vector generated for that spot (first peak correlation, filled vector, failed vector etc). This list was arranged by the location of the spot working across the studied area in rows starting at the top of the image. These vector files were loaded into MATLAB to create a matrix for each, and a check was made to remove unsuitable any vector values. The checked matrix of vector files was then stacked, such that the output of this code is 3D matrix of X and Y coordinates, U and V velocities and vector type, with time as the Z axis.

```
%% RoySoft 2009
%% Written by G. Hassall
%% Based on codes by K. Chung and G. Neal

%% Input to specify the number of vector files to be loaded
nfiles = input ('Last Frame? (e.g. 499) >> ')

%% Move to directory containing vector files
cd ('C:\Users\Guy\Desktop\March Airflow Vectors\21
meters\10000kg');

%% Load first vector (where name of file is specified)
fname3 = ['10000 kghr000000.T000.D000.P001.H001.L.vec'];
s=csvread([fname3],1,0);

%% Conversion of Cartesian coordinates to polar coordinates
[m,n] = size(s);
r = zeros(m,11);
r(:,1) = s(:,1)-80.7;
r(:,2) = s(:,2)+700.4;
[r(:,3),r(:,4)] = cart2pol(r(:,1),r(:,2));
r(:,5) = (r(:,3)-1.5707);
r(:,6) = ((s(:,3)).*(cos(r(:,5))))-((s(:,4)).*(sin(r(:,5))));
r(:,7) = ((s(:,4)).*(cos(r(:,5))))+((s(:,3)).*(sin(r(:,5))));

%% Rearrangement of polar coordinate data back into 5 column
matrix
t = zeros(size(s));
t(:,1) = s(:,1);
t(:,2) = s(:,2);
t(:,3) = r(:,6);
t(:,4) = r(:,7);
t(:,5) = s(:,5);
G=t;

%% Load remaining vector files as a loop (where number of
files is specified by input above)
for i = (1 : nfiles);
if i < 10
fname3 = ['10000
kghr','00000',int2str(i),'.T000.D000.P001.H001.L.vec'];
elseif 100 > i & i > 9
fname3 = ['10000
kghr','0000',int2str(i),'.T000.D000.P001.H001.L.vec'];
elseif 1000 > i & i > 99
fname3 = ['10000
kghr','000',int2str(i),'.T000.D000.P001.H001.L.vec'];
else
```

```
fname3 = ['10000
kghr','00',int2str(i),'.T000.D000.P001.H001.L.vec'];
end
if exist (fname3)>0;
s=csvread([fname3],1,0);

%% Conversion of Cartesian coordinates to polar coordinates
[m,n] = size(s);
r = zeros(m,11);
r(:,1) = s(:,1)-80.7;
r(:,2) = s(:,2)+700.4;
[r(:,3),r(:,4)] = cart2pol(r(:,1),r(:,2));
r(:,5) =(r(:,3)-1.5707);
r(:,6) = ((s(:,3)).*(cos(r(:,5))))-((s(:,4)).*(sin(r(:,5))));
r(:,7) = ((s(:,4)).*(cos(r(:,5))))+((s(:,3)).*(sin(r(:,5))));

%% Rearrangement of polar coordinate data back into 5 column
matrix
t = zeros(size(s));
t(:,1) = s(:,1);
t(:,2) = s(:,2);
t(:,3) = r(:,6);
t(:,4) = r(:,7);
t(:,5) = s(:,5);
G2=t;

%%%Stacking data onto the first data file, constructing a 3D
matrix%%%
G=cat(3,G,G2);
end
end
clear G2;

%% Removal of false vector velocity values (5th column less
than 1)
[D,L]=find(G(:,5,:)<1);
for l=1:length(D);
    G(D(l),3:4,L(l))=NaN;
    l=l+1;
end

%% Changing of all filled vector 5th column values to 1
[D,L]=find(G(:,5,:)>1);
for l=1:length(D);
    G(D(l),5,L(l))=1;
    l=l+1;
end

%% Save 3D Matrix
```

```
savefile = '3dmatrixcylindercoord.mat';
save(savefile, 'G')

%% Return to directory containing MATLAB Codes
cd ('C:\Users\Guy\Desktop\PIV MATLAB Codes');
```

A.1.2 Calculation and plotting of velocity and turbulence parameters

Velocity and turbulent parameters were calculated from the 3D matrix. The data in the matrix was first rearranged into a square shape where the velocity values for each interrogation window were arranged such that they re-created the layout of the image captured. Once rearranged these values were either averaged, or used for calculations of the parameters required in the form a matrix which represents the area of the image captured, allowing contour plots of the parameters calculated over this area to be produced.

```
%% RoySoft 2009
%% Written by G. Hassall
%% Based on codes by K. Chung and G. Neal

%% Move to directory containing 3D matrix
cd ('C:\Users\Guy\Desktop\March Airflow Vectors\21
meters\10000kg');

%% Load 3D matrix
load 3dmatrixcylindercoord.mat

%% Input to specify the number of spots in the image
f = input('number of spots?')

%% Input to specify velocity value for nomralising against
s = input('air inlet tangential velocity (m/s)?')

%% Reshaping the matrix into 3D materix in square shape
sizeG=size(G);
sizeG=sizeG(3);
for i = 1:1:sizeG;
U=G(:,3,i);
UU=reshape(U,f,[]);
Umatrix(:,:,i)=UU;
V=G(:,4,i);
```

```
VV=reshape(V,f,[]);
Vmatrix(:,:,i)=VV;
Vec=G(:,5,i);
VVec=reshape(Vec,f,[]);
Vecmatrix(:,:,i)=VVec;
clear U UU V VV Vec VVec;
end;

%% Creating matrices for velocity and turbulent parameters
Umean = nan(f,f);
Vmean = nan(f,f);
RMSU = nan(f,f);
RMSV = nan(f,f);
RSUV = nan(f,f);
RSSUV = nan(f,f);
RSSSUV = nan(f,f);
RSSSSUV = nan(f,f);
TKE = nan(f,f);
URes = nan(f,f);
RMSURes = nan(f,f);
RMSSURes = nan(f,f);
TurbInU = nan(f,f);
TurbInV = nan(f,f);
Turbinures = nan(f,f);
TurbinURes = nan(f,f);
STDU = nan(1000,1);
STDV = nan(1000,1);
RMSUU = nan(f,f);
RMSVV = nan(f,f);
STDUV = nan(1000,1);
UURes = nan(1000,1);

%% Loops to load velocity data for each spot and calulate
parameters
for i=1:f;
    for j = 1:f;
        U = squeeze(squeeze(Umatrix(i,j,:)));
        V = squeeze(squeeze(Vmatrix(i,j,:)));
        UX = squeeze(squeeze(Umatrix(i,j,:)));
        VX = squeeze(squeeze(Vmatrix(i,j,:)));
        NU = find(~isnan(U));
        NV = find(~isnan(V));
        U = U(NU);
        V = V(NU);
        AU=size(U);
        AV=size(V);
        Kount(i,j)=AU(1);
        if AU(1) > 1
        Umean(i,j)=mean(U);
```

```
        Vmean(i,j)=mean(V);
        URes (i,j) =
((((Umean(i,j).^2))+((Vmean(i,j)).^2)).^0.5);
        for h=1:Kount(i,j);
           UZ = U(h,1);
           VZ = V(h,1);
           STDU(h,1) = ((UZ-(Umean(i,j))).^2);
           STDV(h,1) = ((VZ-(Vmean(i,j))).^2);
           STDUV(h,1) = ((UZ-(Umean(i,j)))*(VZ-(Vmean(i,j))));
           UURes = (((UZ.^2)+(VZ.^2)).^0.5);
           STDURes(h,1) = ((UURes - (URes(i,j))).^2);
        end
                RMSU(i,j)=(std(U,1))^2;
                RMSV(i,j)=(std(V,1))^2;
                RMSUU(i,j) = (sum(STDU)/1000);
                RMSVV(i,j) = (sum(STDV)/1000);
                TKE(i,j)= 3/4*(RMSU(i,j)+RMSV(i,j))^(1/2);
                RMSURes(i,j) =
((((RMSU(i,j).^2))+((RMSV(i,j)).^2)).^0.5);
                RMSSURes(i,j)= (sum(STDURes)/1000);
        Udash = U-Umean(i,j);
        Vdash = V-Vmean(i,j);
        RSUVL=Udash.*Vdash;
        RSUV(i,j)=mean(RSUVL);
        RSSUV(i,j) = (((sum(STDUV))/1000));
        RSSSUV(i,j) = ((((sum(STDUV))/1000))/s);
        RSSSSUV(i,j) = (((sum(STDUV))/1000));
        TurbInU (i,j) = (RMSU(i,j)/Umean(i,j));
        TurbInV (i,j) = (RMSV(i,j)/abs(Vmean(i,j)));
        Turbinures (i,j) = ((RMSURes(i,j)/URes(i,j))*100);
        TurbinURes (i,j) = ((RMSSURes(i,j)/URes(i,j))*100);
        end
    end
end

%% Plot tangential velocity
Umeanplot = rot90(Umean);
a=figure;
axes('FontSize',14)
X = linspace(0,161.4,63);
Y = linspace(0,161.4,63);
contourf(X,Y,Umeanplot,50,'linestyle','none');
set(gca,'DataAspectRatio',[1 1 1])
caxis([0.0 2.5]);
colorbar('FontSize',14)
title ('Above Nozzle - High Flowrate: Tangential
Velocity','FontSize',14)
xlabel('x position (mm)','FontSize',14)
ylabel('y position (mm)','FontSize',14)
```

```
%% Plot radial velocity
Vmeanplot = rot90(Vmean);
b=figure;
axes('FontSize',14)
X = linspace(0,161.4,63);
Y = linspace(0,161.4,63);
contourf(X,Y,Vmeanplot,50,'linestyle','none');
set(gca,'DataAspectRatio',[1 1 1])
caxis([-1.0 0.5]);
colorbar('FontSize',14)
title ('Above Nozzle - High Flowrate: Radial
Velocity','FontSize',14)
xlabel('x position (mm)','FontSize',14)
ylabel('y position (mm)','FontSize',14)

%% Plot velocity magniutude
UResplot = rot90(URes);
c=figure;
axes('FontSize',14)
X = linspace(0,161.4,63);
Y = linspace(0,161.4,63);
contourf(X,Y,UResplot,50,'linestyle','none');
set(gca,'DataAspectRatio',[1 1 1])
caxis([0.0 2.5]);
colorbar('FontSize',14)
title ('Above Nozzle - High Flowrate: Velocity
Magnitude','FontSize',14)
xlabel('x position (mm)','FontSize',14)
ylabel('y position (mm)','FontSize',14)

%% Plot velocity magnitude with velcity vectors
UResplot = rot90(URes);
c=figure;
axes('FontSize',14)
X = linspace(0,161.4,63);
Y = linspace(0,161.4,63);
contourf(X,Y,UResplot,50,'linestyle','none');
set(gca,'DataAspectRatio',[1 1 1])
caxis([0.0 2.5]);
colorbar('FontSize',14)
title ('Above Nozzle - High Flowrate: Velocity
Magnitude','FontSize',14)
xlabel('x position (mm)','FontSize',14)
ylabel('y position (mm)','FontSize',14)
hold on
scale = 0.75;
quiver(X,Y,Umeanplot, Vmeanplot, scale,'k','LineWidth',0.5);
hold off
```

```
%% Plot TKE
TKEplot = rot90(TKE);
d=figure;
axes('FontSize',14)
X = linspace(0,161.4,63);
Y = linspace(0,161.4,63);
contourf(X,Y,TKEplot,50,'linestyle','none');
set(gca,'DataAspectRatio',[1 1 1])
caxis([0.0 0.5]);
colorbar('FontSize',14)
title ('Above Nozzle - High Flowrate: Turbulent Kinetic Energy
','FontSize',14)
xlabel('x position (mm)','FontSize',14)
ylabel('y position (mm)','FontSize',14)

%% Plot Reynolds stresses
RSSSSUVplot = rot90(RSSSSUV);
e=figure;
axes('FontSize',14)
X = linspace(0,161.4,63);
Y = linspace(0,161.4,63);
contourf(X,Y,RSSSSUVplot,500,'linestyle','none');
set(gca,'DataAspectRatio',[1 1 1])
caxis([0.0 0.03]);
colorbar('FontSize',14)
title ('Above Nozzle - High Flowrate: Reynolds
Stresses','FontSize',14)
xlabel('x position (mm)','FontSize',14)
ylabel('y position (mm)','FontSize',14)

%% Plot normalised Reynolds stresses
RSSSUVplot = rot90(RSSSUV);
e=figure;
axes('FontSize',14)
X = linspace(0,161.4,63);
Y = linspace(0,161.4,63);
contourf(X,Y,RSSSUVplot,500,'linestyle','none');
set(gca,'DataAspectRatio',[1 1 1])
caxis([0.0 0.01]);
colorbar('FontSize',14)
title ('Above Nozzle - High Flowrate: Normalised Reynolds
Stresses','FontSize',14)
xlabel('x position (mm)','FontSize',14)
ylabel('y position (mm)','FontSize',14)

%% Plot turbulence intensity
guy4 = rot90(TurbinURes);
g=figure;
```

```
axes('FontSize',14)
X = linspace(0,161.4,63);
Y = linspace(0,161.4,63);
contourf(X,Y,guy4,1000,'linestyle','none');
set(gca,'DataAspectRatio',[1 1 1])
caxis([0 8]);
colorbar('FontSize',14)
title ('Above Nozzle - High Flowrate: Turbulence Intensity
Velocity Magnitude','FontSize',14)
xlabel('x position (mm)','FontSize',14)
ylabel('y position (mm)','FontSize',14)

%% Return to directory containing MATLAB Codes
cd('C:\Users\Guy\Desktop\PIV MATLAB Codes');
```

A.1.3 Calculation and plotting of transience and periodicity parameters

Time dependent and transient parameters were calculated by loading the 3D matrix. The velocity data for a specific interrogation spot was then copied from the 3D matrix and manipulated to allow velocity to be plotted as a function of time (signal plots) using the first code shown below. This velocity data was also saved and then loaded up by the second code shown below so that transient parameters could be calculation and Fast Fourier Transform analysis conducted and the results plotted.

```
%% RoySoft 2009
%% Written by G. Hassall
%% Based on codes by K. Chung and G. Neal

%Directory/folder for vector files
cd ('C:\Users\Guy\Desktop\March Airflow Vectors\15 meters\8000
kg');
%%%Load 3D matrix%%%
%%%%%%%%%%%%%%%%%%%%%%%%%%%%%%%%%%%%%%%%%%%%%%%%%%%%%%%%%%%%%%%%%%%%%%%%
%%%%%%%%
load 3dmatrixcylindercoord.mat

% Obtaining correct rwo number to look up correct spot from 3D
matrix
f = input('number of spots?') %enter number of spots image is
split into
r = input('spot position x?')
```

```
t = input('spot position y?')
q=((t-1)*f)+r; %row number to look up corresponding spot on
image

% Tangential Velocities for Spot
A=G(q,3,:); %"cuts" out velocity values for U of particular
spot
m=size (G, 3); %number of velocity values to be used
B = squeeze(A); %turns 1x1 3D matrix in A to column of
velocity values
spota=zeros(m,3); %generate matrix to have time and velocity
in 2 columns
spota(:,1)=(1:m); %but time values in, 1 second per row,
1,2,3,4.....
spota(:,2)=B(:,1); %copy in velocity values next to time
values
savefile = ['Tangential Velocity Spot X-',int2str(r),' Y-
',int2str(t),'.mat'];
save(savefile, 'spota');

x=spota(:,1); %single column with time vales
y=spota(:,2); %single column with velocity values
figure
axes('FontSize',14)
h = plot (x,y,'r'); %plots velocity vs time
ylim([-1.0 4.0]);
title (['Below Nozzle - High Flowrate: Tangential Velocity in
Spot X-',int2str(r),' Y-',int2str(t),' over
Time'],'FontSize',14)
xlabel ('time (seconds)','FontSize',14)
ylabel ('Velocity (ms-1)','FontSize',14)
saveas(h,['Tangential-Velocity Vs time (line) Spot X-
',int2str(r),' Y-',int2str(t),]) %saves velocity vs time plot

figure
axes('FontSize',14)
h = plot (x,y,'r.'); %plots velocity vs time
ylim([-1.0 4.0]);
title (['Below Nozzle - High Flowrate: Tangential Velocity in
Spot X-',int2str(r),' Y-',int2str(t),' over
Time'],'FontSize',14)
xlabel ('time (seconds)','FontSize',14)
ylabel ('Velocity (ms-1)','FontSize',14)
saveas(h,['Tangential-Velocity Vs time (points) Spot X-
',int2str(r),' Y-',int2str(t),]) %saves velocity vs time plot

[n,xout] = hist(B,10); %"bins" values to give groups for
histogram plot
z=figure
```

```
axes('FontSize',14)
bar(xout,n,'r'); %plots frequency against velocity "bin"
values
ylim([0 800]);
xlim([-1.0 4.0]);
title (['Below Nozzle - High Flowrate: Tangential Velocity
Histogram in Spot X-',int2str(r),' Y-
',int2str(t),],'FontSize',14)
xlabel ('Velocity (ms-1)','FontSize',14)
ylabel ('Frequency','FontSize',14)
saveas(z,['Tangential-Velocity-Histogram Spot X-',int2str(r),'
Y-',int2str(t),]) %saves velocity histogram

% V Velocities for Spot
A=G(q,4,:); %"cuts" out velocity values for V of particular
spot
m=size (G, 3); %number of velocity values to be used
B = squeeze(A); %turns 1x1 3D matrix in A to column of
velocity values
spota=zeros(m,2); %generate matrix to have time and velocity
in 2 columns
spota(:,1)=(1:m); %but time values in, 1 second per row,
1,2,3,4.....
spota(:,2)=B(:,1); %copy in velocity values next to time
values
savefile = ['Radial-Velocity Spot X-',int2str(r),' Y-
',int2str(t),'.mat'];
save(savefile, 'spota');

x=spota(:,1); %single column with time vales
y=spota(:,2); %single column with velocity values
figure
axes('FontSize',14)
h = plot (x,y,'g'); %plots velocity vs time
ylim([-2.5 2.5]);
title (['Below Nozzle - High Flowrate: Radial Velocity in Spot
X-',int2str(r),' Y-',int2str(t),' over Time'],'FontSize',14)
xlabel ('time (seconds)','FontSize',14)
ylabel ('Velocity (ms-1)','FontSize',14)
saveas(h,['Radial Velocity Vs time (line) Spot X-
',int2str(r),' Y-',int2str(t),]) %saves velocity vs time plot

figure
axes('FontSize',14)
h = plot (x,y,'g.'); %plots velocity vs time
ylim([-2.5 2.5]);
title (['Radial Velocity in Spot X-',int2str(r),' Y-
',int2str(t),' over Time'],'FontSize',14)
xlabel ('time (seconds)','FontSize',14)
```

```
ylabel ('Velocity (ms-1)','FontSize',14)
saveas(h,['Radial Velocity Vs time (points) Spot X-
',int2str(r),' Y-',int2str(t),]) %saves velocity vs time plot

[n,xout] = hist(B,10); %"bins" values to give groups for
histogram plot
z=figure
axes('FontSize',14)
bar(xout,n,'g'); %plots frequency against velocity "bin"
values
ylim([0 800]);
xlim([-2.5 2.5]);
title (['Below Nozzle - High Flowrate: Radial Velocity
Histogram in Spot X-',int2str(r),' Y-
',int2str(t),],'FontSize',14)
xlabel ('Velocity (ms-1)','FontSize',14)
ylabel ('Frequency','FontSize',14)
saveas(z,['Radial Velocity-Histogram Spot X-',int2str(r),' Y-
',int2str(t),]) %saves velocity histogram

% Resultant velocity for spot
A=G(q,3,:); %"cuts" out velocity values for U of particular
spot
m=size (G, 3); %number of velocity values to be used
B = squeeze(A); %turns 1x1 3D matrix in A to column of
velocity values
spota=zeros(m,2); %generate matrix to have time and velocity
in 2 columns
spota(:,1)=(1:m); %but time values in, 1 second per row,
1,2,3,4.....
spota(:,2)=B(:,1); %copy in velocity values next to time
values
D=G(q,4,:); %"cuts" out velocity values for V of particular
spot
E = squeeze(D); %turns 1x1 3D matrix in A to column of
velocity values
spota(:,3)=D(:,1); %copy in velocity values next to time
values

ures=zeros(size(spota,1),2);
ures(:,1)=spota(:,1);%copies the time values in ures matrix
ures(:,2)=((((spota(:,2).^2))+((spota(:,3).^2))).^0.5);
savefile = ['Resultant Velocity Spot X-',int2str(r),' Y-
',int2str(t),'.mat'];
save(savefile, 'ures');

x=ures(:,1); %single column with time vales
y=ures(:,2)./2.05; %single column with velocity values
figure
```

```
axes('FontSize',16)
h = plot (x,y,'b'); %plots velocity vs time
ylim([0.0 2.0]);
title (['Below Nozzle - High Flowrate: Velocity Magnitude Spot
X-',int2str(r),' Y-',int2str(t),' over Time'],'FontSize',14)
xlabel ('time (seconds)','FontSize',16)
ylabel ('Normalised Velocity','FontSize',16)
saveas(h,['Resultant Velocity Vs time (line) Spot X-
',int2str(r),' Y-',int2str(t),]) %saves velocity vs time plot

figure
axes('FontSize',14)
h = plot (x,y,'b.'); %plots velocity vs time
ylim([-1.0 4.0]);
title (['Below Nozzle - High Flowrate: Velocity Magnitude Spot
X-',int2str(r),' Y-',int2str(t),' over Time'],'FontSize',14)
xlabel ('time (seconds)','FontSize',14)
ylabel ('Velocity (ms-1)','FontSize',14)
saveas(h,['Resultant Velocity Vs time (points) Spot X-
',int2str(r),' Y-',int2str(t),]) %saves velocity vs time plot

[n,xout] = hist(y,10,'b'); %"bins" values to give groups for
histogram plot
z=figure
axes('FontSize',16)
bar(xout,n); %plots frequency against velocity "bin" values
ylim([0 800]);
xlim([0.0 2.0]);
title (['Below Nozzle - High Flowrate: Velocity Magnitude
Histogram Spot X-',int2str(r),' Y-
',int2str(t),],'FontSize',14)
xlabel ('Normalised Velocity','FontSize',16)
ylabel ('Frequency','FontSize',16)
saveas(z,['Resultant Velocity-Histogram Spot X-',int2str(r),'
Y-',int2str(t),]) %saves velocity histogram

cd ('C:\Users\Guy\Desktop\PIV MATLAB Codes');



%% RoySoft 2009
%% Written by G. Hassall

%Directory/folder for vector files
cd ('C:\Users\Guy\Desktop\March Airflow Vectors\15 meters\8000
kg');
%%%Load 3D matrix%%%
```

```
%%%%%%%%%%%%%%%%%%%%%%%%%%%%%%%%%%%%%%%%%%%%%%%%%%%%%%%%%%%%%%%%%%%%%%%%
%%%%%%%%

% Obtaining correct rwo number to look up correct spot from 3D
matrix
r = input('spot position x?')
t = input('spot position y?')

load (['Resultant Velocity Spot X-',int2str(r),' Y-
',int2str(t),'.mat']);

p=size (ures,1); %time period of measurement ie number of
velocity measurements (usually 1000 secs)
ubar=zeros (p,14); %matrix for storing results
ubar(:,1:2)=ures(:,1:2); %makes 1st and 2nd columns in ubar
time and velocity

%%Continious mean calculation and plot

for i= (1:p);
    ubar(i,3)= mean(ubar(1:i,2));

end

%% continious standard deviation
for i= (1:p);
    ubar(i,10)= std(ubar(1:i,2));

end

x=ubar(:,1); %single column with time vales
y=ubar(:,3); %single column with velocity values
figure
axes('FontSize',14);
h = plot (x,y,'k'); %plots velocity vs time
title (['Below Nozzle - High Flowrate: Continious Mean of
Velocity Magnitude in Spot X-',int2str(r),' Y-
',int2str(t)],'FontSize',14)
xlabel ('time (seconds)')
ylabel ('Mean Velocity Magnitude (ms-1)')
saveas(h,['Mean Velocity Magnitude Spot X-',int2str(r),' Y-
',int2str(t),]) %saves plot

x=ubar(:,1); %single column with time vales
y=ubar(:,3); %single column with velocity values
figure
axes('FontSize',14);
h = plot (x,y,'k'), axis([0 1000 0 3]); %plots velocity vs
time
```

```
title (['Below Nozzle - High Flowrate: Continious Mean of
Velocity Magnitude in Spot X-',int2str(r),' Y-
',int2str(t)],'FontSize',14)
xlabel ('PIV Image Pairs Analysed')
ylabel ('Mean Velocity Magnitude (ms-1)')
saveas(h,['Mean Velocity Magnitude Spot scaled X-
',int2str(r),' Y-',int2str(t),]) %saves plot

x=ubar(:,1); %single column with time vales
y=ubar(:,10); %single column with velocity values
figure
axes('FontSize',14)
h = plot (x,y,'k'), axis([0 1000 0 0.4]); %plots velocity vs
time
title (['Below Nozzle - High Flowrate: Continious Standard
Deviation of Velocity Magnitude in Spot X-',int2str(r),' Y-
',int2str(t)],'FontSize',14)
xlabel ('PIV Image Pairs Analysed')
ylabel ('RMS Velocity Magnitude (ms-1)')
saveas(h,['std Velocity Magnitude Spot scaled X-',int2str(r),'
Y-',int2str(t),]) %saves plot

%%Mean every 5 points calculation and plot
z = (p/5)
for i = (1:z);
    c = (i+(4*i));
    ubar(c,12) = mean(ubar(((c-4):c)),2));
    ubar(c,11) = c;
end

x=ubar(:,11); %single column with time vales
y=ubar(:,12); %single column with velocity values
figure
axes('FontSize',14)
h = plot (x,y,'.'); %plots velocity vs time
title (['Below Nozzle - High Flowrate: Mean Velocity Magnitude
for every 5 seconds in Spot X-',int2str(r),' Y-
',int2str(t)],'FontSize',14)
xlabel ('time (seconds)')
ylabel ('Mean Velocity Magnitude (ms-1)')
saveas(h,['Mean Velocity Magnitude for every 5 points Spot X-
',int2str(r),' Y-',int2str(t),]) %saves plot

%%Mean every 10 points calculation and plot
z = (p/10)
for i = (1:z);
    c = (i+(9*i));
    ubar(c,14) = mean(ubar(((c-9):c)),2));
    ubar(c,13) = c;
```

```
end

x=ubar(:,13); %single column with time vales
y=ubar(:,14); %single column with velocity values
figure
axes('FontSize',14)
h = plot (x,y,'.'); %plots velocity vs time
title (['Below Nozzle - High Flowrate: Mean Velocity Magnitude
for every 10 seconds in Spot X-',int2str(r),' Y-
',int2str(t)],'FontSize',14)
xlabel ('time (seconds)')
ylabel ('Mean Velocity Magnitude (ms-1)')
saveas(h,['Mean Velocity Magnitude for every 10 points Spot X-
',int2str(r),' Y-',int2str(t),]) %saves plot

%%Mean every 20 points calculation and plot
z = (p/20)
for i = (1:z);
    c = (i+(19*i));
    ubar(c,5) = mean(ubar(((c-19):c)),2));
    ubar(c,4) = c;
end

x=ubar(:,4); %single column with time vales
y=ubar(:,5); %single column with velocity values
figure
axes('FontSize',14)
h = plot (x,y,'.'); %plots velocity vs time
title (['Below Nozzle - High Flowrate: Mean Velocity Magnitude
for every 20 seconds in Spot X-',int2str(r),' Y-
',int2str(t)],'FontSize',14)
xlabel ('time (seconds)')
ylabel ('Mean Velocity Magnitude (ms-1)')
saveas(h,['Mean Velocity Magnitude for every 20 points Spot X-
',int2str(r),' Y-',int2str(t),]) %saves plot

%%Mean every 50 points calculation and plot
z = (p/50);
for i = (1:z);
    c = (i+(49*i));
    ubar(c,7) = mean(ubar(((c-49):c)),2));
    ubar(c,6)= c;
end

x=ubar(:,6); %single column with time vales
y=ubar(:,7); %single column with velocity values
figure
axes('FontSize',14)
h = plot (x,y,'.'); %plots velocity vs time
```

```
title (['Below Nozzle - High Flowrate: Mean Velocity Magnitude
for every 50 seconds in Spot X-',int2str(r),' Y-
',int2str(t)],'FontSize',14)
xlabel ('time (seconds)')
ylabel ('Mean Velocity Magnitude (ms-1)')
saveas(h,['Mean Velocity Magnitude for every 50 points Spot X-
',int2str(r),' Y-',int2str(t),]) %saves plot

%%Mean every 100 points calculation and plot
z = (p/100)
for i = (1:z);
    c = (i+(99*i));
    ubar(c,9) = mean(ubar(((c-99):c)),2));
    ubar(c,8)=c;
end

x=ubar(:,8); %single column with time vales
y=ubar(:,9); %single column with velocity values
figure
axes('FontSize',14)
h = plot (x,y,'.'); %plots velocity vs time
title (['Below Nozzle - High Flowrate: Mean Velocity Magnitude
for every 100 seconds in Spot X-',int2str(r),' Y-
',int2str(t)],'FontSize',14)
xlabel ('time (seconds)')
ylabel ('Mean Velocity Magnitude (ms-1)')
saveas(h,['Mean Velocity Magnitude for every 100 points Spot
X-',int2str(r),' Y-',int2str(t),]) %saves plot

%% Periodicity Analysis For actual signal
velo = ures (:,2);
Y = fft(velo);
N = length(Y);                  %%Gets length of Y
Y(1) = [];                      %%Removes the first component
of Y, which is simply the sum of the data
power = abs(Y(1:(N/2))).^2;
nyquist = 1/2;
freq = (1:N/2)/(N/2)*nyquist;
figure
axes('FontSize',14)
h=plot(freq,power), grid on
title (['Below Nozzle - High Flowrate: Periodogram of Velocity
Magnitude in Spot X-',int2str(r),' Y-
',int2str(t)],'FontSize',14)
ylabel('Power')
xlabel('Frequency(cycles/second)')
saveas(h,['Periodogram Spot X-',int2str(r),' Y-',int2str(t),])
%saves plot
```

```
figure
axes('FontSize',14)
period = 1./freq;
h = loglog(period,power), grid on
title (['Below Nozzle - High Flowrate: Power Vs Period of
Velocity Magnitude in Spot X-',int2str(r),' Y-
',int2str(t)],'FontSize',14)
ylabel('Power')
xlabel('Period(seconds/cycle)')
saveas(h,['Power Vs Period Spot X-',int2str(r),' Y-
',int2str(t),]) %saves plot
savefile = ['transisance.mat'];
save(savefile, 'ubar');

%%Settings for Moving Average
a = 1;
b = [1/4 1/4 1/4 1/4];

%%Moving Average
velo1 = filter(b,a,velo);
Y1 = fft(velo1(10:990,:));
N = length(Y1);                    %%Gets length of Y
Y1(1) = [];                        %%Removes the first component
of Y, which is simply the sum of the data
power = abs(Y1(1:(N/2))).^2;
nyquist = 1/2;
freq = (1:N/2)/(N/2)*nyquist;
figure
axes('FontSize',14)
h=plot(freq,power), grid on
title (['Below Nozzle - High Flowrate: Periodogram of Filtered
(moving average) Velocity Magnitude in Spot X-',int2str(r),'
Y-',int2str(t)],'FontSize',14)
ylabel('Power')
xlabel('Frequency(cycles/second)')

figure
axes('FontSize',14)
period = 1./freq;
h = loglog(period,power), grid on
title (['Below Nozzle - High Flowrate: Power Vs Period of
Filtered (moving average) Velocity Magnitude in Spot X-
',int2str(r),' Y-',int2str(t)],'FontSize',14)
ylabel('Power')
xlabel('Period(seconds/cycle)')

cd('C:\Users\Guy\Desktop\PIV MATLAB Codes');
```

A.2 Particle Dynamics Codes (Chapter Six)

Chapter Six presents results from PIV studies of detergent particles moving through the spray dryer.

A.2.1 Image Manipulation

The first step in image analysis was to identify the greyscale value required as the threshold for turning greyscale images to binary. The following is an example of the MARLAB codes used to threshold greyscle images to binary before PIV cross-correlation and image analysis. This code loads up and thresholds the images in a dataset as a loop.

```
%% RoySoft 2009
%% Written by G. Hassall

%% Image processing: Binary Coverter

%% Input required values
nfiles = input ('Last Frame? (e.g. 499) >> ')

%Directory/folder for Image files
cd ('G:\Guys PIV\PIV Particles\15m\1000kg air 6000kg slurry');

fnameA = ['1000kg slurry 6000kg air Thurs 9th
Oct002000.T000.D000.P000.H000.LA.tif'];

IA = imread([fnameA]);
level = 0.13;
bwA = im2bw(IA,level);
bwA = im2uint8(bwA);
res = [150,150];

cd ('G:\Guys PIV\PIV Particles\15m\1000kg air 6000kg slurry
binary');

imwrite(bwA,fnameA,'tiff','Compression','none','Resolution',re
s);

cd ('G:\Guys PIV\PIV Particles\15m\1000kg air 6000kg slurry');
```

```
fnameB = ['1000kg slurry 6000kg air Thurs 9th
Oct002000.T000.D000.P000.H000.LB.tif'];

IB = imread([fnameB]);
level = 0.13;
bwB = im2bw(IB,level);
bwB = im2uint8(bwB);
res = [150,150];

cd ('G:\Guys PIV\PIV Particles\15m\1000kg air 6000kg slurry
binary');

imwrite(bwB,fnameB,'tiff','Compression','none','Resolution',re
s);

cd ('G:\Guys PIV\PIV Particles\15m\1000kg air 6000kg slurry');

%%%The rest of files are loaded here as a loop%%%
for i = (1 : nfiles);
if i < 10
fnameA = ['1000kg slurry 6000kg air Thurs 9th
Oct00200',int2str(i),'.T000.D000.P000.H000.LA.tif'];
elseif 100 > i & i > 9
fnameA = ['1000kg slurry 6000kg air Thurs 9th
Oct0020',int2str(i),'.T000.D000.P000.H000.LA.tif'];
elseif 1000 > i & i > 99
fnameA = ['1000kg slurry 6000kg air Thurs 9th
Oct002',int2str(i),'.T000.D000.P000.H000.LA.tif'];
else
fnamea = ['1000kg slurry 6000kg air Thurs 9th
Oct00',int2str(i),'.T000.D000.P000.H000.LA.tif'];
end
if exist (fnameA)>0;

IA = imread([fnameA]);
level = 0.13;
bwA = im2bw(IA,level);
bwA = im2uint8(bwA);
res = [150,150];

cd ('G:\Guys PIV\PIV Particles\15m\1000kg air 6000kg slurry
binary');

imwrite(bwA,fnameA,'tiff','Compression','none','Resolution',re
s);

cd ('G:\Guys PIV\PIV Particles\15m\1000kg air 6000kg slurry');

end
```

```
end

%%%The rest of files are loaded here as a loop%%%
for i = (1 : nfiles);
if i < 10
fnameB = ['1000kg slurry 6000kg air Thurs 9th
Oct00200',int2str(i),'.T000.D000.P000.H000.LB.tif'];
elseif 100 > i & i > 9
fnameB = ['1000kg slurry 6000kg air Thurs 9th
Oct0020',int2str(i),'.T000.D000.P000.H000.LB.tif'];
elseif 1000 > i & i > 99
fnameB = ['1000kg slurry 6000kg air Thurs 9th
Oct002',int2str(i),'.T000.D000.P000.H000.LB.tif'];
else
fnameB = ['1000kg slurry 6000kg air Thurs 9th
Oct00',int2str(i),'.T000.D000.P000.H000.LB.tif'];
end
if exist (fnameB)>0;

IB = imread([fnameB]);
level = 0.13;
bwB = im2bw(IB,level);
bwB = im2uint8(bwB);
res = [150,150];

cd ('G:\Guys PIV\PIV Particles\15m\1000kg air 6000kg slurry
binary');

imwrite(bwB,fnameB,'tiff','Compression','none','Resolution',re
s);

cd ('G:\Guys PIV\PIV Particles\15m\1000kg air 6000kg slurry');

end
end

%Directory/folder for PIV image files
cd ('C:\Users\Guy\Desktop\PIV MATLAB Codes');
```

A.2.2 Image Analysis

Once the images were thresholded image analysis was conducted to obtain data and results on particle size, concentration and volume fraction, averaged over the entire dataset. The

code below loads the binary images created by the code shown in §0 and then uses image analysis algorithms built into MATLAB to obtain the data required.

```
%% RoySoft 2009
%% Written by G. Hassall

%% Image processing: Data Generation

%Directory/folder for Image files
cd ('F:\Guys PIV\PIV September\Test 1000kg 6000kg
air\RawData');

%% Input required values
nfiles = input ('Last Frame? (e.g. 499) >> ')
cal = input ('calibration meters per pixel? >> ')

s=csvread('1000-6000above spot size 16.csv');

%% Radial incremenets data sets collection matrices

totmwdia = nan(16,16, nfiles);

totvol = nan(16,16, nfiles);

totnum = nan(16,16, nfiles);

finmwdia = nan(16,16);

finvol = nan(16,16);

finnum = nan(16,16);

finconc  = nan(16,16);

finload = nan(16,16);

findia  = nan(16,16);

findiaplot = nan(16,16);

finconcplot = nan(16,16);

finloadplot = nan(16,16);

warning off MATLAB:divideByZero
warning off all
```

```
%% Load up first image

fname2 = ['Test 1000kg 6000kg
air001000.T000.D000.P000.H000.LA.tif'];

I = imread([fname2]);

%% background function on image

background = imopen(I,strel('line',100,1));
I2 = imsubtract(I,background);

%% Thresholding

level = 0.34;
bw = im2bw(I2,level);

%% Stats Calculation on thresholded image

[labeled,numObjects] = bwlabel(bw,4);

STATS = regionprops(labeled,'all');

dia = ((cat(1, STATS.EquivDiameter))*cal);;
pos = cat(1, STATS.Centroid);
area = (cat(1, STATS.Area)*(cal^2));

%% volume calc

vol = zeros(numObjects,1);

for h = (1:numObjects);

vol (h,1) = ((((dia(h,1))^3)*pi)/6);

end

%% Arrange all data with position of each particle

posvdia = zeros(numObjects,7);
posvdia(:,1) = pos(:,1);
posvdia(:,2) = pos(:,2);
posvdia(:,3) = dia(:,1);
posvdia(:,5) = vol(:,1);

%%Calculating weight diameter parameters

posvdia(:,6) = (posvdia(:,3).^3);
posvdia(:,7) = (posvdia(:,3).^4);
```

```
%% Binning of all properties based on particle position

for i = (1:16);
    for j = (1:16);

ymax = (i*64);
xmax = (j*64);
ymin = (ymax-63);
xmin = (xmax-63);

spot = find(posvdia(:,2)>ymin & posvdia(:,2)<ymax &
posvdia(:,1)>xmin & posvdia(:,1)<xmax);
spotdia = posvdia(spot,3);
mspotdia = mean(spotdia);

spotx3 = posvdia(spot,6);
spotx4 = posvdia(spot,7);

%% Size distribution binning for each radial position

spotnum = numel(spotdia);
totnum (i,j,1) = spotnum;

spotvol = posvdia(spot,5);
totspotvol = sum(spotvol);
totvol (i,j,1) = totspotvol;

spotxx3 = sum(spotx3);
spotxx4 = sum(spotx4);
mwdia (i,j,1) = (spotxx4/spotxx3);

end
end

%%%The rest of files are loaded here as a loop%%%
for z = (1 : nfiles);
if z < 10
fname3 = ['Test 1000kg 6000kg
air00100',int2str(z),'.T000.D000.P000.H000.LA.tif'];
elseif 100 > z & i > 9
fname3 = ['Test 1000kg 6000kg
air0010',int2str(z),'.T000.D000.P000.H000.LA.tif'];
elseif 1000 > z & i > 99
fname3 = ['Test 1000kg 6000kg
air001',int2str(z),'.T000.D000.P000.H000.LA.tif'];
else
fname3 = ['Test 1000kg 6000kg
air00',int2str(z),'.T000.D000.P000.H000.LA.tif'];
```

```
end
if exist (fname3)>0;

I = imread([fname3]);

%% background function on image

background = imopen(I,strel('line',100,1));
I2 = imsubtract(I,background);

%% Thresholding

level = 0.34;
bw = im2bw(I2,level);

[labeled,numObjects] = bwlabel(bw,4);

STATS = regionprops(labeled,'all');

dia = ((cat(1, STATS.EquivDiameter))*cal);;
pos = cat(1, STATS.Centroid);
area = (cat(1, STATS.Area)*(cal^2));

%% volume calc

vol = zeros(numObjects,1);

for h = (1:numObjects);

vol (h,1) = ((((dia(h,1))^3)*pi)/6);

end

warning off MATLAB:divideByZero
warning off all

%% Arrange all data with position of each particle

posvdia = zeros(numObjects,7);
posvdia(:,1) = pos(:,1);
posvdia(:,2) = pos(:,2);
posvdia(:,3) = dia(:,1);
posvdia(:,5) = vol(:,1);

%%Calculating weight diameter parameters

posvdia(:,6) = (posvdia(:,3).^3);
posvdia(:,7) = (posvdia(:,3).^4);
```

```
%% Binning of all properties based on particle position

for i = (1:16);
    for j = (1:16);

ymax = (i*64);
xmax = (j*64);
ymin = (ymax-63);
xmin = (xmax-63);

spot = find(posvdia(:,2)>ymin & posvdia(:,2)<ymax &
posvdia(:,1)>xmin & posvdia(:,1)<xmax);
spotdia = posvdia(spot,3);
mspotdia = mean(spotdia);

spotx3 = posvdia(spot,6);
spotx4 = posvdia(spot,7);

%% Size distribution binning for each radial position

x = (z+1);

spotnum = numel(spotdia);
totnum (i,j,x) = spotnum;

spotvol = posvdia(spot,5);
totspotvol = sum(spotvol);
totvol (i,j,x) = totspotvol;

spotxx3 = sum(spotx3);
spotxx4 = sum(spotx4);
totmwdia (i,j,x) = (spotxx4/spotxx3);

end
end

end
end

for i = (1:16);
    for j = (1:16);

        A = squeeze(totnum(i,j,:));
        AN = find(~isnan(A));
        A = A(AN);
        finnum (i,j) = mean (A);
        finconc (i,j) = (finnum(i,j) / s(i,j));
        B = squeeze(totvol(i,j,:));
        BN = find(~isnan(B));
```

```
        B = B(BN);
        finvol (i,j) = mean (B);
        finload (i,j) = (finvol(i,j) / s(i,j));
        C = squeeze(totmwdia(i,j,:));
        CN = find(~isnan(C));
        C = C(CN);
        finmwdia (i,j) = mean (C);
        findia (i,j) = (finmwdia(i,j) * 1000000);

    end
end

%% Plot mean diamater

a=figure;
findiaplot = flipdim(findia,1);
axes('FontSize',14)
X = linspace(0,142.3,16);
Y = linspace(0,142.3,16);
contourf(X,Y,findiaplot,50,'linestyle','none');
set(gca,'DataAspectRatio',[1 1 1])
set(gca,'DataAspectRatio',[1 1 1])
caxis([0 1000]);
colorbar('FontSize',14)
title ('1.00 Slurry 6000kghr-1 Air Above Nozzle: Mean Particle
Diameter','FontSize',14)
xlabel('x position (mm)','FontSize',14)
ylabel('y position (mm)','FontSize',14)
savefile = 'findiaplot.mat';
save(savefile, 'findiaplot')

%Plot concentration
b=figure;
finconcplot = flipdim(finconc,1);
axes('FontSize',14)
X = linspace(0,142.3,16);
Y = linspace(0,142.3,16);
contourf(X,Y,finconcplot,50,'linestyle','none');
set(gca,'DataAspectRatio',[1 1 1])
caxis([0 50000000]);
colorbar('FontSize',14)
title ('1.00 Slurry 6000kghr-1 Air Above Nozzle: Mean Particle
Concentration','FontSize',14)
xlabel('x position (mm)','FontSize',14)
ylabel('y position (mm)','FontSize',14)
savefile = 'finconcplot.mat';
save(savefile, 'finconcplot')

%% Plot loading
```

```
c=figure;
finloadplot = flipdim(finload,1);
axes('FontSize',14)
X = linspace(0,142.3,16);
Y = linspace(0,142.3,16);
contourf(X,Y,finloadplot,50,'linestyle','none');
set(gca,'DataAspectRatio',[1 1 1])
caxis([0.0 0.001]);
colorbar('FontSize',14)
title ('1.00 Slurry 6000kghr-1 Air Above Nozzle: Mean Particle
Volume Fraction','FontSize',14)
xlabel('x position (mm)','FontSize',14)
ylabel('y position (mm)','FontSize',14)
savefile = 'finloadplot.mat';
save(savefile, 'finloadplot')

%Directory/folder for PIV image files
cd ('C:\Users\Guy\Desktop\PIV MATLAB Codes');
```

A.2.3 Particle PIV data handling and Plotting

PIV cross correlation was conducted with the binary images created using the code shown in §0, using the TSI PIV software. The output from this analysis was loaded into a 3D matrix and the velocity parameters are calculated in a similar manner to those in (§0).

```
%% RoySoft 2009
%% Written by G. Hassall
%% Based on codes by K. Chung and G. Neal

%Directory/folder for vector files
cd ('C:\Users\Guy\Desktop\particle vec files\above
nozzle\1000-6000');
%%%Load Vector Files%%%
%%%%%%%%%%%%%%%%%%%%%%%%%%%%%%%%%%%%%%%%%%%%%%%%%%%%%%%%%%%%%%%%%%%%%%%%
%%%%%%%%
nfiles = input ('Last Frame? (e.g. 499) >> ')
fname3 = ['Test 1000kg 6000kg
air004934.T000.D000.P049.H000.L.vec'];
%%One vector file is loaded here, assuming first file ends
with 00000.vec%%
s=csvread([fname3],1,0);
G=s;
%%%The rest of files are loaded here as a loop%%%
for i = (4935 : nfiles);
```

```
if i < 10
fname3 = ['Test 1000kg 6000kg
air00100',int2str(i),'.T000.D000.P049.H000.L.vec'];
elseif 100 > i & i > 9
fname3 = ['Test 1000kg 6000kg
air0010',int2str(i),'.T000.D000.P049.H000.L.vec'];
elseif 1000 > i & i > 99
fname3 = ['Test 1000kg 6000kg
air001',int2str(i),'.T000.D000.P049.H000.L.vec'];
else
fname3 = ['Test 1000kg 6000kg
air00',int2str(i),'.T000.D000.P049.H000.L.vec'];
end
if exist (fname3)>0
s=csvread([fname3],1,0);
G2=s;
G=cat(3,G,G2);
end
end
clear G2;

%remove false values
[D,L]=find(G(:,5,:)<1);%finds all where 'false' is indicated
by the software
for l=1:length(D);
    G(D(l),3:4,L(l))=NaN;%sets the velocities and the 5th
column to zero for the false vectors
    l=l+1;
end

%removing filled vectored errors
[D,L]=find(G(:,5,:)>1);%finds all where 3G software has
added/filled vector
for l=1:length(D);
    G(D(l),5,L(l))=1;%sets the 5th column to one for the
filled vectors
    l=l+1;
end

% Enter correct number of spots for width and hieght of image
for reshaping
f = input('number of spots?') %enter number of spots image is
split into
%%%%%%%%%%%%%%%%%%%%%%%%%%%%%%%%%%%%%%%%%%%%%%%%%%%%%%%%%%%%%%%
%%%%%%%%%%%%%

%x increases down rows
%y increases along columns
sizeG=size(G);
```

```
sizeG=sizeG(3);

for i = 1:1:sizeG;  %%works through loop for i values from 1
to size of G
U=G(:,3,i);         %% Cuts out U velocities from G matrix
UU=reshape(U,f,[]); %% moves column of U velocities in U
matrix into 63 by 63 square matrix(top left is X1, Y1 and
bottom left is Xn, Y1)
Umatrix(:,:,i)=UU;  %% Creates 3D U matrix with each U value
stacked behind previous
V=G(:,4,i);         %% as above for V
VV=reshape(V,f,[]);
Vmatrix(:,:,i)=VV;
Vec=G(:,5,i);               %% cuts of the CHC column from the
3D matrix G
VVec=reshape(Vec,f,[]);     %% creates 63 by 63 matrix as
above
Vecmatrix(:,:,i)=VVec;      %% stacks matrices
clear U UU V VV Vec VVec;
end;

% remove NaN entries
Umean = nan(f,f);         %% set up required matrices to be
filled (f= no spots)
Vmean = nan(f,f);
RMSU = nan(f,f);
RMSV = nan(f,f);
RSUV = nan(f,f);
TKE = nan(f,f);
URes = nan(f,f);
for i=1:f;
    for j = 1:f;            %% Runs a loop from 1 to 63 to
generate all of below for each column of matrix
        U = squeeze(squeeze(Umatrix(i,j,:)));   %% cuts out
row by row from 3D stack on Umatrix (63 by 63 matrix of each
value stacked in turn)
        V = squeeze(squeeze(Vmatrix(i,j,:)));
        NU = find(~isnan(U));                   %%
        NV = find(~isnan(V));
        U = U(NU);
        V = V(NU);
        AU=size(U);
        AV=size(V);
        Kount(i,j)=AU(1);                       %% counts
number of vectors in each spot over the full time period of
study
        if AU(1) > 1
        Umean(i,j)=mean(U);
        Vmean(i,j)=mean(V);
```

```
          URes (i,j) =
((((Umean(i,j).^2))+((Vmean(i,j)).^2)).^0.5);
             for h=(1 : AU);
            UZ = U(h,1);
            VZ = V(h,1);
            UURes (h,1) = (((UZ.^2)+(VZ.^2)).^0.5);
         end
     UResSTD (i,j) = STD(UURes);
         end
     end
end

%Plot Tangential Velocity
Umeanplot = rot90(Umean);

%Plot Radial Velocity
Vmeanplot = rot90(Vmean);

%Plot Resultant Velocity
UResplot = rot90(URes);
UResplot(15:16,:) = nan;
UResplot(1,:) = nan;
%Umeanplot = rot90(Umean);
%Umeanplot(15:16,:) = nan;
Umeanplot(1,:) = nan;
%Vmeanplot = rot90(Vmean);
%Vmeanplot(15:16,:) = nan;
Vmeanplot(1,:) = nan;
c=figure;
axes('FontSize',14)
X = linspace(0,142.4,15);
Y = linspace(0,142.4,15);
contourf(X,Y,UResplot,50,'linestyle','none');
caxis([0.0 0.5]);
set(gca,'DataAspectRatio',[1 1 1])
colorbar('FontSize',14)
title ('Above Nozzle - Low Slurry Flowrate and Low Air
Flowrate : Velocity Magnitude','FontSize',14)
xlabel('x position (mm)','FontSize',14)
ylabel('y position (mm)','FontSize',14)
hold on
scale = 0.75;
quiver(X,Y,Umeanplot, Vmeanplot, scale,'k','LineWidth',1);
hold off

cd('C:\Users\Guy\Desktop\PIV MATLAB Codes');
```

Appendix B – Wall Deposition Example Calculations

This appendix shows example calculations of how the amount of deposition in different areas and entire area of the spray dryer was calculated and turned into a yield expression. In order to calculate deposition over the entire area of dryer, it was then split into sections and the deposition per unit area values obtained were extrapolated over these areas to estimate the total amount of material deposited over these sections. By summing the material deposited in these sections, the total amount of material deposited over the entire dryer was obtained and compared to the total amount of slurry sprayed during the entire period of dryer operation, enabling calculation of a yield value.

The first stage in this calculation was to split the spray dryer into sections, each of which contained a measurement location. Figure B.1 shows how the dryer was split into these simplified geometries, cylinders for the dryer shell and a cone for the dryer cone. The area of the walls in each of these sections was calculated (using basic geometry equations) and the areas calculated for each are displayed in Table B.1.

Table B.1: Detergent Formulations for Impact Experiments

Section	Shape	Height (m)	Diameter (m)	Wall Area (m^2)
10.5 m to 18 m	Cylinder	7.5	1.7	40.1
7.5 m to 10.5 m	Cylinder	3.0	1.7	16.0
4.5 m to 7.5 m	Cylinder	3.0	1.7	16.0
0 m to 4.5 m	Cylinder	4.5	1.7	24.0
cone	Cone	2.2	1.7	11.0
Total				107.1

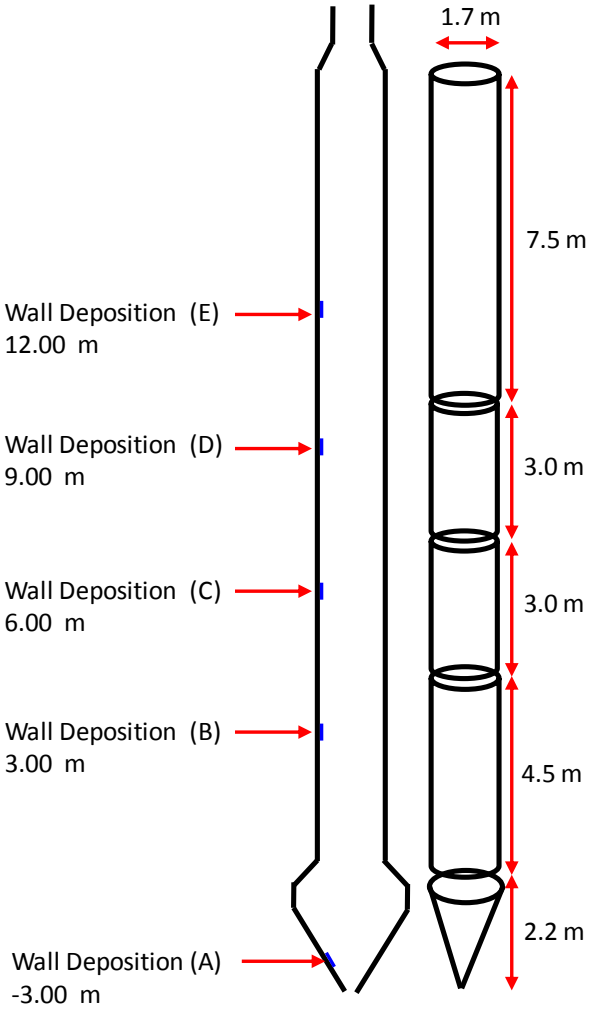

Figure B.1: Sections used in estimation of spray dryer internal wall area

The total amount of material deposited over the entire area of each section was calculated by multiplying the deposition per unit area calculated through the measurements (§3.4) by the total area of each section as shown in Table 3.2. Summing these figures allowed the total deposition on the dryer to be calculated, thus giving an estimation of the amount of slurry lost to wall deposition during dryer operation.

Appendix C – Fluid Dynamics in a Detergent Spray Dryer (Further Data)

This Appendix displays extra results and data that were not included in Chapter five but do have relevance on the fluid dynamics in spray dryers.

C.1 Normalised Time Averaged Flow Fields

Figure C.1 shows the same flow fields with velocity values normalised against the inlet tangential velocity values for each experimental condition as displayed in Table 5.1 (§5.2).

Comparing the normalised values of velocity magnitude for the three flow fields displayed for different flow rates of air the higher position (Figure C.1 a, b and c) shows how normalised velocity does not increase with increasing airflow rate. This indicates that the structure of the flow (vortex) is affected by flow rate and can be described as self-impating.

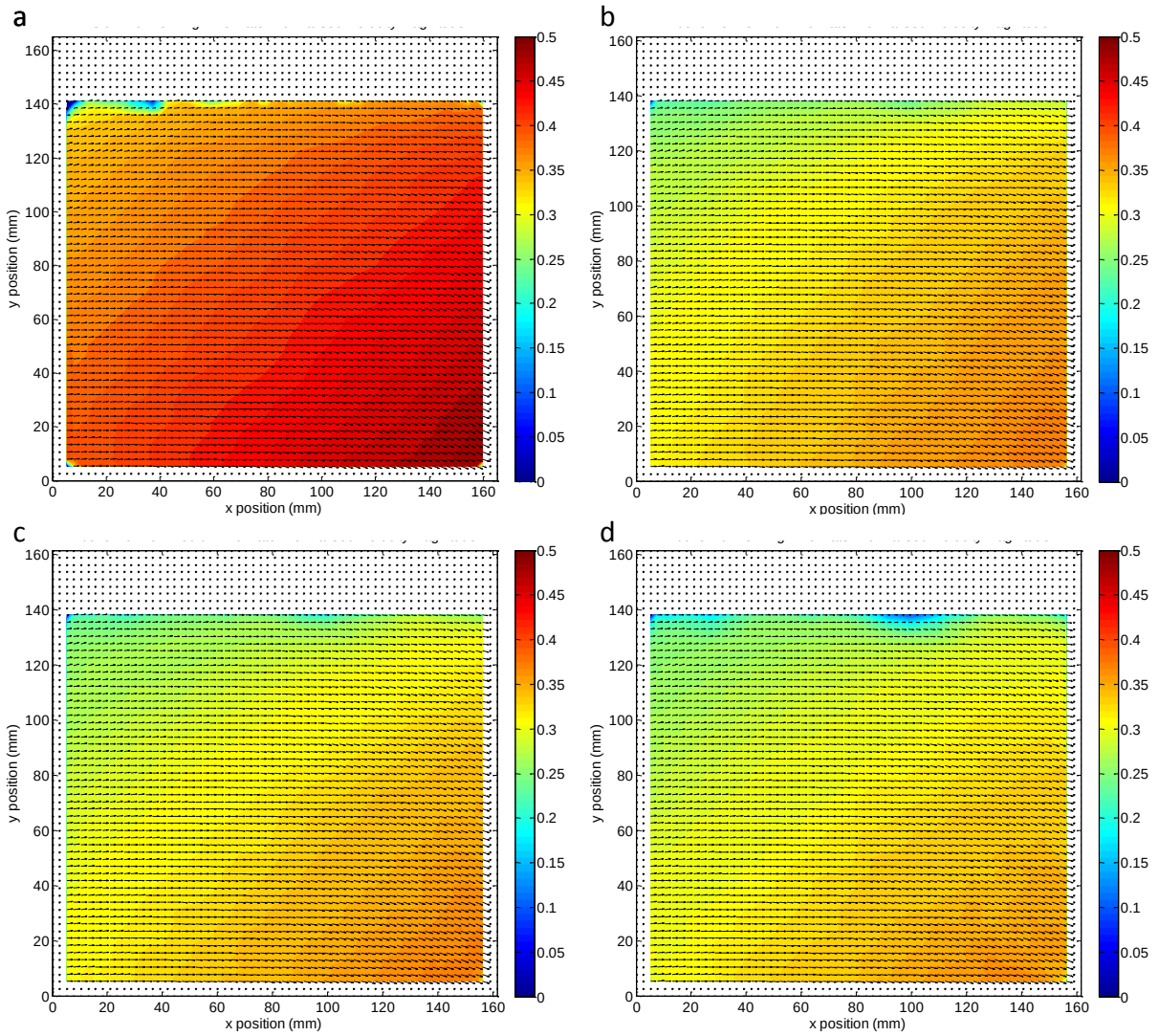

Figure C.1: Flow Field Plots of Velocity Magnitude Normalised Values: (a) low-position with high-flowrate, (b) high-position with low-flowrate, (c) high-position with medium-flowrate and (d) high-position with high-flowrate.

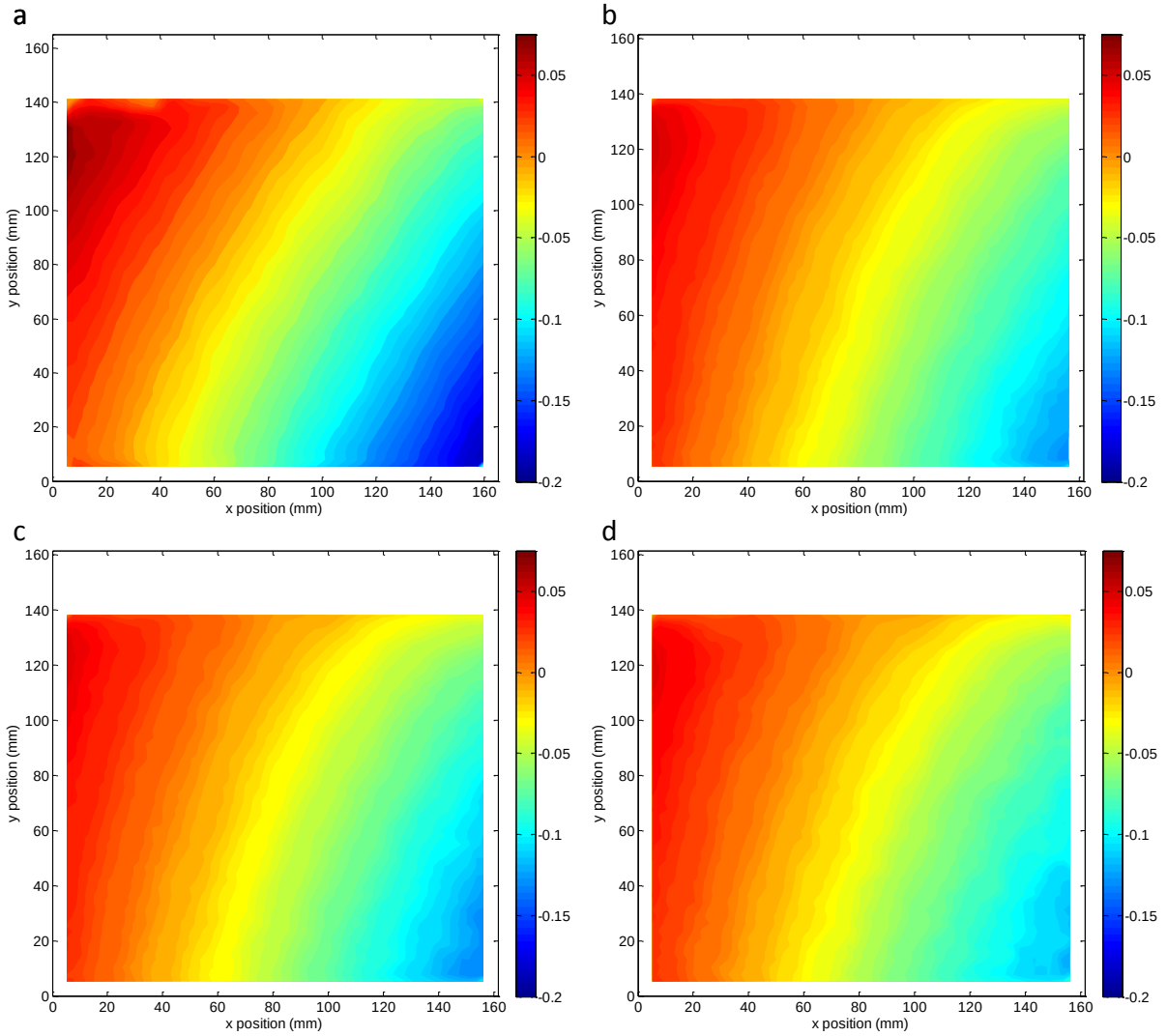

Figure C.2: Flow Field Plots of Normalised Values of Radial Velocity: (a) low-position with high-flowrate, (b) high-position with low-flowrate, (c) high-position with medium-flowrate and (d) high-position with high-flowrate.

As with the velocity magnitude, and radial velocity, normalised values of radial and tangential velocities, Figure C.2 and Figure C.3, show similar trends and again indicate that the vortex is self impating.

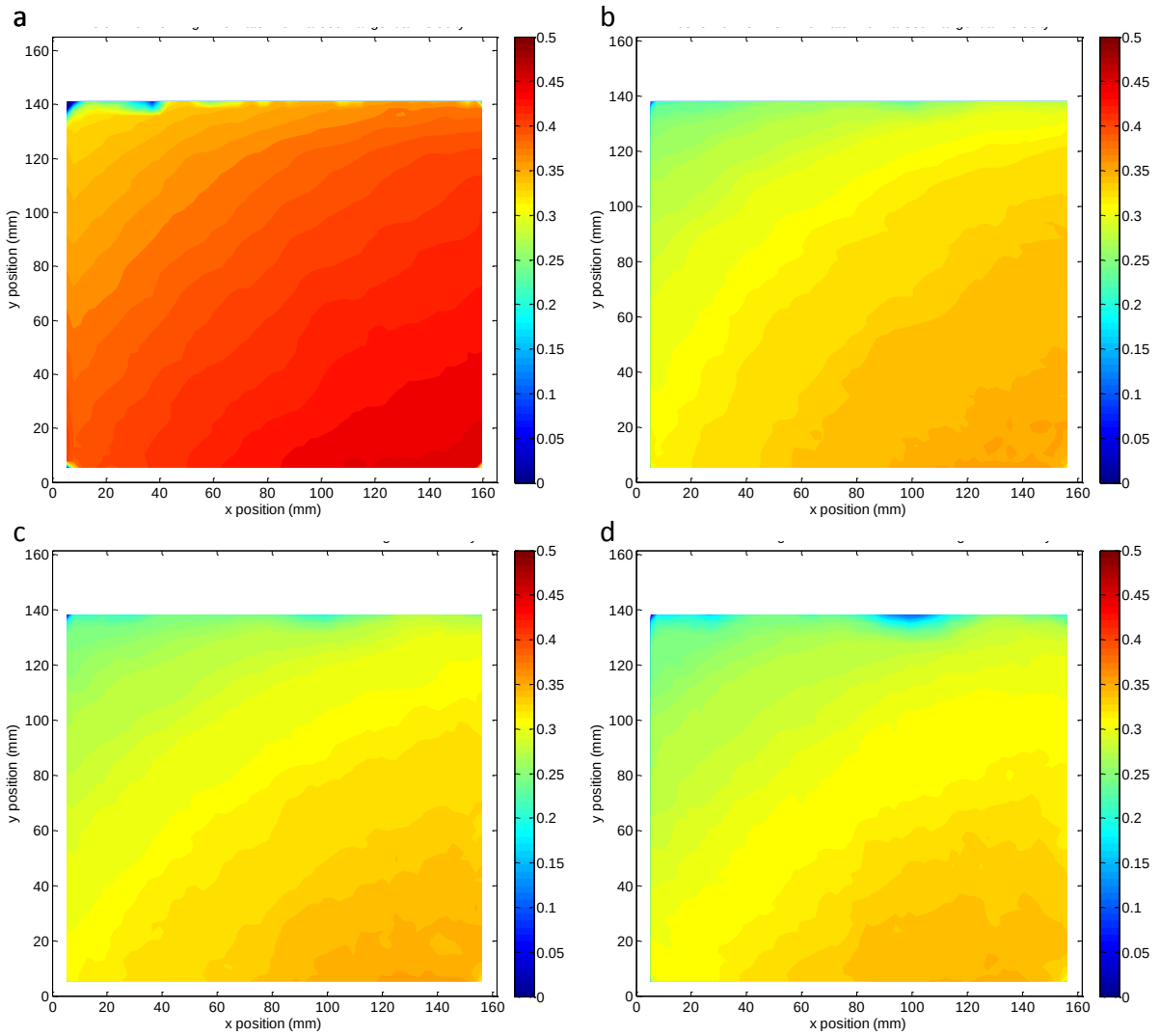

Figure C.3: Flow Field Plots of Normalised Values of Tangential Velocity: (a) low-position with high-flowrate, (b) high-position with low-flowrate, (c) high-position with medium-flowrate and (d) high-position with high-flowrate.

C.2 Turbulent Parameters

C.2.1 Turbulent Kinetic Energy

Figure C.4 shows plots of turbulent kinetic energy (§2.5.3) for all experimental conditions. Values of TKE between 0.2 and 0.5 $kJkg^{-1}$ are seen in the lower position and values between 0.1 and 0.5 $kJkg^{-1}$ in the higher position (excluding edge effects as seen on previous plots).

Values of TKE would be expected to reflect the same trends as turbulence intensity (§5.4) and indeed this is the case. In position L, TKE appears to increase with distance from the wall as with the turbulence intensity, again this trend is not so obvious in position H. Increasing flow rate appears to increase TKE values, as was seen with the turbulence intensity. This means that more of the fluid's energy is dissipated though turbulence in the lower position (closer to the air inlets) and also as flow rate is increased.

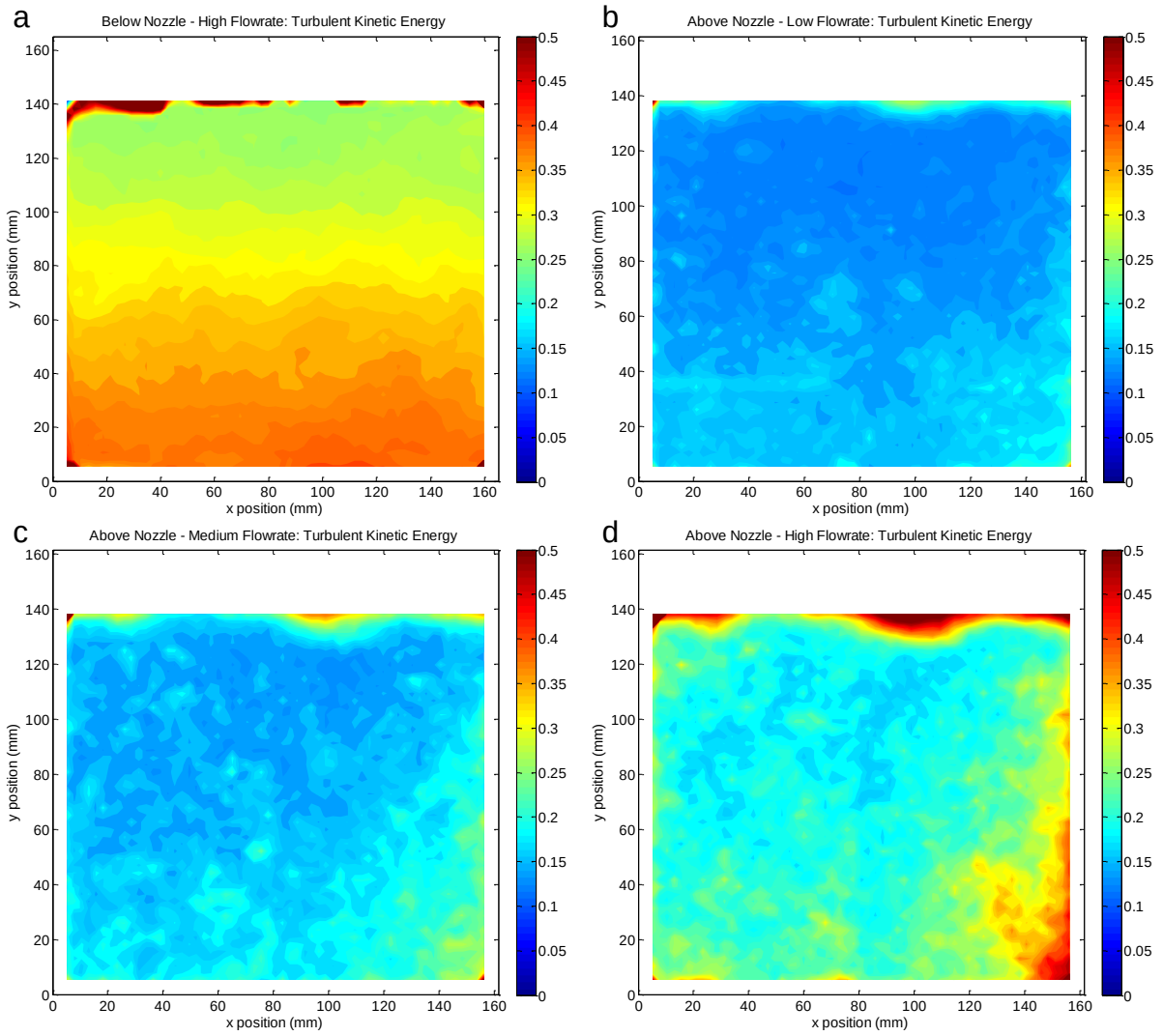

Figure C.4: Turbulent Kinetic Energy Plots: (a) low-position with high-flowrate, (b) high-position with low-flowrate, (c) high-position with medium-flowrate and (d) high-position with high-flowrate.

C.2.2 Reynolds Stresses

Reynolds stress (§ 2.5.3) values for all experimental conditions are shown in Figure C.5. The largest values of Reynolds stresses are seen in the lower position – high flowrate (a) conditions, ranging from 0.0 to 0.04. increasing the air flowrate in the higher experimental position (b) to (c) to (d) increases the values of Reynolds stresses seen, from 0.0 to 0.01 for the low flow, through to 0.0 to 0.02 at medium flow and then 0.0 and 0.04 at high flowrate.

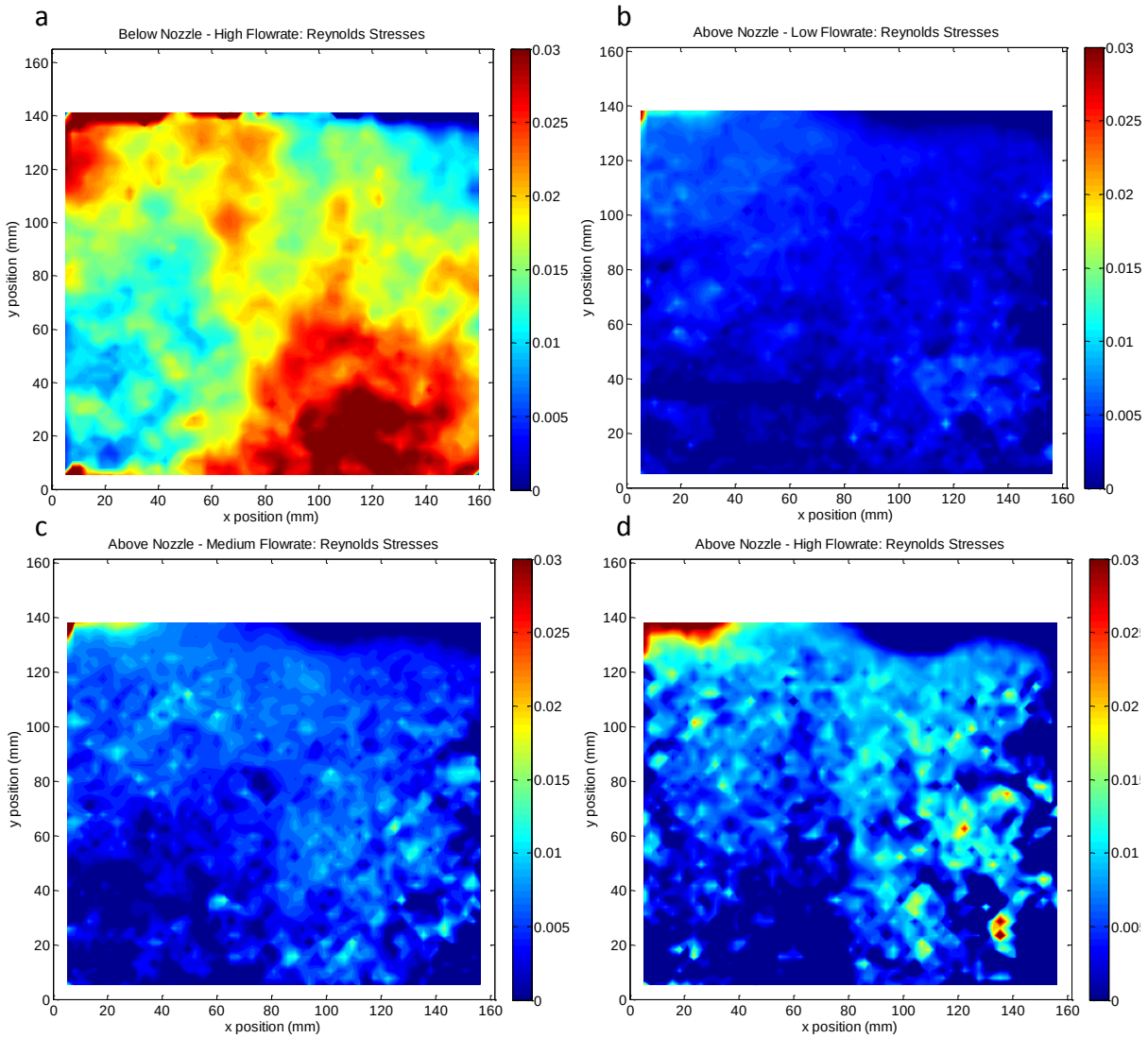

Figure C.5: Reynolds Stress Plots: (a) low-position with high-flowrate, (b) high-position with low-flowrate, (c) high-position with medium-flowrate and (d) high-position with high-flowrate.

These values and how they increase with decreasing distance to the air inlets and increase with increasing flowrate further reflect the trends in turbulence shown by all turbulent parameters calculated. Increasing values of Reynolds stresses show increased force being applied on the steady flow by the fluctuating component and therefore increased levels of turbulent motion in the flow. Similar trends can be seen in Figure C.6, which shows values of Reynolds stresses normalised against tangential inlet air velocity for each experimental condition.

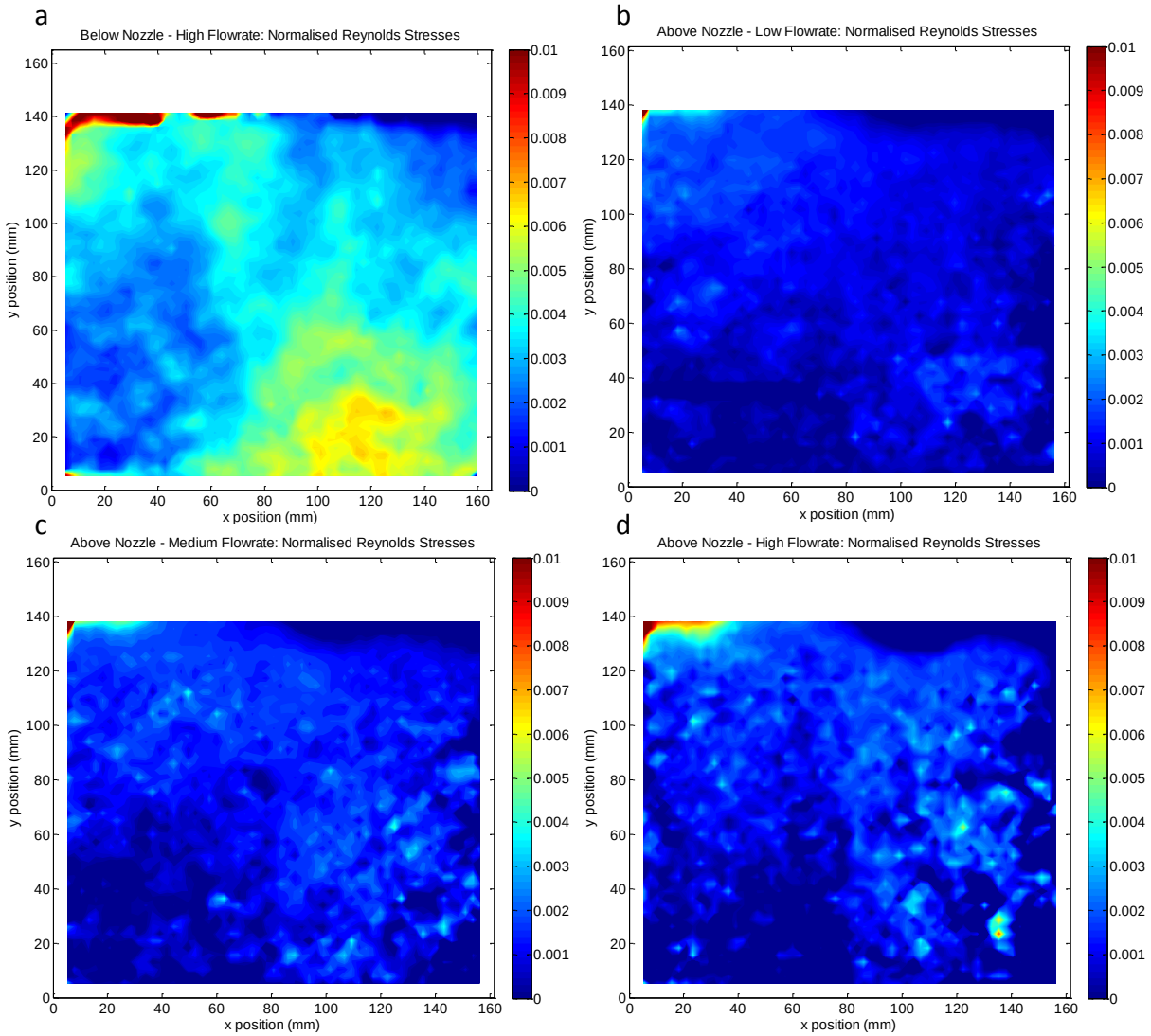

Figure C.6: Normalised Reynolds Stress Plots: (a) low-position with high-flowrate, (b) high-position with low-flowrate, (c) high-position with medium-flowrate and (d) high-position with high-flowrate.

Appendix D – Particle Dynamics Analaysis Methods

The complexity of the images captured, *i.e.* the range of grayscale values, presented a challenge in terms of developing a suitable analysis route that would allow particle size, concentration and loading details to be obtained as well as allowing PIV cross-correlation to be conducted to obtain particle velocity fields (§3.5.5). In this section, the nature of the captured images and the steps taken to develop a suitable image analysis route are described. Details on how particle size, concentration and loading parameters were calculated are given along with details on how cross-correlation was conducted to obtain particle flow fields. The possible errors encountered in this work are also reviewed.

D.1 PIV Images Captured

The nature of the images captured during these experiments presented a challenge in terms of obtaining quantitative data through image analysis and cross correlation. Examples of images captured are shown in Figure D.1.

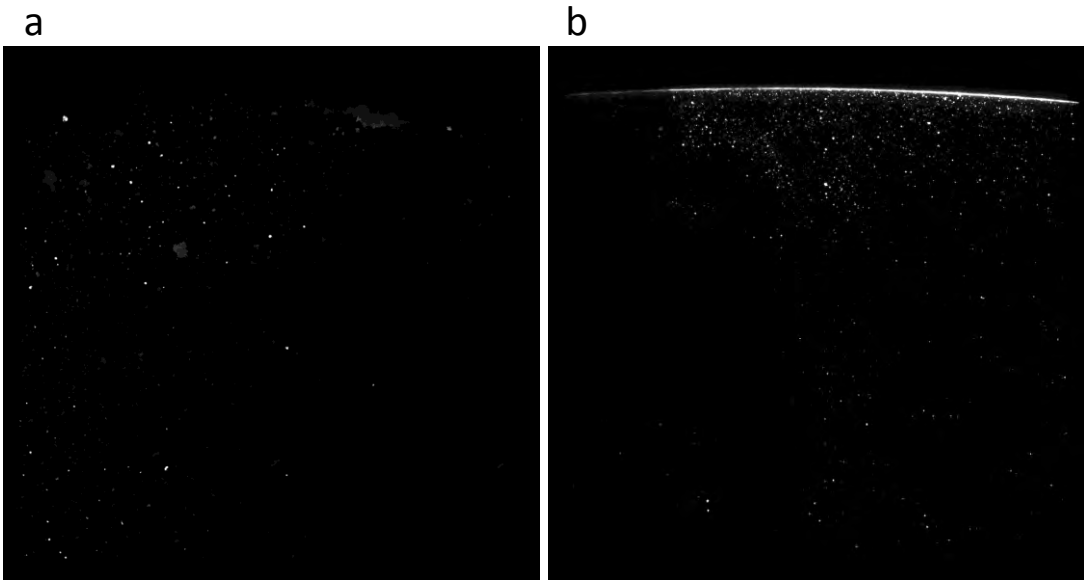

Figure D.1: Example of PIV Images captured (a) position L; (b) position H)

In both of the images, a range of brightness is observable for the particles (grayscale values). In addition the image shown for Position H appears brighter (contains more pixels of higher grayscale values) than that in the lower position. Grayscale histograms of these images are displayed in Figure D.2, so that the spread of values can be studied quantitatively. The peak of the distribution position H is further to the right, indicating the presence of a greater number of brighter pixels than for position L.

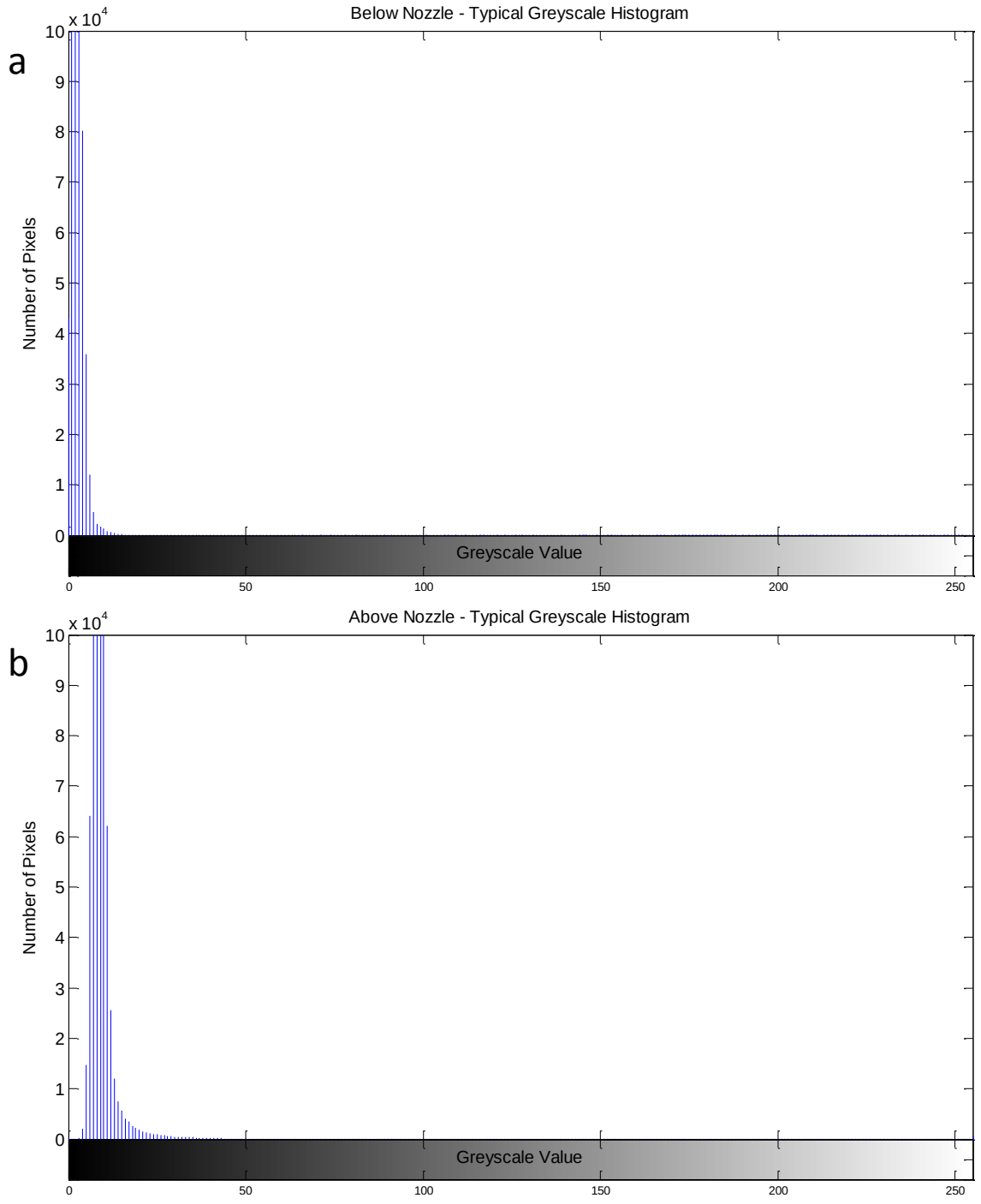

Figure D.2: Histograms of greyscale values for the images shown in Figure 6.1: (a) position L; (b) position H.

The ranges of grayscale values exhibited by the images require investigation of the phenomena leading to these results. Four main phenomena/issues have been considered:

- *Dissipation* of light by particles between the laser-source and image area and between the image area and camera.
- *Reflection/scattering* of laser light could illuminate particles outside of the laser sheet.
- The development of a gradient in light intensity within the laser sheet as it behaves as a *Gaussian beam* beyond its waist.
- Issues with the large *pixel resolution* used, meaning that the number of pixels covering each particle is low and therefore results in half occupied pixels with lower grayscale values.

A further important question is whether all particles visible in the image are fully within the laser sheet or whether some visible particles are partly or completely outside it.

Each of these issues will now be discussed in more detail before final conclusions on what can be seen in these images, and why, are drawn.

Dissipation – light dissipated by the in-plane particles within the laser sheet will cause reduction in intensity with distance away from the laser source. In addition scattered light will be dissipated by out of plane particles present between the measurement plane and the camera. Both will cause in-plane particles to appear to be less bright (giving lower grayscale values). As the particle loading in the dryer varies with both space and time, the amount of light dissipated will vary between different areas of the images and between frames. Additionally, images above the nozzle (position H) would experience less dissipation due to lower particle loading, giving brighter images (higher grayscale values). Conversely below

the nozzle (position L) where particle loading is known to be higher, the images are less bright. Figure 6.1 gives circumstantial evidence to support this hypothesis.

Reflection / Scattering of Light – light reflected and scattered from the dryer walls and particles within the dryer results in light travelling outside of the laser sheet, meaning that particles outside of the laser sheet volume can appear to be illuminated in images. This phenomena has been reported before, for imaging of gas-liquid flows in stirred tanks using PIV (Chung *et al.* (2009)). This was kept to a minimum by ensuring the depth of field of the camera was as fully contained in the laser sheet as possible.

Gaussian Beam – the laser sheet used can be considered as Gaussian in the vertical plane. At the waist in the laser sheet, the light can be considered to be truly coherent with no gradient in intensity through the vertical plane. Beyond the waist, the beam diverges such that its thickness in the vertical plane increases, causing a gradient in intensity of the light to develop across the vertical plane. The laser sheet then ceases to be a coherent light source and will illuminate particles to different grayscale values, depending on their position within the laser sheet. Calculations of the thickness of a Gaussian laser sheet are covered later (§D.3).

Pixel Resolution – To maximise the field of view within the tower, a large pixel size was used (120-150 µm pixel^{-1}). Consequently particles in the flow smaller than 150 µm (or those larger than 150 µm but only partially within the laser sheet) may not cover an entire pixel. This will give a lower than expected grayscale value and may indeed be indistinguishable from background noise in the image.

Since each of the phenomena above is equally possible it is most likely that the characteristics of the images are a product of all four working in combination. This prompts an interesting question as to whether the particles seen are all inside the laser sheet; in turn this presents an interesting quandary in terms of which particles are included in the image analysis and which are discarded.

D.2 Image Analysis – Choice of Threshold

The challenge in particle detection is the selection of a threshold value with which to binarize the image; *i.e.* choice of a grayscale value above which all pixels are taken to be particles and therefore white, and below which every pixel is background and therefore black. Once obtained binary images can be used to obtain particle parameters using the image analysis toolbox of MATLAB 7.1 software (Mathworks Inc.).

Initially the automated threshold calculation algorithm "*graythresh*" within the image analysis toolbox of MATLAB 7.1 software (Mathworks Inc.), was considered to be the obvious choice for calculating a threshold level for images. This algorithm uses Otsu's method, which chooses the threshold to minimise the intraclass variance of the black and white pixels. This is achieved by assuming that the image contains two classes of pixels (foreground and background), and therefore there is a bimodal distribution of grayscale values on the image histogram. The optimum threshold value is then calculated to separate the two classes such that their combined spread (intra-class variance) is at a minimum value.

The main issue with employing this algorithm is the assumption that there is a bimodal distribution of grayscale values in the image to be thresholded. This is clearly not the case for images captured during this work as shown in Figure D.2. Despite these concerns, data

was produced using this algorithm and results for particle volume fraction is shown in Figure D.3.

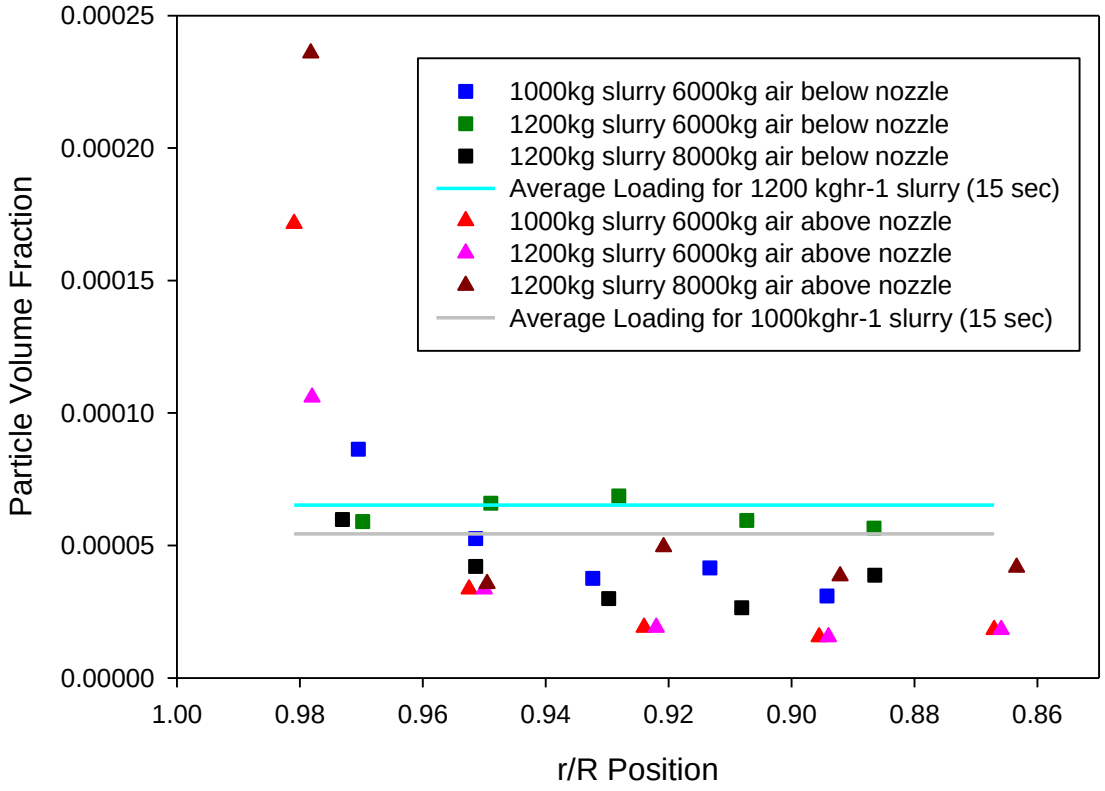

Figure D.3: Particle Volume Fraction as a Function of Radial Position Calculated with graythresh algorithm

The horizontal lines of this graph represent a mean particle volume fraction, with a residence time of 15 seconds (an expected residence time, Amador (2009)), this was calculated by dividing the volume of the amount of slurry sprayed within 15 seconds by the total volume of the dryer, to give a volume fraction. Examination of this data and comparison with the mean particle volume fraction calculated, shows that, apart from very close to the wall, the measured particle volume fraction is lower than the mean value. In practice, it would be expected that the particle concentrations would be higher over the whole measured area, since it is well known that the maximum particle volume fraction is

close to the dryer wall (Bayly (2008)), owing to particles being thrown out towards the wall by the centripetal forces of the swirling air flow. Therefore it can be concluded that Otsu's method over estimates the required threshold value, selecting only the brightest particles in the images and excluding many pixels which represent particles. Since this method was the only automated method available in the image analysis toolbox of MATLAB 7.1 software (Mathworks Inc.), it was decided to develop a manual method for identifying the threshold values.

The first step in the development of a thresholding method was to examine how changing the threshold value (greyscale value running from 0 to 256) affected the number of particles detected in an image. Examples of these plots are shown in Figure D.4, where the number of particles are plotted on a logarithmic scale. Figure D.4 a is taken for a dataset at position H and Figure D.4 b is taken at position L. Each sub-figure shows data from five images (A, B, C, D and E selected from evenly spaced points throughout the dataset) to demonstrate the variation.

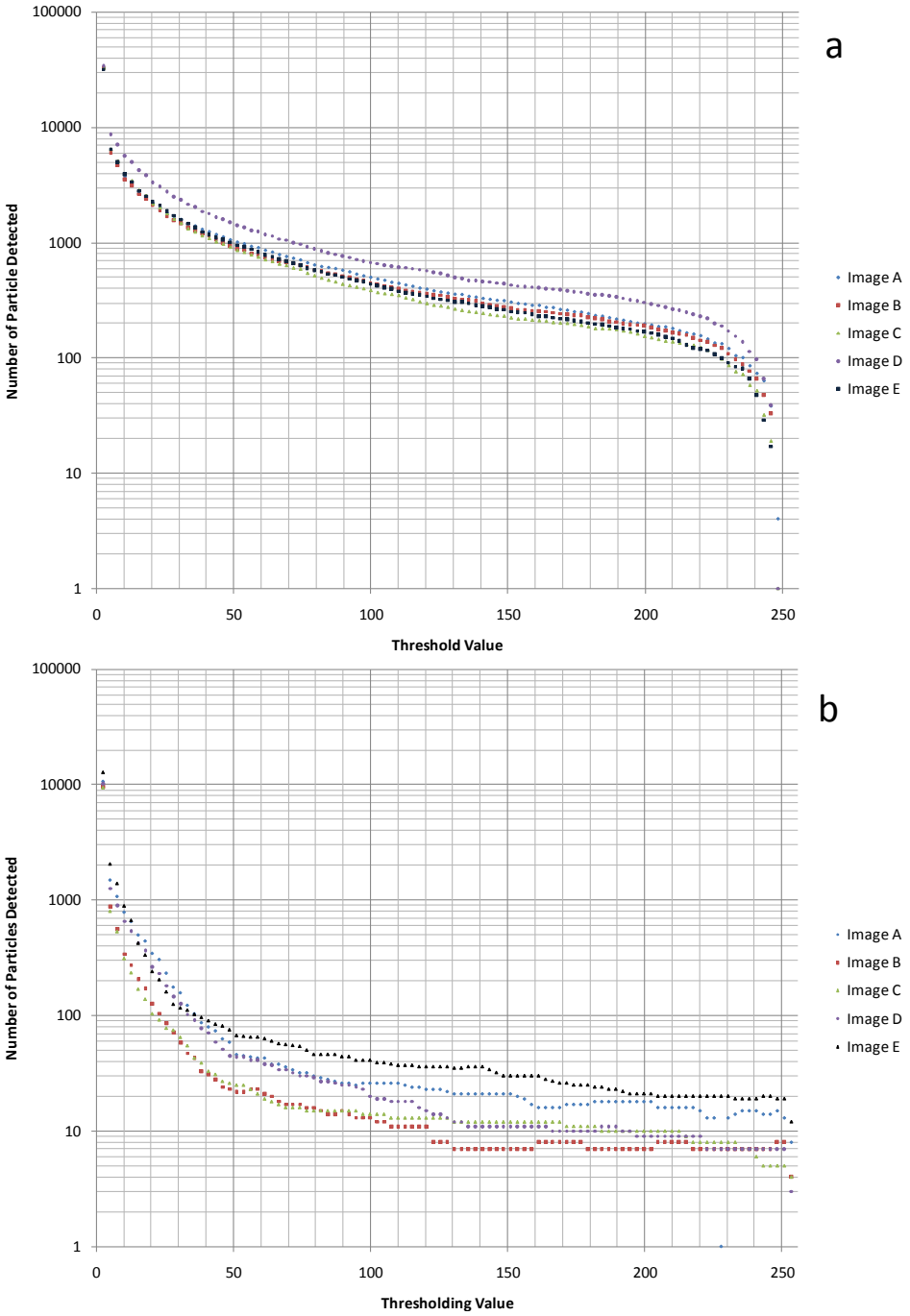

Figure D.4: Number of particles detected as a function of threshold value: (a) position H; (b) position L

For all images, the number of particles can be seen to initially decrease rapidly with increasing threshold value after which the number of particles detected changes less rapidly. For the below nozzle data, the number of particles detected appears to reach a plateau of

shallow gradient, for the above nozzle data, this is less apparent. These plots show that the effect of thresholding value on the number of particles detected is always present, but is less significant once threshold values increase beyond greyscale values of 51 particularly for the below nozzle data.

The basis used for obtaining a thresholding value for all image sets was to assume that only particles in focus could be in the laser sheet. Therefore the grayscale values of in and out-of-focus particles could form the basis for choice of threshold level. This was achieved by manually surveying a selection of images from each dataset and identifying in and out-of-focus particles. The range of grayscale values seen in each was summarised, allowing the minimum grayscale value for in-focus particle to be identified. This was used as the threshold, thus ensuring all out-of-focus particles were classed as background. Figure D.5 gives an example of this process, where particles are selected from the image, (Figure D.5a) based on their focus; their corresponding grayscale values are noted on Figure D.5b.

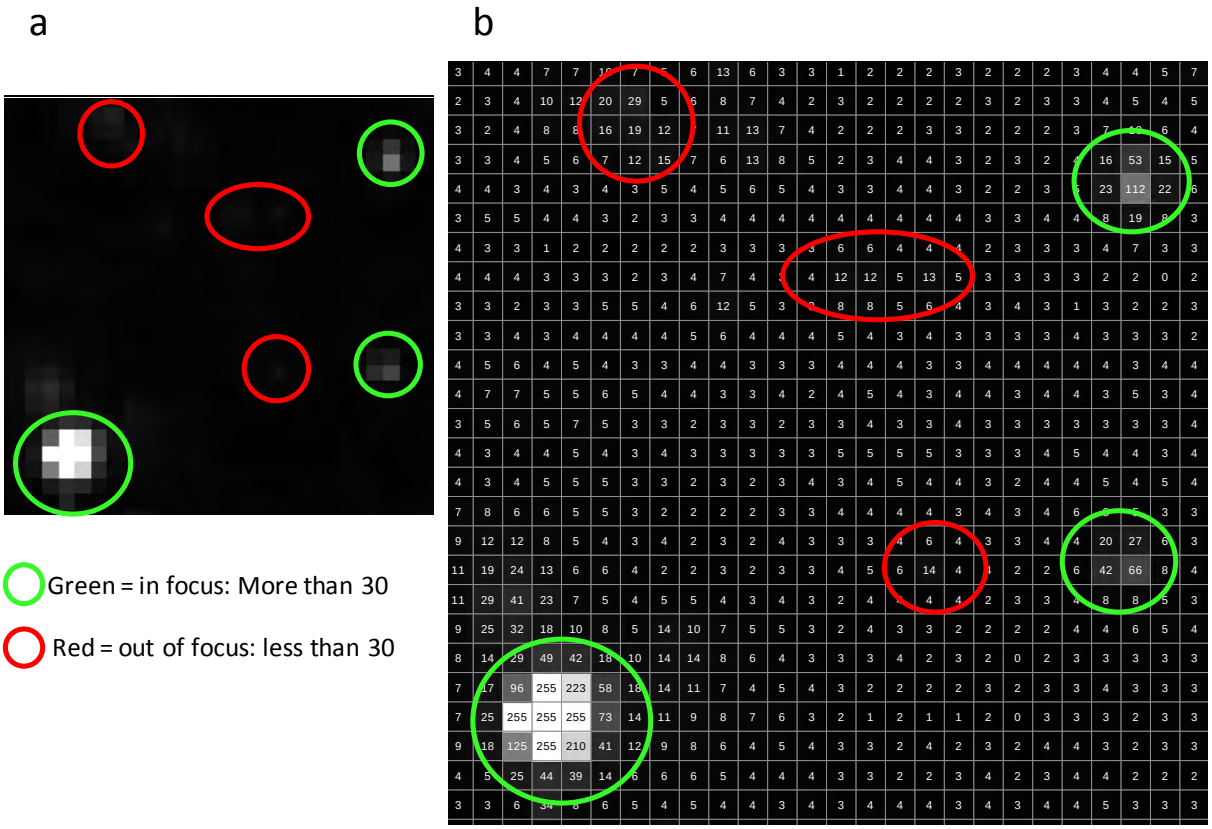

Figure D.5: (a) Example of particle selection to obtain threshold value; (b) corresponding grayscale values.

Table D.1 shows values for both the manually calculated threshold value (used in the final analysis) and the threshold value calculated by the graythresh algorithm. The value produced by the latter is always greater than the manually calculated value, and this difference, is responsible for the lower particle volume fractions calculated using the graythresh algorithm. Examining the contents of Table D.1 leads to the conclusion that the differences in greyscale values between graythresh and the manual method are very small in position H and hugely different in position L. This observation can be explained by considering the differences in the images obtained from the two positions, as shown in the previous sections (Figure D.1 to D.4). These differences mean that the graythresh algorithm, which assumes a binary distribution of greyscale values works better position H images,

where there is a smaller range of greyscale values than position L images (for the reasons listed in D.1). Therefore the more successful application of graythresh to position H images results in a greyscale value for thresholding closer to the one obtained through the manual method, where as for position L, the graythresh algorithm fails to get close to the manual method value. Example of the MATLAB codes written for this analysis are displayed in Appendix A.

Table D.1: Thresholding levels for all datasets

Relative Slurry Flowrate		**Air Flowrate ($kghr^{-1}$)**	**Graythresh Thresholding grayscale Value**	**Manual Thresholding grayscale Value**
Position H	1.00	6000	102	87
	1.20	6000	108	95
	1.20	8000	102	92
Position L	1.00	6000	100	33
	1.20	6000	92	28
	1.20	8000	97	26

D.3 Calculation of Size, Conentration and Loading Parameters

Once binary images were obtained using the manual method for obtaining the threshold, the "*regionalprops*" algorithm within the MATLAB image analysis toolbox was used to automatically calculate and list key parameters for each particle in the binary image. This algorithm works by identifying and numbering each particle and then creating a matrix

which lists selected parameters of each particle. For the purpose of this work, for each particle, the position of the centroid was listed as a pair of x and y coordinates along with the equivalent diameter of a circle with the same area as the particle *i.e.*

$$d_A = \left(\frac{4A_P}{\pi} \right)^{1/2} \quad \text{(D.1)}$$

Where A_P is the particle area as measured by the algorithm and d_A is the area equivalent diameter.

This matrix of particle properties and positions was created for 1 image in each image pair obtained, (2000 images per experimental condition) and then all of the individual image matrices were collated and used to calculate mean data for the whole set of images. The particle data were sorted as function of position within the image based on the centroid coordinates; by binning particles based on their position, plots of particle parameters as a function of position within the image were created. Mean particle diameter data was calculated as the mean diameter of all particles located with each area, as the image was split into a 16 × 16 grid of equally sized squares. The value given by MATLAB was converted from pixels into metres or micrometres. Particle size distributions were calculated by binning particles based on their diameters, so that a count per diameter in pixels could be created. This count was then turned into a mass fraction of the total number of particles assuming spherical particles with a constant density across all diameters. The bin sizes used were then converted from pixels into metres or micrometres.

To calculate the number concentration and volume fraction of particles in the image or a specific area of the image, the volume occupied by the laser sheet is required. The depth of

the lasersheet was calculated at the two extremes of the image area, as shown in the cross-section in Figure D.6. The cross-sectional area of the image was then calculated by treating this as a trapezium, thusly:

$$A = \frac{1}{2} y(z_1 + z_2) \qquad \text{(D.2)}$$

The value of the cross-sectional area obtained was then multiplied by the value of the x dimension of the image area, to give the representative volume. This calculation was repeated for each image, or section of image as required.

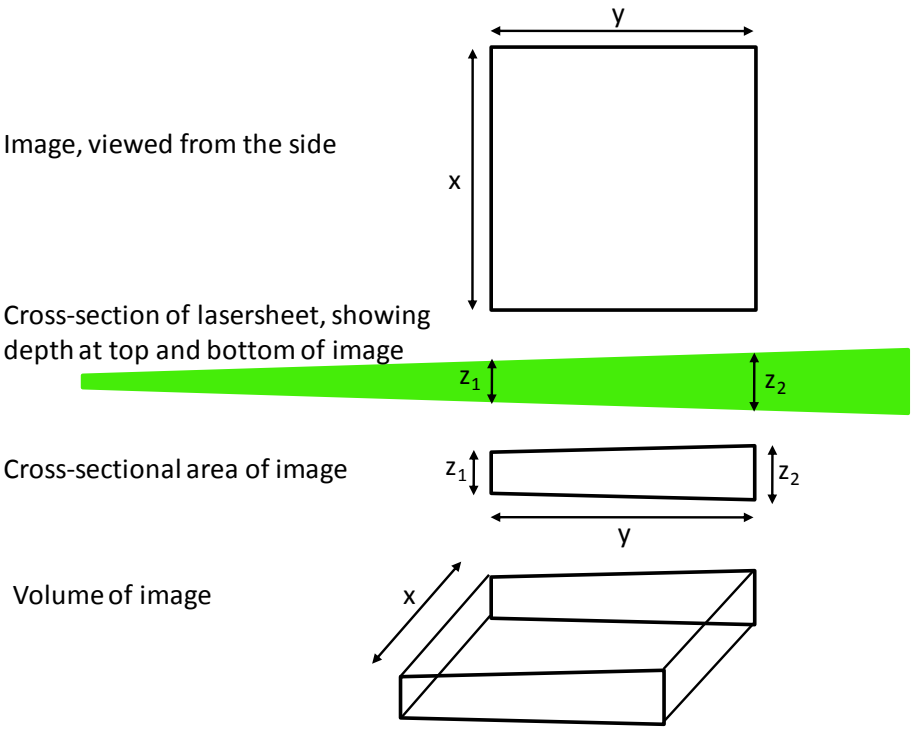

Figure D.6: Area of lasersheet covered by image

The thickness of the lasersheet was calculated by using assuming it acted as a Gaussian beam. The divergence of a Gaussian beam beyond its waist is shown in Figure D.7.

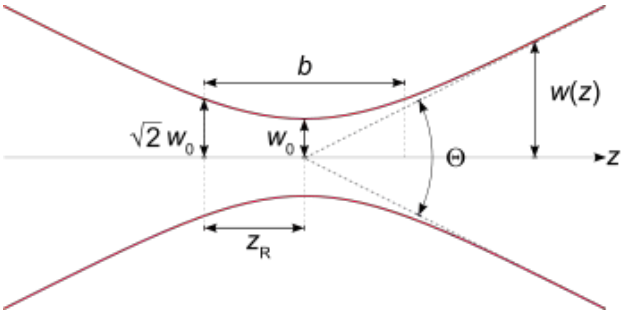

Figure D.7: The divergence of a Gaussian beam around the waist

The value of $w(z)$, half the thickness of the laser sheet as a function of distance from its waist, as shown in Figure D.7, was calculated using equation (D.3), given below:

$$w(z) = w_0\sqrt{1+\left(\frac{z}{z_R}\right)^2} \tag{D.3}$$

The Rayleigh length (Z_R), is calculated using equation (D.4) below. The Rayleigh length is the distance from the waist at which the cross section of the beam (thickness in this case) has doubled.

$$z_R = \frac{\pi w_0^2}{\lambda} \tag{D.4}$$

In addition the angular spread of the sheet can be calculated as shown below, note Θ in Figure D.7 is twice the value given using equation (D.5).

$$\theta \cong \frac{\lambda}{\pi w_0} \tag{D.5}$$

To obtain particle number concentrations the total number of particles in each area of the image was divided by the volume calculated for each specific area of the image. To obtain particle volume fractions, particle volume, V_P was calculated using spherical equivalence ('regionalprops' algorithm in MATLAB)

$$V_P = \frac{\pi d_A^{\,3}}{6} \tag{D.6}$$

The volume of particles in each area of the image was then summed and divided by the volume calculated for each specific area of the image, to give the volume fraction.

D.4 Particle PIV Cross-Correlation

Cross-correlation of PIV images was conducted using binary images produced using the method developed in §D.2 thus reducing errors from particles not in the focus (calibration) range of the camera.

The high-resolution PIV algorithm (Nyquist grid) within the TSI Insight 3G software supplied with the PIV equipment was used to conduct cross-correlation of the binary images. The settings used in this algorithm were chosen to minimise errors in the calculation of the velocity vectors. No velocity vector was produced for an interrogation spot containing less than 16 particles and particles below 2 pixels in size were ignored. Hence particles less than 400 µm in diameter were not included in this analysis. To maximise the number of particles in each integration spot whilst maintaining a reasonable resolution, an interrogation spot size of 64 × 64 pixels was used. Cross-correlation was conducted for 2000 image pairs (4 seconds) for each experimental condition. The velocity vector files were processed using MATLAB 7.1 software (Mathworks Inc.), in a similar manner to that of the air flow vectors (§3.5).

D.5 Sources of Potential Error in Analysis Methods

The images captured presented a significant challenge in developing image analysis routes which would allow reliable data to be obtained and minimise error. However, despite these efforts there are still several significant potential sources of error that need to be considered in this analysis. Also of note is that the vast majority of errors are systemic, with the consequence that comparison between datasets can be made with confidence although absolute values of the parameters may be shifted from the true values. Sources of systemic error are:

Thresholding Value – the grayscale value chosen for thresholding represents the cut-off for particles to be included in the analysis, therefore this can influence all results produced. Owing to the fact that different thresholding values were used for different data-sets (which have differing grayscale distributions) then the influence of this potential error can change between datasets. The effect of this error was examined in Figure D.4.

Focusing – it is assumed that the depth of field is larger than the lasersheet thickness and therefore all illuminated particles are in focus, and furthermore in focus particles are within the lasersheet. If particles are out of focus this will lead to their diameter being incorrectly calculated, in turn affecting size and loading data. In addition out of focus particles may be included or rejected by thresholding. This error is systemic between datasets in the same experimental position as the camera was only focused once in each position (f-stop kept constant). Since the camera was carefully focused this error is minimised.

Resolution – as discussed previously, a large pixel resolution was used during this work to maximize the area imaged. This means that the number of pixels covering each particle is

low and therefore results in half occupied pixels with lower grayscale values. This introduces an error in partly illuminated pixels that can be eliminated during thresholding, meaning that particle size can be underestimated, or in the worst case small particles can be eliminated. Issues with how particle shape is displayed by a small number of pixels can also lead to errors with how the equivalent diameter is calculated. This error comes from mis-estimation of particle size owing to resolution and is expressed as an absolute error of ±1 pixel on mean particle diameter plots (Figure D.2). This error was not accounted for on volume calculations due to being combined with errors on assuming spherical particles, as discussed next.

Orientation and shape of particles – using the equivalent diameters will not only create errors on the diameters calculated, but will also introduce errors into calculating particle volumes. In addition, assuming that all particles are spherical will also introduce errors as detergent powders are known to be irregularly shaped, meaning that volumes are under/over estimated. Errors could also be introduced by the orientation of particles in the laser sheet, although this could be eliminated if it is assumed that their orientation is random due to the large number of particles imaged.

Appendix E – Particle Characterisation and Impacts Statistical Analysis

The purpose of this appendix is to display the full datasets for the statistical analysis conducted on the particle impacts results shown in Chapter 7.

E.1 Correlation of all Variables

Presented in table E.1 below is the correlation values obtained between all of the variables examined in Chapter 7. This table is formatted by colour to aid visualisation of the trends, yellow cells indicate little correlation between the two variables, and green cells mean that there is a positive correlation between the two variables, meaning they increase/decrease with each other and red cells mean there is a negative correlation between then variables and one increases/decreases the other. The shade of green/red shown in the cell indicates the strength of the correlation, with darker greens showing stronger positive correlations and darker reds showing stronger negative correlations.

		Particle Properties											Impact			Response					
		LAS content	SiO2 content	Representative Diameter	Envelope Density	Apparent Density	Moisture Content	eRH	Unconfined Young's Modulus	Unconfined Yield Stress	Confined Yield Stress	Confined Joint Stress	Impact Velocity	Normal Impact Velocity	Impact Angle	Breakage Fraction	Number of Fragments	Restitution Coefficient	Normal Restitution	Rebound Angle from Impact	Rebound Angle from Surface
Particle Properties	LAS content	1.00	-0.28	0.00	-0.50	-0.81	0.15	-0.01	-0.84	-0.88	0.16	-0.08	0.01	0.01	0.00	-0.04	-0.01	-0.10	-0.07	-0.02	-0.03
	SiO2 content	-0.28	1.00	0.00	-0.11	-0.14	0.62	-0.49	0.01	0.49	0.40	0.34	0.00	0.00	0.00	-0.02	-0.10	0.09	0.20	0.00	0.03
	Representative Diameter	0.00	0.00	1.00	0.67	-0.34	0.59	0.12	-0.20	0.10	-0.30	-0.48	0.00	0.00	0.00	0.62	0.62	0.00	-0.23	0.08	0.07
	Envelope Density	-0.50	-0.11	0.67	1.00	0.38	0.07	0.29	0.51	0.37	-0.39	-0.13	-0.01	-0.01	0.00	0.34	0.36	0.04	-0.13	0.06	0.04
	Apparent Density	-0.81	-0.14	-0.34	0.38	1.00	-0.59	0.31	0.92	0.50	-0.17	0.18	-0.02	-0.02	0.00	-0.22	-0.22	0.06	0.05	0.00	-0.02
	Moisture Content	0.15	0.62	0.59	0.07	-0.59	1.00	-0.17	-0.49	0.05	0.25	-0.24	0.01	0.01	0.00	0.36	0.30	0.03	-0.09	0.05	0.08
	eRH	-0.01	-0.49	0.12	0.29	0.31	-0.17	1.00	0.29	-0.35	0.15	-0.36	0.00	0.00	0.00	0.02	0.02	-0.04	-0.27	0.03	0.00
	Unconfined Young's Modulus	-0.84	0.01	-0.20	0.51	0.92	-0.49	0.29	1.00	0.61	-0.07	0.23	-0.02	-0.02	0.00	-0.17	-0.17	0.07	0.07	0.00	-0.01
	Unconfined Yield Stress	-0.88	0.49	0.10	0.37	0.50	0.05	-0.35	0.61	1.00	-0.17	0.08	-0.01	-0.01	0.00	0.14	0.10	0.11	0.13	0.02	0.04
	Confined Yield Stress	0.16	0.40	-0.30	-0.39	-0.17	0.25	0.15	-0.07	-0.17	1.00	-0.03	0.02	0.02	0.00	-0.26	-0.30	0.02	0.04	-0.02	-0.02
	Confined Joint Stress	-0.08	0.34	-0.48	-0.13	0.18	-0.24	-0.36	0.23	0.08	-0.03	1.00	-0.01	-0.01	0.00	-0.41	-0.39	0.02	0.30	-0.06	-0.05
Impact	Impact Velocity	0.01	0.00	0.00	-0.01	-0.02	0.01	0.00	-0.02	-0.01	0.02	-0.01	1.00	0.86	0.00	0.59	0.58	-0.02	-0.23	0.09	0.11
	Normal Impact Velocity	0.01	0.00	0.00	-0.01	-0.02	0.01	0.00	-0.02	-0.01	0.02	-0.01	0.86	1.00	0.45	0.59	0.59	-0.48	-0.49	-0.38	-0.31
	Impact Angle	0.00	0.00	0.00	0.00	0.00	0.00	0.00	0.00	0.00	0.00	0.00	0.00	0.45	1.00	0.13	0.13	-0.95	-0.70	-0.98	-0.93
Response	Breakage Fraction	-0.04	-0.02	0.62	0.34	-0.22	0.36	0.02	-0.17	0.14	-0.26	-0.41	0.59	0.59	0.13	1.00	0.87	-0.17	-0.39	-0.03	0.02
	Number of Fragments	-0.01	-0.10	0.62	0.36	-0.22	0.30	0.02	-0.17	0.10	-0.30	-0.39	0.58	0.59	0.13	0.87	1.00	-0.18	-0.40	-0.03	0.00
	Restitution Coefficient	-0.10	0.09	0.00	0.04	0.06	0.03	-0.04	0.07	0.11	0.02	0.02	-0.02	-0.48	-0.95	-0.17	-0.18	1.00	0.71	0.94	0.86
	Normal Restitution Coefficient	-0.07	0.20	-0.23	-0.13	0.05	-0.09	-0.27	0.07	0.13	0.04	0.30	-0.23	-0.49	-0.70	-0.39	-0.40	0.71	1.00	0.60	0.60
	Rebound Angle from Impact	-0.02	0.00	0.08	0.06	0.00	0.05	0.03	0.00	0.02	-0.02	-0.06	0.09	-0.38	-0.98	-0.03	-0.03	0.94	0.60	1.00	0.91
	Rebound Angle from Surface	-0.03	0.03	0.07	0.04	-0.02	0.08	0.00	-0.01	0.04	-0.02	-0.05	0.11	-0.31	-0.93	0.02	0.00	0.86	0.60	0.91	1.00

Figure E.1: Correlation values of particle impacts variables

E.2 Modelling of Response Variables

To further understand the effect of impact pararmeters, particle size and formulation on impact behaviour, response surface models were fit to the three main responses, namely breakage fraction, restitution coefficent and rebound angle. Terms not significant at the 5% significance level were removed from the model, meaning that only the key parameters were used in these models.

E.2.1 Breakage Fraction

As shown previously, Figure E.2 shows that the largest effects on breakage fraction are from rep. diameter and impact velocity. For both of these effects the biggest impact occurs moving from low to mid levels with the effect flattening off at higher levels, this is particularly evident for rep diameter. By optimising the model to minimise breakage fraction it can be seen that this occurs at the mid level of SiO2, and low levels of the other 3 factors.

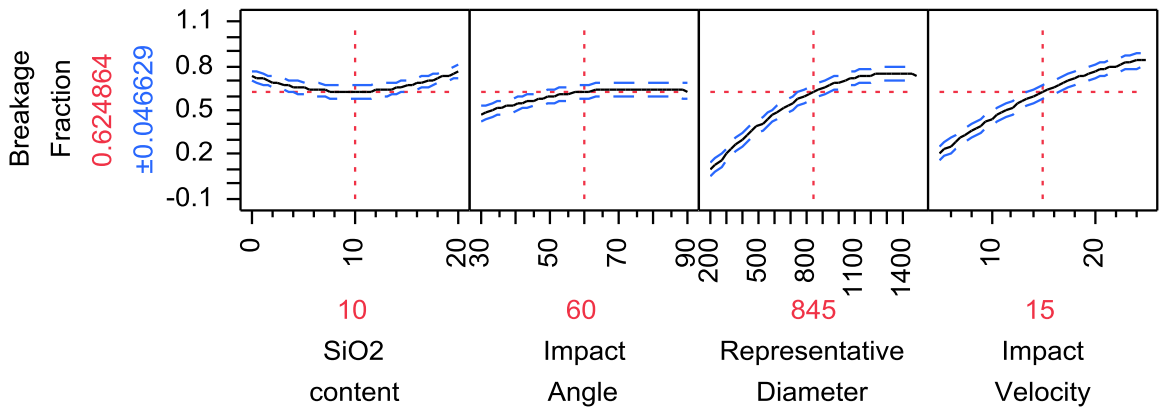

Figure E.2: Breakage fraction response models for key parameters

E.2.2 Restitution Coefficent

Figure E.3 shows that the largest effect on restitution coefficient comes from impact angle. Other parameters that have significant, but much smaller effects, are LAS and SiO_2 content, representative diameter and impact velocity.

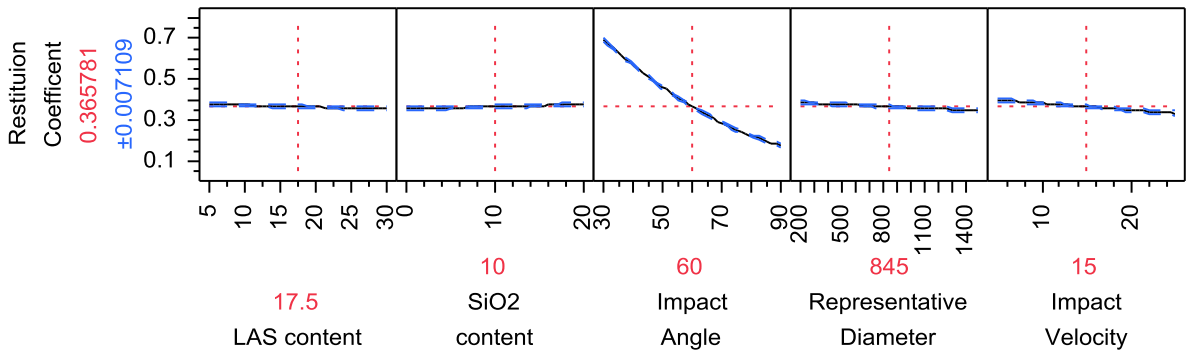

Figure E.3: Restitution Coefficent response models for key parameters

E.2.3 Rebound Angle from Impact

Figure E.4 shows that the largest effect on rebound angle from the impact comes from impact angle, as with restitution coefficent. Other parameters that have significant, but much smaller effects, are LAS and SiO_2 content, representative diameter and impact velocity.

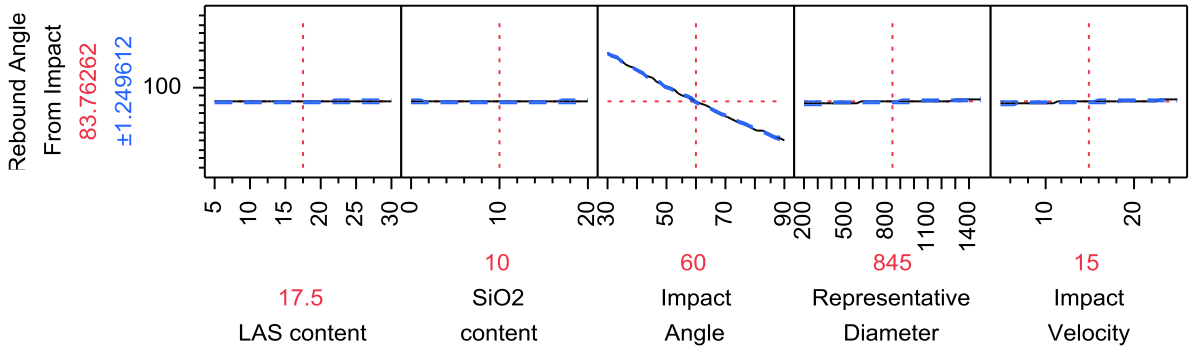

Figure E.4: Rebound angle from impact response models for key parameters